Dissertation

submitted to the

Combined Faculties of the Natural Sciences and Mathematics
of the Ruperto-Carola University of Heidelberg, Germany

for the degree of

Doctor of Natural Sciences

Put forward by

Florian Jörg

born in: Bretten, Germany
Oral examination: 22 June, 2022

From ^{222}Rn measurements in XENONnT and HeXe to radon mitigation in future liquid xenon experiments

1st Referee: Priv.-Doz. Dr. Teresa Marrodán Undagoitia
2nd Referee: JProf. Dr. Loredana Gastaldo

From ^{222}Rn measurements in XENONnT and HeXe to radon mitigation in future liquid xenon experiments

While overwhelming evidence has been found for the existence of dark matter in our universe, its true nature remains a mystery. The XENONnT experiment has recently completed its commissioning and is now on the quest to solve this puzzle. This endeavor is threatened by the background caused by the emanation of ^{222}Rn. In this work, a first estimate of the experiment's radon concentration will be given. Furthermore, the capabilities of the distillation-based radon removal system are demonstrated.
For future liquid xenon (LXe) based experiments, the ^{222}Rn-induced background needs to be suppressed even further. A novel radon mitigation technique using surface coatings has been investigated. Very promising reduction factors of more than three orders of magnitude have been achieved with electrochemically plated copper layers, applied to radium implanted stainless steel samples.
Additionally, the interactions of alpha particles from ^{222}Rn and electrons from ^{83m}Kr have been studied in the Heidelberg Xenon (HeXe) time projection chamber (TPC). Field dependent measurements of the electron drift velocity as well as the charge and light yield are presented. For both, an emphasis was put on the regime of low drift fields, to improve the modeling and reconstruction in future LXe detectors.

^{222}Rn Messungen in XENONnT und HeXe, sowie Methoden zur Radonreduktion für zukünftige flüssig Xenon Detektoren

Obwohl viele Hinweise auf die Existenz dunkler Materie hindeuten, bleibt deren grundlegende Beschaffenheit weiterhin ungeklärt. Das kürzlich in Betrieb genommene XENONnT Experiment, begibt sich nun auf die Suche nach einer Antwort auf diese Frage. Das Gelingen dieses Unterfangens wird maßgeblich vom Untergrund aufgrund der ^{222}Rn Emanation beeinflusst. Eine erste Abschätzung der Radonkonzentration, sowie deren mögliche Reduktion mithilfe einer neuen Destillationsanlage werden in dieser Arbeit dargelegt.
Zukünftige flüssig Xenon Detektoren stellen deutlich höhere Anforderungen an die Reduktion dieses Untergrunds. Diese können nur mithilfe neuartiger Methoden zur Radonreduktion bedient werden. Diesbezüglich wurden sehr vielversprechende Ergebnisse mit elektrochemisch deponierten Kupfer Schichten erreicht. Mit deren Hilfe ließsich die Radonemanation von Radium implantierten Edelstahlproben um mehr als drei Größenordnungen reduzieren.
Weiterhin wurde die Wechselwirkung zwischen Elektronen und Alphateilchen mit flüssigem Xenon untersucht. Vermessen wurde die Feldstärkenabhängigkeit der Xenon Szintillation und Ionisation, sowie die Driftgeschwindigkeit von Elektronen. Ein besonderes Augenmerk wurde hierbei auf den Bereich niedriger Feldstärken gelegt, wodurch sich die Modellierung und Rekonstruktion zukünftiger Detektoren verbessern lässt.

To my beloved father

Contents

1 From dark matter particles to light signals

> Darkness cannot drive out darkness:
> only light can do that.
> Hate cannot drive out hate:
> only love can do that.
>
> — Martin Luther King Jr.
> *A Testament of Hope*

There is growing evidence that our universe contains a large amount of dark matter (DM). From recent observations we know that it is about five times more abundant than ordinary matter [1]. With several theories being discarded already by the sustained null results of experimental searches for DM, proof for its true nature is yet to be found. Finding the answer to this question would solve one of the main puzzles in today's physics. The present work is centered around dual-phase xenon time projection chambers (TPCs) [2], which belong to one of several detector technologies that are set out on this quest. This introductory chapter will start with a brief overview of the indications for the existence of DM and the possible ways for its detection. More complete accounts of the subject can be found for example in [3–5]. Afterwards, the working principle of a xenon TPC is introduced using the recently commissioned XENONnT experiment [6] as an example, followed by an outlook into the future of this technology.

1.1 The dark matter in the universe

1.1.1 Evidence for dark matter

The earliest hints for non-luminous matter were encountered by Fritz Zwicky [7] in the 1930s and by Vera C. Rubin [8] in the late 1970s. Both observed a mismatch in the movement of celestial objects with their expectation from Newtonian mechanics. It was found for example by Rubin that the outer stars of several galaxies circle their center with velocities that are too high to remain gravitationally bound. This is illustrated on the example of the M33 galaxy [9] in figure 1.1. It shows the rotational velocity (rotation curve) of stars and neutral hydrogen, as a function of distance R from the galactic center. With the declining gravitational force outside of the central region of the galaxy, a decrease of the velocity with $1/\sqrt{R}$ is expected [3]. This is in contradiction to the observed slightly increasing orbital speed as function of the radius.

It is known that Newtonian gravity is only approximately correct. The theory of general relativity (GR) is for example needed to correctly describe Mercury's peri-

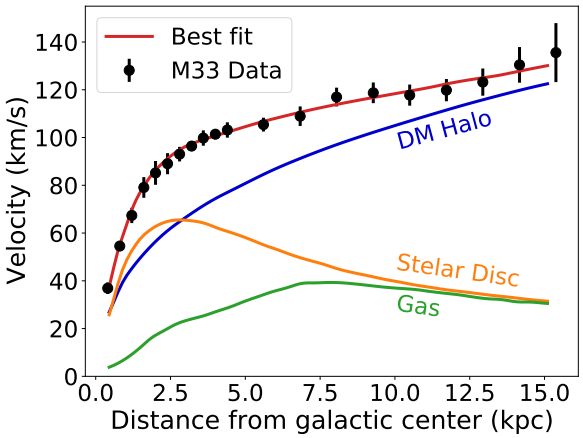

Figure 1.1: Rotation curve of the M33 galaxy. The observed velocity dependence as a function of the distance (black •) is explained by contributions from stellar disc (orange), galactic gas (green) and the dark matter halo (blue). Figure adapted from [9].

helion precession [10] [1]. Similarly, it might fail to correctly predict the gravitational force at a typical galactic length scale. This motivated the introduction of a modified Newtonian dynamics (MOND) (see e.g. [12]), as well as other theories of modified gravity. Though MOND can resolve the discrepancy found in the rotation curves of galaxies, it typically fails to simultaneously explain the further evidences for DM [3].

A more accepted explanation for the observed rotation curves is by assuming that the galaxy is embedded into an extended DM halo. It is thought to be constituted by individual constituents which circle the galaxy on Keplarian orbits. For the Milky Way they would have an average density of $0.3\,\mathrm{GeV/c^2/cm^3}$ and a mean velocity of $220\,\mathrm{km/s}$ at the location of the Sun [4]. The hypothesis that the halo is made up by massive compact halo objectss (MACHOs) like black holes, rouge planets or brown dwarfs [3, 4], is disfavored by gravitational microlensing surveys [14, 15]. The same holds true for most types of the hypothetical primordial black holes [16]. Therefore, one of the most plausible explanations is that DM consists of elementary particles, similarly to "ordinary" baryonic matter.

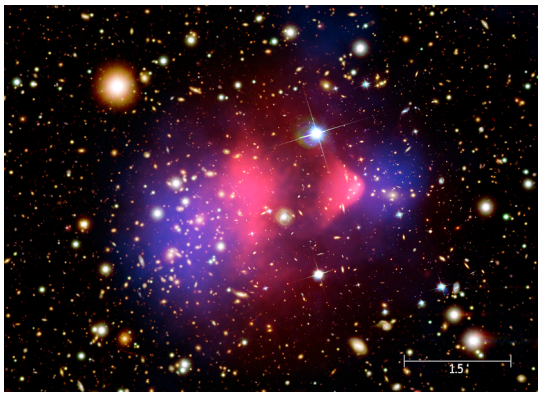

Figure 1.2: Composition of an optical and X-ray image (pink) overlain with the mass distribution obtained from weak gravitational lensing (blue) of the Bullet-Cluster (1E 0657-56). Figure taken from [13].

Further evidence for the DM existence has been gathered using weak gravitational lensing [17]. It leads to distorted images of background galaxies by a massive object in the foreground and can be used to map out the matter distribution of an object. One of the most famous objects with such a mapping is the Bullet Cluster (1E

[1] Similar to introducing DM to explain the rotation curves, it had been speculated that a *hidden* planet (Vulcan) is the cause for the observed deviation [11].

0657-56) shown in figure 1.2. The optical images taken by the Magellan and Hubble telescopes capture the aftermath of the collision of two galaxy clusters. While the constituent galaxies of both clusters crossed without significant interaction, the intergalactic gas of both clusters collided and decelerated. This resulted in a significant increase of temperature and emission of X-rays as detected by the Chandra observatory and overlain in pink. Shown in blue is the mass distribution determined from weak gravitational lensing. It reveals a clear offset between the colliding gas clouds containing the majority of the baryonic matter and the centers of gravity of both sub-clusters [18]. This observations is a clear indication for a larger amount of non-baryonic matter, showing very little self-interaction. A systematic analysis of 72 colliding galaxy clusters determined such a displacement in the majority of cases [19].

Furthermore, dark matter is presumed to be essential for the formation of the large-scale structure which permeates our universe. Two different impressions of this "cosmic web" [20] are compared in figure 1.3. Shown in blue are the results from three different galaxy surveys [21–23], while the outcome of the *Millennium* N-body simulation [24] is shown in red. This simulation tracks the formation of structures

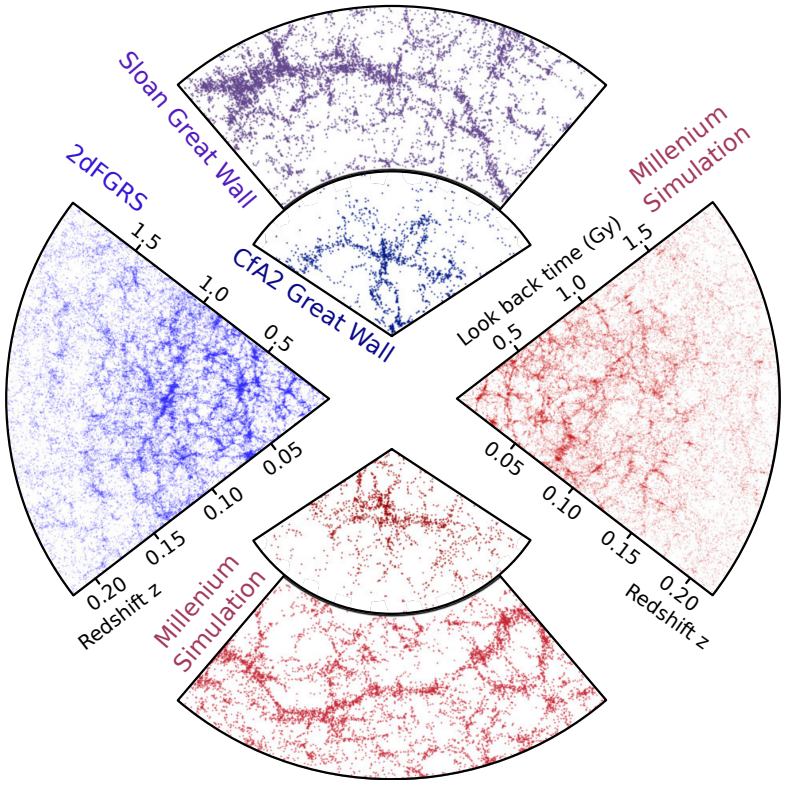

Figure 1.3: Observed large-scale structure in the distribution of galaxies in the universe (blue). Shown in red color is the converted outcome of the *Millennium* N-body simulation [24]. The simulation reproduces very similar structures as are observed in today's universe from a slightly perturbed initial DM distribution. Figure adapted from [25].

in a virtual universe following the ΛCDM cosmological standard model. It assumes that the universe is filled with baryonic matter, "cold" – non-relativistic – dark matter (CDM), as well as dark energy in form of the cosmological constant (Λ) [26]. This model is also used to explain the temperature fluctuations which are imprinted in the cosmic microwave background (CMB) [1]. The striking similarity between the

simulated and the observed structure shown in figure 1.3 is a clear evidence of the existence of DM.

These observations put several constraints on the properties which the DM particles need to have. The most important ones are summarized below, while a detailed discussion can be found, for example, in [27]. To interact gravitationally, the DM particles must be massive. They are allowed to participate in the weak interaction, while their interactions via the electromagnetic or strong force need to be strongly suppressed or even absent. Furthermore, they need to be stable with respect to the age of the universe. The standard model (SM) of particle physics offers only the neutrino, which fulfills all criteria [2]. Their relativistic speed however, makes them "hot" dark matter and their fermionic character limits their maximum density due to phase-space arguments [29]. Therefore, SM neutrinos constitute only a subdominant fraction of the DM in the universe. Without another suitable candidate in the SM, the existence of dark matter is a clear indication for beyond standard model (BSM) physics. Notable candidates from BSM theories are for example sterile neutrinos [30] and axion-like particles [31]. Another important group of candidates are so-called weakly interacting massive particles (WIMPs), which emerge from several BSM theories [4]. They are predicted over a range of masses between $1\,\mathrm{GeV/c^2}$ up to $100\,\mathrm{TeV/c^2}$, with interaction cross-sections in the range of 10^{-41} to $10^{-51}\,\mathrm{cm^2}$ [4, 32].

1.1.2 Dark matter detection

Three different search strategies are followed in the attempt to detect DM. They can be subdivided into direct and indirect detection, as well as colliders searches [5]. Where each strategy corresponds to one of the indicated directions in the simplified Feynman diagram sketched in figure 1.4 [3]. Reading the graph in the bottom-up direction it represents the production of DM particles out of SM particles. Such reactions are searched for at particle accelerators such as the large hadron *collider* (LHC). Since the DM particles have a very low interaction probability, they will not leave any traces in the detectors surrounding the interaction point. However, they will leave their imprint in the energy momentum balance of the reaction. As they leave the detector undetected, they can be searched for in events featuring an imbalance in the traverse momentum of the produced particles. A more detailed review of the possible signatures and reactions can be found for example in [33]. The latest results from LHC experiments however did not reveal any

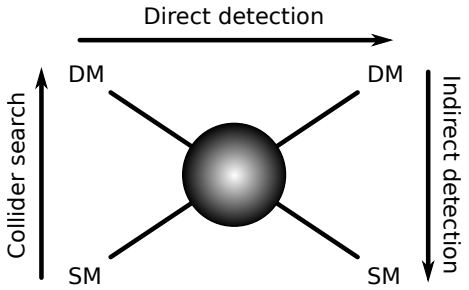

Figure 1.4: Sketch of the three approaches for DM detection. Figure adapted from [3].

[2] Though the SM does not include a neutrino mass, it is known from the observation of neutrino oscillations [28], that they are not massless.

deviation from the SM prediction [34, 35].

The top-down direction in figure 1.4 describes the annihilation of two DM particles into a pair of SM particles. If the DM particles have a finite lifetime, SM particles could also emerge from their decay. *Indirect* searches for DM search for these particles in astrophysical sources such as the galactic center or the sun in which a high DM density is expected. Suitable annihilation or decay products for such searches are, for example, gamma- and x-rays, as well as neutrinos and anti-matter particles like positrons or anti-hydrogen [5, 36].

When reading figure 1.4 in the left-to-right direction, it describes the scattering between DM and SM particles. Such *direct* interactions are searched for using low-background experiments with large target masses. The kinetic energy of the DM particles can lead to a measurable energy deposition E from the DM particle to a particle in the detector medium. The differential event rate $dR\,/\,dE$ is given by [3, 4, 37]

$$\frac{dR}{dE} = \frac{\rho_\chi}{m_\chi \cdot m_A} \cdot \int_{v_{\min}}^{v_{\text{esc}}} v \cdot f(v,t) \cdot \frac{d\sigma}{dE}(E,v)\, dv\,, \tag{1.1}$$

where m_χ and m_A are the respective masses of the DM and SM particles; ρ_χ denotes the average density of DM particles at the location of the Earth, and $f(v,t)$ is their velocity distribution function in the detector's rest frame. This distribution then needs to be convoluted with the differential interaction cross-section σ. To exceed the detectors energy threshold, a minimum velocity $v_{\min}$ is required. At the same time, no particles will have velocities larger than the Milky-Way's escape velocity v_{esc}. Due to the rotation of the Earth around the sun, the relative DM velocity distribution $f(v,t)$ changes over the course of the year, leading to an annual modulation of the event rate.

Depending on the medium, the deposited energy is channeled into scintillation photons, production of electron-ion pairs (ionization) or lattice excitation (phonons) [3]. Phonons are usually measured via a temperature increase using transition edge sensor (TES) in cryogenically operated detectors, while electrons are drifted to a read-out and amplification region [4]. Scintillation photons can be measured using sensitive photo detectors, such as photomultiplier tubes (PMTs). Due to quenching effects, the ratio between the relative amount of signal in each of these channels depends on the interaction type. This allows detectors which simultaneously measure more than one signal to distinguish between different interaction types.

Most parameters of equation 1.1, such as ρ_χ and $f(v,t)$ are determined from astrophysical inputs. This leaves the two parameters m_χ and σ as the typical parameter space in which direct detection experiments report their results. Figure 1.5 shows a compilation of results from different direct DM detection experiments in this space. Open curves represent upper limits on the spin-independent interaction cross section σ [3]. The curves feature a minimum framed by a steep increase towards lower masses and a more shallow increase for higher mass particles. Since the DM density

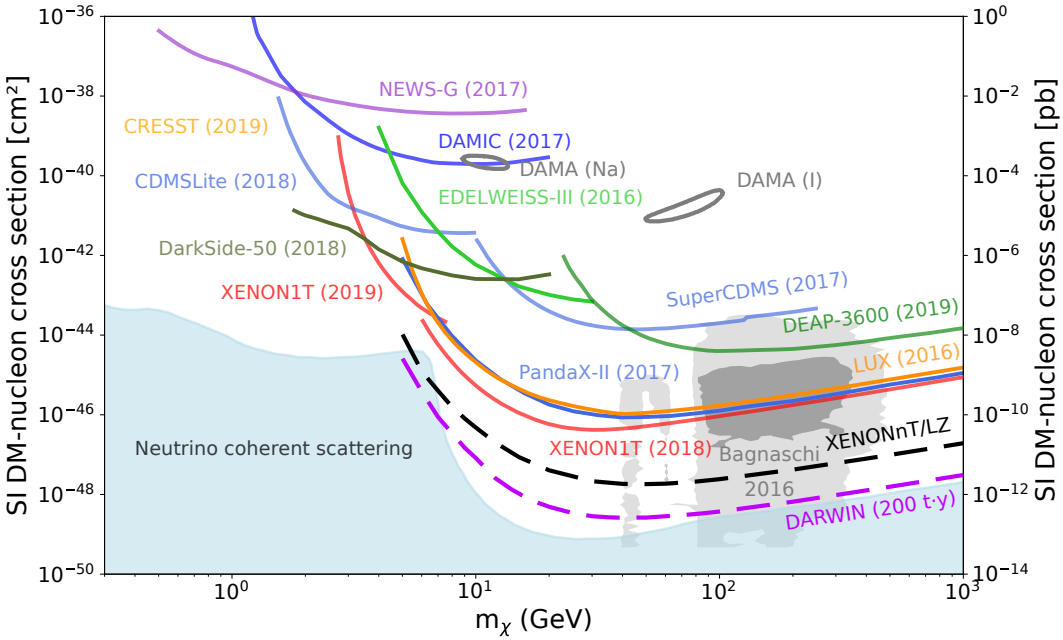

Figure 1.5: Collection of various upper limits on the spin-independent dark matter interaction cross-section reported by direct detection experiments. The region in which interactions from neutrinos becomes a dominant background for xenon targets is indicated by the shaded blue region. Figure adapted from [38] and supplemented by the projected limits (dashed lines) published in [39], as well as in gray the signal contours of the DAMA experiment as given in [3]. A signal prediction from a minimal supersymmetric extension of the standard model (MSSM) after Bagnaschi et al. [40] is shown as a gray shaded area.

ρ_χ is constant, the number density decreases for higher values of m_χ, which leads to a decrease of the scattering rate given in equation 1.1. For lower masses the energy transfer onto the target nuclei becomes inefficient and does not allow to exceed the energy threshold of the detector, causing a rapid loss of sensitivity towards the left side [3].

The elliptic gray contours correspond to a long-standing signal claim made by the DAMA/LIBRA collaboration which uses high-purity NaI scintillating crystals. They have observed an annual modulation of their event rate at a significance of almost 13 σ over more than 20 cycles [41]. However, a compatible signal has neither been observed in the XENON100 dual-phase xenon TPC [42], nor in the NaI-based scintillation detector ANAIS-112 [43]. The figure also shows a predicted signal region from the minimal supersymmetric standard model (MSSM), which is expected to be accessible by the current and next generation of liquid xenon (LXe) experiments. The blue region in the lower part of figure 1.5 indicates the expected discovery limit for xenon-based experiments due the irreducible background from coherent elastic neutrino-nucleus scattering (CEνNS) of Solar and atmospheric neutrinos. More details about this so-called neutrino "fog" or "floor" can be found, for example, in [44]. The projected sensitivity of the future DARWIN experiment [39] is expected to reach this limit in order to fully explore the remaining parameter space.

1.2 Liquid xenon time projection chambers for rare-event searches

The low signal expectations in experiments searching for rare events, such as interactions of DM particles require extremely low background rates. This is also true for experiments searching for the neutrinoless double beta decay ($0\nu\beta\beta$) which is reviewed for example in [45]. So far, these searches have usually returned empty handed, calling for a continuous improvement of the sensitivity of the used detectors. Dual-phase xenon TPCs have proven to be exceptionally successful in this regard. Figure 1.6 illustrates that the sensitive mass of past experiments of this type has increased by three orders of magnitude over slightly more than a decade [6, 46–52]. At the same time, their electronic recoil (ER) background rate was reduced by roughly a factor of ten thousand.

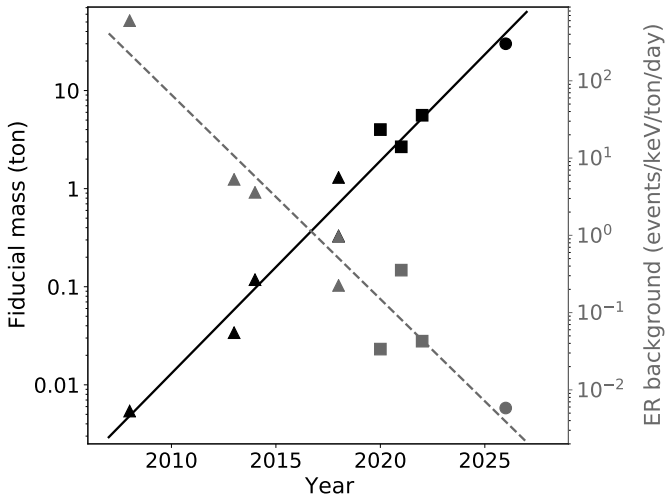

Figure 1.6: Past experiments employing LXe TPCs (▲) [46–50] showed a steady increase of their fiducial mass over the past decade. Detectors being operated at present times (■) [6, 51, 52] have meanwhile reached masses of several tons. This increase is matched by a continuous decrease of their background rate (gray). Surpassing all previous experiments in terms of mass and background will be the planned DARWIN [39, 53] experiment (●). Figure adapted from [54] (modified).

After a description of the working principle of a dual-phase xenon TPC and outlining the XENONnT experiment [6], the different background sources of this detector are introduced. For this work, the most important background contribution is the one caused by the emanation of ^{222}Rn. Its mitigation will be crucial for the future DARWIN observatory, which is aims to continue the trend shown in figure 1.6 [39, 53].

1.2.1 Working principle of the XENONnT detector

A labeled rendering of the XENONnT detector is shown in figure 1.8. The polygonal active volume of the detector is roughly 1.3 m in diameter and about 1.5 m in height and contains 5.9 tons of LXe [6]. Particles interacting with the LXe can lead to the emission of prompt vacuum ultraviolet (VUV) scintillation photons at a wavelength of 175 nm [55], as well as to the formation of electron-ion pairs.

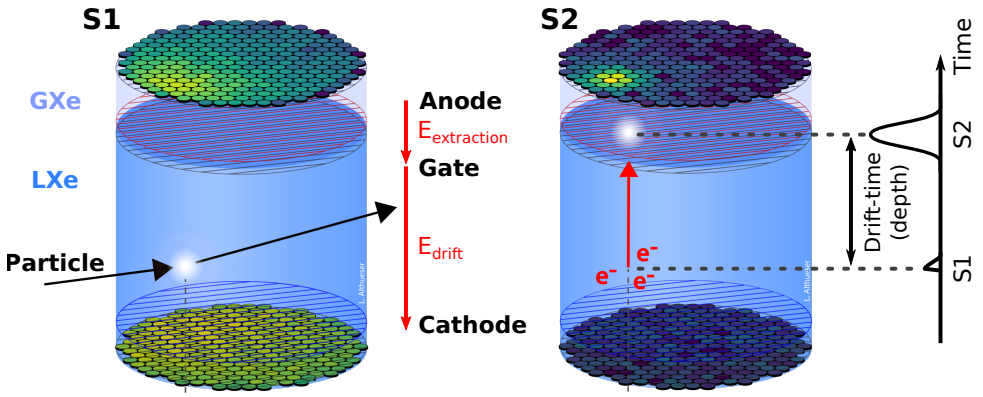

Figure 1.7: Working principle of a dual-phase xenon TPC. Particles interacting with the LXe lead to prompt scintillation (S1, left side) and ionization (S2, right side). The S2 signal is delayed relative to the S1 signal by the drift time of the electrons. A corresponding event waveform is sketched along the right frame. Figure courtesy of Lutz Althüser (modified).

The primary scintillation signal (S1) is detected by a total of 494 Hamamatsu R11410-21 3-inch PMTs, arranged in arrays at the top and the bottom of the detector. Several semi-transparent high voltage (HV) electrodes are situated in two electrode stacks at the top and bottom of the detector. They are made from stainless steel wires, to allow the scintillation light from inside the detector to reach the PMT arrays [6]. An electric field is applied between a cathode (bottom) and gate electrode (top), to drift the produced electrons from the interaction site to the top of the active volume [2]. At the top, the electrons are extracted from the LXe phase using a strong electric field [56], which is applied between the gate and an anode electrode situated 8 mm above the gate [6]. Electrons are accelerated in the gaseous xenon (GXe) by the strong field and produce a secondary scintillation light signal (S2), which is proportional to the number of extracted electrons. The height of the LXe level is maintained between both electrodes using a pressurized diving bell. The interaction position along the depth axis is estimated from the delay time between the S1 and S2 signal, while the x-y-coordinate is determined from the distribution of S2 photons among the PMTs in the top array. This is illustrated in figure 1.7.

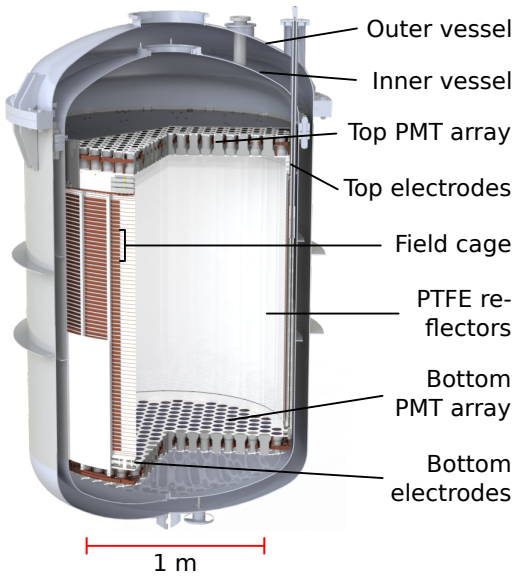

Figure 1.8: Rendering of the XENONnT time projection chamber. Figure adapted from [6].

Both signals can be diminished by impurities that are dissolved in the LXe. The

amount of electrons is reduced by their attachment to electronegative impurities, such as oxygen, during their drift in the detector [2, 57]. While S1 scintillation photons are attenuated by impurities like water which have a high absorption cross section in the VUV region [58]. To retain the sensitivity and resolution of the detector, such impurities must be removed from the LXe by continuous purification. XENONnT is the first LXe experiment to be equipped with a liquid purification system to fulfill this task [6]. The increased throughput of the plant results in a lower impurity concentration when compared to the more conventional GXe purification method. Data concerning the ^{222}Rn emanation of this system has been analyzed and is presented in chapter 2.

1.2.2 Background sources in LXe TPCs

As introduced in section 1.1 it is well possible that DM particles, such as WIMPs, interact via the weak force. This allows them to transfer a small recoil energy between 1 to 100 keV [37] by elastic scattering off the xenon nuclei. The energy would then be deposited in subsequent interactions of the recoiling nucleus in the LXe, leading to detectable S1 and S2 signals. Such an event is referred to as a nuclear recoil (NR). For gamma and beta particles, an energy transfer onto an electron in the atomic shell of the xenon via the electromagnetic force is much more likely. These events are correspondingly called electronic recoil (ER). In LXe TPCs both interaction types can be distinguished from each other due to their different dE/dx, resulting in different scintillation and ionization yields [3]. This is illustrated in figure 1.9 for data from the XENON1T experiment [59] and also further discussed in section 7.2.

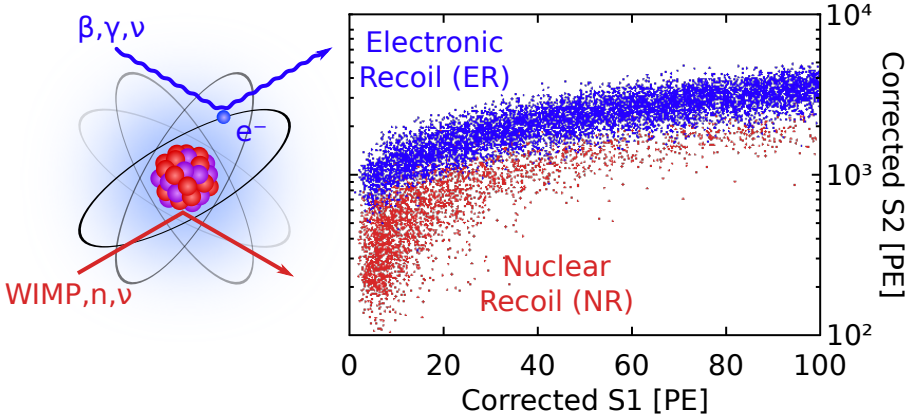

Figure 1.9: Separation between ER (blue) and NR (red) events in the XENON1T experiment. Figure taken from [60] (modified).

The expected background contributions in the region of interest (ROI) for the WIMP search in the XENONnT detector are illustrated in figure 1.10 for the two signal types [6]. A major contribution to the NR background comes from neutrons. They are of special concern, since they also interact via the weak force and can

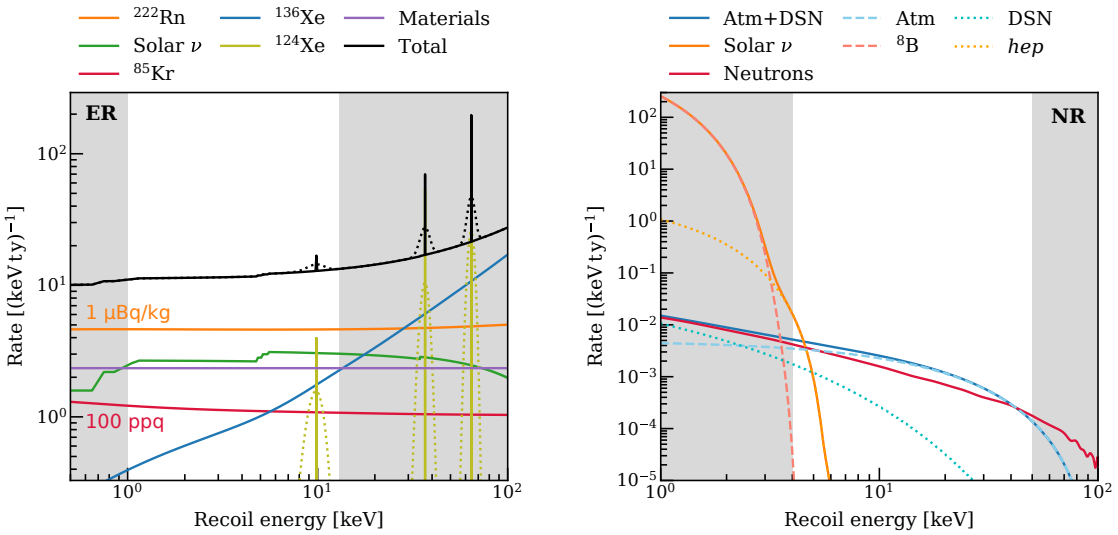

Figure 1.10: Expected composition of the background spectrum in XENONnT for a 4 ton fiducial volume in the ROI for the WIMP search (white areas). Emanation of ^{222}Rn (orange) contributes the most to the ER background (left), followed by solar neutrinos (green) and external detector materials (purple). Smaller contributions are from ^{85}Kr (red) and the double-beta decay of ^{136}Xe (blue), as well as from the double-electron capture of ^{124}Xe [61] (olive). The NR background (right) from radiogenic neutrons (red) is reduced by the neutron veto, to a similar level as the one expected from coherent elastic neutrino-nucleus scattering. The contributions from solar neutrinos (orange), as well as from atmospheric and diffuse super nova neutrinos (blue) are shown. Figure adapted from [6].

therefore mimic a WIMP interaction. They are mainly released in (α, n) reactions, to which fluorine atoms are especially susceptible [62]. Therefore the thickness of the polytetrafluoroethylene (PTFE) reflectors surrounding the active volume (see also figure 1.8), was minimized based on the findings reported in [63, 64] and discussed in chapter 6. Additionally, the neutron background is reduced to the level indicated in figure 1.10 using a novel neutron veto system. It surrounds the detector and will be able to identify 87% [6] of the neutrons interacting in the LXe. Additional contributions to the NR background are expected from the coherent elastic scattering of atmospheric and astrophysical neutrinos (CEνNS).

Though background events due to ERs can be rejected with efficiencies exceeding 99.5% [48, 65, 66], their abundance with respect to NR events is larger by about three orders of magnitude (see scales in figure 1.10). To reduce this background, the experiment is suited deep underground in the Laboratori Nazionali del Gran Sasso (LNGS), where an average rock overburden of 1400 meters attenuates the cosmic muon flux by six orders of magnitude [67]. The detector is embedded in a water tank with a height and diameter of 10 meters to shied it against external gamma particles and neutrons [68]. Besides background sources located outside of the experiment, trace amounts of radioactive impurities are contained in the detector materials used to build the cryostat, photosensors and the PTFE reflectors. These materials need to meet strict requirements regarding their radioactive impurity concentration and are

carefully pre-selected in dedicated material assays [69, 70]. Furthermore, the *external* material background is strongly reduced in the innermost detector volume by the efficient self-shielding property of LXe. Therefore, the DM search is constrained to a so-called fiducial volume of 4 tons [6], making use of the three-dimensional position reconstruction capabilities of the detector.

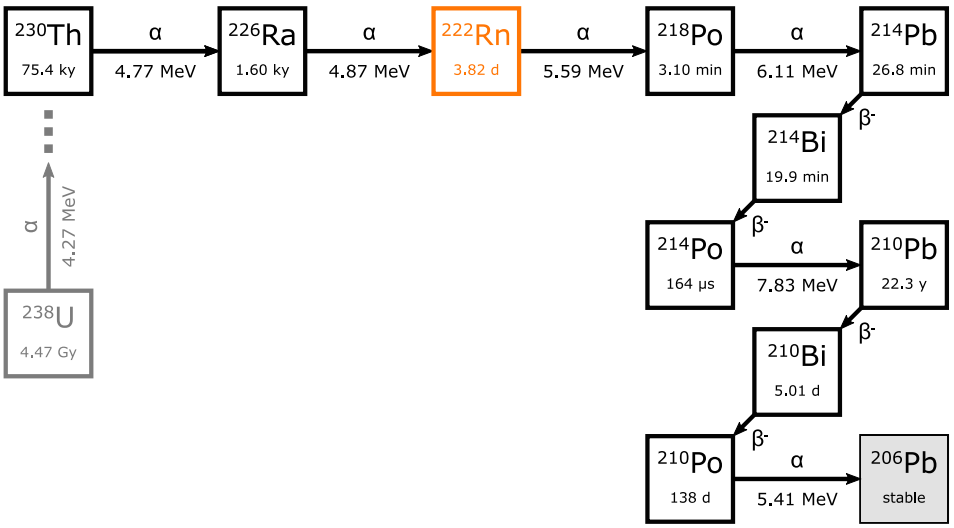

Figure 1.11: Section of the primordial uranium decay series. Figure adapted from [71].

This fiducialization however, does not help against radioactive impurities which are homogeneously mixed with the LXe. Most important representatives of these so-called *internal* background sources are the two noble gases ^{85}Kr as well as ^{222}Rn. ^{85}Kr is removed by an initial refinement of the xenon inventory using cryogenic distillation [72, 73]. Due to its anthropogenic origin [74], it is not continuously produced in the experiment and its continuous removal was not required in past experiments [73]. To detect an increase of the krypton concentration due to air leaks or out-gassing, it is regularly measured using rare gas mass spectrometry [75].

^{222}Rn on the other hand is a part of the primordial decay series of ^{238}U which is shown in figure 1.11. Since it is contained as a trace impurity in nearly all detector materials, it is constantly produced and released from surfaces which are in contact with liquid or gaseous xenon. The beta decay of ^{214}Pb with an end-point energy of about 1 MeV [76] is expected to be the dominant source of ER events for recoil energies $\lesssim$ 30 keV. An ambitious goal for the ^{222}Rn concentration in the XENONnT experiment of 1 µBq/kg has been set [6]. To reach this goal a dedicated radon assay of all used components has been performed which results in an projected radon concentration of 4.2 µBq/kg [70]. To close the gap between the design goal and the expected emanation, the XENONnT detector features a dedicated radon removal system. Similar to the case of ^{85}Kr, it removes radon from the xenon by cryogenic distillation as has been previously proven in [77–79]. More details about this system will be provided in [80]. A first measurement of the radon concentration in the

XENONnT experiment is presented in chapter 2, together with an evaluation of the possible improvements related to the radon removal system.

1.3 A bright future ahead: The DARWIN project

There is a strong motivation to fully explore the range of WIMP-nucleon interaction cross-sections until the neutrino detection limit shown in figure 1.5 is reached. This can be achieved by a next-generation LXe detector, with an exposure exceeding 200 t·y [39]. Besides this, such a detector can also be used to search for the $0\nu\beta\beta$ of ^{136}Xe, as well as for measurements of atmospheric and astrophysical neutrinos, and further studies. An overview of the various scientific measurements and searches that can be explored is given in [81].

One concept for such a detector is envisioned by the DARWIN collaboration. It features a dual-phase xenon TPC with 2.6 meters in height and diameter [83]. The experiment is designed for a total of 50 tons of LXe, from which 40 tons are located within the instrumented volume [39]. While several design choices of the experiment are still to be decided, its stringent background requirements are pre-determined by the experiment's scientific goals. They foresee an improvement in the ^{222}Rn concentration by one order of magnitude with respect to XENONnT to the level of 0.1 µBq/kg [84, 85]. The challenge implied by this number is illustrated in figure 1.12. It shows the anti-correlation between the achieved radon concentrations in past LXe experiments [6, 51, 78, 79, 86–89] and their respective xenon masses m. The amount of radon emanation in an experiment is approximately proportional to its internal surface area. Therefore, their radon concentration roughly follows a $m^{-1/3}$ trend expected from the decrease of the surface-to-volume ratio (dashed red line). Note, that contributions from peripheral systems such as the purification and cryogenic systems are neglected in this approximation. The figure clearly shows, that in case of the DARWIN experiment [39], the simple up-scaling of detector mass will be insufficient to reach the required radon concentration. Therefore, the existing radon mitigation techniques need to be improved and extended by new approaches, such as the coating-based radon barriers which are discussed in chapter 4.

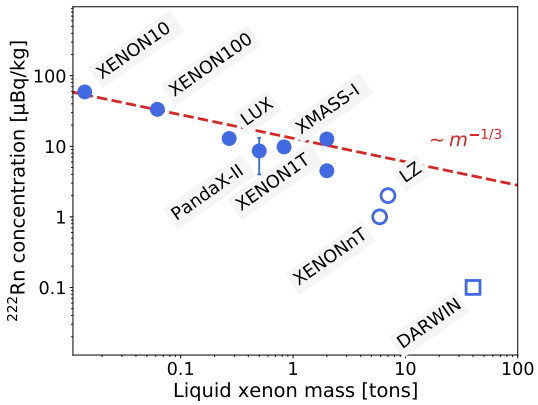

Figure 1.12: Achieved ^{222}Rn concentrations in past LXe experiments (filled circles). They roughly follow a $m^{-1/3}$ dependence (dashed red line) expected from the reduction in surface-to-volume ratio. The projected radon concentrations of future experiments (open circles) and for the future DARWIN experiment (open square) rely on novel radon mitigation strategies. Figure courtesy of Masaki Yamashita [82] (modified).

2 Detection of radon-induced alpha events in the XENONnT experiment

The XENONnT experiment is expected to have an unprecedented high sensitivity for interactions of weakly interacting massive particles (WIMPs) and other rare processes. This sensitivity crucially depends on the amount of background as has been detailed in section 1.2.2. Especially the radon-induced background needs special attention as it is expected to dominate all other background sources. Gaseous ^{222}Rn is released from trace impurities of ^{226}Ra present in almost all detector components. Due to its long half-life, it can enter and homogeneously distribute itself in the liquid xenon (LXe) volume of the experiment. The β-decays of ^{214}Pb are of special concern as they lead to low energy electronic recoil (ER) events. These can mimic a dark matter interaction and increase the background rate for searches focused on low energy ERs such as reported in [90].

In this chapter, a measurement of the radon concentration during the commissioning phase of the XENONnT detector is presented. First, the focus will be put onto the identification and correction of the signals stemming from the alphas emitted by ^{222}Rn and its subsequent decay products. Afterwards, the influence of different operations throughout the commissioning phase onto the radon concentration will be evaluated. This allows to give an estimate of the radon emanation of the LXe purification system, as well as the possible improvements that can be gained by the operation of the radon removal unit (see section 1.2.2). An additional analysis of alpha interactions using data which has been collected while the detector was still filled with gaseous nitrogen is also presented. Results from both analyses are then set into context to the experiment's expected radon emanation rate obtained by the dedicated radon screening campaign [79].

2.1 Identification of radon-induced alpha decays in liquid xenon

The commissioning of a new detector involves many operations, resulting in frequent changes of the detector parameters. Since these changes can lead to variations in the height of the LXe level in the time projection chamber (TPC) the gate electrode can become uncovered from LXe in some periods. As a precaution in order to prevent breakdowns of the strong electric field between gate and anode electrode, the extraction field has been kept turned off for most of the time. Therefore, most of the data does not contain any signal from collected charges (S2). However, some

important detector characteristics like for example the radon concentration can still be evaluated in a meaningful way using the prompt scintillation signal (S1) only.

Especially the mono energetic alpha events from ^{222}Rn and its subsequent decay products can be observed due to their high energies. The part of the ^{222}Rn decay chain (see figure 1.11 in the previous chapter) which is relevant for the following discussion is repeated below.

$$\begin{aligned}\ldots\, ^{222}\mathrm{Rn} &\xRightarrow[3.8\,\mathrm{d}]{5.6\,\mathrm{MeV}} {}^{218}\mathrm{Po} \xRightarrow[3.1\,\mathrm{min}]{6.1\,\mathrm{MeV}} {}^{214}\mathrm{Pb} \xrightarrow[27\,\mathrm{min}]{\beta} {}^{214}\mathrm{Bi} \xrightarrow[20\,\mathrm{min}]{\beta} {}^{214}\mathrm{Po} \\ &\xRightarrow[160\,\mu\mathrm{s}]{7.8\,\mathrm{MeV}} {}^{210}\mathrm{Pb} \xrightarrow[22\,\mathrm{y}]{\beta} {}^{210}\mathrm{Bi} \xrightarrow[5.0\,\mathrm{d}]{\beta} {}^{210}\mathrm{Po} \xRightarrow[138\,\mathrm{d}]{5.4\,\mathrm{MeV}} {}^{206}\mathrm{Pb}\ . \end{aligned} \tag{2.1}$$

As can be seen it contains four alpha decays (double arrows) with typical energies above 5 MeV. These energies lead to bright S1 signals, which can be selected from the background with a high efficiency.

First, the different variables, selections, and signal corrections are introduced in section 2.1.1. The reconstruction of the alpha spectrum is shown in section 2.1.2 and the fiducial mass of this analysis is estimated in section 2.1.3, using a short stable period during which S1 & S2 data is available. The time evolution of the light yield and the radon concentration is shown in section 2.1.5. Here special emphasis will be put on the impact of the LXe purification system as well as the reduction by the radon removal system.

2.1.1 Event selection and signal corrections

The amount of light detected by a photomultiplier tube (PMT) is usually expressed as the amount of photoelectrons (PE) which are released from its photo-cathode. These electrons get multiplied and digitized resulting in a waveform which contains the time distribution of the detected light signal. This raw waveform information is then processed by a software [91, 92] and summed over all PMT channels in order to extract pulse parameters like the total amount of detected light (`area`) or the duration (median `width`) of the pulse.

This allows to define a region of interest (ROI) that rejects a large fraction of events from interactions which are less relevant for this study such as external gamma rays and beta decays. Figure 2.1 shows the definition of this region for data taken over approximately 20 hours. As the alpha events produce bright light signals most of the background events can be rejected by requiring that the detected `area` is within $[20 - 120]$ kPE. By additionally requiring that the `width` of the pulses is between 40 ns and 200 ns a few remaining spurious events can be removed.

Correction of the light signal

The amount of light which is produced by the interaction of an alpha particle with the LXe is proportional to the alpha particle energy. This allows to distinguish decays from the different isotopes of the decay chain (equation 2.1) based on the

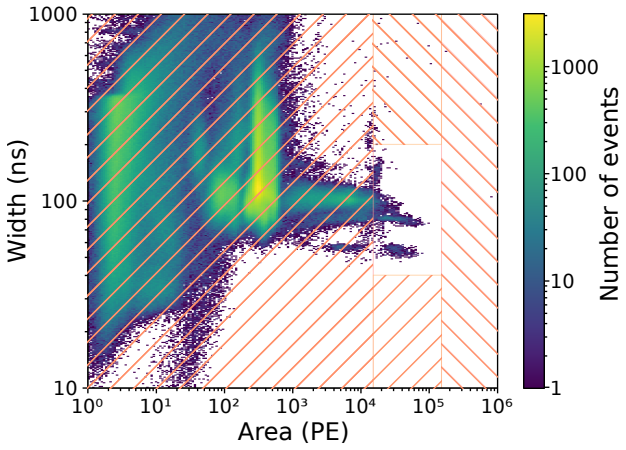

Figure 2.1: `Area` and pulse `width` of scintillation signals in LXe recorded over approximately 20 hours during the commissioning phase of the XENONnT detector. The ROI used to select alpha events (non-hatched area) is indicated. Events at lower `areas` are caused for example by external gamma rays and beta interactions.

`area` of the events. However, the probability to detect the produced light with the PMTs depends on the position of the decay inside the detector. The light collection efficiency (LCE) is typically highest for events happening close to the bottom PMT array and decreases for positions higher up in the TPC. This is because of the total reflection of the light at the liquid-gas phase transition resulting in most of the S1 light being always detected by the PMTs in the bottom array. This effect needs to be corrected for in order to reconstruct the alpha event spectrum properly.

Typically the z- coordinate can be reconstructed accurately by the time-delay between the prompt S1 and the delayed S2 signal. Since the present study uses S1-only information the depth of the interaction need to be determined differently. A good proxy for the z-coordinate is given by the relative amount of light detected by the PMTs in the top array (`area fraction top`, `AFT`). Values close to zero correspond to events happening close to the bottom of the detector, while events close to the liquid-gas interface feature an `AFT` value slightly smaller than 0.6. Though these events happen near the top PMT array, more than 40% of their scintillation light is detected by the PMTs in the bottom array. This is because of the total reflection of the light on the liquid-gas inter-phase. The population of events with an `AFT` $>$ 0.6 is caused by proportional scintillation (S2) signals, happening above the liquid phase.

For the events falling in the selected ROI this dependence of the `area` as a function of `AFT` value is shown in figure 2.2. At least three bent lines between `AFT` values of about 0.1 to 0.55 are visible alongside several background populations which will not be further detailed. As expected from the LCE the detected amount of light increases with decreasing values of the `AFT` variable.

To correct for this effect, a model of the dependence needs to derived based on the shown data. For this the events from two of the alpha lines are first coarsely selected using the dashed cyan box. The data is then divided into slices of the `AFT` value between 0.09 and 0.55. The median `area` for each slice is then determined as indicate by the red dots. These points are then fit using a phenomenological model

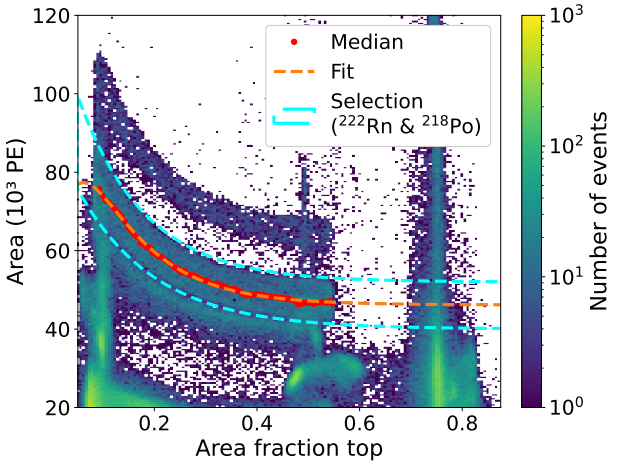

Figure 2.2: Dependence of the detected light (`area`) on the interaction height within the detector. The height is estimated by the fraction of light detected by the top photo multiplier array (`area fraction top, AFT`). It is corrected for using the median profile (red dots) fit the model function given in equation 2.2 (orange dashed line).

function of the form:

$$\texttt{area} = a_0 \cdot e^{-\frac{a_1 - \texttt{AFT}}{a2}} \cdot \left(1 - e^{-\frac{a_1 - \texttt{AFT}}{a3}}\right) + a_4 \,. \tag{2.2}$$

The shape of the function can be adjusted by the five parameters a_0 to a_4 which are determined by the fit resulting in the dashed orange function shown in figure 2.2.

This function is then used to calculate an `area` correction factor for each event based on its `AFT` value. The correction is defined such that it is relative to a central position in the detector (`AFT` = 0.25). Figure 2.3 shows the `corrected area` as a function of the `AFT`. It can be seen that the correction almost fully accounts for

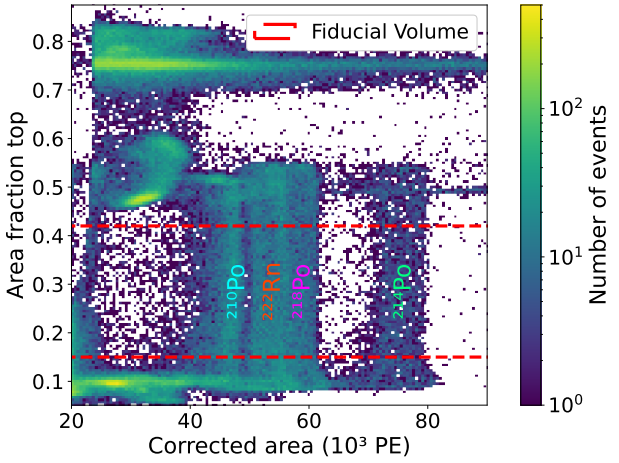

Figure 2.3: Alpha emission lines in liquid xenon after applying the correction to the detected amount of light. The lowermost line in `corrected area` corresponds to alpha decays of ^{210}Po, while the broader central line contains alpha decays of ^{222}Rn and ^{218}Po. The uppermost line is from decays of ^{214}Po. The dashed red lines indicate the fiducial volume typical chosen in the analysis.

the geometric dependence resulting in the three alpha emission lines to be almost straight over the `AFT` range. The lowest vertical line corresponds to events from alpha decays of ^{210}Po while the highest vertical line is due to ^{214}Po alphas. The broader vertical line in between the two (around 57 kPE) contains the decays of ^{222}Rn and ^{218}Po. For events at `AFT` values of around 0.1 a sharp decrease of the detected area can be observed. This is likely due to signal saturation of events happening close to the bottom PMT array which cannot be fully accounted for by the correction.

To reconstruct the alpha spectrum a fiducial region in `AFT` between 0.15 and 0.42 is chosen as indicated by the two dashed red lines in figure 2.3. In this region the resolution is best and other background populations are strongly suppressed.

Before the estimation of the LXe mass selected by this fiducial volume will be given in section 2.1.3 the reconstruction of the spectrum using the `corrected area` variable will be presented.

2.1.2 Reconstruction of the spectrum

The spectrum of `corrected area` can be obtained by projecting the events shown in figure 2.3 onto the area axis. To enhance the resolution of the spectrum only the events inside the fiducial volume selection are taken. The resulting spectrum is shown in figure 2.4. The spectrum features again three main populations from the

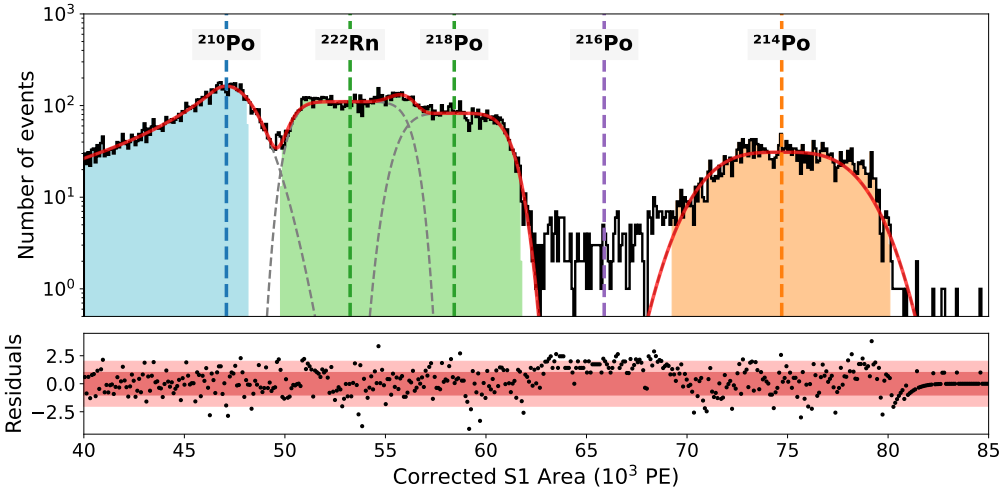

Figure 2.4: S1-only spectrum the `corrected area` of alpha events in liquid xenon. The spectrum is fit (red line) by the sum of the four individual alpha emission lines (dashed gray functions) of ^{222}Rn, ^{218}Po, ^{214}Po and ^{210}Po. An additional subdominant contribution from ^{216}Po, which is part of the decay chain of ^{232}Th (see equation 3.7) is visible, but not part of the fit. The highlighted regions are used to determine their individual contributions to the overall rate.

alpha decays of ^{210}Po (blue region) and ^{214}Po (orange region) as well as the clustered region from ^{222}Rn and ^{218}Po (green region). The spectrum is fit using the sum of four individual functions which describe each alpha emission line separately (red line), where the dashed gray lines indicate the contribution from each individual alpha line. While the shape of the ^{210}Po peak is found to be well described by a Crystal-Ball (CB)-function (see equation D.1 in the appendix for function definition), the peak shapes of the other lines feature a rather unusual shape. In contrast to the expected Gaussian shape, these lines have a flat top part with Gaussian left and right flanks. They are found to be well described by a generalized Gaussian distribution [1] [93] of

[1] This distribution function is also referred to as the exponential power distribution or Subbottin distribution.

the form:

$$f(x) = \frac{\beta}{2\sigma\Gamma(1/\beta)} \cdot e^{-(|x-\mu|/\sigma)^{\beta}} . \tag{2.3}$$

γ denotes the gamma function and β is the shape parameter of the distribution. By changing the parameter β allows to continuously transition between the heavy-tailed Laplace distribution ($\beta = 1$), a Gaussian distribution ($\beta = 2$) and the uniform distribution ($\beta \to \infty$). The parameter σ describes the width of the distribution similar to the standard deviation in case of a Gaussian distribution.

The unusual peak shape can be explained by the radial dependence of the LCE that cannot be corrected for using the S1-only data. Photons from events happening in the center of the TPC feature a higher probability to be detected by either of the two PMTs arrays as events close to the walls. This effect is illustrated in figure 2.5 showing the corrected S1 `area` as a function of the squared radius of the event as reconstructed using S1 & S2 data. Using the additional radial information the two alpha emission lines from ^{222}Rn and ^{218}Po can be resolved separately and this dependence could be corrected for. However, since most data taken throughout the commissioning phase have been acquired in the S1-only mode, such a correction is not straight forward. Future version of such studies however can make use of a naive S1-only radial position reconstruction allowing for a significantly enhanced resolution of the alpha spectrum [94]. As can be seen from figure 2.5 without such a correction the resulting emission lines will overlap producing the flat top shape that is observed in figure 2.4. Furthermore, this overlap results in the small enhancement of detected events between the ^{222}Rn and ^{218}Po lines which is correctly reproduced by the fit function based on the generalized Gaussian functions.

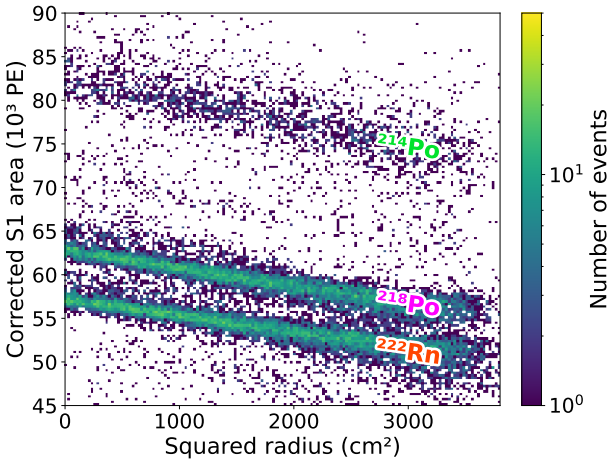

Figure 2.5: Illustration of the radial dependence of the detected light for alpha events. The squared radius is estimated using the reconstructed event position from S1 & S2 data. Unlike in the case of the presented S1-only analysis the emission lines from ^{222}Rn and ^{218}Po can now be resolved separately.

The observed shape of the ^{210}Po line differs from the other isotopes as it does not feature the same flat top distribution. Due to the long half-life of ^{210}Pb and ^{210}Po (see decay-scheme in equation 2.1) these decays are not caused by emanated ^{222}Rn present in the LXe but come from the plate out of radon daughters during the construction of the experiment. Therefore, these events are expected to be

located on the polytetrafluoroethylene (PTFE) walls of the detector, where they all feature roughly the same LCE. While the other three emission lines closely follow a linear relation between their `corrected area` (dashed vertical lines) and their corresponding alpha decay energies, this is not the case for the ^{210}Po line. Its fitted position (vertical dashed blue line) is found to be shifted towards lower areas by roughly 9%, likely due to the reduced LCE at the wall. Furthermore, the visible tailing of this line towards lower energies could be a result of partial energy loss of the alpha particles in the PTFE material.

Another subdominant contribution to the spectrum can be seen in between the lines of ^{218}Po and ^{214}Po. The slight excess of events in this region probably stems from the α decay of ^{216}Po which is a decay product of ^{220}Rn which is part of the primordial thorium decay series (see equation 3.7). An estimation of the resulting radon concentration and event rates of the different isotopes will follow in section 2.1.4. But before that the fiducial mass enclosed in the fiducial volume selection needs to be calculated.

2.1.3 Estimation of fiducial mass

In order to deduce the radon concentration from the observed event rate inside the selected fiducial volume the amount of LXe inside this volume needs to be estimated. However, this volume is selected based on the `AFT` values of the events, which is not directly proportional to the z-coordinate in the TPC. Therefore, an estimate based on the collected S1-only data alone is not possible. Luckily throughout some period in the commissioning phase the detector conditions were stable enough to safely turn on the extraction field, allowing for simultaneous detection of S1 and S2 signals. This allows to match the observed `AFT` values of alpha events to the `drift-time` values they correspond to. Figure 2.6 shows that as expected a clear anti-correlation between the two variables.

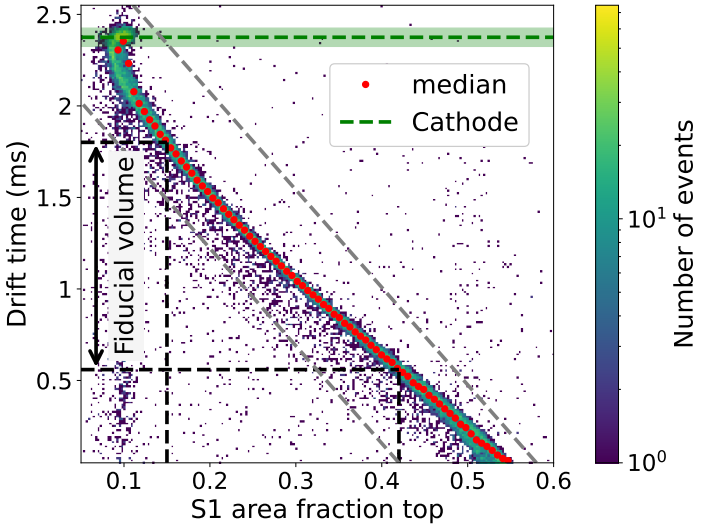

Figure 2.6: Anti-correlation between event `drift time` (y-axis) and S1 `AFT` (x-axis) for radon alpha events. The median of the main population is indicated by the red markers (•), while the estimated cathode position and its uncertainty are shown by the dashed green line and shaded green region respectively. The vertical dashed black lines show the range of the S1 `AFT` selection used for the analysis (see figure 2.3). It is translated into a fiducial volume (horizontal black lines) using the profile.

The distribution is profiled using 75 bins in `AFT` in a range between 0.09 and 0.55.

Within each slice the median of the distribution is computed as illustrated by the red dots. To reduce the bias from other background populations, the parallelogram indicated by the dashed gray lines is used to coarsely select the main part of the population in the drift time.

The additional information from the charge signal allows to add two further selection criteria besides the ones shown in figure 2.1. While the electrons which are produced at the interaction site are drifted upwards in the detector they also undergo a random motion. This leads to a broadening of the charge distribution as a function of their `drift time` that can be described by a diffusion law [2]. The spread of the arrival-time of the charge distribution (`s2 width`) at the extraction region can therefore be utilized to reject nonphysical events. Furthermore, a requirement on the minimum `s1 area` and `s2 area` is employed in order to reject events induced by high energy gamma rays. Note that these selections are only applied to get the correspondence between the `AFT` values and the `drift time` of events but not for the final determination of the radon concentration.

Using a linear interpolation of the profiled distribution allows to translate the fiducial range defined via the `AFT` values into an equivalent selection in the `drift time` as indicated by the dashed red lines shown in figure 2.6. The uncertainty on this range is estimated by variation of the number of bins as well as by changing between the median and the mean for the profiling and is found to amount for about 1%. Furthermore the maximum drift time needs to be determined. As can be seen in figure 2.6, there is an accumulation of events at a `drift time` value of about 2.4 ms which corresponds to events located at the cathode electrode in the XENONnT detector (dashed green line). The respective `drift time` value and its uncertainty is estimated by hand to be (2.375 ± 0.05) ms. With this, the fraction of the fiducial volume with respect to the active volume of the detector can be computed to be $(52.3 \pm 1.2)\%$.

This fraction can be translated into the fiducial mass by multiplying it with the total amount of active LXe in the detector. From the dimension of the XENONnT TPC as stated in [6] and the LXe density at a temperature of $-96°$C and a pressure of 1.93 bar [95] an active mass of (5.92 ± 0.09) tons can be computed. This number agrees with the value reported in [6]. The uncertainty on the active mass is estimated from PTFE machining tolerances of 0.5% [96] as well as from changes of the LXe density of up to by 0.4% due to temperature fluctuations ($\Delta T = 2$ K). A fiducial mass of this analysis of (3.08 ± 0.08) tons is derived.

2.1.4 Measurement of the radon concentration and ^{210}Po surface activity of the XENONnT experiment

As can be seen from the alpha spectrum shown in figure 2.4 each isotopes features a slightly different number of counts. For ^{210}Po this can be understood easily since it comes from radon daughter plate-out onto the PTFE walls during the construction phase of the detector and is therefore not directly related to radon concentration of

LXe while the experiment is being operated. Plate-out of radon daughters could be also a reason for the lower detected activity found for ^{218}Po and ^{214}Po with respect to the rate of ^{222}Rn. The predominantly positively charged decay products [97] have a certain probability to be drifted out of the analysis volume towards the cathode which is biased by a negative high voltage (HV). Similar behavior has been already observed in the XENON1T experiments [79].

Measurement of the radon concentration

The significant overlap of the alpha lines from ^{222}Rn and ^{218}Po in the S1-only data adds a systematic uncertainty to the estimation of the ^{222}Rn activity. Since ^{218}Po is only removed from the analysis volume due to plate-out its rate is always lower than the one of ^{222}Rn. A lower limit of the ^{222}Rn rate can therefore be derived by averaging the rate found in both lines (green shaded area in figure 2.4). The isotope ratio can also be derived directly from the spectrum of the S1-only data via the fit with equation 2.3. This would lead to an estimate of the ^{218}Po rate being only about 70% of the ^{222}Rn rate. As can be seen the proposed fit function based on the generalized Gaussian distribution is a sufficient but not highly accurate description of the peak shape. The most reliable estimate is obtained when using the data taken with S1 and S2 information. As shown in figure 2.5 the decays from both isotopes can be clearly distinguished when the full three dimensional position of the events is reconstructed. From this data a ratio between the activity of ^{218}Po and the one from ^{222}Rn of 92% can be derived.

Therefore, this ratio is taken to derive the best estimate for the ^{222}Rn rate using the S1-only data. Together with the fiducial mass derived in section 2.1.3 this yields the radon concentration of the XENONnT detector of

$$\mathrm{R}\left(^{222}\mathrm{Rn}\right) = \left(3.61 \pm 0.07(\mathrm{stat})^{+0.6}_{-0.3}(\mathrm{syst})\right)\,\mu\mathrm{Bq/kg}\,.$$

Here the systematic uncertainty is chosen such as to cover the range of the above mentioned ratios between ^{218}Po and ^{222}Rn. The statistical uncertainty contains the uncertainty from the amount of observed events as well as the uncertainties related to the size of the fiducial volume. Comparing this value for the radon concentration with the value of $\left(4.2\,^{+0.5}_{-0.7}\right)$ µBq/kg which is predicted by the dedicated screening campaign reported in [70] shows reasonable agreement. Note that value represents the initial radon concentration of the experiment, and does not include the improvements made possible by the radon removal system which will be quantified in section 2.1.5.

Estimation of ^{210}Po surface activity

Radon is not only present in the LXe but also in the clean-room air during the assembly of the XENONnT TPC. It is known that radon daughters tend to plate out on the PTFE parts of the detector where especially the long-lived radon daughters

^{210}Po and ^{210}Pb will persist throughout the lifetime of the experiment [98]. Therefore, the surface activity will limit the maximum size of the fiducial volume accessible in analyses focusing on low-energy events. The presented commissioning data allows to also make an estimate of the ^{210}Po surface activity. For this the ^{210}Po alpha line is selected from the spectrum shown in figure 2.4. Similar to the estimation of the fiducial volume shown in section 2.1.3 the amount of PTFE surface within the fiducial volume can be estimated to be $(3.27 \pm 0.08)\,\mathrm{m}^2$. Here the uncertainty is only estimated from the tolerances in the manufacturing, without the impact of temperature changes onto the LXe density. Normalizing the rate to this surface then yields a ^{210}Po surface activity of

$$\mathrm{R}\left(^{210}\mathrm{Po}\right) = (5.04 \pm 0.18)\ \frac{\mathrm{mBq}}{\mathrm{m}^2}\,.$$

A dedicated measurement of the ^{210}Po surface alpha activity of the XENONnT PTFE panels has been carried out and is reported in [70]. The found activity of $(20\pm3)\,\mathrm{mBq/m^2}$, however, is significantly larger than the one obtained in the present study. Possible reasons for this discrepancy are still under investigation. As a comparison the ^{210}Po surface alpha activity in the XENON1T experiment was estimated between 5 and 32 $\mathrm{mBq/m^2}$ [99, 100].

2.1.5 Time dependence of the light yield and radon concentration

The commissioning data analyzed in this study can be subdivided into two major time intervals. During the first one, the LXe purification system has been tested, while the second phase is dedicated to the radon distillation column (see also section 1.2.1). In this section the impact of different operating modes of these two systems on the concentration of ^{222}Rn in the detector will be investigated. However, the operation of those systems does not only affect the radio purity but also the general amount of impurities in the xenon. As a higher impurity concentration can lead to stronger attenuation of the vacuum ultraviolet (VUV) scintillation photons, the detected amount of light from the alpha interactions is subject to changes throughout the commissioning phase. These changes are accounted for by a time-dependent alpha event selection. Therefore, the section starts off with a qualitative study of the light yield evolution of the alpha events.

Light yield evolution

Figure 2.7 shows the evolution of the `corrected area` from alpha events during the commissioning of the XENONnT detector. From top to bottom, the emission lines from ^{214}Po, the combined line from ^{222}Rn and ^{218}Po, as well as the line of ^{210}Po appear as horizontal bands. At lower values of the `corrected area`, the background contribution from high-energy gamma particles can be seen. The positions of the

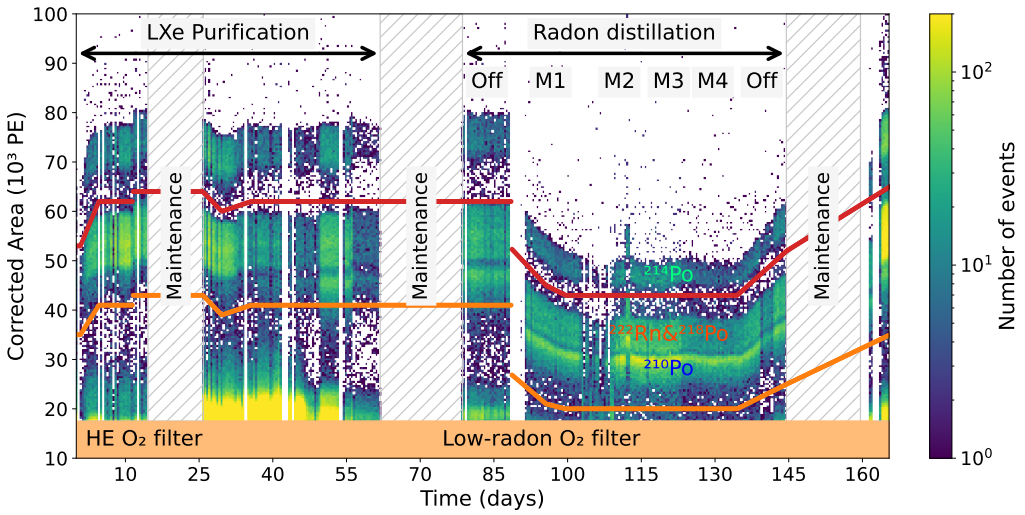

Figure 2.7: Evolution of the light yield from radon alpha events during the commissioning of the XENONnT detector. The red and orange lines indicate the time dependent selection of the ^{214}Po emission line, as well as the combined lines from ^{210}Po, ^{222}Rn and ^{218}Po. The two main time periods of the data set, as well as the different operating modes of the radon distillation system (M1 - M4) are outlined by the two arrows on top. The lower bar shows, whether the high-efficiency (HE) filter (blue) or the low-radon filter (orange) was in use by the LXe purification system.

lines show a clear time dependence throughout the different phases of data taking. To prevent a biased estimation of the radon rate, the selection of radon-induced alpha events is modeled time dependent, following the red and orange lines. They are defined by a linear interpolation between manually chosen support points and used to remove the well separated events from ^{214}Po (above the red line), as well as the gamma-induced background (below the orange line). Events between both lines are from ^{210}Po, ^{222}Rn and ^{218}Po. They will be used for the further evaluation of the radon concentration in the detector.

Starting from the left of the figure, it can be seen that the light yield first steeply increases and then saturates while the high-efficiency (HE) O_2 filter is being operated in the LXe purification system (blue interval). After a short maintenance interruption, the data taking was continued with the low-radon oxygen filter installed in the LXe purification system (orange period). The phase of the LXe purification commissioning was ended by another maintenance operation and is followed by the commissioning of the radon removal system.

Around day 85 ("Radon distillation off"), an extended period of stable data taking allowed to turn on the extraction field in order to simultaneously measure prompt scintillation (S1) and charge (S2) signals. Data from this period is used to derive the `AFT`-based signal correction that has been introduced in section 2.1.1. The correction is then applied to data from all periods, under the assumption that the changing impurity level has a subdominant influence on the performance of the correction. This phase is also used for the estimation of the fiducial mass as presented in section 2.1.3 and to derive the ratio between ^{222}Rn and ^{218}Po which has been used in

section 2.1.4.

The commissioning of the radon distillation system contains four different modes (M1 - M4), which are detailed further in the next paragraph. With the start of the system (M1), a strong decrease of the light yield has been observed. This is explained by an increased outgassing rate from the new system, which has not been in contact with the ultra pure LXe before. The light yield then stabilized on a lower level, showing only small fluctuations throughout commissioning of the remaining modes (M2 - M4). At the end of its commissioning (Off), a moderate increase of the light yield can be seen. After another maintenance period, the high LXe purity was then restored using the high-efficiency O_2 filter.

Time evolution of the radon concentration

For both commissioning periods, the time dependent selection of ^{210}Po, ^{222}Rn and ^{218}Po events is used as shown in figure 2.7. The rate of ^{222}Rn is then inferred by subtracting the rate of ^{210}Po as measured in section 2.1.4 and applying the ratio between ^{222}Rn and ^{218}Po as found using S1 & S2 data. Note that this assumes the ^{210}Po rate to be constant throughout the commissioning phase. If this assumption does not hold, a small bias of up to 10% could be introduced onto the estimated radon rate.

Figure 2.8 shows the radon evolution during the commissioning of the LXe purification system. The evolution is fit by a piece wise continuous function, which

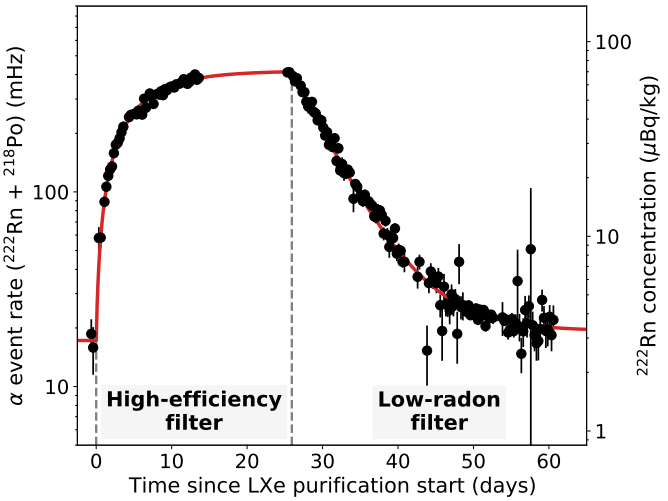

Figure 2.8: Evolution of the ^{222}Rn induced alpha event rate during operation of the two different oxygen filters in the LXe purification system. Data acquired during the commissioning phase of the XENONnT experiment.

recursively describes the radon rate $A(t)$ in each interval i. It is given by the decay of the remaining radon activity ($A(t_{i-1})$) present in the system at the end of the previous interval (t_{i-1}), and the in-grow of the activity towards a new equilibrium value A_i

$$A(t) = A(t_{i-1}) \cdot \exp\left(-\frac{t - t_{i-1}}{\tau_{222Rn}}\right) + A_i \cdot \left(1 - \exp\left(-\frac{t - t_{i-1}}{\tau_{222Rn}}\right)\right) . \tag{2.4}$$

Starting from a constant and low level, the radon rate increases by more than one order of magnitude after the high-efficiency filter is added to the system. This filter was used to purify the bulk of the xenon inventory in order to rapidly approach a sufficient level of purity. Several weeks later this filter was exchanged by a filter which features a much lower radon emanation rate (low-radon filter). The radon concentration decays within the following weeks as expected from the ^{222}Rn half-life and approaches a constant level similar to the one prior to the start of the LXe purification.

The extracted values for A_i in each interval can be used to determine the radon emanation of both filters. Before the LXe purification system has been included, an absolute ^{222}Rn emanation rate of $A_0 = (26 \pm 3)\,\mathrm{mBq}$ is found. The additional emanation coming from the purification system, together with the low-radon filter $(A_2 - A_0)$ is estimated to be $(3 \pm 3)\,\mathrm{mBq}$. This can be converted into an upper limit of 8.2 mBq (95% C.L.), which is compatible with the expected emanation of $(3.6 \pm 2)\,\mathrm{mBq}$ from this system that has been obtained by the dedicated radon measurement [70]. The additional radon emanation from the high-efficiency filter $(A_1 - A_0)$, is estimated to be $(606 \pm 5)\,\mathrm{mBq}$. Normalized to the mass of the used filter material of approximately 0.5 kg, a radon emanation of $(1.21 \pm 0.01)\,\mathrm{Bq/kg}$ can be inferred. This is about three times higher than the emanation determined at room temperature using a different batch of the same material [70]. Since the emanation from another sample of this material is even smaller by a factor of 24, the difference is likely explained by a large variation of the radon emanation between different material batches.

The commissioning of the radon removal system contained tests of several operation modes (M1 - M4). Where the modes differ mainly in the way the xenon is extracted from the experiment and fed into the radon distillation column. During the first period (M1) the system was exclusively fed with LXe exiting the LXe purification system. For modes M2 and M3 additional gaseous xenon (GXe) was extracted from the cryogenic system and added into the column for distillation. With the difference between the two modes being a higher GXe extraction flow in the latter. During the last interval (M4) additional GXe has been extracted from the two cable feed-through vessels of the XENONnT experiment. Figure 2.9 summarizes the radon evolution during this phase, allowing to quantify the possible radon reduction of each tested mode separately. The evolution is again modeled using the piece wise continuous function (red line) given in equation 2.4. Though this function allows to infer the radon concentrations in each interval, it poses only an effective description of the system. Since it does neither contain any information on the distribution of radon sources in the system nor the different extraction flows used in each mode, it does not allow to extract further system parameters such as the radon xenon separation efficiency. A more detailed model [101] will be discussed in [80].

As shown in figure 2.7 the light yield of the LXe decreased significantly during the first commissioning interval (M1). This adds an important systematic uncertainty to the measurement causing the fiducial volume to effectively shrink as the LXe purity decreases. With the decreased purity the attenuation length of LXe for the

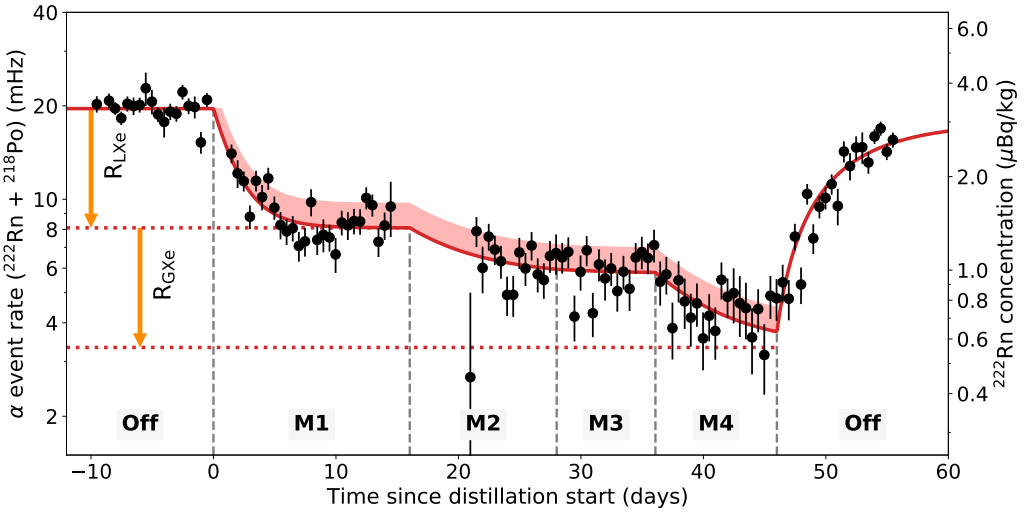

Figure 2.9: Evolution of the radon concentration during commissioning of the radon removal unit. The different modes correspond to LXe only distillation (M1), LXe & GXe distillation (M2 & M3) as well as LXe distillation in combination with an optimized GXe extraction flow (M4). Red shaded band symbolizes size of systematic uncertainty due to changes of LXe purity.

scintillation light becomes shorter. The estimation of the fiducial volume in the S1-only analysis relies on the correspondence between the `AFT` and the `drift-time` observed in S1 & S2 data (see figure 2.6). This correlation is expected to become stretched along the `AFT` axis as events happening in the lower part of the detector will lead to less detected light in the top PMT array while the effect on the bottom PMTs is less pronounced. The size of this effect was estimated using additional S1&S2 data collected during the period of lower purity. Neglecting this systematic would lead to an underestimation of the radon concentration of about 20% during the distillation. Since the time dependence of this systematic cannot be evaluated easily it was decided to not correct the data for this effect but treat it as a systematic uncertainty as indicated by the red shaded band in figure 2.9. The effect furthermore manifests by the steep decrease of the radon rate in interval M1 which is incompatible with the lifetime of ^{222}Rn. To still obtain a good description of the data in this period an effective lifetime of $\tau_{\mathrm{M1}} = (1.9 \pm 0.2)$ days was determined by the fit.

In the LXe-only mode (M1) the radon reduction is mainly determined by the speed at which the xenon can be processed by the plant. At the operating flow of 200 SLPM the mass of the full xenon inventory of the experiment was distilled approximately every 5 days. Assuming that the xenon leaving the system is completely free of radon, this would translate to a reduction factor of about 2.1 in the experiment [101]. From the data shown in figure 2.9 the reduction factor of the LXe-only mode can be estimated to be

$$R_{\mathrm{LXe}} = 2.42 \pm 0.07\,(\mathrm{stat})\,{}^{+0}_{-0.5}\,(\mathrm{syst})\,.$$

Where the asymmetric systematic uncertainty reflects the possible variation of 20%

in the fiducial volume due to the changed purity conditions. This shows that the distillation column is able to remove radon from the LXe inventory with a reduction factor being in agreement with the prediction based on the processed xenon flow.

The extraction and distillation of additional GXe sampled from the cryogenic system of the experiment allows a further reduction of the radon concentration (M2 - M3). By this, radon can be removed from the system before it dilutes in the large LXe inventory from which it is more difficult to remove. The increased removal efficiency reflects in additional reduction factors of $(1.43 \pm 0.07_{\,\mathrm{stat}})$ and $(1.40 \pm 0.09_{\,\mathrm{stat}})$ for M2 and M3 respectively. Where the higher extraction flow in M3 compared to M2 did not yield a significant difference in the radon reduction. For M4 additional GXe from the two cable feed through vessels has been extracted. This led to another significant decrease of the radon concentration of

$$\mathrm{R_{GXe}} = 2.4 \pm 0.2$$

with respect to the radon concentration achieved by the LXe-only mode. Note that the additional reduction factors for the GXe modes (M2 - M4) are not affected by the aforementioned systematic uncertainty since they are compared to interval M1 in which the LXe purity is already low. The combination of both modes will allow to reach or even surpass the radon concentration of 1 µBq/kg for which the XENONnT experiment was designed for.

2.2 Alpha events in gaseous nitrogen

Prior to the filling of the XENONnT detector with LXe, several tests and measurements were carried out while the system has been evacuated and filled with nitrogen. These tests included first characterization measurements of the PMTs as well as the radon emanation measurements described in [70]. Data has been acquired throughout some of those periods which allows to independently study alpha events in the detector.

First the light production via fluorescence in nitrogen will be discussed together with the identification of these events in the XENONnT detector. Afterwards the time-dependence of the alpha-induced event rate will be analyzed and conclusions on the ^{222}Rn emanation as well as the ^{210}Po surface activity will be drawn.

Fluorescence of nitrogen

The fluorescence of nitrogen is exploited by several experiments studying air-showers from ultra-high energy cosmic rays like the Pierre Auger observatory [102]. The fluorescence of nitrogen is mainly located in the ultraviolet (UV) regime between wavelengths of 300 nm and 400 nm [103]. Figure 2.10 shows the nitrogen fluorescence spectrum reported on in [103, 104] for excitation with an electron beam. The different lines correspond to emissions from different electronic transitions. Since the nitrogen is in molecular form, these lines are broadened to a band structure due to the

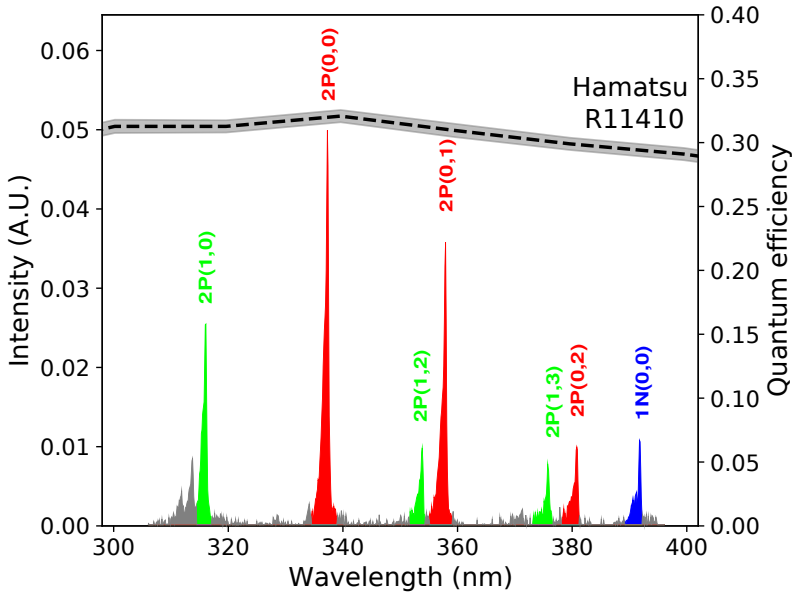

Figure 2.10: Fluorescence spectrum of electrons in dry air [103] with wavelength dependent quantum efficiency of the R11410 PMTs used in the XENONnT experiment [105].

additional rotational and vibrational degrees of freedom of the diatomic molecules. The wavelength dependent detection efficiency of the Hamamatsu R11410 PMTs is indicated by the dashed black line in the figure on the right y-axis as has been measured in [105]. It can be seen that the PMTs used in the XENONnT experiment have an almost constant quantum efficiency throughout the nitrogen fluorescence spectrum which means that these photons are expected to occur in the nitrogen-filled detector.

Indeed, an additional population of events can be observed in the XENONnT data as soon as the detector is filled with nitrogen. Figure 2.11 compares events PMT signal recorded under vacuum (left) and in a nitrogen atmosphere (right). Shown

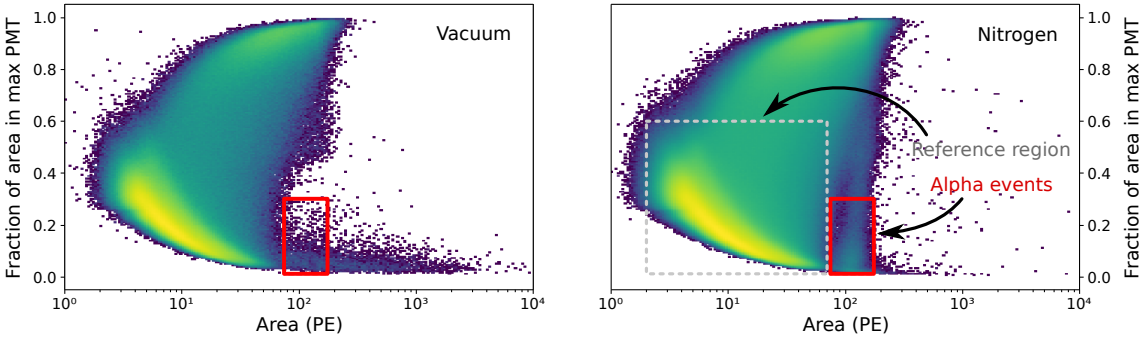

Figure 2.11: Comparison of data taken in vacuum (left) and nitrogen (right). A discrete population at an `area` of approximately 100 PE is visible only in the nitrogen data (red box). These events are compatible with the fluorescence of nitrogen caused by interactions of alpha particles. A reference region containing mostly background events is indicated in gray.

is the detected `area` as a function of the fraction of area detected by the PMT seeing the most signal in each event. This variable describes how much an event is localized within a single PMT. Lower values correspond to events in which the light is more equally distributed among the participating PMTs, whereas values closer to one mean that most of the light has been detected by one individual PMT. It can be seen that the population enclosed in the red selection is only present in the data collected with nitrogen inside the detector. A likely origin of those events is therefore the fluorescence of nitrogen. Events at lower energies are likely caused by external gamma radiation.

The fluorescence yield of pure nitrogen for 5.3 MeV alpha particles has been measured to be around 1000 photons [106]. Where the fluorescence yield for air is found to be significantly lower [103, 107]. Assuming a typical photon detection efficiency of the order of 10% [108] [2], this matches with the occurrence of alpha induced events in the XENONnT data at around 100 PE. The time width of the events falling into the red selection is found to be of the order of 50 ns [109]. The different lifetimes of the excited nitrogen states have been measured for example in [103] and are found to lie between 30 ns to 65 ns. Since this is also compatible with the observations from the XENONnT nitrogen data strengthens the hypothesized origin of these events to come from alpha particles interacting with the gaseous nitrogen.

Time evolution of the event rate

For the radon emanation measurements reported in [70], the detector was filled repeatedly with radon-free nitrogen. The gas is then left in the detector for a period of approximately one week in order to allow the emanated radon to accumulate. Throughout this period, data with the PMTs was occasionally collected. After this time, a fraction of the gas is extracted to conduct the radon measurement using an electrostatic radon monitor.

There are two sources of alpha emission in the XENONnT detector. Alpha particles can either be emitted by ^{210}Po which has deposited on the internal surfaces of the detector during construction or by emanated ^{222}Rn as well as its subsequent decay products (see equation 2.1). In section 2.1 the data acquired in LXe is used allowing to distinguish both contributions due to the different decay energies of the respective isotopes. Since the energy resolution in gaseous nitrogen is too poor to resolve the different alpha emission lines based on their energy a similar study is not possible. However, the rate of both contributions is expected to show different time dependencies after the detector is filled with nitrogen. Due to the accumulation of ^{222}Rn in the gas the radon emanation induced activity increases over time. In contrast to the activity of ^{210}Po which can be assumed to stay constant over the duration of each measurement.

Figure 2.12 shows the time evolution of the detected rate of events selected by the box illustrated in figure 2.11 (blue markers). The x-axis shows the duration in days

[2] Note that this is only an order of magnitude estimate. This approximate value corresponds to a liquid xenon-filled detector and for photons at the liquid xenon scintillation wavelength.

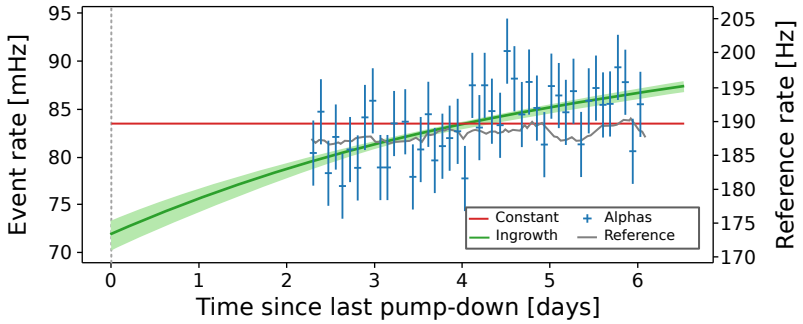

Figure 2.12: Evolution of the rate of alpha candidate events (blue markers) in nitrogen as a function of time after nitrogen filling of the detector. The data is fit (green line) with a model describing the radon in-growth in the detector together with a constant rate (equation 2.5). The rate found in the reference region shown in figure 2.11 is indicated in gray. The fit of the alpha data with a constant is shown by a red line for comparison.

since the detector has been filled with nitrogen. On the right hand y-axis the rate found in a reference region located in the gamma background is shown. Illustrated by the green line is a fit of the data with the expected radon in-growth function.

$$R(t) = R_{\text{const}} + R_{\text{ingr}} \cdot \left(1 - e^{-\lambda_{222Rn} \cdot t}\right) , \tag{2.5}$$

where the constant contribution R_{const} is used to describe the fraction of the rate from ^{210}Po decays and the in-growth amplitude R_{ingr} describes the alpha events induced by ^{222}Rn, ^{218}Po and ^{214}Po and λ_{222Rn} is the decay constant of ^{222}Rn.

Table 2.1 compares the extracted rate values for the three nitrogen fillings that have been performed. It can be seen that the extracted values for R_{const} are found to

Table 2.1: Comparison of the extracted event rates for the three nitrogen fillings that were performed with the XENONnT detector.

Filling	R_{const}	R_{ingr}
First	(72 ± 2) mHz	(22 ± 5) mHz
Second	(63 ± 2) mHz	(20 ± 4) mHz
Third	(67 ± 3) mHz	(12 ± 5) mHz

be similar between the three measurements. In this study there is no selection of a fiducial volume. Therefore the complete internal surface as calculated in section 2.1.3 needs to be considered. This is estimated to be 9.6 m^2. From the measured value an approximate surface activity of (7 ± 0.5) mBq per square meter would be inferred, which is roughly 40% higher than the value measured using the LXe data above. For the radon induced rate the average of the three fillings yields (18 ± 6) mHz. Note that this value reflects the summed activity from the ^{222}Rn as well as its daughters. Some of these decay products will plate-out on the walls of the detector. This adds

a large uncertainty on the estimation of the ^{222}Rn, since the exact ratio with which each of them is detected is not known. Two limiting cases can be considered in order to give a lower and an upper bound. For the lower bound it is assumed that the rate is shared by all three isotopes in equal parts, while for the upper bound it is assumed that the full rate stems only from decays of ^{222}Rn. This contains the radon emanation rate between (6±2) mBq and (18±6) mBq.

This emanation rate cannot be directly compared to emanation of the full XENONnT detector as measured using the LXe data shown in section 2.1.4. That is because the nitrogen has not been circulated through the system leading to a potentially inhomogeneous distribution of the radon in the system. However, the location and size of the radon sources is known from the dedicated radon screening campaign reported in [70]. Summing the emanation of the components closest to the TPC gives a radon emanation rate of about 11 Bq. The fact that this falls into the above stated interval makes the hypothesized origin of these events to be from radon induced alpha decays very plausible.

2.3 Summary and discussion

The ambitious scientific goals of the XENONnT experiment can only be achieved, if the challenging requirements on the experimental backgrounds are not overstepped. One of the most important background contributions arises from the constant emanation of ^{222}Rn from materials in the detector. Two different studies have been presented in this chapter, to quantify the amount of ^{222}Rn in the detector via its induced alpha decays. The data which has been evaluated, was collected during the commissioning phase of the detector. This allowed to additionally investigate the impact of the new radon removal unit, as well as the LXe purification system onto the radon concentration.

The first study uses data which has been recorded when the detector was already filled with LXe. For most of the time however, it was not operated as a TPC, since the field which is necessary for the charge extraction was turned off. This precaution was taken due to the quickly changing detector conditions during the commissioning phase. The developed analysis therefore only relies on the information of the S1 signals to measure the radon rate. Estimation of the fiducial mass and the complete reconstruction of the alpha energy-spectrum was done using additional data with S1 & S2 signals, which was acquired during a short time period. With this it was possible to measure the ^{222}Rn concentration of the XENONnT experiment to be $\left(3.6\,^{+0.7}_{-0.3}\right)$ µBq/kg. This is slightly less than the radon concentration of $\left(4.2\,^{+0.5}_{-0.7}\right)$ µBq/kg which is predicted by the dedicated radon screening campaign [70]. For the second study, data from earliest stages of commissioning is used, during which the detector was filled with gaseous nitrogen. Exploiting the fluorescence light of the nitrogen, allowed to detect alpha particles emitted by ^{222}Rn, as well as its decay products. The poor energy resolution of the nitrogen-filled detector, however, does not allow for a full reconstruction of the alpha energy spectrum.

Therefore, the time dependence of the alpha event rate is used to distinguish the contribution of ^{210}Po deposited on the surface and ^{222}Rn from emanation. Still, this analysis has rather large uncertainties and the results agree with the ones from the first study only on an order of magnitude level.

Using the presented S1-only analysis furthermore allowed to keep track of the radon concentration during the commissioning of the radon removal system. The system is able to remove radon from xenon by means of cryogenic distillation (see e.g. [77–79]). It is able to simultaneously operate in two modes, in which xenon can be fed into the system in gaseous and/or liquid form. For the GXe-only mode, a maximum reduction of the ^{222}Rn concentration in the detector by a factor of 2.4 ± 0.2 has been determined. An additional reduction by a factor of $2.42 \pm 0.07\,(\text{stat})\,^{+0}_{-0.5}\,(\text{syst})$ has been achieved for the combined LXe and GXe extraction mode. This result is affected by a simultaneous decrease of the scintillation light yield, resulting in the systematic uncertainty. Throughout the first campaign of scientific data taking, the system has been operated only in GXe mode, which will allow to reach a radon concentration of less than 2 µBq/kg. The design goal of 1 µBq/kg for the XENONnT detector [6], can be slightly surpassed by the combination of both removal modes.

The XENONnT detector is also the first large-scale LXe experiment employing a LXe purification system to remove chemical impurities from the xenon. It allowed to reach an unprecedented large electron lifetime of more than 10 ms [110]. Two different types of oxygen filters have been used throughout the commissioning phase. A filter with high-efficiency and a large oxygen capacity has been used first to remove the bulk amount of impurities from the xenon inventory. Its radon emanation was expected to be prohibitively large for a continued operation throughout the scientific data taking period. This assumption was confirmed by the presented S1-only analysis. Therefore, a second oxygen filter having a lower radon emanation rate has been installed, after an appreciable purity level was reached. Its low radon emanation was confirmed in the presented data analysis. Despite its smaller oxygen capacity, this filter proved to be capable to maintain the high purity over an extended amount of time. The combination of both filters made it possible to operate the detector at a never reached level of LXe purity, while meeting the extremely low background requirements of the experiment.

3 Production and characterization of stainless steel radon sources

The radioactive noble gas ^{222}Rn is omnipresent in our environment. A large fraction of our annual radiation exposure is due to the decay of radon and its subsequent decay products [111]. But also the minute radon concentrations which are present in experiments searching for rare events can be a serious concern for the sensitivity of such detectors as detailed in section 1.2.2. Therefore, serious effort is spent during the planning, construction and operation phase of such experiments to reduce as good as possible the amount of radon in the experiment.

Different strategies for the reduction of the ^{222}Rn-induced background in such detectors are being followed and are further detailed in chapter 4. One of the most important measures against radon are material screening campaigns allowing to select construction materials with a low radon emanation (see for example [70, 79, 112, 113]). For the regular calibration of the radon detectors used in such campaigns, reliable sources with a well known amount of radon emanation need to be available. But also studies for novel techniques of radon mitigation like the coating-based radon barriers introduced in chapter 4 heavily, rely on these sources. Especially for the latter, radon emanation coming from stainless steel surfaces is of special interest. Though stainless steel radon sources have been prepared for example by electroplating of ^{226}Ra (see e.g. [114]), such a deposit changes the surface which might pose a problem for those studies. This chapter describes a novel approach which uses ion implantation to produce a mostly unaltered stainless steel radon source.

Two sources have been produced in the past [71] at the isotope separation online device (ISOLDE) at CERN for which a detailed characterization is presented in the first half of this chapter. Besides their application in the studies of radon mitigation, these sources proved to be very useful also for the calibration of alpha spectrometers [115, 116] and novel radon detectors [117]. The second part of the chapter is focused on results from an alternative implantation method which uses the recoil of the ^{224}Ra nucleus following the alpha decay of ^{228}Th.

3.1 Production and characterization of a ^{226}Ra implanted stainless steel radon source

Ion implantation is a widely applied technique for example in the semi-conductor industry [118], where a beam of accelerated ions is used to embed atoms just below the surface of a sample. Using a radioactive ion beam (RIB) allows to also implant

non stable isotopes like for example ^{226}Ra. By this an initially clean material like for example stainless steel can be artificially contaminated to provide a measurable amount of radon emanation. In contrast to a deposition of radium on the sample surface as for example recently reported in [114], an implantation is expected to maintain the original properties of the surface mostly unchanged. This is a mandatory requirement for the application of these samples in the studies presented in chapter 4.

3.1.1 Implantation of the samples at the ISOLDE facility

The implantation of the samples took place in 2017 using the RIB provided by the ISOLDE facility at CERN [120]. Figure 3.1 schematically shows the working principle of the facility. Among various other short and long-lived isotopes, the ^{226}Ra used for the implantation has been previously produced by bombardment of an uranium carbide target with a total of about 1.2×10^{18} protons. Due to the long half-life of ^{226}Ra (see equation 3.2), it remains inside the target, which allowed to carry out the actual implantation without an additional proton irradiation of the target (*off-line*). The ^{226}Ra was released from the heated target via diffusion, ionized using a surface ionization source and accelerated to an energy of 30 keV. The ion beam was cleaned from other medium and long-lived isotopes released by the target, using the general purpose separator (GPS) analyzing magnet. An average beam current of approximately 3 pA was obtained for the selected atomic mass number of 226. Afterwards the beam is directed into the implantation chamber where the two samples (*sample A* & *sample B*) were mounted. They are cut from 1 mm thick stainless steel sheets and are approximately 2 cm × 2 cm in size. Before shipping the samples to CERN they have been thoroughly degreased using acetone and 2-propanol. During the implantation, the RIB was swept across the center of each sample, covering an area of 1 cm × 1 cm. The expected depth distribution of ^{226}Ra below the surface of the stainless steel sample can be simulated using the "stopping and range of ions in matter" (SRIM) code [121] and is shown in figure 3.2. It is expected that the ions are located at a mean depth of 7.9 nm below the surface with a standard deviation of the distribution of 2.3 nm. This shallow implantation depth allows 21% - 23% of the radon produced inside the sample to

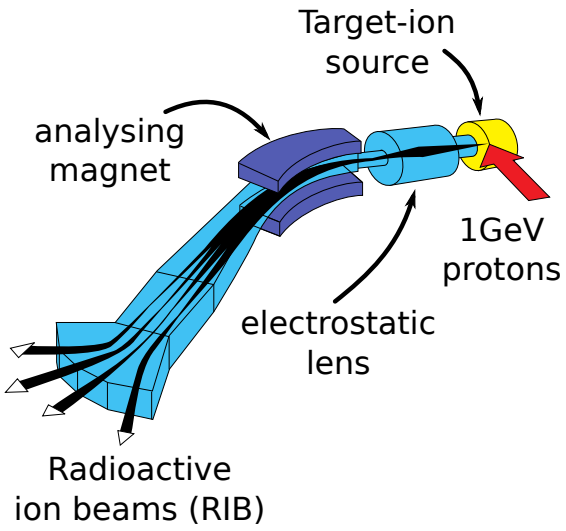

Figure 3.1: Sketch illustrating the ISOLDE facility used for the production of the ^{226}Ra implanted samples. Figure taken from [119].

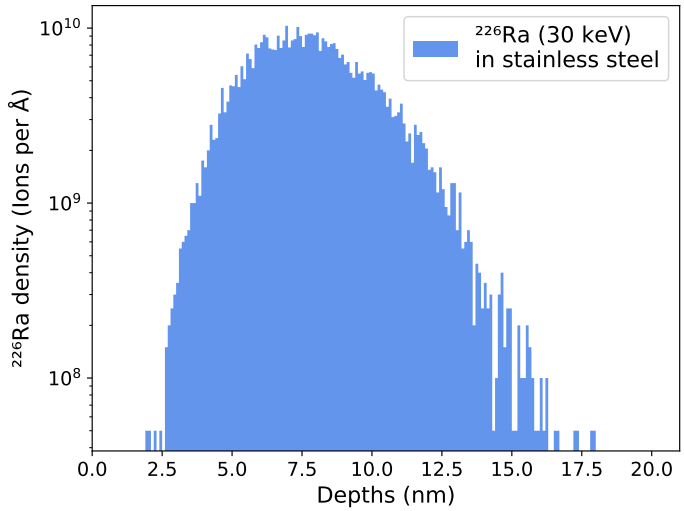

Figure 3.2: Expected depth distribution of implanted ^{226}Ra ions in the stainless steel sample as simulated using SRIM [121]

escape by recoil (see section 3.3).

In this proof-of-principle implantation each sample got implanted with about 5×10^{11} atoms of ^{226}Ra [71]. Multiplying this number with the radium decay constant, $\lambda_{226\mathrm{Ra}}$, directly yields the expected ^{226}Ra activity of the sample

$$\begin{aligned} A_{226\mathrm{Ra}} &= N_{226\mathrm{Ra}} \cdot \lambda_{226\mathrm{Ra}} \\ A_{226\mathrm{Ra}} &\approx 7\,\mathrm{Bq}\,. \end{aligned} \tag{3.1}$$

The mechanical stability of the implantation has been tested by wiping the implanted sample using an ethanol soaked filter paper. It was found that despite its shallowness only about 0.2% of the activity could be removed suggesting a sufficient mechanical stability.

The measurements presented in the next sections are aimed at the validation of the activity, as well as the determination of the available radon emanation from the samples. The characterization measurements are followed by a description of various short-lived contaminants, which have been present in the samples shortly after their implantation.

3.1.2 Spectrometric measurements

The implanted radium atoms are decaying according to the uranium decay series. For reference, the relevant part of this series is given below:

$$\begin{aligned} {}^{226}\mathrm{Ra} &\xRightarrow[1600\,\mathrm{y}]{4.9\,\mathrm{MeV}} {}^{222}\mathrm{Rn} \xRightarrow[3.8\,\mathrm{d}]{5.6\,\mathrm{MeV}} {}^{218}\mathrm{Po} \xRightarrow[3.1\,\mathrm{min}]{6.1\,\mathrm{MeV}} {}^{214}\mathrm{Pb} \\ &\xrightarrow[27\,\mathrm{min}]{\beta} {}^{214}\mathrm{Bi} \xrightarrow[20\,\mathrm{min}]{\beta} {}^{214}\mathrm{Po} \xRightarrow[160\,\mu\mathrm{s}]{7.8\,\mathrm{MeV}} {}^{210}\mathrm{Pb} \xrightarrow[22\,\mathrm{y}]{\beta} \ldots \end{aligned} \tag{3.2}$$

The alpha transitions of the chain are indicated by double arrows with their corresponding alpha particle energies. Isotopes following the decay of ^{210}Pb are neglected here because the half-life of ^{210}Pb is much longer than the time-frame following the implantation.

Based on the alpha energy, decays of ^{226}Ra can be clearly distinguished from the decays of the other isotopes present in the chain. Similarly, there is a characteristic gamma particle with an energy of 186.2 keV being emitted following some of the ^{226}Ra decays. Therefore, the amount of implanted ^{226}Ra activity can be determined directly using alpha and gamma spectrometry. For these measurements, each sample has been installed into a cylindrical high density polyethylene (HDPE) holder with an outer diameter of 2.7 cm where it is fixed in place using a holder ring as shown in figure 3.3. This holder allows for safe handling of the sample and ensures that it is placed at a fixed position inside the spectrometers.

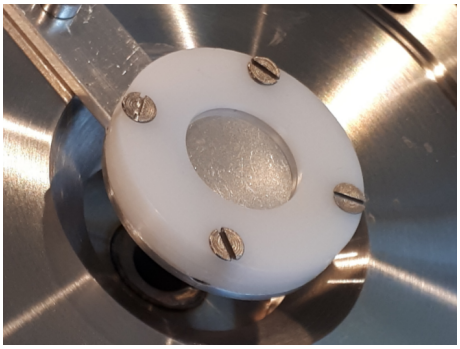

Figure 3.3: Photograph of the implanted stainless steel sample inside the holder used for the spectrometric measurements.

Alpha spectrometry

The alpha spectrometers use a windowless Hamamatsu S3204-09 silicon positive intrinsic negative (PIN) diode with an active detection surface of $18 \times 18\,\mathrm{mm}^2$ [122] for alpha particle detection. The diode is mounted on the top flange of a vacuum vessel, where it is facing the active side of the implanted sample. During the measurement the pressure inside the spectrometer needs to be kept below the millibar level to reduce the energy loss of the alpha particles as they cross the space between the sample surface and the diode. Note that the alpha particles will lose an additional 0.1% of their initial energy within the thin stainless steel layer covering the implantation site. However, this is well below the energy resolution of the PIN diode and the resulting small shift in the energy spectrum is not visible. The negative (electrons) and positive (holes) charge carriers produced in the PIN diode by the impinging alpha particles are collected on the anode and cathode plane of the diode. After pre-amplification, both signals are fed into a differential amplifier [123] before the height of the resulting signal is digitized using a FAST ComTec MCA-3 multichannel analyzer. Since the signal height is proportional to the amount of deposited charge in the diode, it gives a measure of alpha particle energy.

Figure 3.4 shows the pulse-height spectrum of *sample A* 1.7 years after the implantation. The spectrum shows the alpha emission lines of ^{226}Ra, ^{222}Rn, ^{218}Po and ^{214}Po which are indicated by blue lines. The spectrum is fit using a sum of four individual Crystal-Ball (CB) functions [124] indicated by the red line showing good

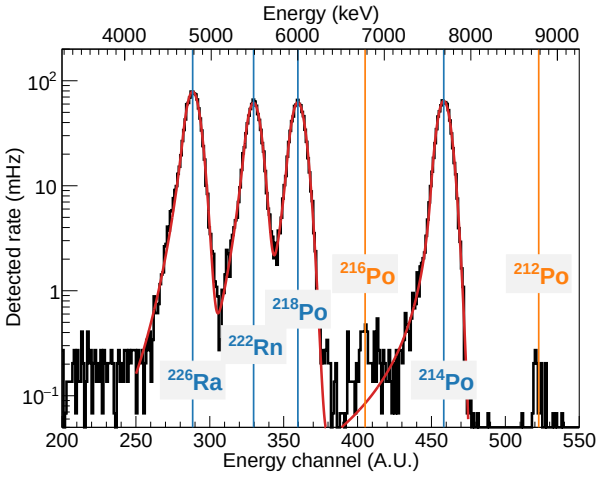

Figure 3.4: Alpha spectrum of *sample A* long (1.7 years) after implantation. Alpha decay lines from ^{226}Ra and subsequent decay products (blue) are clearly visible. Subdominant lines from isotopes belonging to the thorium decay series (orange) are visible as well.

agreement with the data (see equation D.1 in the appendix). This function is commonly used to describe the shape of alpha emission peaks detected by silicon PIN diodes (e.g. [125]) since it combines a Gaussian probability density function (PDF) with a power-law tailing towards lower energies. The tailing is explained by events in which part of the alpha energy is lost inside the insensitive regions of the diode. Further small contributions to the spectrum are visible, which can be attributed to ^{216}Po and ^{212}Po (orange lines), which are part of the primordial thorium decay series. The presence of these isotopes will be discussed in more detail in section 3.1.4.

For the measurement shown in figure 3.4, the sample has been placed inside the HDPE holder and put onto the tray of the spectrometer described in [115, 125]. The distance between the sample surface and the diode was chosen to be (1.2 ± 0.2) cm, resulting in a geometrical detection efficiency of $\left(11.2\,^{+2.9}_{-2.2}\right)$ % as estimated using a Monte-Carlo simulation.

To reduce any potential bias from events belonging to the tail region of ^{222}Rn, the ^{226}Ra activity is determined using the normalization constant of the CB-function. This number is then corrected for the geometric detection efficiency mentioned above, to obtain the implanted activity of ^{226}Ra which amounts to $\left(8.70 \pm 0.06\,(\text{stat})\,^{+2.0}_{-1.8}\,(\text{syst})\right)$ Bq. From the spectrum it can be also seen that the detected rates of the subsequent decay products of ^{226}Ra (^{222}Rn, ^{218}Po and ^{214}Po) are lower by about 25%. This can be explained by the fraction of gaseous ^{222}Rn emanating from the sample as will be described in section 3.1.3. The emanated radon can distribute in the large volume of the spectrometer vessel, where it mostly evades any further detection.

A similar alpha spectrum has been acquired for the implanted *sample B* using a similar spectrometer. For this measurement the distance between the sample and the diode was increased to (10.7 ± 0.3) cm. While the larger distance significantly reduces the geometric detection efficiency to only $\left(2.23\,^{+0.11}_{-0.15}\right) \times 10^{-3}$, it also reduces the uncertainty of the detection efficiency due to uncertainties in the distance measurement. Using this measurement an implanted ^{226}Ra activity into *sample B* of $\left(9.13 \pm 0.10\,(\text{stat})\,^{+0.7}_{-0.4}\,(\text{syst})\right)$ Bq is determined.

As can be seen in figure 3.3 a small part of the sample is covered by the holder ring. Since the ring has a circular opening with a diameter of $(1.9 \pm 0.2)\,\mathrm{cm}$ [126] and the RIB was swept across an area of about $1\,\mathrm{cm} \times 1\,\mathrm{cm}$ around the center of the sample, none of the activity should be covered by the ring. To verify this assumption the alpha spectrometric measurements have been repeated under identical conditions but with the holder ring carefully removed.

Table 3.1: Comparison of the detected alpha activities from ^{226}Ra of both samples with and without the holder ring present. Note that both samples were measured in different setups with very different detection efficiencies. The last row reports the activity after its correction for the detection efficiency.

Measurement	*Sample A*	*Sample B*
Detected rate (mHz)	-	-
with holder	$972 \pm 8_{\,\mathrm{stat}}$ *	$20.3 \pm 0.3_{\,\mathrm{stat}}$
without holder	$977 \pm 11_{\,\mathrm{stat}}$ *	$20.5 \pm 0.3_{\,\mathrm{stat}}$
Det. efficiency	$\left(11.2\,^{+2.9}_{-2.2}\right)\,\%$	$\left(2.23\,^{+0.11}_{-0.15}\right)\,‰$
Implanted activity (Bq)	$8.70 \pm 0.06_{\,\mathrm{stat}}\,^{+2.0}_{-1.8\,\mathrm{syst}}$	$9.13 \pm 0.10_{\,\mathrm{stat}}\,^{+0.7}_{-0.4\,\mathrm{syst}}$

* Data taken from [126].

In table 3.1 the detected activities for the four measurements are reported together with their statistical uncertainties. Note that for the direct comparison between both cases the uncertainty from the detection efficiency can be neglected, since the setup was kept identical. As can be seen for each sample both measurements are in good agreement. The majority of the implanted activity is therefore indeed confined within $(1.9 \pm 0.2)\,\mathrm{cm}$ around their center.

Gamma spectrometry

Besides the measurements of the alpha particle energies, gamma spectra of both samples have been acquired using the high purity germanium (HPGe) spectrometer described in [127]. During the measurement the chamber is constantly flushed with nitrogen to remove radon from the inside. The detector itself is a 0.63 kg p-type HPGe crystal, surrounded by a copper, steel, and lead shield with a minimum thickness of 16 cm. A cutaway sketch of the detector and its shielding is shown in figure 3.5. Additional multi-wire proportional chambers surround the active volume and are used as active muon veto [128]. The detector is suited in the shallow underground laboratory at the Max-Planck-Institut für Kernphysik (MPIK) where it is shielded by an overburden of 15 meter water equivalent (mwe) [129].

By the decay of ^{226}Ra into ^{222}Rn, the daughter is produced in an excited nuclear state in about 6% of the cases. The new formed nucleus then rapidly de-excites under emission of a 186.2 keV gamma particle [76]. Just as for the alpha spectrometer the probability with which this gamma particle can be detected depends on the geometry of the setup. However, not all gamma particles reaching the detector deposit their full energy within the HPGe crystal. So in addition to the geometric efficiency, the full-absorption probability needs to be taken into account. Both effects are estimated using a GEANT4 [130] based Monte-Carlo simulation. The combined detection efficiency then amounts to $(10.2 \pm 1.2)\%$ [128]. Finally the rate needs to be corrected for the fact that only in 6% of the disintegrations the gamma is emitted.

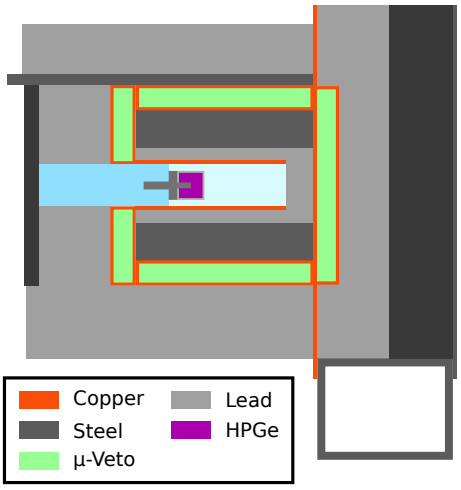

Figure 3.5: Sketch of the HPGe gamma spectrometer showing the interleaved shielding layers. Figure adapted from [128].

Figure 3.6 shows a HPGe gamma spectrum of *sample B* 3.4 years after implantation. Emission lines from ^{226}Ra (red) as well as from its daughter isotopes ^{214}Pb (yellow) and ^{214}Bi (blue) can be seen. The lines are on top of a continuous background distribution caused by gamma particles depositing only a fraction of their full energy within the HPGe crystal as well as from residual cosmic rays. The inset shows a zoom-in of the region close to the 186.2 keV emission line of ^{226}Ra. Highlighted by the darker red color is the region within which the line activity A_{sig} is evaluated, while its side bands (light red) are used to estimate the background of

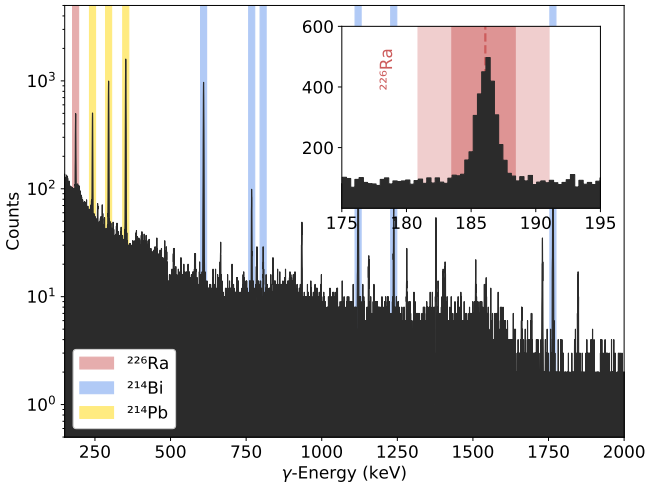

Figure 3.6: HPGe spectrum of *sample B* recorded 3.4 years after the implantation. The energy region close to the emission line of ^{226}Ra (red) at an energy of 186.2 keV is enlarged in the inset. Emission lines from the daughter isotopes ^{214}Pb (yellow) and ^{214}Bi (blue) are highlighted as well.

the line A_{bkg}. The activity A_{226Ra} of ^{226}Ra is then evaluated as

$$A_{226Ra} = \frac{A_{sig} - A_{bkg}}{\epsilon_{det} \cdot \epsilon_{BR}}\,, \tag{3.3}$$

where ϵ_{BR} is the 6% probability for the emission of the 186.2 keV gamma particle and ϵ_{det} is the detection efficiency as described above.

The determined activities for the implanted ^{226}Ra are then found to be $(7.4 \pm 0.1\,(\text{stat}) \pm 0.9\,(\text{syst}))$ Bq and $(8.4 \pm 0.3\,(\text{stat}) \pm 1.0\,(\text{syst}))$ Bq for *sample A* and *sample B* respectively. As already observed using the alpha spectrometer the implanted activity in *sample B* seems to be larger by about 13% compared to the one of *sample A*. The results from gamma and alpha spectrometry are found to be in agreement given their systematic uncertainties.

For the two short-lived daughter isotopes ^{214}Pb and ^{214}Bi the gamma spectrum shows an activity which is lower by approximately 2 Bq (see also table 4.3 in chapter 4). The different rate can be explained by the radon emanation of the samples. Note that both isotopes are located after ^{222}Rn in the decay scheme (see equation 3.2). Radon which is emanated from the sample is either removed by the nitrogen flushing or it distributes inside the plastic dish housing the sample holder such that the subsequent decays feature a reduced geometric detection efficiency. Both effects would lead to a reduction in the detected activity of these subsequent decay products. In section 3.1.3 the exact quantification of the ^{222}Rn emanation will be discussed.

3.1.3 Measurement of radon emanation

The primary motivation for the production of the samples was their application as radon sources. Two different measurements determining the amount of radon emanation from the samples were carried out and will be described in this section. The radon emanation rate at room temperature was measured for both samples using miniaturized proportional counters, whereas the low-temperature dependence of the emanation was assessed for *sample B* using an electrostatic radon monitor.

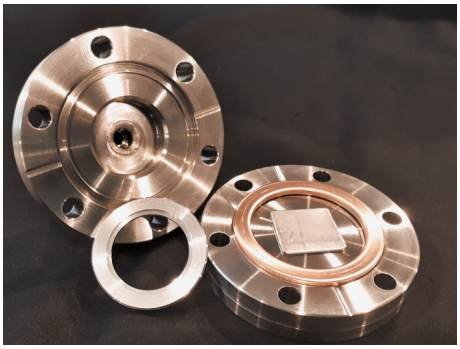

Figure 3.7: Photograph of the vessel used for the radon emanation measurements of the implanted stainless steel samples. The aluminum ring in the front is used to fix the sample in place.

For both measurements the sample was placed into a gas-tight emanation vessel as shown in figure 3.7. It is made from two CF-40 flanges between which the sample is centered using the depicted aluminum ring with a 24.1 mm wide, concentric opening. Before each measurement, the emanation vessel is filled with helium and the sample

is left for emanation for several days. During this emanation time the radon activity $A_{222Rn}(t)$ inside the vessel *grows-in* towards an equilibrium in which the rate of decaying ^{222}Rn atoms equals the radon release rate of the sample.

$$A_{222Rn}(t) = A_{em} \cdot \left(1 - e^{-\lambda_{222Rn} \cdot t}\right) . \tag{3.4}$$

Here λ_{222Rn} is the decay constant of ^{222}Rn and A_{em} the radon emanation rate of the sample. For the measurement the accumulated radon is extracted from the emanation vessel together with the helium carrier gas. Radon is retained in an activated carbon trap which is cooled using liquid nitrogen, while the carrier gas can be pumped away. The radon trap is then heated up to release the radon again in order to transfer it into either one of the two detectors mentioned above. The amount of emanated radon can then determined by the counting the number of decays observed in the detector.

Note that the top flange of the emanation vessel features a concentric 6.55 mm deep and 24.67 mm wide recess (see figure 3.7), such that a minimum clearance between the sample surface and the vessel walls of about 5.6 mm is maintained. This is important since recoiling ^{222}Rn atoms can have sufficient kinetic energy to get implanted into the steel vessel where they would potentially be lost for the measurement. The mean range of the ^{222}Rn recoil was estimated using SRIM to amount to about 4.5 mm in a helium atmosphere of 100 mbar. Therefore, a minimal helium pressure of 200 mbar has been chosen for all emanation measurements presented in the following.

Emanation at room temperature

For the emanation measurements carried out at room-temperature conditions, the local radon screening facility at the MPIK detailed in [79, 131] has been used. It uses miniaturized proportional counters which were originally developed for the GALLEX solar neutrino experiment [132]. After the radon sample is released from the carbon trap it is cleaned from potential impurities that could affect the counting process. It is then filled into the counter volume of about 1 cm^3 together with a counting gas mixture of 10% methane and 90% argon (P10). Alpha decays from radon as well as its subsequent decay products are then counted for a certain amount of time. The number of observed alpha events is then corrected for the known background rate of the counter as well as the radon detection efficiency of the counter. Together with the counting duration, this yields the amount of extracted radon from the emanation vessel.

Two measurements have been carried out for each of the two implanted samples, for which the results are shown in figure 3.8. For each sample both measurements are found to be in very good agreement. The weighted average of both measurements is (2.07 ± 0.05) Bq and (2.00 ± 0.05) Bq for *sample A* and *sample B* respectively. For three out of the four measurements emanation took place in a helium atmosphere at a pressure of 1050 mbar. With the exception of the first measurement of *sample*

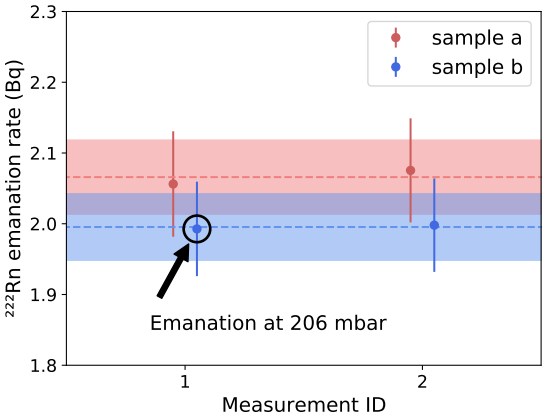

Figure 3.8: Radon emanation of both ^{226}Ra implanted stainless steel samples at room temperature as measured using miniaturized proportional counters.

B, for which a significantly lower helium pressure of only 200 mbar has been chosen. As the resulting radon emanation rate is found to be compatible with the other measurement of that sample, a strong pressure dependence can be ruled out.

Comparing the radon emanation rate to the total implanted ^{226}Ra activity it can be seen that only between 20% to 28% of the ^{222}Rn produced in the sample is able to make its way out of the sample. This emanation fraction is in good agreement with the expected fraction for a purely recoil-driven emanation process as will be discussed in section 3.3. So it can be concluded that the majority of the radon escapes from the sample by recoil with the release via diffusion playing a subdominant role.

Emanation at low temperatures

The difference between a recoil and a diffusion dominated emanation process becomes even more clear when looking at the temperature dependence of the emanation rate. While a diffusion dominated process exhibits a strong temperature dependence, the emanation rate for a recoil driven process is expected to be mostly independent with temperature. Studying the behavior of the sample at low temperatures is also necessary for any potential application of the source in a cryogenic environment in the future.

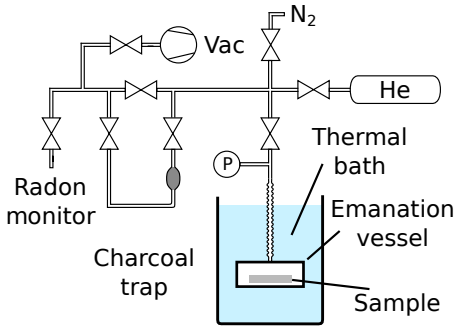

Figure 3.9: Sketch of the setup used to study the temperature dependence of the radon emanation from the ^{226}Ra implanted stainless steel sample

The temperature during the emanation is maintained constant using a thermal bath filled with 4 liters of a 2:1 mixture of ethylene glycol (anti-freeze) and water. Its temperature is regulated using an (HAAKE EK 90) immersion cooler and monitored by a PT100 temperature sensor. To reduce the heat influx from the out-

side, the emanation vessel (figure 3.7) holding the implanted *sample b* is connected to the extraction setup shown in figure 3.7 via a 30 cm long bellow. A magnetically coupled stirrer has been used to guarantee the homogeneity in the thermal bath. For each measurement the emanation vessel has been filled with helium to a pressure of (203 ± 3) mbar. After an emanation duration of about one week, the carrier gas was extracted together with the accumulated radon using a turbo molecular pump (TMP). The radon was separated from the helium carrier by an activated carbon trap held at liquid nitrogen temperature. Following the extraction, the radon was released by heating the trap to 150 °C, and transferred for counting into the electrostatic radon monitor described in [133] by a stream of gaseous nitrogen.

The radon monitor is equipped with the same type of silicon PIN diode as is used for the alpha spectrometers described in section 3.1.2. However, the monitor is filled with 1050 mbar of nitrogen and does not detect the alpha particle emitted in the decay of ^{222}Rn. It relies on the collection of the positively charged radon daughters [134] by an electric field, applied between the grounded detector vessel and the PIN diode, which is biased by a negative high voltage (HV) of 1 kV. Following the decay scheme shown in equation 3.2, alpha particles emitted in the subsequent decays of ^{218}Po and ^{214}Po can then be detected [1]. Since ^{214}Po has the highest decay energy, events from this decay can be selected easily from the spectrum. Furthermore it features a slightly higher detection efficiency compared to ^{218}Po. The combined collection and detection efficiency of the radon monitor was measured to be (35 ± 2) % in two reference measurements using a radon source with a known radon emanation rate of (52 ± 3) mBq.

Besides the detection efficiency, the following effects are also taken into account and corrected for to determine the ^{222}Rn emanation rate of the sample from the number of observed ^{214}Po decays. Since the emanation duration is approximately one week long, the amount of collected radon is always lower than the emanation rate of the sample (see equation 3.4). Similarly the measurement duration is not infinite and therefore a certain fraction of the collected radon will be left over when the measurement is stopped. Also there is a small fraction of the radon which already decays during the transfer from the emanation vessel via the carbon trap into the monitor. And lastly the first hours of data will be left out from the analysis, because in this period the activity of ^{214}Po is not in equilibrium with the ^{222}Rn activity (see equation 3.2).

Figure 3.10 shows the radon emanation rate of the implanted *sample B* as a function of the bath temperature. The error bars along the x-axis represent the standard deviation of the bath temperature throughout the emanation process. The uncertainty on the measured activity combines the counting uncertainty from the number of observed ^{214}Po decays, as well as the uncertainty on the detection efficiency and the ones resulting from time variations in the measurement procedure.

It is found that the emanation rate is stable within 5% for temperatures down

[1] Any activity observed at the energy of ^{210}Po cannot be from the sample, due to the long half-life of ^{210}Pb.

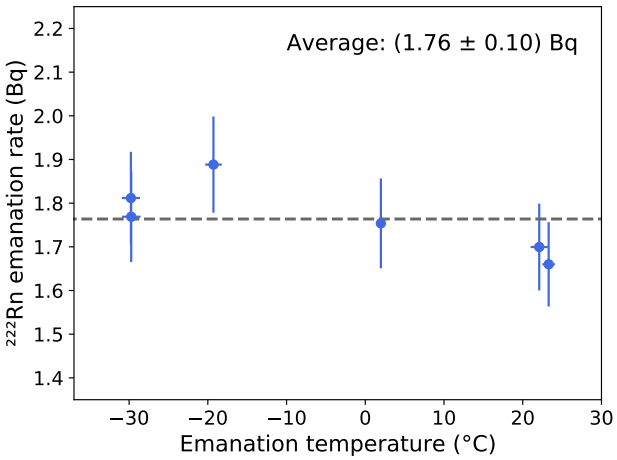

Figure 3.10: Dependence of the ^{222}Rn emanation of the implanted *sample B* on the temperature

to −30 °C. Note that the average emanation rate measured using the electrostatic radon monitor is however 12% lower than the one measured using miniaturized proportional counters at room temperature. Possible reasons for this discrepancy include a bias in the estimation of the detection efficiency as well as slight losses of radon during the transfer procedure, which are not accounted for. Despite this slight discrepancy the measurement shows no strong temperature dependence of the emanation rate, which strengthens the previous hypothesis of a recoil dominated emanation process.

3.1.4 Contamination by short-lived isotopes

All results shown until now are obtained from measurements carried out more than one year following the implantation. Shortly after the implantation, both samples contained a significant amount of additional activity from several short-lived isotopes. Since most of them are close to the mass number of ^{226}Ra, it is believed that they got co-implanted due to an imperfect mass separation. This section focuses on the identification and quantification of these isotopes.

A *cool-down* period of several weeks had to be waited in order to safely ship the samples from CERN to MPIK. Right after their arrival first alpha and gamma spectrometric measurements have been carried out. Figure 3.11 shows an alpha spectrum of *sample B* acquired only 13 weeks after the implantation. The data of this measurement has originally been reported in [115], and was re-analyzed for this work. It shows a multitude of alpha emission lines, with the ten most prominent ones being fit using a sum of individual Crystal Ball [124] functions, modeling each peak separately. Figure 3.12 shows the linear relation between their fitted mean positions and the corresponding literature values of their alpha energies, confirming the correct attribution of the identified emission lines. The red line shows the result of a linear

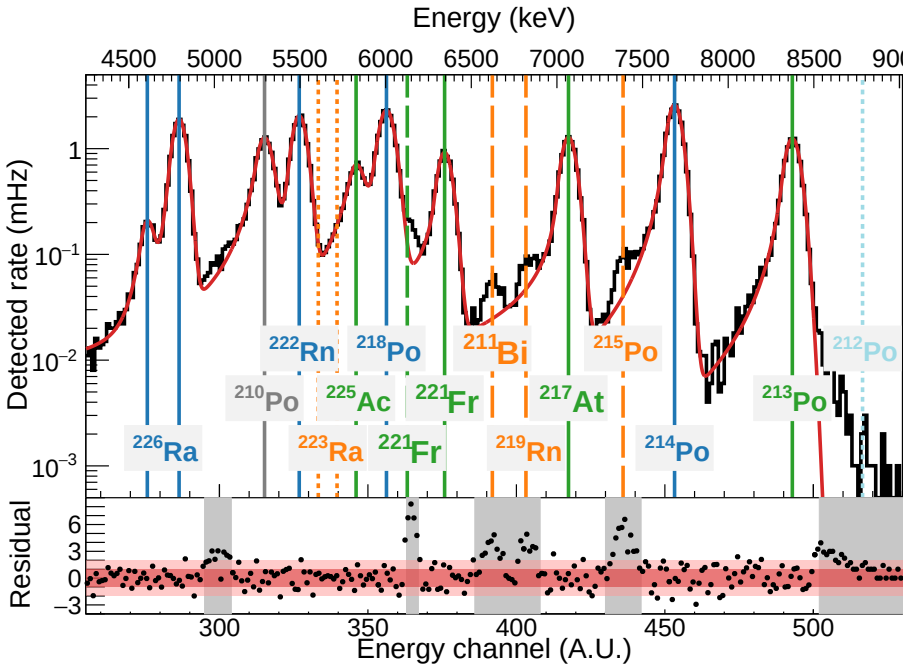

Figure 3.11: Resulting alpha spectrum of implanted *sample B* carried out only 13 weeks after the sample has been implanted. The spectrum reveals contributions of several radioactive decay chains indicated using different colors. The most prominent lines are fit using individual Crystal ball functions [124], where gray indicated regions are excluded from the fit (measurement originally reported in [115]).

fit to the data points which can be used to derive the energy calibration (upper x-axis in figure 3.11). The identified alpha emission lines can be attributed to isotopes belonging to the three decay chains of ^{226}Ra (blue), ^{225}Ra (green) and ^{227}Th (orange). For the measurement the sample has been placed (13.2 ± 0.2) cm away from the Si-PIN diode, which results in a detection efficiency of $(1.47 \pm 0.04) \times 10^{-3}$. The vacuum inside the spectrometer was maintained below millibar level by continuous pumping.

The activity in ^{226}Ra as well as its subsequent decay products (see equation 3.2) has been discussed already in detail in section 3.1.2. One difference in the present spectrum is that a subdominant alpha line from ^{226}Ra with a branching fraction of about 6% and an alpha energy of 4.68 MeV [76] can be resolved separately. This is likely because of a better energy resolution as compared to the alpha spectrum shown in figure 3.4. Furthermore, the alpha emission line of ^{210}Po is visible. This is, however, a known background contribution present on the PIN diode and therefore not representative for the activity of the sample.

The second largest contribution to the spectrum is from isotopes belonging to the

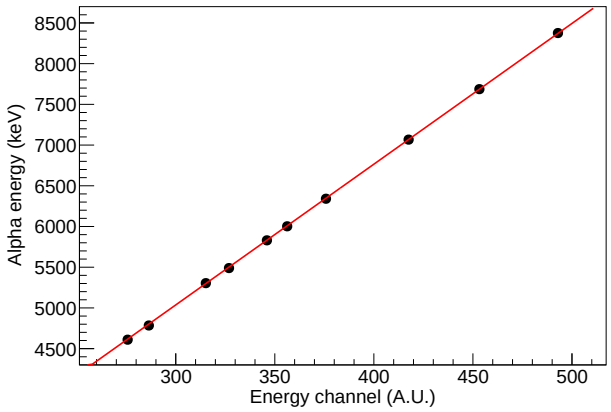

Figure 3.12: Extracted positions from the alpha lines shown in figure 3.11 as a function of their alpha emission energies. The linear fit indicated by the red line agrees well with the data points, indicating good linearity of the instrument response.

decay series of ^{225}Ra (green) which is given below

$$^{225}\mathrm{Ra} \xrightarrow[15\,\mathrm{d}]{\beta} {}^{225}\mathrm{Ac} \xRightarrow[10\,\mathrm{d}]{5.9\,\mathrm{MeV}} {}^{221}\mathrm{Fr} \xRightarrow[4.9\,\mathrm{min}]{6.5\,\mathrm{MeV}} {}^{217}\mathrm{At}$$
$$\xRightarrow[32\,\mathrm{ms}]{7.2\,\mathrm{MeV}} {}^{213}\mathrm{Bi} \xrightarrow[46\,\mathrm{min}]{\beta} {}^{213}\mathrm{Po} \xRightarrow[4.2\,\mu\mathrm{s}]{8.5\,\mathrm{MeV}} {}^{209}\mathrm{Pb} \tag{3.5}$$

Note that only the line from ^{225}Ac is visible in the alpha spectrum, since ^{225}Ra itself decays via a beta decay. Therefore, the presence of ^{225}Ra inside the sample cannot be directly constrained. Since the half-lifes of ^{225}Ra and ^{225}Ac are slightly different, an indirect conclusion can be drawn via the time evolution of the subsequent decay products. For this, the alpha emission line of ^{213}Po is best suited, since it is well separated from the low-energy tail regions of the other isotopes.

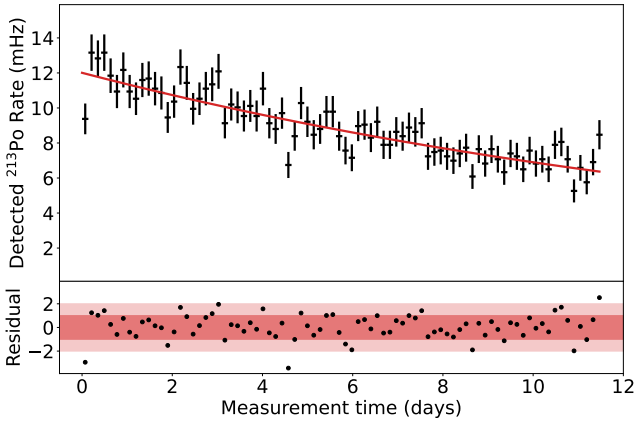

Figure 3.13: Time evolution of the detected event rate of ^{213}Po alpha decays in *sample A*. The measurement has been started 13 weeks after the implantation took place. The red line indicates the fit of the data as described in the text.

Figure 3.13 shows the detected rate of ^{213}Po alpha events as a function of the measurement duration. The time evolution of the ^{213}Po activity is defined by a system of coupled differential equations which represents the decay series of equation 3.5. Its solution is found using the same method as is introduced in section 3.2.2 and

fit to the data, to extract the relative amount of ^{225}Ra and ^{225}Ac. After correcting for the detection efficiency, their activities right after implantation are found to be $(104 \pm 24\,(\text{stat}) \pm 3\,(\text{syst}))$ Bq for ^{225}Ra and $(2.21 \pm 0.6\,(\text{stat}) \pm 0.06\,(\text{syst}))$ kBq for ^{225}Ac.

Further alpha lines appear in the spectrum when looking at the residuals between the data and the fit function (lower panel of figure 3.11). Since these lines are rather small, they have not been included into the fit of the spectrum and the corresponding regions indicated by gray bands have been excluded to prevent a bias. The excess located around an energy of 6.2 MeV (green dashed line) is likely caused by an additional alpha transition of ^{221}Fr having a branching fraction of about 1%. The remaining peaks (orange dashed lines) can be attributed to the decays of isotopes belonging to the decay series of ^{227}Th.

$$\begin{aligned} {}^{227}\text{Th} &\xrightarrow[19\,\text{d}]{6.0\,\text{MeV}} {}^{223}\text{Ra} \xrightarrow[11\,\text{d}]{5.7\,\text{MeV}} {}^{219}\text{Rn} \xrightarrow[4.0\,\text{s}]{6.8\,\text{MeV}} {}^{215}\text{Po} \\ &\xrightarrow[1.8\,\text{ms}]{7.4\,\text{MeV}} {}^{211}\text{Pb} \xrightarrow[36\,\text{min}]{\beta} {}^{211}\text{Bi} \xrightarrow[2.1\,\text{min}]{6.6\,\text{MeV}} {}^{207}\text{Tl} \end{aligned} \tag{3.6}$$

The activity of this chain is estimated using small regions around the corresponding alpha emission lines from ^{211}Bi, ^{219}Rn, and ^{215}Po. The background contributions from the low-energy tails of ^{217}At and ^{214}Po are estimated and subtracted using the fit function and the activities from the three lines are averaged. As ^{223}Ra is much further away from ^{226}Ra in its atomic mass than ^{227}Th, it seems more likely that ^{227}Th has been co-implanted into the samples. Under this assumption, an initial activity of ^{227}Th of $(2.53 \pm 0.09\,(\text{stat}) \pm 0.07\,(\text{syst}))$ Bq can be estimated.

As mentioned already in section 3.1.2 the alpha spectrum of *sample A* shows additional small peaks from the alpha decays of ^{212}Po and ^{216}Po (see figure 3.4). Both isotopes are part of the primordial thorium decay chain given in equation 3.7 (see next section). The presence of this decay chain is confirmed independently by HPGe measurements revealing the gamma emission line of ^{208}Tl at an energy of 2.61 MeV. That these isotopes are present even 1.7 years after the implantation requires that a rather long lived mother isotope got implanted in the sample. The most likely explanation is that either ^{228}Th and/or ^{228}Ra with have half-lifes of 1.9 years and 5.8 years respectively got co-implanted in the sample. The activity present in these isotopes was estimate based on the ^{212}Po activity found in the measurement shown in figure 3.4 and is found to be $\left(13 \pm 2\,(\text{stat}) \,^{+3}_{-2}\,(\text{syst})\right)$ mBq.

Though a systematic uncertainty on the detection efficiency has been evaluated, there are other sources of uncertainties in the above estimations. ^{213}Po for example, is preceded by three alpha decays in the decay chain given in equation 3.5. Since in every alpha decay there is a 25% chance that the daughter nuclei is ejected from the sample, ^{213}Po has only a probability of approximately 42% to remain inside the sample for its decay. Nuclei which are recoiling out of the sample, can get implanted at another location inside the spectrometer, from which their subsequent alpha decay features a different detection efficiency. Therefore, the measured activities are converted into an order of magnitude estimation for their comparison shown in ta-

ble 3.2. From the activities right after implantation (second column), the absolute

Table 3.2: Order of magnitude comparison between the activities found for the different short-lived isotopes present in the samples. The second column gives the estimated implanted activity whereas the last column shows the ratio between the number of ions with respect to the number of implanted ^{226}Ra ions.

Isotope	Implanted activity	Number ratio wrt. ^{226}Ra
^{226}Ra	$\mathcal{O}(10)$ Bq	1
^{225}Ra	$\mathcal{O}(100)$ Bq	10^{-4}
^{225}Ac	$\mathcal{O}(1)$ kBq	10^{-3}
^{227}Th	$\mathcal{O}(1)$ Bq	10^{-5}
^{228}Th /^{228}Ra	$\mathcal{O}(10)$ mBq	10^{-6}

number of implanted ions of the respective isotope can be calculated using equation 3.1. The ratio with respect to the number of implanted ^{226}Ra ions is listed in the third column and gives an approximate measure for the purity of the RIB.

On implanted *sample B*, another unexpected contribution by ^{139}Ce was identified using HPGe gamma spectrometry. The single gamma emission line observed at an energy of 165.9 keV is shown in the inset of figure 3.14. Three subsequent measurements over the period of 1 year following the implantation have been carried out, showing the expected decrease of activity in this line as shown in figure 3.14. The

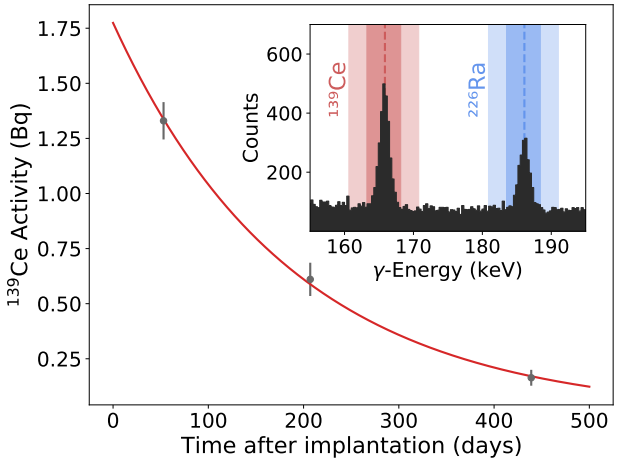

Figure 3.14: Evolution of the ^{139}Ce activity found in *sample B* using HPGe gamma spectrometry. The red line indicates the fit of the data points with an exponential function. Shown in the inset is the region of the gamma spectrum close to the ^{139}Ce and ^{226}Ra emission lines. The activity of each line is evaluated within the darker shaded areas, while the background is estimated from the left and right side bands shaded slightly brighter.

red line shows a fit of the three data points with an exponential function yielding a half-life of (130 ± 5) d which is in very good agreement with the literature half-life of this isotope ($T_{1/2}(^{139}\text{Ce}) = 137.6$ days) [135]. Co-implantation like for the other

short-lived isotopes seems an unlikely explanation for ^{139}Ce since its mass number is far away from ^{226}Ra. At this point it stays unclear how this isotope arrived on one of the two samples.

In conclusion, the usability of the samples as sources of radon emanation is not negatively affected by the initial presence of those short-lived isotopes. After a cool-down period of several months, their activity is vanished with only a small fraction remaining from ^{228}Ra/^{228}Th.

3.1.5 Summary and comparison

In this section, two radon sources which were produced by implantation of ^{226}Ra are described. The samples have been implanted with a radium activity of about 7 Bq each using the RIB of the ISOLDE facility located at CERN. The implantation is located about 8 nm below the sample surface which proved to be sufficient to achieve mechanical stability against wiping. The amount of implanted activity has been confirmed by independent gamma and alpha spectrometric measurements as summarized in table 3.3. Shortly after the implantation a significant activity in several short-lived isotopes was detected in both samples. Luckily these contaminants did quickly decay away without a lasting impact on the usability of the samples. Both samples provide a comparable radon emanation rate of about 2 Bq. The observed emanation fraction of 20% to 28% is well explainable by a purely recoil driven emanation process. This assumption is strengthened further by the absence of a temperature dependence of the emanation rate. Table 3.3 summarizes the different results obtained in this section.

Table 3.3: Comparison of the results from HPGe spectrometry, alpha spectrometry and radon emanation of the two implanted stainless steel samples.

Measurement	Result (Bq)	
	Sample a	*Sample b*
Implantation	about 7	about 7
^{222}Rn emanation	2.07 ± 0.05	2.00 ± 0.05
γ-spectrometry	$7.4 \pm 0.1_{\,\mathrm{stat}} \pm 0.9_{\,\mathrm{syst}}$	$8.4 \pm 0.3_{\,\mathrm{stat}} \pm 1.0_{\,\mathrm{syst}}$
α-spectrometry	$8.70 \pm 0.06_{\,\mathrm{stat}}\ ^{+2.0}_{-1.8\,\mathrm{syst}}$	$9.13 \pm 0.10_{\,\mathrm{stat}}\ ^{+0.7}_{-0.4\,\mathrm{syst}}$

The method of ^{226}Ra implantation using an ion beam has also been applied recently to produce sources of ^{222}Rn emanation made from tungsten and aluminum. This independent study is reported on in [136] and concludes on very similar properties of the produced sources as compared to the ones produced in this work.

3.2 Production of ^{220}Rn emanating sources using recoil implantation

Section 3.1 describes the production of two ^{222}Rn emanating stainless steel samples. They have been obtained by implantation of ^{226}Ra ions at the ISOLDE facility. Their stainless steel surface and sufficient emanation of ^{222}Rn makes these samples ideal to study the reduction of radon emanation by surface coatings (see chapter 4). However, their production required considerable effort and time, making these samples too valuable to spend them for the necessary pre-tests of the coating procedure. Therefore, these pre-tests were conducted on similar samples implanted with ^{224}Ra instead of ^{226}Ra using an in-house setup. It utilizes the recoil energy of 96.5 keV which is transferred onto the radium following the alpha decay of ^{228}Th. Both isotopes are part of the primordial thorium decay chain, from which the section relevant for the following discussion is shown below.

$$
\begin{array}{l}
{}^{228}\mathrm{Th} \xrightarrow[1.9\,\mathrm{y}]{5.5\,\mathrm{MeV}} {}^{224}\mathrm{Ra} \xrightarrow[3.7\,\mathrm{d}]{5.8\,\mathrm{MeV}} {}^{220}\mathrm{Rn} \xrightarrow[55\,\mathrm{s}]{6.4\,\mathrm{MeV}} {}^{216}\mathrm{Po} \xrightarrow[145\,\mathrm{ms}]{6.9\,\mathrm{MeV}} {}^{212}\mathrm{Pb} \\
\qquad\qquad\qquad\qquad 36\% \nearrow \xrightarrow[61\,\mathrm{min}]{6.2\,\mathrm{MeV}} {}^{208}\mathrm{Tl} \xrightarrow[3.1\,\mathrm{min}]{\beta} \searrow \\
\xrightarrow[11\,\mathrm{hrs}]{\beta} {}^{212}\mathrm{Bi} \qquad\qquad\qquad\qquad\qquad\qquad\qquad\qquad {}^{208}\mathrm{Pb} \\
\qquad\qquad\qquad\qquad 64\% \searrow \xrightarrow[61\,\mathrm{min}]{\beta} {}^{212}\mathrm{Po} \xrightarrow[300\,\mathrm{ns}]{9.0\,\mathrm{MeV}} \nearrow
\end{array}
\tag{3.7}
$$

With this method it was possible to rapidly produce samples with a large enough radon emanation for those pre-tests. Unfortunately, the faster production comes along with two significant limitations visible from the decay scheme shown above (equation 3.7). The implanted ^{224}Ra is short-lived and decays inside the sample with a half-life of about 3.7 days. Therefore, each sample can only be used for approximately three weeks following the implantation before its activity becomes too low. Furthermore, the samples emanate ^{220}Rn instead of ^{222}Rn which has only 55 seconds of half-life. This is about four orders of magnitude smaller than the half-life of ^{222}Rn, that is the primary radon isotope considered in the coating studies described in chapter 4. It is expected that this should have a strong impact especially on any diffusion-driven emanation process.

Furthermore, it is expected that also the depth distribution of the ^{224}Ra atoms differs with respect to the samples implanted using the ion beam. The ion beam guarantees that the ions arrive perpendicular to the sample surface, whereas the source emits nuclei isotropically. Since nuclei can reach the surface under shallow angles they will cover less depth before being stopped, which leads to a more shallow and broad distribution. Also the thickness of the ^{228}Th source can contribute to a more shallow implantation, since ^{224}Ra nuclei will loose part of their energy already in the source material. Figure 3.15 shows the expected ^{224}Ra implantation profiles from an isotropic source using two assumptions on the thickness of the source. An

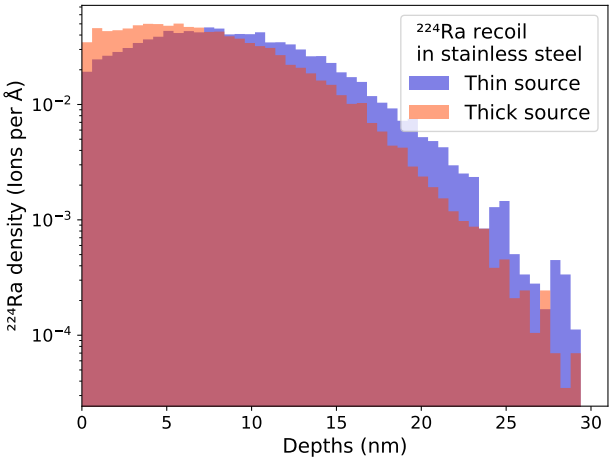

Figure 3.15: Expected depths profile for implanted ^{224}Ra utilizing the recoil from the ^{228}Th alpha decay. The distributions are simulated using SRIM [121] for the ideal case of an infinitely thin (blue) and an extended (red) ^{228}Th source. The more shallow implantation for the thick source is a result of the energy loss of the ^{224}Ra atoms inside the source material.

average implantation depths of 8.9 nm is expected from an infinitely thin (blue) source, while this decreases to 6.3 nm for a very thick source (red). Despite the unknown thickness of the source, the real implantation profile needs to fall somewhere in between these two cases. Surprisingly, the mean implantation depths is very similar to the 7.9 nm of the sample implanted with ^{226}Ra ions with an energy of 30 keV, which is owed to the higher implantation energy from the recoil. Note that a production of a recoil implanted ^{226}Ra source is in principle also possible via the alpha decay of ^{230}Th $\xrightarrow{4.8\,\mathrm{MeV}}$ ^{226}Ra. Loading a sample with a ^{226}Ra activity of 10 Bq within an implantation duration of 1 month would require a ^{230}Th activity of 0.5 MBq. Since the thickness of such a source needs to be limited to $\lesssim 10$ nm in order to not shield off the recoiling ^{226}Ra nuclei, the required ^{230}Th mass of 0.7 mg must be spread over an area of roughly 60 cm^2. Such a source was neither available, nor could it be obtained, rendering this alternative unfeasible.

Despite the mentioned short comings and differences the ^{224}Ra implanted samples proved very useful. In the following sections the setup used for recoil implantation of square stainless steel samples will be described and data from measurements of these samples will be shown.

3.2.1 Setup for recoil implantation

A kinetic energy E_{kin} of 96.8 keV is transferred onto the ^{224}Ra daughter nucleus by the alpha decay of ^{228}Th. It is a consequence of the energy conservation in this two-body process and given by

$$E_{kin} = \left(1 - \frac{M_d}{M_m}\right) Q_\alpha \,, \tag{3.8}$$

where Q_α is the energy released in the alpha decay and M_d and M_m are the mass numbers of ^{224}Ra and ^{228}Th, respectively [137]. At atmospheric pressure, this energy is rapidly lost such that in air the typical range of the ^{224}Ra nucleus is only approx-

imately 76 µm. Therefore, the implantation needs to be carried out in a vacuum vessel.

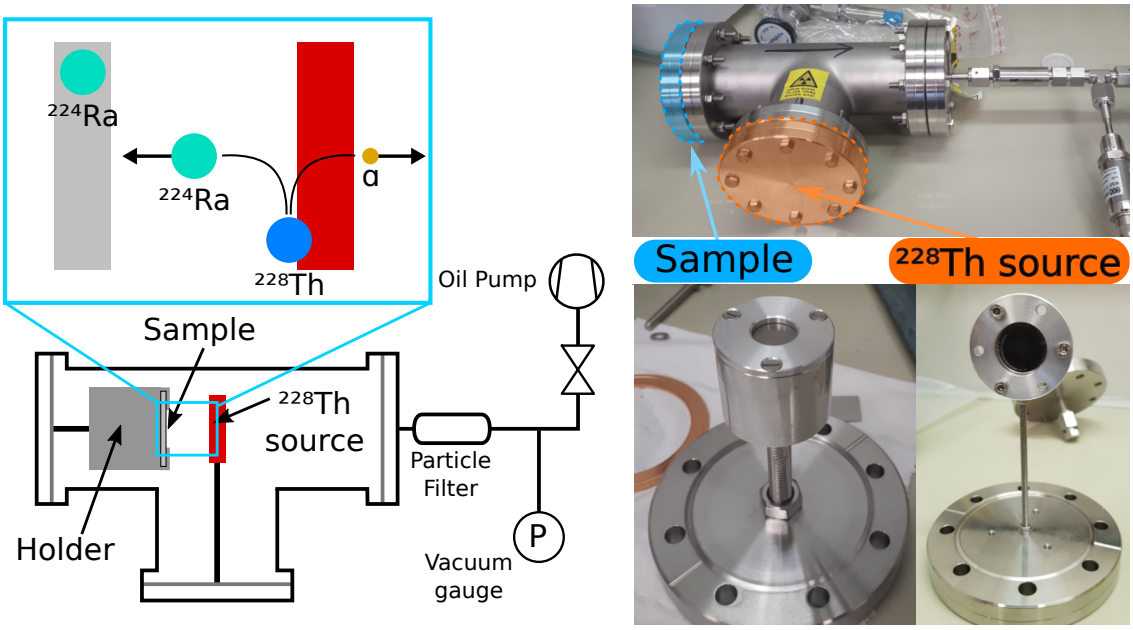

Figure 3.16: Schematic of the setup used for the recoil implantation of ^{224}Ra into stainless steel samples using an open ^{228}Th source in a vacuum vessel (**left**). Pictures of the sample holder assembly, ^{228}Th source inside its holder as well as the implantation vessel (**right**).

Figure 3.16 shows a sketch and a picture of the setup, as well as the holder of the sample and the source. The implantation vessel consists of a CF-63 t-piece with an arm length of 21 cm which is connected to a vacuum pump and a Pirani pressure gauge.

The thorium source consists of a circular stainless steel disc with a ^{228}Th activity of about 5 kBq at the time the implantations took place [138]. It was mounted inside a circular holder and attached to the central flange of the t-piece as shown in figure 3.16. The source was positioned in the center of the stainless steel pipe with the active surface facing towards the left. The cylindrical sample holder shown in figure 3.16 has been mounted to the left-hand flange. The square samples are held in place by a holder ring with an opening diameter of (14.90 ± 0.05) mm. This diameter has been chosen to resemble a similar spread of the implantation as for the samples implanted at the ISOLDE facility (see section 3.1.1). The sample holder is fixed to the left-hand flange using a threaded rod, which can be used to adjust the distance between the sample and the thorium source. A distance of (9.7 ± 1.1) mm between the sample and the thorium source has been chosen for all implantations carried out in this work. This distance allows $(7.8^{+0.9}_{-0.8})\%$ of the emitted ^{224}Ra to get implanted.

During the implantation the vacuum pump was kept running to mitigate possible pressure increases from out-gassing components inside the vessel. Leak tightness of the setup has been confirmed by regular pressure readings which were showing

always less than 1×10^{-1} mbar. The number of ^{224}Ra atoms implanted in the sample is expected to increase towards an equilibrium characterized by the rate of newly implanted atoms being equal to the decay rate of atoms in the sample. This is very similar to the activity evolution of the radon in-growth given in equation 3.4. The typical implantation duration was chosen to be one week in order to achieve approximately 75% of the equilibrium activity. After finishing the implantation the sample is removed from the holder and placed into the HDPE holder shown in figure 3.5 for the measurements described in the next section.

3.2.2 Measurements of recoil implanted samples

A set of four samples (*sample 1-4*) has been implanted with ^{224}Ra using the described setup. After the implantation, their radon emanation has been measured using the electrostatic radon monitor introduced in section 3.1.3. Due to the short half-life of ^{220}Rn, a transfer using an activated carbon trap is not possible. Therefore, the sample is placed directly into the hemispheric detector bowl throughout the measurement.

Alpha spectrum from electrostatic collected ^{220}Rn daughters

Emanated ^{220}Rn decays in the nitrogen-filled detector vessel following the decay scheme shown in equation 3.7. Similar to the case of ^{222}Rn, the daughter isotopes typically carry a positive charge. This allows for their electrostatic collection on the PIN diode, where their subsequent alpha decays can be detected. Figure 3.17 shows the energy spectrum from *sample 2* right after its implantation. The spectrum

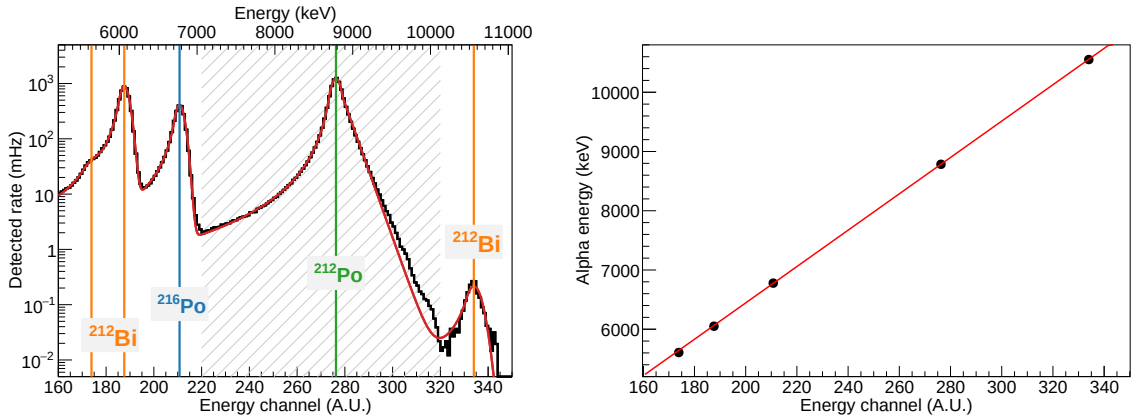

Figure 3.17: Left: Spectrum of the alpha decay energy of the electrostatically collected radon daughters from the recoil-implanted *sample 2*. A typical selection region for ^{212}Po events is indicated by the hatched area. **Right:** Mean positions of the alpha lines extracted from the fit of the spectrum as a function of their literature values. The red line shows a linear fit to the data points.

features three main alpha emission lines, which are from ^{212}Bi, ^{216}Po and ^{212}Po (from left to right). The high activity of the sample right after implantation, makes

two additional rare alpha decay-modes of ^{212}Bi observable. Especially curious is the right most line with an extraordinary high energy of 10.8 MeV, that is commonly referred to as "long range alpha emission" (see e.g. [139–141]). It is emitted in a direct alpha-transition from ^{212}Bi to ^{208}Pb, which occurs only in 0.01% of the cases [76].

The complete spectrum is fit with a sum of five individual functions, modeling each alpha emission line separately. A regular Crystal-Ball (CB) function [124] (see equation D.1 in the appendix) is chosen for the three lines of ^{212}Bi (orange lines), as well as for the one of ^{216}Po (blue line). The short half-life of ^{212}Po of 300 ns leads to a coincident detection of its alpha decay with the preceding beta decay of ^{212}Bi. This leads to a pronounced tailing of that line towards the higher energy side (see figure 3.17). The peak shape is phenomenologically described by a CB function featuring an exponential right-hand side tailing (see equation D.3 in the appendix for the function definition). Besides a minor remaining missmodelling of the ^{212}Po peak, the complete spectrum is well described by this function (red). A linear relation between the fitted line positions and their alpha energies reported in the literature [76] is found as shown in the right panel of figure 3.17.

The ^{220}Rn emanation rate of each sample is estimated based on the detected ^{212}Po activity. Thanks to the high energy of this line, events from the decay of ^{212}Po can be selected without significant background contribution from other isotopes using the gray-hatched area indicated in figure 3.17 [2]. Furthermore, this isotope features a higher detection efficiency compared to for example ^{216}Po.

Time evolution of ^{212}Po activity and determination of ^{220}Rn emanation of the samples

Because of the decay of ^{224}Ra, the emanation rate of the sample is not constant over the duration of the measurement making the analysis significantly more complex. Adding up to this there is a non-trivial time evolution introduced by the decay chain itself. While ^{220}Rn and ^{216}Po have very short half-lifes and rapidly approach the equilibrium emanation rate, this is not true for ^{212}Po and ^{212}Bi which are delayed by the almost 11 hour long half-life of ^{212}Pb (see decay chain in equation 3.7). The time evolution of the number of atoms $N_i(t)$ of the isotope i which is part of a decay chain is governed by a system of coupled differential equations

$$\begin{aligned}
\frac{dN_0(t)}{dt} &= -\lambda_0 N_0(t) \\
\frac{dN_1(t)}{dt} &= +\lambda_0 N_0(t) - \lambda_1 N_1(t) \\
&\vdots \\
\frac{dN_n(t)}{dt} &= +\lambda_{n-1} N_{n-1}(t) - \lambda_n N_n(t)\,,
\end{aligned} \tag{3.9}$$

[2] The tiny contribution from long-range alphas of ^{212}Bi can be neglected.

where λ_i denotes the decay constant of isotope i. As can be seen from equation 3.9, the abundance of the first isotope in the chain is simply given by its decay. For the other isotopes the evolution is determined by their decay, as well as by their production from the parent isotope in the chain. The solution for this problem was first found by Bateman in 1910 [142]. Following the approach outlined in [143] the problem can be conveniently solved by re-writing it in a matrix formulation. The `numpy.linalg` package from Python was then used to solve the problem numerically. The number of each isotope in the chain can then be computed at any given time for an arbitrary choice of initial conditions. The activity $A_i(t)$ for isotope i can calculated by multiplication of the number of atoms $N_i(t)$ of this isotope with the isotope's decay constant λ_i.

$$A_i(t) = N_i(t) \cdot \lambda_i \tag{3.10}$$

Figure 3.18 illustrates how the solution of this problem looks like for an initial activity of 1 Bq in ^{224}Ra, with no subsequent decay products present at time zero. Since the half-lifes involved in the chain span many orders of magnitude the evolution

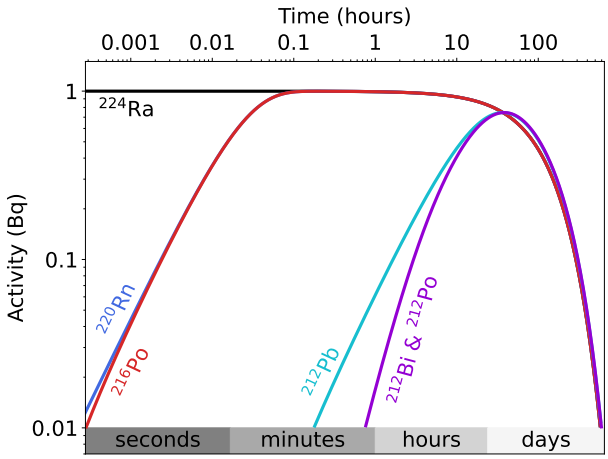

Figure 3.18: Time evolution of the activities of the different isotopes from the decay of a sample with initially only ^{224}Ra. Note that the evolution is shown using a double logarithmic scale. See also the decay chain given in equation 3.7.

is shown using a double-logarithmic scale. It can be seen that activities of the later isotopes in the decay chain are first increasing and approaching an equilibrium with the activity of ^{224}Ra. They then follow the overall decreasing rate of ^{224}Ra due to its decay with a half-life of about 3.7 days. Note that the lines from ^{212}Po and ^{212}Bi are indistinguishable from each other, since both isotopes are practically always in equilibrium because of the short half-life of ^{212}Po.

Figure 3.19 shows the time evolution of the rate of ^{212}Po events for the measurement of *sample 2* during the first week following its implantation. As expected the detected activity first increases and then follows the decay of ^{224}Ra inside the sample. The red line indicates a fit of the data points with the solution of equation 3.9 describing the expected time evolution of the ^{212}Po activity. Besides a systematic

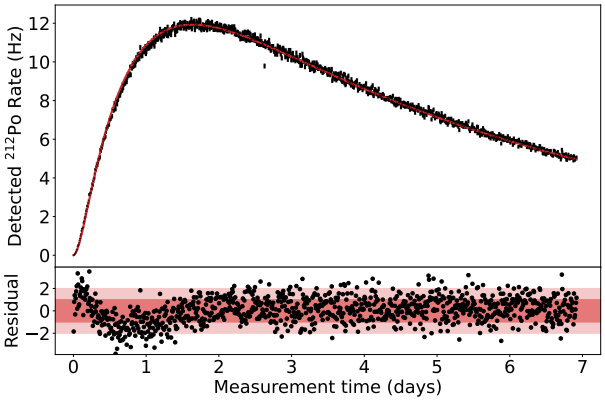

Figure 3.19: Time evolution of the ^{212}Po activity of the recoil implanted *sample 2*. As expected the activity first rises and then decays. The solid line indicates a fit of the data with the solution of the coupled differential equations.

mismatch at the beginning of the measurement the residuals shown in the lower panel of figure 3.19 indicate good agreement between the data points and the fit function. This fit is then used to extract the initial amount of detected radon emanation from each sample.

Note that the extracted rate needs to be corrected for the collection and detection efficiency of the radon monitor. As done in [138], the combined collection and detection efficiency for ^{212}Po can be assumed to be similar to the one of ^{214}Po from the decay of ^{222}Rn, which has been measured using a reference source to be $(35 \pm 2)\,\%$ (see section 3.1.3). Accounting for the branching ratio for ^{212}Po of 64%, a detection efficiency for ^{220}Rn of $(22.4 \pm 1.3)\,\%$ can be assumed for this method.

The extracted ^{220}Rn emanation rates for all four samples right after implantation are summarized in table 3.4. It can be seen that the implantation procedure yielded

Table 3.4: Collection of results acquired for samples produced by recoil implantation of ^{224}Ra .

Sample	$A_{220\mathrm{Rn}}(t_0)$	Duration	Calculated yield
Sample 1	$(41.59 \pm 0.03_{\mathrm{stat}} \pm 2_{\mathrm{syst}})$ Bq	7 days	73.4%
Sample 2	$(71.73 \pm 0.03_{\mathrm{stat}} \pm 4_{\mathrm{syst}})$ Bq	13 days	91.5%
Sample 3	$(42.20 \pm 0.03_{\mathrm{stat}} \pm 2_{\mathrm{syst}})$ Bq	7 days	73.4%
Sample 4	$(44.31 \pm 0.03_{\mathrm{stat}} \pm 3_{\mathrm{syst}})$ Bq	7 days	73.4%

reproducible results of the initial radon emanation rate. The exception being the sample implanted for a duration of two weeks which shows a significantly larger initial emanation that cannot be explained by the slightly increased implantation yield alone. Reasons for this discrepancy are currently unknown and need to be investigated by repeating a such a prolonged implantation.

Measurement using the alpha spectrometer

For *sample 3* an additional measurement using a similar alpha spectrometer to the one described in section 3.1.2 has been carried out. The alpha spectrum acquired over a duration of two hours one week after the implantation of the sample is shown in figure 3.20. It features four clearly visible lines matching the emission energies of

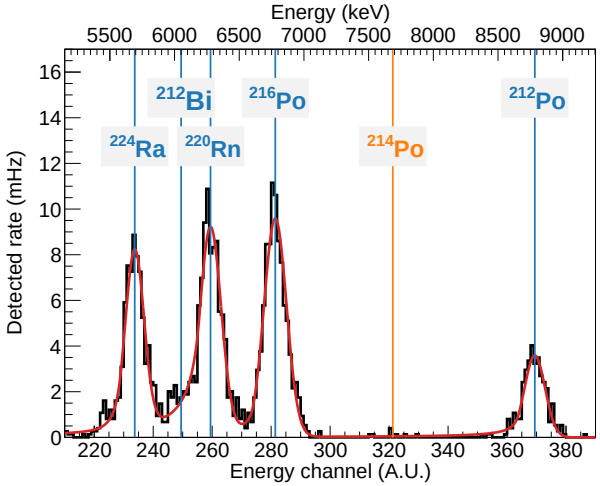

Figure 3.20: Alpha spectrum of the ^{224}Ra recoil implanted *sample 3* acquired one week after implantation. The four alpha emission lines of ^{224}Ra, ^{220}Rn, ^{216}Po and ^{212}Po are clearly visible and fit by the sum of four individual Crystal-Ball functions (red line).

^{224}Ra, ^{220}Rn, ^{216}Po and ^{212}Po. The line of ^{212}Po is significantly lower than the other lines and the one of ^{212}Bi is hidden by the low-energy tail of ^{220}Rn. This is caused by the short duration of the measurement, during which the activity of ^{212}Pb from emanated ^{220}Rn in the detector is still very low (see figure 3.18).

The distance between the sample surface and the PIN diode of the spectrometer was (10.7 ± 0.3) cm, translating to a geometric detection efficiency of $\left(2.23\,^{+0.11}_{-0.15}\right) \times 10^{-3}$ (see section 3.1.2). After correcting for the detection efficiency, the activity found in the emission line of ^{224}Ra amounts to $\left(28.59 \pm 1.6(\text{stat})^{+1.4}_{-1.9}(\text{syst})\right)$ Bq. Where the statistical uncertainty comes from the uncertainty of the fit function (red line) and the systematic uncertainty is due to the uncertainty of the detection efficiency. Correcting this activity for the decay over the period of one week until the alpha spectrum has been acquired gives an initial implanted activity of:

$$A_{224\text{Ra}}(t_0) = \left(106 \pm 6(\text{stat})^{+5}_{-7}(\text{syst})\right)\ \text{Bq}$$

The ^{228}Th source used for the implantation ejects ^{224}Ra at a rate of (282.1 ± 0.1) atoms/s/kBq [138]. Given the geometric implantation efficiency of the setup of $(7.8\,^{+0.9}_{-0.8})\%$, an equilibrium implantation rate of $(110\,^{+13}_{-12})$ Bq is expected. This is in good agreement with the result obtained from the alpha measurement. Furthermore, this measurement allows to estimate the fraction of emanated ^{220}Rn from the sample. Comparing the implanted ^{224}Ra with the initial ^{220}Rn emanation rate as reported in table 3.4, gives an emanation fraction of $\left(40 \pm 2(\text{stat})^{+5}_{-4}(\text{syst})\right)\%$.

3.3 Model for the radon emanation fraction

Sections 3.1 & 3.2 describe two different types of radon sources produced by implantation of radium into stainless steel. The first type of radon source was produced by implantation of ^{226}Ra at the ISOLDE facility. Where each of the two samples received an activity of approximately 8 Bq in ^{226}Ra. It is found that from this activity a fraction of around 25% is released by the samples in form of emanated ^{222}Rn. The second type of sample has been implanted with approximately 100 Bq of ^{224}Ra utilizing the recoil from the decay of ^{228}Th. The ^{220}Rn emanation rate of these samples was measured to be around 40 Bq, allowing to conclude an emanation fraction of approximately 40%. In this section, a simple estimation of the emanation fraction of radium implanted samples will be given and compared with the observed emanation fractions of the samples described earlier.

Linear model for recoil emanation

Radon nuclei formed by the alpha decay of radium, receive a fixed amount of momentum due to the recoil. This enables them to traverse a certain range inside the material before they are stopped. Figure 3.21 illustrates this scenario for the case that the recoiling nuclei travel along straight lines and do not change their direction due to scattering. To escape from the sample the distance to the closest surface d needs to be shorter or equal to the recoil range R of the radon nucleus. For a fixed depth z_i at which a radon particle is formed, this distance is given by

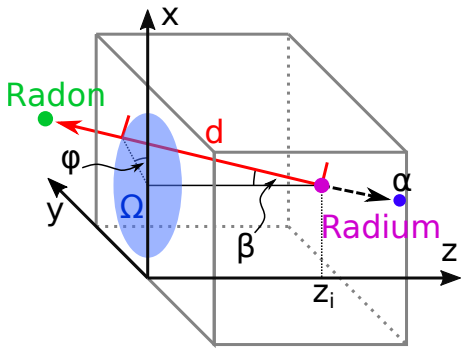

Figure 3.21: The traversed range d of a radon daughter nucleus formed at a depth z_i is given by its emission angle β with respect to the surface normal. Where Ω describes the enclosed solid angle for all smaller values of β.

$$d = \frac{z_i}{cos(\beta)} \,. \tag{3.11}$$

Where β describes the angle with respect to the surface normal under which the particle is emitted (see figure 3.21). This allows to define the critical angle β_{crit}

$$\begin{aligned} &\cos(\beta_{crit}) = \frac{z_i}{R} \\ \iff\ &\beta_{crit} = \arccos\left(\frac{z_i}{R}\right) \quad , \text{ for } \mathrm{z_i} \leq \mathrm{R} \,. \end{aligned} \tag{3.12}$$

For all emission angles within the interval $[-\beta_{crit}, ..., +\beta_{crit}]$, the radon particle is able to escape the sample.

Since the problem is spherically symmetric the rotation around the azimuth angle φ does not change the distance to the surface. Therefore the emission region for suc-

cessful emanation becomes a cone with an opening angle of β_{crit}. This is illustrated by the blue shaded region Ω in figure 3.21. The amount of solid angle enclosed by this cone is given by integrating in spherical coordinates.

$$\Omega = \int_0^{2\pi} \int_0^{\beta_{crit}} \Big(\sin(\beta) \Big) \, d\beta \, d\varphi = 2\pi \cdot (1 - \cos(\beta_{crit})) \; . \tag{3.13}$$

Using this formulation, allows to give a first approximation of the emanation fraction F by comparing the size of Ω to the full solid angle of 4π.

$$F = \frac{\Omega}{4\pi} = \frac{1}{2} \cdot \big(1 - \cos(\beta_{crit})\big) \, . \tag{3.14}$$

Inserting the value for β_{crit} from equation 3.12 yields the emanation fraction as a function of the ratio between implantation depth and recoil range

$$\begin{aligned} F &= \frac{1}{2} \cdot \left(1 - \cos\left(\arccos\left(\frac{z_i}{R}\right)\right)\right) \\ &= \frac{1}{2} \cdot \left(1 - \frac{z_i}{R}\right) , \text{ for } \mathrm{z_i} \leq \mathrm{R} \, . \end{aligned} \tag{3.15}$$

It can be seen that under these very simplified assumptions the emanation fraction is anti-proportional to the ratio between implantation depth and recoil range. If the activity would be located exactly on the surface ($z_i = 0$) the resulting emanation fraction would be 1/2. This is expected as the recoil of one half of the radon particles would be directed into the sample. As the implantation depth approaches the possible recoil range ($z_i = R$), the emanation fraction becomes zero, since the produced radon daughters cannot escape from the sample anymore. If the implantation depths gets larger than the recoil range ($z_i > R$), the expression becomes nonphysical, since the emanation fraction would be negative. The dependence of emanation fraction on the ratio z_i/R is shown in figure 3.22. For the two samples implanted with 30 keV ^{226}Ra ions at the ISOLDE facility, mean implantation depth of 8 nm is expected (see figure 3.2). The mean range of the recoiling ^{222}Rn in stainless steel (8.0 g/cm^3) is expected to be 15 nm as has been estimated using the SRIM code. With this, equation 3.15 predicts an emanation fraction of 23.3% for these samples, which is very close to their measured emanation fraction.

Note that in this linear model the simplifying assumption is made that all implanted ions are located at one specific depth z_i and have one fixed range R within the material. In reality the implantation depth as well as the recoil range follow certain probability density functions (PDFs). A more realistic description is obtained by the two additional models which are introduced in appendix C. In the first one the implantation and recoil distribution are assumed to follow a Gaussian distribution, while the second one uses the profiles predicted by the SRIM Monte-Carlo simulation.

Comparison between prediction and data

The predictions of all three models are included in the comparison shown in figure 3.22, as a function of the ratio between mean implantation depth and recoil range. For fractions between depth and range smaller than roughly 0.8, all three

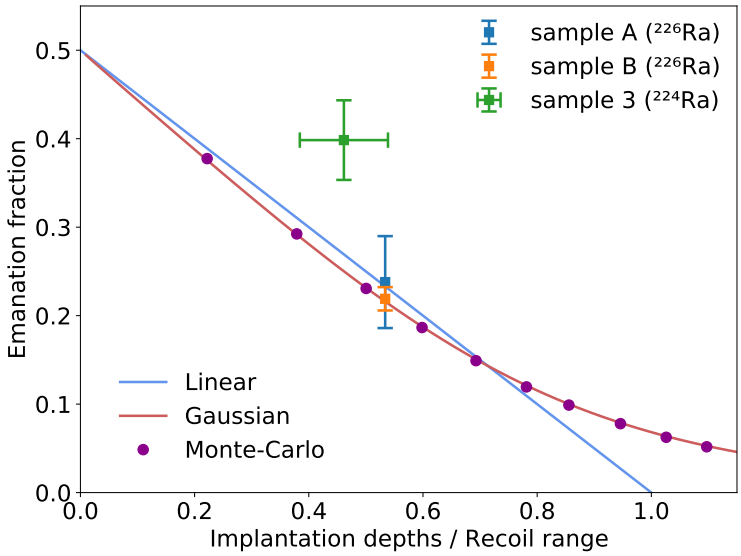

Figure 3.22: Expected dependence of the radon emanation fraction from the different models discussed in this section and in appendix C. The observed values for the emanation fraction of the two ^{226}Ra and one of the ^{224}Ra implanted samples are indicated by square markers.

models predict rather similar emanation fractions. Only for ratios larger than that, the linear approximation (blue) predicts significantly lower values and becomes non-physical for ratios larger than one. The results from the Gaussian (red) and the Monte-Carlo method (purple •) are in very good agreement and predict a more physical asymptotic dependence of the emanation fraction in this case.

Indicated by the green marker is the observed emanation fraction from ^{224}Ra implanted *sample 3*. The increased uncertainty on the implantation depths stems from the less precisely known implantation profile as shown in figure 3.15. Its emanation fraction is significantly higher than the prediction of any of the proposed models. Either the detection efficiency of the electrostatic radon monitor for ^{220}Rn has been largely underestimated, and/or the real implantation is much more shallow than expected from the simulation.

The emanation ^{222}Rn emanation fractions from the two samples implanted with ^{226}Ra are indicated by the orange and blue markers. Their position on the x-axis is determined from simulated implantation and recoil distributions shown in C.1 in appendix C. The uncertainty on the y-axis is includes the systematic uncertainty of the implanted activity as reported in table 3.3. Both samples show an excellent agreement with the prediction of the models for recoil driven emanation. Therefore, the conclusion can be drawn that radon is released predominantly by recoil with the

contribution from diffusion playing a subdominant role.

3.4 Discussion and outlook

In this chapter two kinds of radon sources have been described which were produced by implantation of radium into stainless steel. The recoil implanted samples offer a very limited applicability due to the short half-life of ^{224}Ra as well as of the emanated ^{220}Rn. On the other hand these samples can be obtained quickly and uncomplicated using an in-house setup. This makes them well suited to study the reproducibility of surface coatings targeted at the reduction of radon emanation as will be presented in the next chapter.

The second type of source was produced by implantation of ^{226}Ra at the ISOLDE facility. The presented results prove that clean and dry stainless steel radon sources can reliably be produced by this novel technique. These samples offer an attractive alternative to liquid radon sources and are ideal samples for the aforementioned coating studies. Building upon the gained experience further implantations can be carried out to meet the future demand of such samples. A major problem experienced in this study was the occurrence of short-lived co-implanted isotopes. Upcoming productions can use the high resolution separator (HRS) magnet of the ISOLDE facility which should mitigate such contamination [120]. Additionally, the resonance ionization laser ion source (RILIS) might be used to achieve a higher selectivity on the chemical element which gets ionized and implanted. Recent studies showed that this source even features an increased ionization efficiency for radium as compared to the surface ionization source used in this work [144]. Therefore, this could also help to reduce the duration of the implantation.

4 Reduction of radon emanation using surface coatings

An experiment's potential to discover rare-events such as dark-matter interactions or the neutrinoless double beta decay ($0\nu\beta\beta$), crucially depends on its sufficiently low background rate. As introduced in section 1.2, the ^{222}Rn-induced background, will be of great importance for the future DARWIN experiment [39]. But also for other liquid xenon-based experiments, such as for example nEXO [145], this background is of great importance and impacts the final sensitivity of these experiments.

Figure 4.1: Staggered approach for mitigation of radon-induced background.

Its reduction will require a well planned radon mitigation strategy. Expressed in a bold and simple way, it should follow the same logic as needs to be followed to prevent global warming: Reduction of greenhouse gas emissions, removal of CO_2 from the atmosphere, taking countermeasures against e.g. flooding and extreme weather conditions [146]. For radon, this staggered strategy translates to the one sketched in figure 4.1. As a first step, radon should be avoided in the experiment by *preventive* measures, such as a careful pre-selection of the construction materials. This is typically done by dedicated radon screening campaigns, such as reported in [70, 79, 112, 113]. Furthermore, strict cleanliness protocols need to be followed during the assembly of the experiment to avoid contamination of material surfaces with radium containing dust particles [70, 112]. Part of the remaining radon emanation can then be continuously *removed* from the liquid xenon (LXe) using adsorption [147] and/or cryogenic distillation [77–79]. As a last resort, remaining radon-induced electronic recoil (ER) events need to be *rejected* from the data at the analysis level. Though this greatly reduces the radon background (see section 1.2), the separation is not perfect and will also remove a fraction of valid events, which reduces the exposure of the experiment. Subject of this chapter is a novel technique that can be used to reduce the radon emanation from materials using surface coatings. As a preventive measure against radon, it can be applied at the earliest stage of the mitigation strategy and therefore has a great potential for reducing the experiments radon budget.

4.1 Fundamental considerations

Just like car paint protects the underlying metal from oxidation, the amount of radon released by a material should be reduced by a thin coating layer sealing its surface. This is sketched in figure 4.2, for the two processes responsible for radon release (recoil and diffusion). To successfully block the radon emanation, the coating must be at least thick enough to fully contain the radon recoil range of the order of a few tens of nanometers. The second requirement the layer needs to fulfill is a sufficient tightness against radon diffusion. Both aspects are further examined in the following sections 4.1.1 and 4.1.2. It is also imperative, that the layer itself must feature a high degree of radio purity, especially with regard to ^{226}Ra, such that it does not contribute to the radon emanation by itself. Furthermore, the layer must be mechanically stable and well adhesive throughout the lifetime of the experiment.

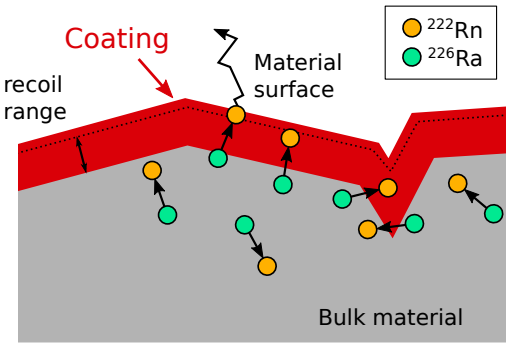

Figure 4.2: Sketch illustrating the idea to mitigate radon emanation using a surface coating

Different coating techniques have been investigated, including vacuum-based processes such as physical vapor deposition (PVD) and chemical vapor deposition (CVD), as well as coatings using an epoxy resin and electrochemical plating (ECP). They will be further detailed in section 4.2. Because of their good availability, past works [71, 126, 148, 149] relied on thoriated tungsten (WTh) electrodes, containing 4% of thorium oxide. Most emanation of these samples is from ^{220}Rn, which is a member of the ^{232}Th decay chain (see equation 3.7) with only a small contribution from ^{222}Rn due to impurities in the material. As introduced in section 1.2.2 the main background concern in LXe time projection chambers (TPCs) is from ^{222}Rn, which differs mainly with regard to its longer half-life of 3.8 days with respect to only 55 seconds for ^{220}Rn. Therefore, especially for diffusion dominated processes the emanation of ^{220}Rn will be strongly suppressed. Moreover, tungsten is not a typical material choice for construction of for example cryostat vessels for LXe experiments. More likely choices are stainless steel (e.g. [6, 150]) or titanium [112]. The material and isotope limitation of the past studies have been successfully overcome in this work by application of the radium implanted stainless steel samples that are introduced in chapter 3. New results for the so-far most promising electrochemical plating (ECP) method are presented in section 4.3. The chapter will be concluded by an outlook towards the future challenges of this technology that remain to be addressed.

4.1.1 Mitigation of recoil driven emanation

When the radon is created, it receives a recoil energy of the order of 100 keV in the alpha decay of radium. To illustrate the reduction of the recoil-driven emanation, a copper layer with a density of 8.92 g/cm^3 is assumed. The penetration depth distribution of into this layer is simulated using "stopping and range of ions in matter" (SRIM) [121]. Its shape is found to be approximately Gaussian, with a mean and standard deviation of $\mu_r = 15.6$ nm, $\sigma_r = 5.4$ nm and $\mu_r = 14.0$ nm, $\sigma_r = 4.4$ nm for ^{220}Rn and ^{222}Rn respectively. The fraction of recoils that are contained by the coating layer, can then be computed using the estimation of the recoil-driven emanation fraction described in section 3.3 and appendix C.

Figure 4.3 shows the expected reduction factors for the recoil emanation of ^{220}Rn and ^{222}Rn as a function of the thickness of an applied copper coating. The 13% higher recoil energy of ^{220}Rn leads to a larger average range in the copper and consequently to a smaller reduction by the coating layer. The coating layers investigated in the following, have thicknesses between roughly 500 nm and 5 µm. Therefore, it the recoil-driven emanation should be fully suppressed.

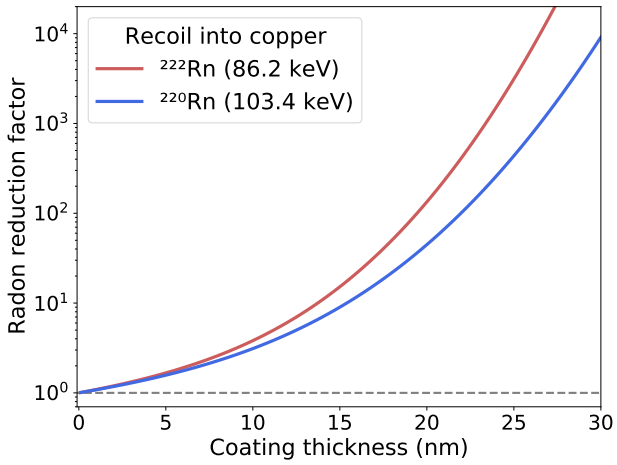

Figure 4.3: Expected reduction of the recoil-driven emanation as function of the thickness of an applied copper layer (8.92 g/cm^3 density). The difference between ^{220}Rn and ^{222}Rn is due to different recoil energies.

Using an electrostatic radon monitor allows for a direct verification of this recoil tightness for samples containing ^{228}Th, such as the aforementioned WTh electrodes. As introduced in section 3.1.3, this detector collects positively charged daughter nuclei emerging from an alpha decay on a Si-PIN diode with an electric field. By the alpha decay of ^{228}Th $\xrightarrow{5.5\,\mathrm{MeV}}$ ^{224}Ra, the daughter nuclei can be ejected from an uncoated surface. This leaves ^{224}Ra in a charged state, which allows for its collection and detection of its subsequent alpha decays on the PIN diode. Therefore, a clear contribution from ^{224}Ra can be seen in the relevant section of the energy spectrum from uncoated WTh electrodes as can be seen in the black histogram shown in figure 4.4. The figure also shows the corresponding region of the spectrum (red), after this electrode has been coated with a 1 µm thick layer using the CVD method described in section 4.2. While the contribution of the ^{220}Rn daughter isotope ^{212}Bi is only slightly suppressed, the peak of ^{224}Ra is not visible anymore. This observation

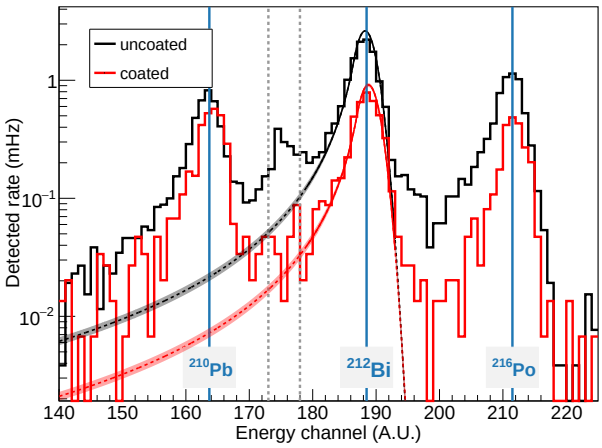

Figure 4.4: Comparison of energy spectra of alpha decays using the electrostatic radon monitor for an uncoated (black) and coated (red) thoriated tungsten electrode. After coating, the contribution from ^{224}Ra (dashed gray lines) is strongly suppressed. To quantify the reduction, the background contribution from ^{212}Bi (fit functions) needs to be taken into account.

allows to conclude, that the layer is sufficiently tight against recoil emanation. The noble gas radon on the other hand, is still released via diffusion.

To quantify the suppression of ^{224}Ra, the background contribution from the low-energy tail of ^{212}Bi needs to be taken into account. For both measurements this contribution is estimated by fitting the ^{212}Bi peak with a Crystal-Ball (CB) function (see equation D.1 in appendix D) as indicated by the solid lines. The region of the radium peaks is excluded from the fit. To reduce the fit uncertainty, the shape of the tail is constrained by the ^{218}Po emission line (not shown) from a reference measurement. The background and data are then integrated and subtracted from each other within the gray lines. This allows to derive a lower limit for the ^{224}Ra reduction of ≥ 4.75 (90% C.L.).

4.1.2 Model for the diffusion of radon through a coating layer

Radon can also escape from the coating layer by diffusion. This process, is driven by the random motion of the particles and described by the diffusion equation (Fick's second law) [151]. For the case of radon, the partial differential equation (PDE) needs to be extended to also account for the decay of radon and becomes

$$\underbrace{\frac{\partial}{\partial t}\eta(x,t) = D\frac{\partial^2}{\partial x^2}\eta(x,t)}_{\text{2nd Fick's law}} - \overbrace{\lambda \cdot \eta(x,t)}^{\text{Decay}}, \qquad (4.1)$$

where η is the searched for radon density at time t and location x, and D and λ are the constants for diffusion and decay of radon. The problem will be solved for the simplified one dimensional case as sketched in figure 4.5. The sample surface ($x = 0$) is covered by a coating layer with a thickness of h.

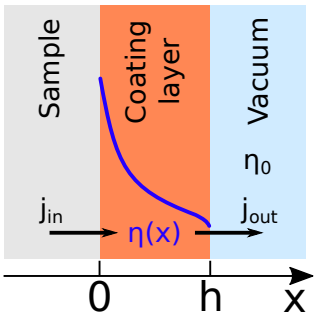

Figure 4.5: Sketch of the simplified model to describe radon diffusion through the coating layer

As a further simplification, the time-independent solution ($\partial_t \eta = 0$) will be computed first. The vanishing time derivative translates the PDE into the following ordinary differential equation (ODE):

$$D\frac{\partial^2}{\partial x^2}\eta(x) - \lambda \cdot \eta(x) = 0\,. \tag{4.2}$$

This has the general solution

$$\eta(x) = A_1 \cdot e^{-x\sqrt{\lambda/D}} + A_2 \cdot e^{+x\sqrt{\lambda/D}}\,. \tag{4.3}$$

The constants $A_{1,2}$ need to be determined from the two boundary conditions at both sides of the coating layer.

On the left side ($x = 0$), the coating is exposed to a constant flux (j_{in}) of radon atoms which are leaving the sample and are implanted into the coating [1]. Using Fick's first law this can be expressed as

$$-D \cdot \frac{\partial}{\partial x}\eta(x)\bigg|_{x=0} = j_{in}\,. \tag{4.4}$$

Note that this condition is different from the one chosen for example in [152–154] to describe the radon diffusion through a membrane which separates a source vessel (high radon concentration) from a receiver vessel (low radon concentration). They assume a constant radon concentration on the entrance of the barrier instead of the constant flux condition of equation 4.4.

The volume surrounding the coating ($x > h$) is typically much larger than the volume of the coating itself. Therefore, radon which leaves the coating is strongly diluted and the radon concentration outside of the coating can be assumed to stay at a negligible level. This is represented by the second boundary condition

$$\eta(h) = \eta_0 = 0\,. \tag{4.5}$$

Both boundary conditions can be used to determine the two unknown factors $A_{1,2}$ in equation 4.3 and the profile of the radon concentration inside the coating layer is found to be

$$\eta(x) = \frac{j_{in}}{\sqrt{\lambda \cdot D}} \cdot e^{-x\sqrt{\lambda/D}} \cdot \left(\frac{e^{2h\sqrt{\lambda/D}} - e^{2x\sqrt{\lambda/D}}}{1 + e^{2h\sqrt{\lambda/D}}}\right)\,. \tag{4.6}$$

An important quantity for the later measurements is the radon flux leaving the coating layer. It can be calculated by evaluating the derivative of the radon concentration at the exiting face $x = h$ and multiplication with the negative diffusion

[1] The range of the recoil inside the coating is usually much smaller than the coating thickness and therefore neglected.

constant.

$$j_{out} = -D \cdot \frac{\partial}{\partial x}\,\eta(x)\Big|_{x=h} = 2j_{in} \cdot \frac{e^{h\sqrt{\lambda/D}}}{e^{2h\sqrt{\lambda/D}}+1} \tag{4.7}$$

Finally, the radon reduction factor R of the coating layer is given by the ratio between the incoming radon flux j_{in} and the exhaled flux j_{out}. It can be simplified to

$$R = \cosh\left(h \cdot \sqrt{\frac{\lambda}{D}}\right) . \tag{4.8}$$

Figure 4.6 shows how the ^{222}Rn reduction factor depends on the coating thickness for different values of the diffusion constant. If the layer is too thin, or the diffusion

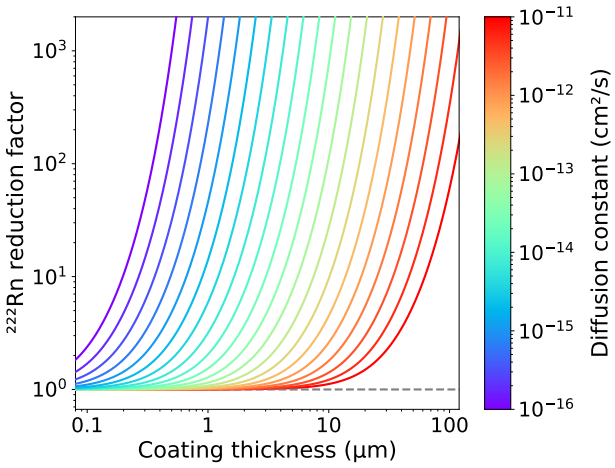

Figure 4.6: Ratio between the outgoing (j_{out}) and incoming (j_{in}) ^{222}Rn flux as a function of the layer thickness h and diffusion constant D. Shown is the steady state result as computed in equation 4.7.

constant is too large, the mean retention time of the radon inside the coating is much shorter than its lifetime. Due to conservation of the particle number, the exhaled radon flux is then equal to incoming flux and the reduction factor is close to one. When the diffusion constant becomes smaller, the reduction factor increases exponentially as a function of the layer thickness, because of the radon decay inside the layer.

The obtained solution is only valid after the steady-state has been reached. A solution for the time-dependent equation 4.1 has been found numerically using `Mathematica` [155]. For this, coating layer is assumed to be initially free of radon ($\eta(x, t = 0) = 0$). Figure 4.7 illustrates how the exhaled radon flux approaches its steady-state value for a layer thickness of 5 µm and four different values of the diffusion constant. The steady state radon flux j_{eq} is calculated using equation 4.7. It can be seen, that depending on the value of the diffusion constant, it can take several months until a sufficient equilibrium is achieved. The small miss-match between the numerical and analytical solution at late times is likely related to the interpolation used by the finite element method (FEM).

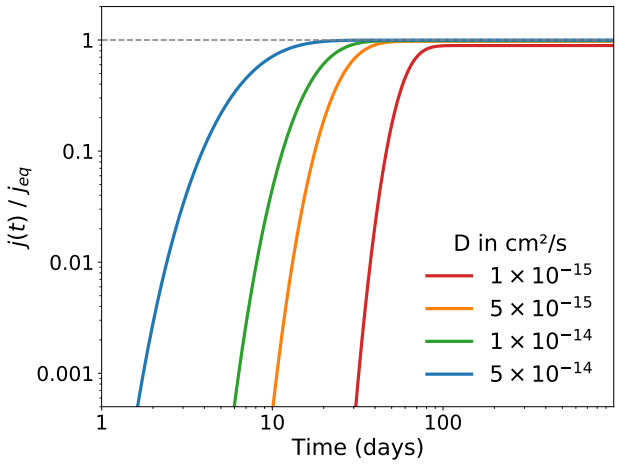

Figure 4.7: Numerical approximation of the time dependent radon flux $j(t)$ leaving the sample for four different choices of the diffusion constant. For better comparison the values are normalized to the respective result from the steady state solution j_{eq} obtained using equation 4.7. For the coating thickness a typical value of 5 µm is assumed.

The model and findings of this section will be used later for the interpretation of the measurement of radon mitigation of the coating layers.

4.2 Explored coating methods and previous results

The different PVD and CVD techniques are briefly sketched in the following section, along with the epoxy coating and the procedure for ECP. With the emphasis being put on the latter, since it yielded so far the most promising results.

Magnetron sputtering

Three batches of 1 mm thick WTh electrodes have been coated in cooperation with the German company EC Europ Coating GmbH [157]. The obtained titanium layers had a thickness between 400 nm to 800 nm. During the process, the titanium is ablated (sputtered) by bombardment of a titanium target with argon ions. Released particles are then transported ballistically to the sample surface, on which they deposit and form the coating layer [158].

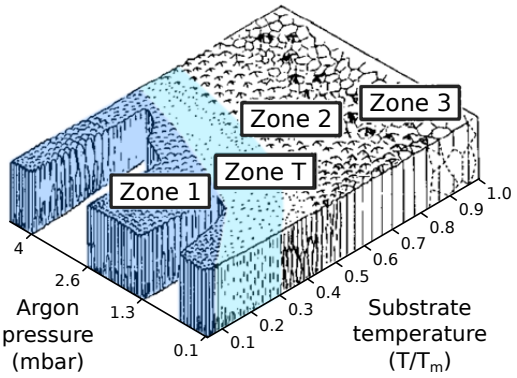

Figure 4.8: Model after Thornton describing the surface morphology of sputtered thin films. The region in which the studied depositions were carried out (Zone 1 & Zone T) is highlighted in blue. Figure adapted from [156].

Figure 4.8 shows the model proposed by Thornton [156, 159], which allows to predict the coating morphology resulting from different choices of the process parameters. It is mainly influenced by the substrate temperature T, which is usually normalized by the melting temperature of the coating material T_m.

The depositions reported in [71, 148] have been carried out at room temperature ($T/T_m \approx 0.15$) in an argon atmosphere of 10^{-2} mbar. Therefore, the coating morphology should be similar to Zone 1 or Zone T (blue), which is dominated by a vertically aligned, columnar structure. This technique showed a maximum ^{220}Rn radon reduction factor of 4.5, which is rather low. It is likely owed to the vertical alignment of the grain boundaries, along which diffusion is typically strongly enhanced (e.g. [160]).

Vacuum plasma spraying

For this process, the coating material is molten and evaporated in a high-velocity argon plasma, into which it is introduced as a fine powder. The plasma accelerates the material towards the sample surface, on which it condensates to form a solid coating layer, as is sketched in figure 4.9 [161].

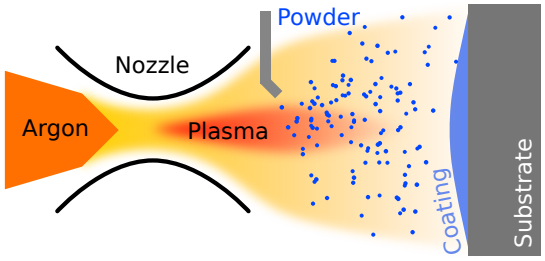

Figure 4.9: Sketch of the vacuum plasma spraying process.

Several WTh electrodes with diameters of 1 mm and 4.8 mm have been coated with copper by Dr. Laure Plasmatechnologie GmbH [162] in Germany. A maximum ^{220}Rn reduction factor of 22±2 has been achieved with this technique for a layer thickness of about 3 µm [71]. However, the reproducibility of these coatings proved to be challenging. This was mostly related to repeated damages of the coating layers by the sample holder.

Chemical vapor deposition

Similar to two previous methods, also CVD is carried out in a low pressure environment. However, the deposition is not done using physical processes, but the layer is formed via chemical reactions. Hydrogenated amorphous carbon (a-C:H) layers have been investigated for their radon mitigation in cooperation with the Belgian company Innovative Coating Solutions SA [163]. These layers belong to the group of diamond like carbon (DLC) coatings [164].

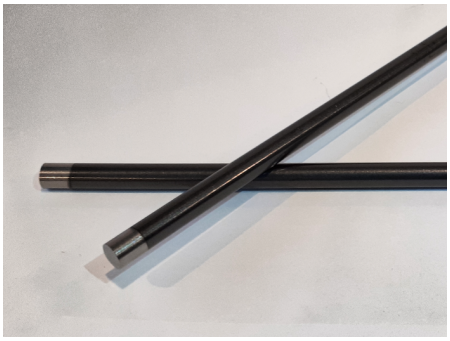

Figure 4.10: The two diamond-like carbon (DLC) coated WTh electrodes. Picture adapted from [149].

Two 4.8 mm thick WTh electrodes have been coated with 1 µm thick (a-C:H) layers on top of a thin adhesion layer. Both electrodes are shown in figure 4.10, before their open tips have been covered by the epoxy resin

discussed below. The coating showed a very good adhesion of the layer even after repeated thermal shock treatments using liquid nitrogen. Unfortunately, the achieved radon mitigation using this coating technique proved to be insufficient. A reduction of a factor of 3 has been observed for ^{220}Rn and for ^{222}Rn the reduction factor was barely significant (1.4±0.3) [149].

Epoxy-based coatings

Previous studies carried out by the SuperNEMO collaboration, indicate a good radon tightness of the vacuum glue Stycast (1264) [165]. Especially for cryogenic applications, Loctite® Stycast 2850FT is recommended in combination with the catalyst CAT 24 LV [166].

The radon mitigation of this resin has been tested using a 4.8 mm thick WTh electrode, to which it was applied via dip-coating in a test tube. Before the application, the resin and catalyst were thoroughly mixed and de-gassed, following the procedure recommended in the data sheet [166]. After the coating, the ^{220}Rn emanation of the sample was suppressed below the detection threshold. A radon reduction factor of at least 70 has been estimated for this coating [149].

Electrochemical plating

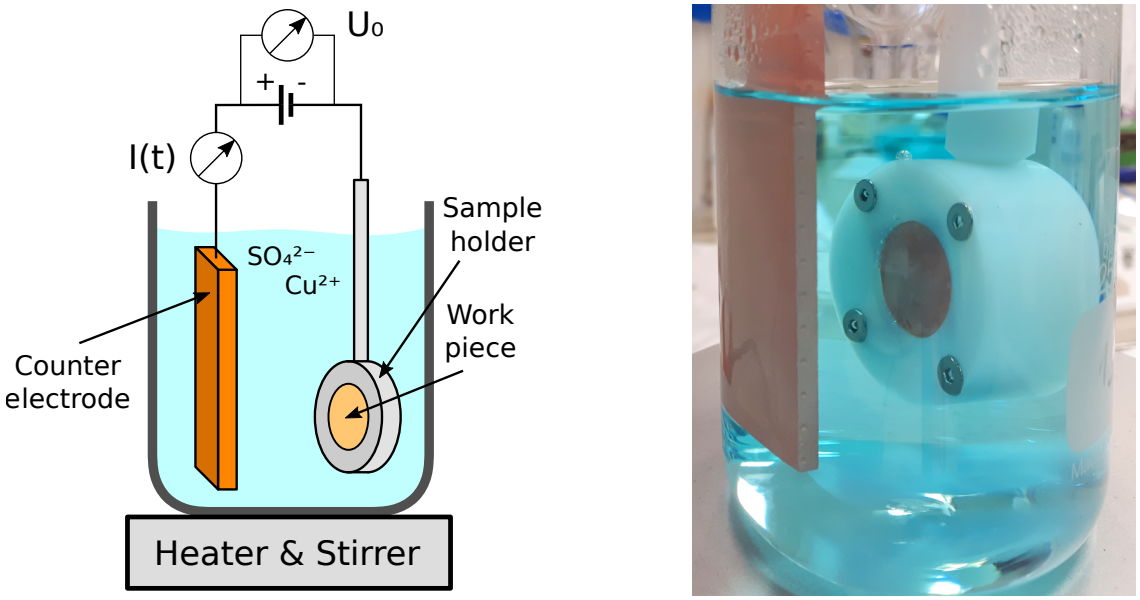

Figure 4.11: Left: Sketch of the used electroplating setup. Figure adapted from [71]. **Right:** Photograph showing the coating process for a stainless steel sample inside the HDPE holder. The copper counter electrode can be seen on the left side of the electrolyte-filled beaker.

Using electrochemical processes such as electroforming, copper can be produced with very low levels of radioactive impurities (see e.g. [167, 168]). Therefore, electrochemical plating (ECP) of copper has been tested for its radon mitigating properties

using a small setup in the Max-Planck-Institut für Kernphysik (MPIK) laboratory. The setup is sketched and shown in figure 4.11 and consists of a 250 ml beaker, filled with an electrolyte solution, into which the sample (right) is submersed together with a counter electrode (left). The electrolyte solution contains 50 mmol/liter copper sulfate ($CuSO_4$) and 1 mol/liter sulfuric acid (H_2SO_4) in de-ionized water. It is heated to about 45°C and agitated using a magnetic stirrer to increase the reactivity. The copper sulfate forms Cu^{2+} ions in the solution, which can be reduced to solid copper on the sample surface, when it is connected to the negative terminal of a power supply. Cu^{2+} ions are constantly replenished by the oxidation of metallic copper from the counter electrode, which is connected to the positive terminal of the power supply.

A Delta Elektronika (SM1540-D) power supply is used together with a Delta Elektronika 232 EXT controller, which allows to read-out and control the power supply by a computer using a custom made software. The evolution of relevant coating parameters like the electric current, as well as the applied voltage, are displayed on the software's graphical user interface (GUI). Furthermore, it shows a real-time estimate of the already deposited mass $m(t)$, together with the current layer thickness $d(t)$. The mass can be obtained from the time integration of the electric current $I(t)$ according to [169]:

$$m(t) = \frac{M_{\mathrm{Cu}}}{2 \cdot e \cdot N_A} \cdot \int_0^t I(t')dt' \qquad \text{and} \qquad d(t) = \frac{m(t)}{\varrho_{\mathrm{Cu}} \cdot A} \tag{4.9}$$

where M_{Cu} is the molar mass of copper, N_A is Avogadro's constant and e is the electron charge. For the estimation of the layer thickness, the deposited mass is divided by the coated surface A and the density of copper. The latter is assumed to be identical to the value of solid copper $\varrho_{\mathrm{Cu}} = 8.92\,\mathrm{g/cm^3}$. The real-time output allows to adjust the coating parameters or terminate the coating as soon as a desired thickness is reached.

The growth rate ($\partial_t\, d(t)$) of the coating, has a major influence on the morphology of the deposited layer [169, 170]. From equation 4.9 it can be seen, that it is proportional to the surface current density $j(t)$, which is defined as the electric current $I(t)$ divided by the sample surface A. The influence of the surface current density on the ^{220}Rn reduction has been systematically studied in [149] and is shown in figure 4.12. The data shows that the highest reduction is obtained for layers deposited close to $j = 10\,\mathrm{mA/cm^2}$. These coatings are found to be bright and shiny in appearance. Note that two of the measurements reported in [149] are not shown in the figure, because their layers turned out to have significant irregularities (whisker growth or darkening). Furthermore, systematic error bars (gray) have been added to account for the variation of the initial ^{220}Rn emanation rate of the used WTh electrodes.

These layers showed, however, very poor adhesion and were easily removed by a piece of strong adhesive tape (tape-test). On stainless steel, good adhesion was obtained for depositions at a much higher current density of $j = 50\,\mathrm{mA/cm^2}$. This deposits appeared dark and powdery. A combination of both layers, allowed to

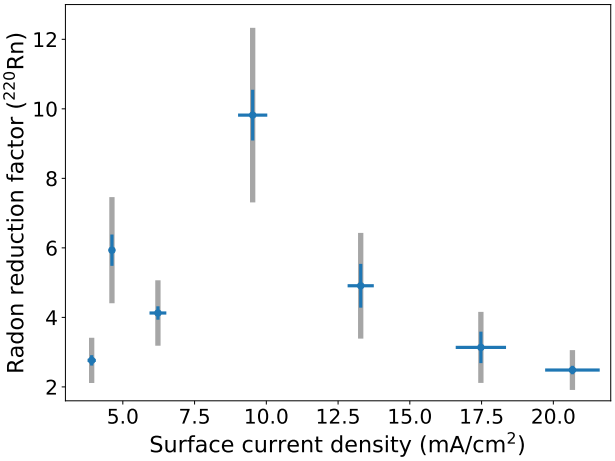

Figure 4.12: Selection of the observed ^{220}Rn reduction factors as function of the applied surface current density. Data correspond to a average coating thickness of 5 µm applied onto thoriated tungsten electrodes. Measurement is originally reported in [149].

obtain adhesive coatings at the desired current density. First, a 1 µm thick adhesion layer at $j = 50\,\mathrm{mA/cm^2}$ is applied, followed by an additional 4 µm thick layer which is deposited at the target current density of $j = 10\,\mathrm{mA/cm^2}$. After thorough pre-tests described in section 4.3.1, this method has been applied to one of the two stainless steel samples that have been implanted with ^{226}Ra at the ISOLDE facility (see section 3.1). The time evolution of this specific coating is illustrated in figure 4.13 and its performance will be discussed in section 4.3.2. It should be men-

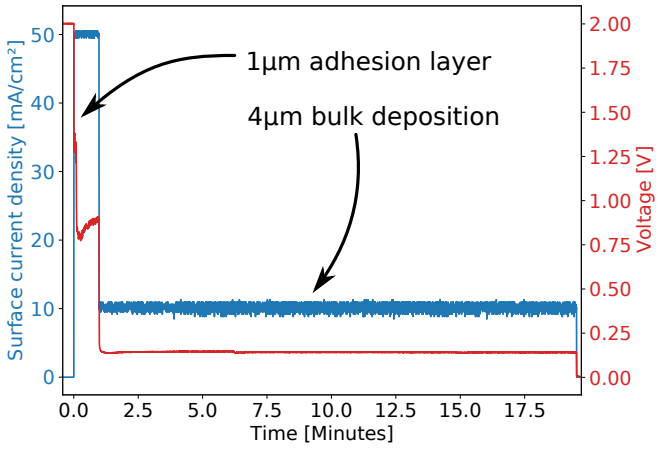

Figure 4.13: Evolution of voltage and current density during the plating of the ^{226}Ra implanted stainless steel sample. A 1 µm thick adhesion layer is deposited at a high current density, followed by an additional 4 µm deposition at a surface current density of $10\,\mathrm{mA/cm^2}$.

tioned however, that a small amount of gas formation (hydrogen) has been observed during the deposition of the adhesion layer. This can influence the estimation of mass and layer thickness using equation 4.9 due to the additional electric charge that is consumed in the hydrogen formation. However, from measurements of the sample's mass increase due to the coating, this effect is found to be small.

The ECP setup can also be used for a gentle removal of an already applied coating layer, by reversing the polarity of the power supply. In that configuration, copper metal is slowly etched from the surface of the coated sample. Figure 4.14 shows the evolution of the applied voltage and surface current density for this procedure. The applied voltage is increased in two steps to a value of 75 mV, at which the bulk

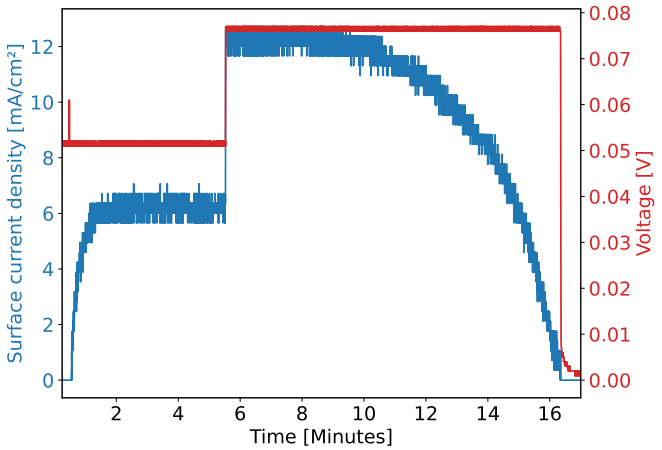

Figure 4.14: Evolution of the applied voltage and current density during the removal of an already applied copper coating from a stainless steel sample.

of the copper is removed. After roughly 10 minutes, the current density starts to decrease and shows a very pronounced drop. This indicates that the removal process approaches its end. As soon as the value has fallen below 1 mA/cm^2, the process is terminated and the sample is removed from the bath. A thin film of copper typically remains on the sample surface, which is removable using a water-soaked lab tissue. This method was applied for the measurements made with the recoil implanted ^{224}Ra samples described in section 4.3.1.

Comparison of reduction factors obtained in previous studies

As an intermediate result, table 4.1 summarizes the highest achieved reduction factors obtained using WTh electrodes in past works [71, 126, 148, 149]. Where available, also the reduction of ^{222}Rn emanated from trace impurities of these electrodes and for ^{224}Ra are reported. The data shows a wide range of results obtained by

Table 4.1: Comparison between the highest achieved reduction factors using the different coating methods in past works [71, 126, 148, 149]. The table only contains results obtained from coatings of thoriated tungsten electrodes, and excludes the results from this work.

Method	Material	Thickness [µm]	Reduction ^{220}Rn	Reduction ^{222}Rn	Reduction ^{224}Ra
Sputtering	Titanium	0.4 - 0.8	4.5	$2.1^{+0.7}_{-0.4}$	$\gtrsim 25$
Plasma spraying	Copper	3	22	-	$\gtrsim 10$
Epoxy resin	Stycast	≈ 200	≥ 74	-	$\gtrsim 100$
Chem. vapor deposition	DLC	1	3	$1.4^{+0.4}_{-0.3}$	≥ 4.75
Electrochem. plating [a]	Copper	5	130	$7.4^{+2.5}_{-1.5}$	$\gtrsim 100$

[a] Results from this work (section 4.3) are not included.

the different methods. Rather low reductions factors were achieved for the two vac-

uum deposition processes, while the plasma spraying yielded a slightly better result. Good reduction factors were found for the epoxy coating, as well as for the ECP method.

Independent of the ^{220}Rn reduction, the contribution from ^{224}Ra is found to be completely suppressed for the coated samples. As explained in section 4.1.1, this indicates that the recoil-tightness of the layers is sufficient. This leaves the diffusion of radon through the coating as the predominant release mechanism. However, using the diffusion model introduced in section 4.1.2, it is impossible to reconcile the observed differences between the reduction factors for ^{222}Rn and ^{220}Rn. Given that the half-life of ^{220}Rn is almost four orders of magnitude shorter compared to the one of ^{222}Rn, a complete suppression of the ^{220}Rn would be expected. Note however that the proposed diffusion model is quite simple and assumes a perfectly homogeneous coating layer. A more advanced model, which includes the diffusion along grain boundaries or the possibility of voids in the coating, might be necessary to correctly explain these observations.

It is important to point out, that table 4.1 shows the highest reduction factors which have been achieved by each method. Additional samples that have been coated by sputtering and plasma spraying, showed ^{220}Rn reduction factors of only 1.2 and 2.3 respectively [71]. Similarly, the reproduction of the ECP method proved to be challenging [126], before the influence of the current density has been measured systematically (see figure 4.12) [149].

4.3 From tungsten to stainless steel

Until now, all results were achieved using thoriated tungsten electrodes and precise reduction factors are predominantly obtained for ^{220}Rn. The important transition from tungsten to more realistic stainless steel samples, is presented in this section. First, the good results obtained with the electrochemically plated copper layers have been validated using the ^{224}Ra recoil implanted samples that have been introduced in section 3.2. Afterwards, the technique was applied to one of the two ^{226}Ra implanted stainless steel samples. This finally allowed to obtain a precise reduction factor for ^{222}Rn on a stainless steel surface.

4.3.1 Coatings applied to recoil implanted samples

As a first step, the efficiency and reproducibility of the ECP procedure on stainless steel was verified using the recoil implanted stainless steel samples described in section 3.2. Since these samples can be implanted with ^{224}Ra using the small in-house setup introduced in section 3.2.1, they are easy to obtain and well suited for those pre-tests. However, the short life-time of ^{224}Ra ($T_{1/2} = 3.7$ days), limits the time during which each sample can be used and makes the analysis slightly more complicated. Each sample underwent a cycle of three individual measurements with a length of one week each following its implantation. In each of the three

measurements, the ^{220}Rn emanation rate of the sample has been measured using the electrostatic radon monitor described in section 3.1.3. As described in section 3.2.2, the radon emanation is determined via the activity of its daughter isotope ^{212}Po, which are selected by their decay energy as shown in figure 3.17.

During the first measurement, the initial emanation of each sample is determined. The sample is then taken out of the monitor, and a 5 µm thick copper coating is applied to it using the ECP procedure. After the coated sample is thoroughly rinsed and dried, its new radon emanation rate is measured in the radon monitor. A third measurement is performed after the coating of the sample is removed using the reversed-voltage method described in section 4.2.

Figure 4.15 shows the evolution of the detected ^{212}Po rate from *sample 1* throughout its three week measurement cycle. For a simpler presentation, the data (black)

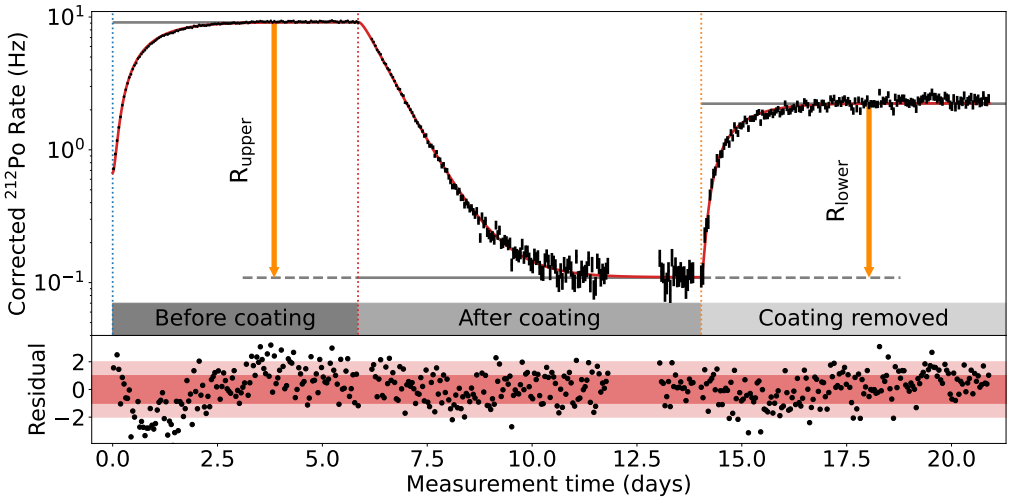

Figure 4.15: Detected ^{212}Po activity from the recoil implanted *sample 1* over the full measurement cycle of approximately 3 weeks. The activity is corrected for the overall decay of the implanted ^{224}Ra in the sample. An upper and lower bound for the reduction factor ($R_{min/max}$) are determined by comparing the ^{220}Rn emanation rates (horizontal gray lines). The red line shows the fit of the data with the model introduced in section 3.2.2. Around day 12 a crash of the DAQ resulted in a short period where no data was taken.

and the fit function (red) are corrected for the overall decay of the ^{224}Ra activity in the sample [2]. The ^{220}Rn emanation rates (gray lines) are then constant during each interval. Their discontinuities come from the reduced (increased) radon emanation due to the coating (the removal of the coating). The amount of emanation in each interval is determined from the fit of the (uncorrected) data with the solution of the Bateman equation (eq. 3.9). Due to the decay of the ^{224}Ra activity, the ^{212}Po activity can only reach a transient equilibrium. This results in its activity being 15% larger compared to ^{224}Ra (see figure 3.18). To simplify the presentation, this effect is corrected for, such that the gray lines in figure 4.15 match the equilibrium rate of ^{212}Po.

[2] Note that the decay still leads to an increase of the statistical uncertainty at later times.

The lower panel in figure 4.15 shows the residuals between the model function and the data. Apart from a slight deviation at the beginning of the measurement cycle, the activity evolution shows very good agreement with the model. To reduce the number of fit parameters, an equilibrium between the initial activities of ^{224}Ra, ^{220}Rn and ^{216}Po (first part of the decay chain), as well as ^{212}Pb, ^{212}Bi and ^{212}Po (second part) is assumed. A repetition of the fit without this constraint yielded a very similar result. Furthermore, the ^{212}Pb activities at the beginning of the second and third interval, are fixed to the remaining ^{212}Pb activity at the end of the previous interval. This constraint can be made, since the collected ^{212}Pb activity will remain on the PIN diode until the beginning of the next interval due to the extended half-life of ^{212}Pb ($T_{1/2} = 10.6$ hours). Therefore, only the initial ^{212}Pb activity in the first interval is left as an additional free fit parameter.

As can be seen, the ^{220}Rn emanation rate after removal of the coating, is significantly lower than the initial emanation rate. This is because a part of the implanted ^{224}Ra is dissolved from the sample into the electrolyte, which will be further discussed at the end of this section. The reduced activity in the coated sample, leads to an overestimation of the radon reduction factor if it is computed as the ratio of emanation in the first and second interval ($\mathrm{R_{upper}}$). Likewise, the ratio between emanation in the third and second interval ($\mathrm{R_{lower}}$) is prone to underestimation of the true reduction factor R of the coating, because activity is also removed during the removal of the coating. However, the true reduction factor R is always within the two bounds, such that

$$\mathrm{R_{lower}} \leq \mathrm{R} \leq \mathrm{R_{upper}} \,. \tag{4.10}$$

To test the reproducibility of the ECP coating procedure, the described measurement cycle has been applied to three of the four recoil implanted samples that are described in section 3.2 (*sample 1*, *3* and *4*). The fourth sample (*sample 2*) has been used for an additional test of the ^{224}Ra removal by the electrolyte which is detailed below. Table 4.2 summarizes the obtained ^{220}Rn reduction factors of the 5 µm thick copper layers for the three tested samples.

Despite a considerable variation between the samples, they all show a suppression of ^{220}Rn by at least one order of magnitude due to the coating. Their upper limits range between two and even three orders of magnitude. Furthermore, all of the applied coatings turned out to be without irregularities, such as darkening or whiskers, that have occurred in past studies [149].

The table also shows the fraction of the sample's remaining activity. While *sample 1 & 3* have both lost about 3/4 of their activity during the coating and its removal, this is not the case for *sample 4*, which has suffered an almost complete removal. The reason for this difference remains unknown. It should be noted however, that during the last measurement of this sample, a malfunction of the detector required an exchange of the PIN diode. Though it is expected that this leads to a slight reduction of the detection efficiency, the large deviation cannot be accounted for.

Table 4.2: Upper and lower limits for the reduction factors of the ^{220}Rn emanation rate using samples implanted with ^{224}Ra via recoil. $R_{lower/upper}$ correspond to the reduction factors as defined in figure 4.15. The last row lists the percentage of the sample's initial activity that remains after the coating is removed. The numbers are corrected for the decay of ^{224}Ra.

Sample	*1*	*3*	*4*
R_{lower}	20.4±0.3	142±8	12.3±1.6
R_{upper}	83.6±1.3	640±37	1050±140
Remaining ^{224}Ra activity	(24.44±0.12)%	(22.18±0.11)%	(1.13±0.03)%

Investigation of ^{224}Ra removal by the electrolyte

The loss of activity was investigated using a "dummy" procedure, in which the second sample (*sample 2*) has been submersed into the electrolyte without being coated. Care was taken, that the temperature and agitation of the bath, as well as the duration were the same as for the standard ECP procedure.

Without the external voltage being applied, the stainless steel and copper surfaces act like a simple battery and produce a potential difference. The time evolution of this voltage is shown in the right of figure 4.16 over the duration of the submersion. The visible decrease of the voltage between the both metals clearly indicates some

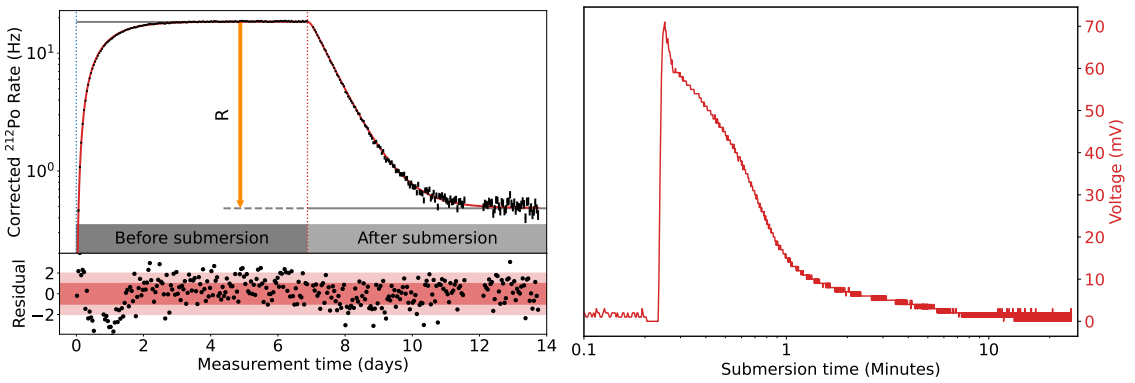

Figure 4.16: Left: Evolution of the corrected ^{212}Po activity detected from *sample 2* before and after its extended submersion into the electrolyte solution. A clear reduction of the implanted ^{224}Ra activity is visible despite there was no coating layer applied during the submersion. **Right:** Evolution of the potential difference between *sample 2* and the copper counter electrode during its 25 minute long submersion into the electrolyte solution (40°C).

sort of change occurring on the sample surface. This is confirmed by the (97.38± 0.02)% reduction of the ^{220}Rn emanation rate of the sample due to the electrolyte treatment (figure 4.16 left). Note however, that during the normal ECP procedure the sample surface is quickly protected by the formed copper layer. To further reduce

the contact time of the steel surface with the electrolyte, the remaining coatings were performed with the voltage being pre-applied to the sample, such that the coating process starts as soon as the sample is submersed.

A likely explanation for the mechanism of removal is the corrosion of stainless steel by the sulfuric acid. The long-term corrosion rate of stainless steel by sulfuric acid is reported in [171]. From extrapolation it can be expected, that 20 µg steel are removed during the 25 minute long submersion. This translates to a material thickness of roughly 10 nm, which is of the same order of magnitude as the expected depth of implantation (see section 3.2.1).

The migration of activity into the electrolyte was confirmed independently using high purity germanium (HPGe) gamma spectrometry (see section 3.1.2). Clear contributions from ^{208}Tl and ^{212}Pb which are part of the decay products of ^{224}Ra were found in the used electrolyte. Subsequent HPGe measurements were also carried out for the solutions used for *samples 3 & 4*. For both samples, ^{224}Ra has been detected in the electrolyte used for the coating, as well as in the one used for its removal. Therefore, the true reduction factor is neither exactly equal to R_{lower} nor to R_{upper}, but indeed in between the both values. In both cases however, slightly more activity was dissolved during the coating step, such that R is probably closer to R_{lower} than it is to R_{upper}.

4.3.2 Coating of a ^{226}Ra implanted sample

One further coating has been applied to verify the promising radon reductions found for the ECP procedure on one of the ^{226}Ra implanted stainless steel samples described in section 3.1. This test finally allows to quantify the reduction of ^{222}Rn emanation from a stainless steel surface. Therefore, it is regarded as the closest to any real-world application so-far. *Sample B* has been chosen for this test which has an implanted ^{226}Ra activity of $(8.4 \pm 0.3_{\,\text{stat}} \pm 1.0_{\,\text{syst}})$ Bq and offers (2.00 ± 0.05) Bq of ^{222}Rn emanation.

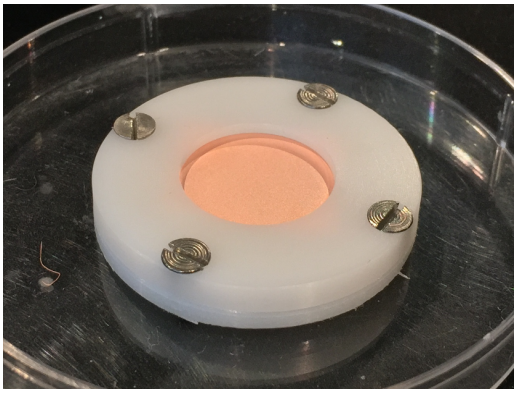

Figure 4.17: Picture of the ^{226}Ra implanted stainless steel *sample B* in the HPGe screening holder after coating

The sample has been coated with 5 µm of copper following exactly the same procedure as has been applied to the ^{224}Ra implanted samples. As shown in figure 4.17, the coating turned out bright and smooth. Also the time evolution of voltage and current density (see figure 4.13, above) shows no indications of irregularities during the deposition process. After the sample has been rinsed from any residues of the electrolyte solution, it has been mounted into the emanation vessel used for the ^{222}Rn measurements by miniaturized proportional counters as is

described in section 3.1.3.

The results from several measurements over the course of almost one year following the coating are summarized in figure 4.18. The applied coating proved to be highly

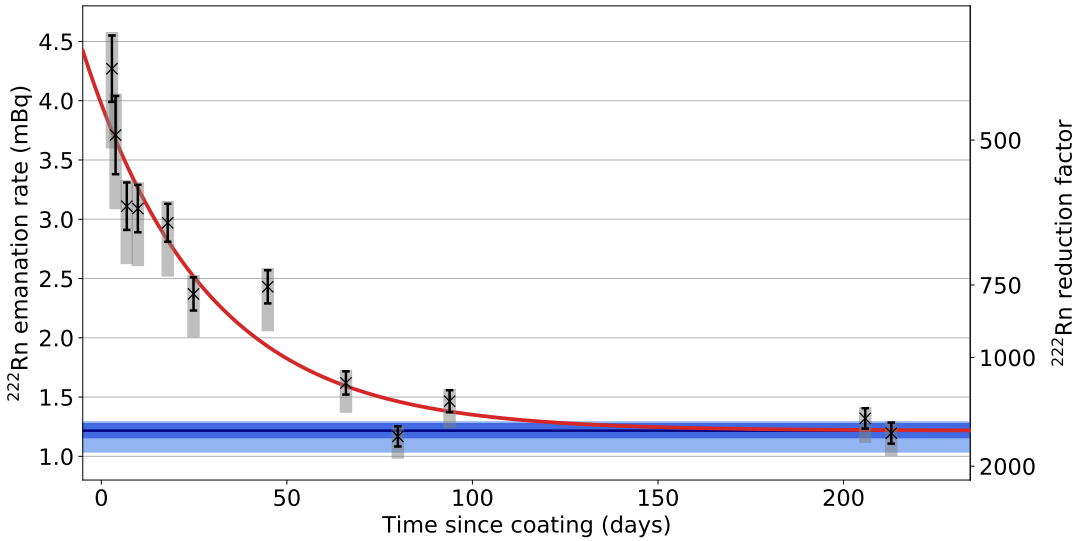

Figure 4.18: Evolution of the ^{222}Rn emanation of the ^{226}Ra implanted stainless steel sample after coating. Black error bars correspond to statistical uncertainty of the emanation measurements. The common systematic uncertainty from the conversion of the remaining activity into the reduction factors (right axis) is reflected by the gray bars. Shown in blue is the expected equilibrium value determined by the fit function drawn in red.

effective and suppresses the emanation by about three orders of magnitude to the level of a few mBq. Furthermore, the data show a clear time-dependence, which will be further discussed at the end of this section. For now, only the equilibrium value of the remaining emanation will be extracted by a fit of the evolution with an exponential function having a constant offset

$$A(t) = A_0 \cdot e^{-t/\tau} + A_{eq}\,, \tag{4.11}$$

that was found to describe the data reasonably well. The time constant with which the emanation decreases is found to be $\tau = (33 \pm 4_{\,\mathrm{stat}})$ days and the expected equilibrium emanation amounts to $A_{eq} = (1.22 \pm 0.06_{\,\mathrm{stat}})$ mBq. Here the statistical uncertainty is from the individual measurements as represented by the black error bars.

The right axis of the figure shows the converted ^{222}Rn reduction factor, which is computed as the ratio between the sample's initial emanation and the emanation after the coating. This conversion introduces two sources of systematic uncertainties, which are indicated by the gray error bars. One contribution is from the 2.5% uncertainty of the sample's initial activity. The second contribution is related to the observed removal of activity from the sample during the coating process. The latter is determined based on additional HPGe measurements of the sample and the used electrolyte.

Approximately one month after the coating of the sample, its implanted ^{226}Ra activity was re-measured in the same HPGe gamma spectrometer setup as described in section 3.1.2. A 8.3% lower activity is found in the 186 keV gamma emission line from ^{226}Ra. An additional measurement of the used electrolyte solution revealed an increased activity in the short-lived radon daughters ^{214}Pb and ^{214}Bi, compatible with the missing amount of activity in the sample. Both results are summarized in table 4.3 and compared to the respective activities prior the coating. The initial

Table 4.3: Comparison of activities for radium and radon daughters in the ^{226}Ra implanted sample before and after coating as well as in the used electrolyte. Measurements carried out using HPGe gamma spectrometry. Table adapted from [172].

Activity		^{226}Ra (186) keV (Bq)	^{222}Rn daughters (Bq)
Sample	uncoated	$8.4 \pm 0.3_{\,\mathrm{stat}} \pm 1.0_{\,\mathrm{syst}}$	6.0 ± 0.3
	coated	$7.7 \pm 0.2_{\,\mathrm{stat}} \pm 0.9_{\,\mathrm{syst}}$	7.2 ± 0.4
Electrolyte	before	-	$\lesssim 0.012$
	after	-	0.34 ± 0.02

^{226}Ra content of the electrolyte is determined from one of the measurements related to the pre-tests with the ^{224}Ra implanted plates. Since there are only trace amounts of ^{226}Ra present in this sample an upper limit of the radium activity can be given which is about 12 mBq.

In contrast to the ^{224}Ra recoil implanted samples, the activity loss of the ^{226}Ra implanted sample is found to be much less severe. This is likely a consequence of the difference in the distribution of the implanted activity in both samples. As shown in figure 3.2, the sample implanted by the radioactive ion beam (RIB) at the ISOLDE facility has less activity located close to the surface compared to the recoil implanted sample (figure 3.15). Assuming that the electrolyte mostly affects the activity located closest to the surface, this difference is to be expected.

The reported reduction factors in figure 4.18 have been corrected to account for the removed activity. A non-uniform removal of activity results in an altered radon emanation fraction of the coated sample, giving rise to a systematic uncertainty. For this, the following two extreme cases are considered. The first case assumes that radium is extracted (leached) out of the uppermost layers, while the stainless steel remains untouched. On average, the implantation depth would become slightly deeper, resulting in a reduced emanation fraction (see section 3.3). For the second case, it is assumed that the electrolyte removes (etches) the steel together with the radium from the sample. In this case the mean depth of the implantation would be reduced, and the emanation fraction of the sample is increased. Note that the second case might be more likely, given the known corrosion of stainless steel in sulfuric acid discussed in the previous section. Still the emanation fractions F for both cases are evaluated using the Gaussian model described in appendix C, to give a conservative

estimate of $F_{\text{coated}} = \left(23.3^{+17}_{-1.2}\right)\,\%$. With this the equilibrium reduction factor R of

$$R = \left(1500 \pm 70\,(\text{stat})\,^{+250}_{-50}\,(\text{syst})\right)$$

can be determined from the value of A_{eq} of the fit function (equation 4.11).

A cross-check of the coating's high efficiency is apparent from the activity of the short-lived ^{222}Rn radon daughters reported in table 4.3. For the uncoated sample, this activity is lower by about 2 Bq when compared to the implanted ^{226}Ra activity. This is explained by the emanated radon from the sample being removed from the measurement chamber due to the constant purge of nitrogen. After the coating is applied both activities are found to be compatible, since the radon emanation is almost completely stopped and the radon daughters decay in the coating layer.

Estimation of an effective radon diffusion constant

As can be seen from figure 4.3, the recoil-driven emanation through a 5 µm thick coating layer should be completely negligible. Therefore, it can be assumed that the remaining radon emanation is released from the sample by the diffusion of radon through the coating.

Using equation 4.7, allows to convert the observed reduction factor R into an effective value of the diffusion constant D_{eff}.

$$D = \left(\frac{h\sqrt{\lambda}}{\cosh^{-1}(R)}\right)^2 \qquad \text{for } h > 0 \text{ and } R > 1 \tag{4.12}$$

$$D_{\text{eff}} = \left(9.0 \pm 0.2\,(\text{stat})\,^{+1.2}_{-1.4}\,(\text{syst})\right) \times 10^{-15}\,\frac{\text{cm}^2}{\text{s}}\,.$$

Where h is again the layer thickness. Note that the coating layer contains many imperfections, such as grain boundaries and displacements. Furthermore, one fifths of the layer thickness is attributed to the powdery adhesion layer, which is deposited at a much higher surface current density. Therefore, its value should be treated as an effective diffusion constant. It is likely larger than the one of metallurgical copper, which is expected to be more compact. The systematic uncertainty contains the propagated uncertainty on the reduction factor, as well as a 7% uncertainty on the thickness of the layer. The latter is estimated from the variation of observed mass increases in the set of the three coated ^{224}Ra recoil implanted samples. The layer thickness was confirmed on an identically coated reference sample by means of a micrometer screw to be 6 ± 1 µm [173].

Values for the radon diffusion constant have been reported for polymers, such as Nylon (10^{-12} cm^2/s) [152] or high density polyethylene (HDPE) (19×10^{-8} cm^2/s) [154], as well as for radon barriers used in the building sector (e.g. [174]). These values are several orders of magnitude larger, compared to the one found for the copper coating. This difference is expected, since the diffusion in metal is typically smaller compared to polymers. No literature values have been found for the diffusion of radon in met-

als. However, measurements on the diffusion of xenon in copper have been reported by Rickers [175] for a temperature of about 500°C and by Kawasaki [176] at about 1000°C. Despite the temperature difference, both authors find similar values for the diffusion constant of 2×10^{-14} and $1\times10^{-14}\,\mathrm{cm}^2/\mathrm{s}$ respectively (see also the discussion in [175]). Though this seems suspiciously close to the value obtained in this work, it needs to be stressed that the present measurements have been carried at much lower temperatures. A diffusion constant in the range between 10^{-38} to $10^{-42}\,\mathrm{cm}^2/\mathrm{s}$ would be expected by extrapolation of these values [175, 176] to room-temperature using the Arrhenius equation [177].

Discussion of the time dependence

The measurements shown in figure 4.18, show a clear decrease of the radon emanation rate with a time constant $\tau = (33 \pm 4)$ days. Possible explanations for this behavior will be discussed in the following. So far, the discussion was based on the steady-state solution ($\partial_t = 0$) of the diffusion equation. Numerical solutions for the time-dependent equation are shown in figure 4.7 for selected values of the diffusion constant D. Starting from an initially radon free coating layer ($\eta(x, t = 0) = 0$), the exhaled radon flux is zero initially and then approaches its equilibrium value. For $D \simeq 10^{-14}\,\mathrm{cm}^2/\mathrm{s}$ the steady-state should be reached after roughly 20 days. This expectation is in clear contradiction to the measurement, which revealed radon from the sample already a few days after the deposition. A large initial radon concentration $\eta_0 \gg \eta(x)$ present in the layer after deposition, could explain an initial radon outflow with a subsequent decrease. The numerical evaluation of such a case, however showed a much faster decrease of the radon emanation ($\tau \approx 0.3$ days), which is also incompatible to the measured data.

The more likely explanation is that the value of the diffusion constant itself decreases over time. One reason for such a decrease could be for example the formation of an oxide layer on the surface of the coating, acting as an additional diffusion barrier for the radon. A time and temperature dependent reduction of the ^{220}Rn emanation rate has been observed for copper coated WTh electrodes in past studies [149]. This coincided with a discoloration of the coating layer, which was attributed to the formation of an oxide layer. In the present case, the sample has been stored under a protective helium atmosphere for most of the time, slightly disfavoring the hypothesis of oxidation. An alternative explanation might be the so-called self-annealing of the copper layer. This behavior has been reported for electroplated copper layers even at room temperature [178–184]. The annealing results in the growth of the microscopic copper crystals, which in turn leads to a decrease in the amount of grain boundaries in the layer. Since diffusion is enhanced along these boundaries [160], such a process will reduce the effective diffusion constant of the material and therefore the radon release.

Regardless of the precise reason, the coating only becomes more effective as a radon barrier over time. So the underlying mechanism does not pose a thread, but on the contrary might even offer a chance. If the change is indeed connected to

an annealing process, this could be exploited by subsequent heat treatments of the coatings to improve their radon mitigation performance.

4.4 Summary and outlook

Contemporary large-scale dual-phase xenon TPCs used for direct dark matter detection such as XENONnT [6], LZ [51] and PandaX-4T [52] will reach unprecedented low levels of experimental backgrounds. The low energy electronic recoil events produced by decay products of ^{222}Rn are expected to be their dominant background contribution. Therefore, future detectors like the planned DARWIN observatory [39], require an even further suppression of the experiment's radon emanation rate.

Reaching this ambitious goal, will require a well coordinated ensemble of techniques for radon prevention and removal, together with analysis strategies for rejection of radon-induced background events. In chapter 2, the performance of the XENONnT radon removal system has been evaluated. Though this system showed an impressive radon reduction, its gain will likely be reduced in a future detector, by the large xenon inventory together with its limited throughput capabilities. Therefore, techniques which prevent radon emanation in the first place will become even more important. A novel approach for the mitigation of radon emanation using surface coatings, showed promising results in previous studies [71, 126, 148, 149]. Several coating techniques have been evaluated, using thoriated tungsten electrodes. The most promising method so far was found to be electrochemical plating (ECP) of copper at an applied surface current density of 10 mA/cm^2.

This technique was further investigated in this work, while two important shortcomings of previous studies have been successfully overcome. So far, the ECP procedure has been mainly applied to tungsten samples emanating predominantly ^{220}Rn. Using the ^{224}Ra implanted samples (see section 3.2), it was possible to also validate the procedure on stainless steel surfaces. Furthermore, one coating has been prepared on the ^{226}Ra implanted stainless sample described in section 3.1. This allowed to measure for the first time the ^{222}Rn reduction from a realistic sample with good sensitivity. A suppression of the ^{222}Rn emanation rate of three orders of magnitude was achieved. From this, an effective diffusion constant of the order of 10^{-14} cm^2/s can be estimated using the derived model for radon diffusion in the coating layer. It is concluded, that the remaining radon escapes from the coating most likely along lattice defects like for example the grain boundaries. The obtained result is very promising and exceeds by far the required radon reduction for a future large-scale experiment.

Future challenges

The promising results obtained in this work are only the first step towards a possible application of this technique in a large-scale experiment. In the following, a non-extensive compilation of the remaining challenges that need to be addressed is given,

along side with possible future studies.

For future large-scale detectors the preparation of uniform, high-quality coating layers on a variety of surfaces will be required. They could cover a range of different shapes and sizes between 0.1 m^2 up to tens of square meters. So far the coatings have been prepared on surfaces of order of few cm^2. To verify the scalability of the technique, a multi-staged approach should be followed, in which the size of coated samples is gradually increased. The radon screening infrastructure at the MPIK offers stainless steel emanation vessels of various sizes. Since their radon emanation rates are known with good precision, the gain in radon reduction by the coating can be directly validated. Furthermore, a reduced emanation rate of these vessels due to the coating can help to increase the sensitivity of future measurements.

The gain in radon reduction heavily depends on the amount of ^{226}Ra that is incorporated in the layer. Due to its low content of radioactive impurities, electroformed copper is a widely applied shielding material for low-background experiments (e.g.[167, 168]). However, the electroforming process is not identical with the ECP method developed for radon mitigation. Therefore, it remains to be shown that the coating is produced free of ^{226}Ra. This could be evaluated by artificially contaminating the electrolyte with radium and measuring the amount of radium incorporated in the coating.

The application of a coating in the cryogenic LXe environment comes with a challenge and a chance. Since the diffusion is strongly suppressed at low temperatures, it is expected that the radon reduction of the coating will be increased. This effect has been observed in [126] for temperatures reaching as low as -90°C. On the other hand, the different thermal expansion coefficients of the coating and substrate will lead to thermal stress, which needs to be absorbed by the coating. Preliminary tests of the effect of repeated thermal shock treatments of copper coated WTh electrodes showed only a minor degradation of the ^{220}Rn reduction [71]. However a more robust and systematic study will be necessary to guarantee the long term stability.

Future large-scale detectors will require to drift electrons in the LXe over distances of several meters. This requires an extremely high chemical purity of the xenon. It must therefore be verified that no harmful impurities like for example residues of the electrolyte solution are dissolved from the coating by the LXe. The Heidelberg Xenon (HeXe) dual-phase xenon TPC has been used in the past to study the impact of polytetrafluoroethylene (PTFE) cleaning methods on the LXe purity [100, 125]. This setup which is described in more detail in the following chapter, can be used to validate the applicability of electrodeposited copper layers under realistic operating conditions. Further validations could also be done using the full-length demonstrator setup, which is currently under construction at the University of Zürich [185].

5 The Heidelberg Xenon detector

The Heidelberg Xenon (HeXe) setup recently received an upgrade to host a dual-phase xenon time projection chamber (TPC). This detector has been employed to measure the transmission of liquid xenon (LXe) scintillation light through polytetrafluoroethylene (PTFE) which will be further detailed in chapter 6. Furthermore, the measurements of the light and charge response of LXe to alpha particles and low-energy electrons (see chapter 7) were performed using this setup. Both studies have also been published in [P1]and [P2], respectively. The setup has been also used to investigate the scintillation pulse shape of alpha events [186, 187] as well as the influence of PTFE cleaning methods on the LXe purity [100, 125]. Before the upgrade essential components of the systems have been applied for studies of the radon depletion in xenon off-gas [77, 133], as well as for measurements of the response of Hamamatsu R11410 photomultiplier tubes (PMTs) to xenon scintillation light [188, 189].

Figure 5.1 shows the layout of the complete system in the laboratory at the Max-Planck-Institut für Kernphysik (MPIK). The TPC is hosted in the cryostat (green)

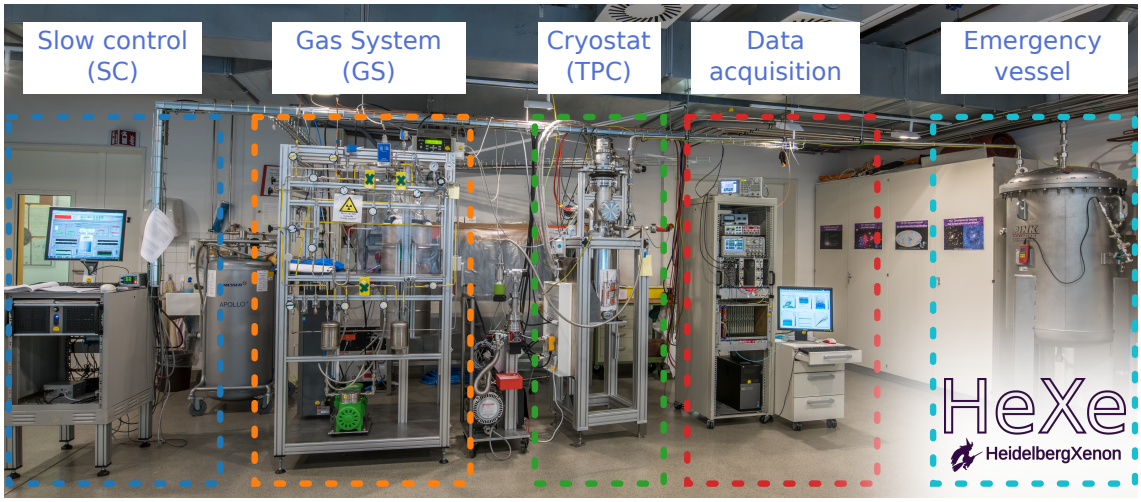

Figure 5.1: Photograph of the HeXe setup in the lab with all sub-systems labeled

and is described in detail in the following section 5.1. Gaseous xenon (GXe) is recirculated and calibration sources can be introduced using the gas system (GS) (orange) which is described in section 5.1.1. The slow control (SC) (blue) and data acquisition (DAQ) (red) systems are used to monitor the system parameters and record the scientific data, and are detailed further in section 5.1.2. Of special importance for the operation of a TPC are the electric fields, which require the application

of high voltage (HV) in the detector. The different HV components will be detailed in section 5.2, while section 5.3 will be dedicated to the simulation and optimization of the electric fields in the detector. The chapter will be concluded with a short outlook on a future upgrade of the detector.

5.1 Dual-phase TPC setup

The TPC consists of a cylindrical active volume with a height of 5 cm and a diameter of 5.6 cm, containing 345 grams of LXe. It is housed in a PTFE support structure which is situated in a vacuum insulated cryostat having an inner diameter of 20.1 cm. A cut-away drawing of the HeXe TPC is shown in figure 5.2 with labels for the most essential components. The active volume is instrumented by two Hamamatsu R6041-406 2-inch PMTs (light green), that feature a metal channel dynode structure and quantum efficiencies (QEs) close to 40%. Their gain is calibrated *in situ* using blue light from an external LED, which is guided towards the active volume by optical fibers. The model-independent method described in [190] is used for the gain estimation with additional details provided in [186]. For a reliable measurement of large light levels (e.g. from alpha particle interactions), thin light attenuators made from PTFE can be placed in front of the PMT windows.

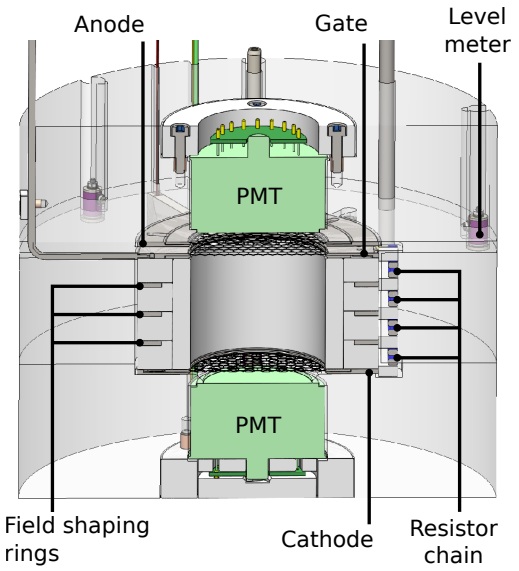

Figure 5.2: Technical drawing of the HeXe time projection chamber. Figure published in [P2].

Three electrode meshes are used to apply the electric fields in the detector which are needed to drift, extract and amplify electrons produced by particle interactions in the LXe. The meshes are accommodated in circular stainless steel holders which are supplied with HV by PTFE insulated cables. The homogeneity of the drift field is enhanced by three field shaping rings (FSRs) placed equidistantly along the drift length. They are connected between the cathode and gate electrode using a series of four 1 GΩ HV resistors acting as voltage dividers. Electrons arriving at the top of the detector are extracted from the LXe phase into the GXe by an extraction field applied between the gate and anode electrode which are 5 mm apart from each other. During normal operation the height of the LXe level is maintained between these two electrodes.

The height of the LXe level is measured by the capacitance change of four cylindrical level meters distributed around the outer circumference of the PTFE support

structure. Three of them have a height of 1 cm to measure the height of the liquid level close to the extraction region. One longer level meter allows to measure the height of the liquid over the full length of the active volume [100]. The LXe temperature is measured using three Pt100 temperature elements placed along the height on the outside of the support structure. An additional sensor which is placed on the top of the structure allows to measure the GXe temperature.

For maintenance of the TPC, for example to insert the PTFE attenuators, the TPC can be moved out from the cryostat. To prevent contamination of the detector by impurities like oxygen and water, such maintenance operations are performed inside a nitrogen flushed glove bag [100, 125].

5.1.1 Gas handling system

The operation of a LXe TPC requires a high chemical purity of the xenon, such that the light and the charge signals are not attenuated by dissolved impurities such as oxygen or water [2]. Therefore, the xenon is constantly recirculated and purified in a hot zirconium getter (SAES MonoTor PS3) using the GS sketched in figure 5.3. Xenon is extracted from the LXe reservoir below the bottom PMT, while the purified

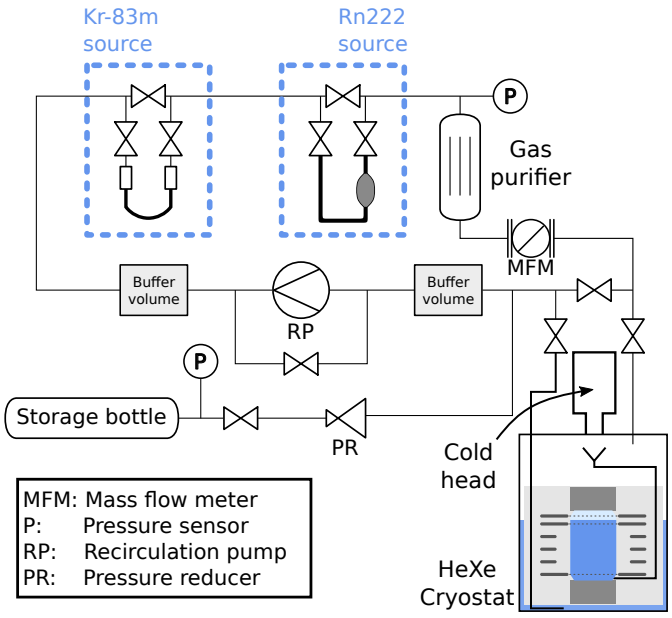

Figure 5.3: Scheme of the HeXe gas handling system used for xenon recirculation, purification and recuperation via cryogenic pumping. Also shown are the two gaseous sources used in this work. Figure published in [P2].

xenon gas is liquefied on a copper surface which is cooled using a helium-driven pulse tube refrigerator (Leybold cool power 140T). It is then guided back into the active volume by a funnel. The recirculation is driven by a KNF double diaphragm pump and the flow rate is adjusted to 2.75 SLPM using a manual bypass valve. The flow is measured by a MKS mass flow meter (MFM).

Furthermore, the GS allows to mix internal calibration sources into the xenon stream. Metastable ^{83m}Kr ($T_{1/2}$ = 1.8 hours) can be transported into the TPC by the recirculation flow from ^{83}Rb loaded zeolite beads stored in an U-shaped

tube [71, 191]. It decays via a short-lived intermediate state under the emission of two conversion electrons with energies of 32.1 keV and 9.4 keV. The long half-life of ^{83}Rb ($T_{1/2} = 86.2$ days) [192] allows for a constant rate of ^{83m}Kr interactions in the detector throughout the duration of the measurement. The second source allows to inject ^{222}Rn into the xenon. Before it can be used, it needs to be loaded with radon, following a similar procedure as is described in section 3.1.3. First, a radon helium mixture is extracted from a aqueous ^{226}Ra source. The radon is then stored using an activated carbon trap held at liquid nitrogen temperature, while the helium carrier gas is removed by pumping. After the trap is warmed up and connected to the GS, the radon can be released into the xenon stream where it slowly decays ($T_{1/2} = 3.8$ days) throughout the duration of the measurement.

The xenon inventory of the system is stored in a high-pressure stainless steel cylinder. During filling of the detector between 2.5 and 3 kg of xenon need to be expanded via a pressure reducer into the cooled cryostat in order to reach the desired LXe level. After the filling is completed, the cylinder is submersed in a bath of liquid nitrogen and the remaining xenon solidifies. At the end of the measurement or in case of an unexpected loss of cooling, the xenon in the system can be recovered into the storage cylinder by cryogenic pumping. Since this method relies only on the availability of liquid nitrogen, xenon can be recovered even in the case of a power outage.

The system is protected against dangerous over pressures by several rupture discs, as well as an over pressure relief valve. To prevent the loss of costly xenon in such a scenario, the system features an over pressure relief vessel (cyan in figure 5.1). It is connected to the cryostat via an in-line rupture disc which bursts at a nominal pressure difference of 3 bar. The vessel has a volume of 480 liters which is sufficient to accommodate the filled xenon in gaseous form at room temperature.

5.1.2 Slow-control, data acquisition and processing

Slow-control and measurement procedure

The various detector parameters such as the pressures and temperatures as well as the xenon flow rate and the height of the liquid level are monitored and recorded by a dedicated SC system (dark blue rack in figure 5.1). It uses a custom designed LabVIEW [193] interface that stores the recorded values in a `PostgreSQL` [194] database from which they can be retrieved for later analysis [186]. The SC system furthermore allows to issue warnings and alarm messages if certain parameters leave a pre-defined range. An independent machine is used to notify HeXe operators in case of a crash of the SC program or computer.

The typical evolution of cryostat pressure (red) and temperature (blue) over the course of a several week long measurement is illustrated in figure 5.4. Before the measurement begins, the cryostat is thoroughly evacuated to a pressure of at least 10^{-4} mbar (not shown). It is then filled with GXe to an absolute pressure of 2 bar, which is recirculated and purified between the cryostat and the GS. Before filling,

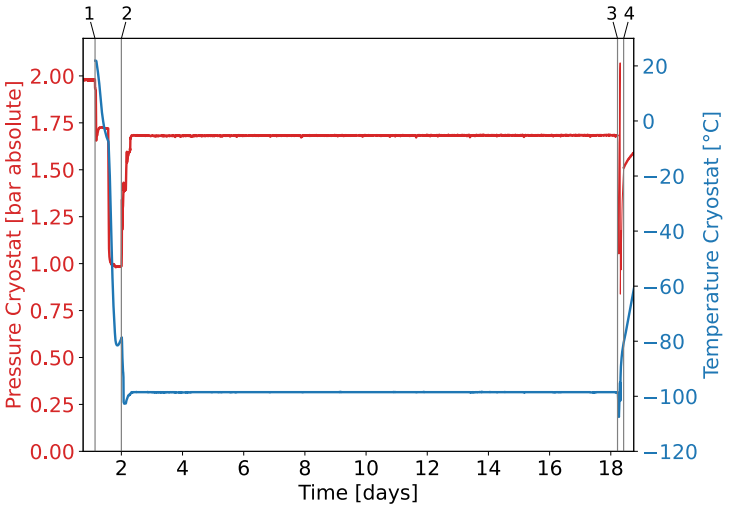

Figure 5.4: Evolution of the cryostat pressure and temperature during a ^{222}Rn measurement. The detector is pre-cooled (1) before additional LXe is filled (2). The measurement is conducted for several weeks during which the temperature and pressure are stable (2-3). It is terminated by the recuperation of the xenon (3), followed by warming up of the detector (4). Figure published in [P2].

the system is pre-cooled in two steps to a temperature of -107.5 °C (1). Additional xenon is then filled and liquefied to the system (2) and the recirculation is started. The system reaches a thermal equilibrium at a pressure of (1.68 ± 0.02) bar and a temperature of (-98.5 ± 0.02) °C. The measurement is carried out during the following weeks of stable operation (2-3). At the end of the measurement (3), the xenon is recovered into the storage cylinder. A residual GXe pressure of roughly 1.5 bar is recirculated in the system to accelerate the warming-up of the detector (4).

Data acquisition and processing

The analogue signals from both PMTs are extracted from the cryostat using a welded coaxial BNC feed-through to minimize the amount of electric noise. The signals are then fed into a custom-built amplifier which amplifies the voltage of each PMT signal by a factor of two and splits the output into two identical copies. The first branch is processed by an analogue trigger logic consisting of a discriminator module and a coincidence unit. Trigger signals are generated if both PMTs signals coincidentally exceed a threshold of -10 mV. The second branch is connected to two input channels of a CAEN V1724 card, which digitizes the PMT waveforms at a sampling rate of 10^8 samples per second and with a voltage resolution of 14 bit. Waveform digitization is triggered either by the analogue logic or by a similar coincidence requirement processed internally by the digitizer. The digitizer is read out using a custom-made software for which further details can be found in [186].

Figure 5.5 shows an example event waveform from a ^{83m}Kr decay after summation of both PMT signals. The two S1 signals (blue) are shown enlarged in the inset of the waveform. As expected from the decay scheme (right panel), the first S1 signal (32.1 keV transition) is quickly followed by a smaller S1 signal due to the delayed 9.4 keV transition. The two S1s are then followed by two S2s (red) that correspond to the charge signals from the two transitions. Note however, that for most events

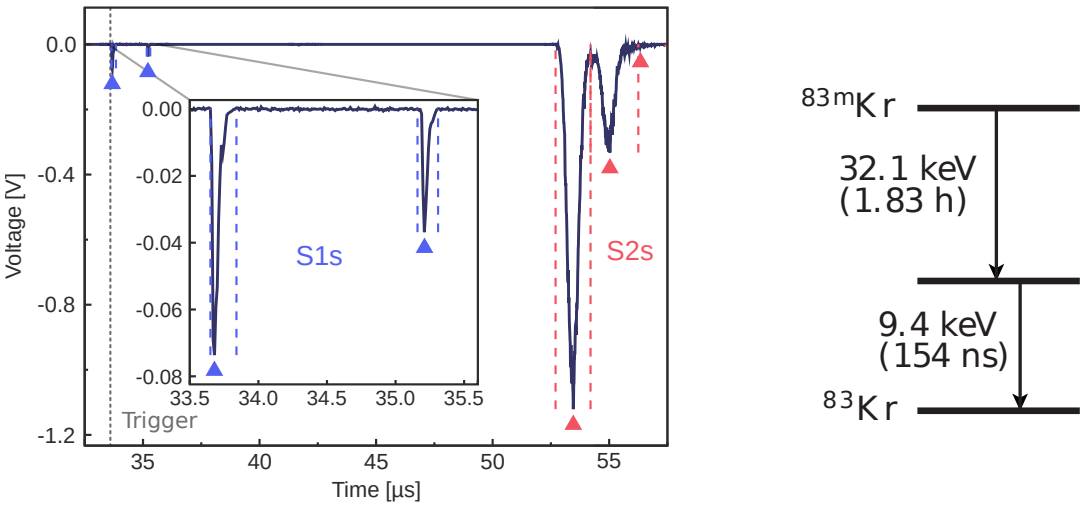

Figure 5.5: Example waveform of a ^{83m}Kr decay recorded in the HeXe TPC. The inset shows a zoom into the region of the two time delayed S1 signals (blue) which are followed by two S2 signals (red). The approximate trigger position (dashed gray line) coincides with the time of the first S1. A simplified version of the decay scheme of ^{83m}Kr is shown on the right of the figure [192]. Figure published in [P2].

the S2 signals have considerable overlap and cannot be resolved separately. Due to the low discriminator thresholds the digitization of an event is usually triggered by the first S1 peak in an event as indicated by the dashed gray line.

The relevant pulse parameters for the later analysis like area, time and width as well as the peak type (S1/S2) are determined from the digitized waveforms using the custom-built software described in [186, 195]. Peaks are identified as excursions from the baseline which exceed the event's baseline fluctuation by a factor of five. Based on their shape, each pulse is then classified as being either an S1 or S2 peak. As can be seen in figure 5.5, the S1 signals are well localized in time with a steep left flank that is followed by a right-hand tail, while S2 signals are much wider and have a more Gaussian shape. For a peak to be classified as an S1, its rise-time needs to be shorter than 200 ns and its width must not be larger than 500 ns, with the rise-time being the duration between the 10$^{\text{th}}$ and 50$^{\text{th}}$ area percentile of a peak and the width being the duration between the 10$^{\text{th}}$ and the 90$^{\text{th}}$ area percentile. A sufficient performance of these classification criteria was confirmed by inspection of several hundreds of event waveforms.

5.2 High-voltage components and software control

HV needs to be supplied to several components in the HeXe detector for its operation. The HV necessary for the operation of the PMTs is generated by a two-channel NHQ 203M module manufactured by iseg Spezialelektronik GmbH [196]. Both PMTs are usually operated slightly below their rated maximum operational voltage of -1 kV. The HV for the three electrodes in the detector is supplied by an

iseg NHR 42 60 module with a maximum output voltage of ±6 kV. Furthermore, this module provides for a high-resolution current readout with a precision of 50 pA [197]. This allows to detect potential connection failures between the FSRs and the cathode and gate electrodes by monitoring the small electrical current flowing through the interconnecting resistor chain. In the following, the feed-through and connector solution as well as the custom-made software used to monitor and control all HV related parameters are described.

5.2.1 High-voltage feed-through and connector

The dielectric strength of GXe is lower by a factor of four to five compared to dry air at the same pressure [198, 199], which increases the risk for HV break-downs. Since typical safe high voltage (SHV) components are rated up to a voltage of 5 kV in air, they were found to be unsuited for the application in the HeXe setup. Different feed-through solutions have been tested for their HV compatibility using a dedicated GXe-filled setup. A satisfying HV performance was achieved only after 10 kV rated SHV connectors were installed (see inset of figure 5.6). The xenon sided ceramic insulator of these connectors is approximately 2.5 cm long, which is roughly twice as long as for the 5 kV rated version. This helps to partially counteract the reduced dielectric strength and allowed to apply voltages of up to ±5 kV in the test setup. Three of these connectors were welded into a CF-40 flange and insulated by additional PTFE tubes to prevent arcing between the three connectors, as well as between the connector and the grounded stainless steel wall surrounding the feed-through. A picture of the feed-through is shown in the left of figure 5.6. This solution

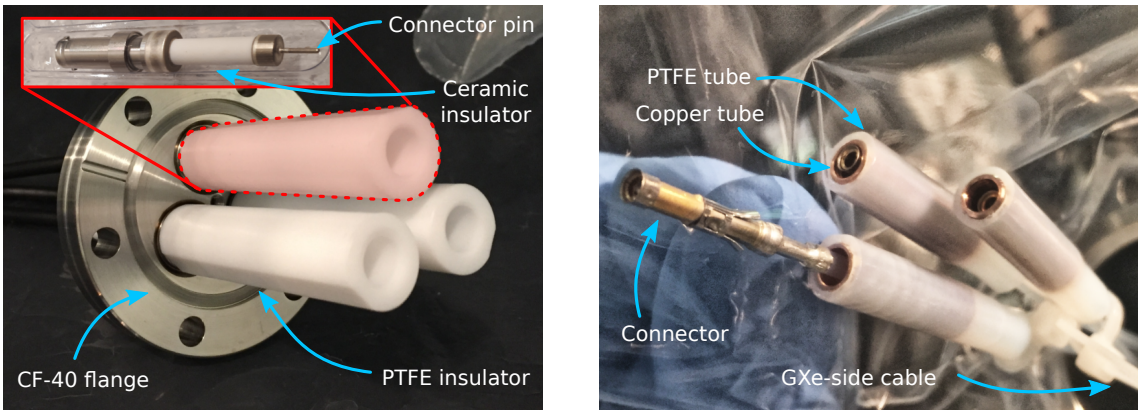

Figure 5.6: Left: Photograph showing the custom-built HV feed-through solution using the weldable connectors shown in the inset. They are rated for up to 10 kV (in air) which allows to tolerate the reduced dielectric strength of GXe. **Right:** Picture of the GXe side PTFE insulated electrode cables. The sharp edges of the connector are shielded by a copper tube which is surrounded by a piece of PTFE hose.

even allowed the temporary application of up to ±6 kV to the cathode and anode electrodes of the HeXe system during the measurements presented in chapter 7.

On the inside of the system, the PTFE insulated HV cables are attached to the small nickel pin at the tip of the ceramic insulator using a clamping connector. As shown in figure 5.6 (right) the connectors are covered by PTFE insulated copper tubes to avoid the high electric fields at the sharp edges of these connectors. The connection of the cable to the electrode is established by clamping the tip of the cable into the electrode holder frame with a screw (more details can be found in [100]).

5.2.2 Software for control of the high-voltage modules

For studies that require to scan over many different values of the drift field, adjustment and record keeping of the different voltages by hand becomes very impractical. Therefore, a Python software was developed that allows for a convenient monitoring and control of all HV-related parameters. The program continuously reads the voltages and electrical currents for each HV channel via the HV modules RS232 or USB interfaces using the `PySerial` [200] package. These values are then stored in the same `PostgreSQL` [194] database that contains the other slow-control parameters of the system [186]. They are also displayed on the program's graphical user interface (GUI) which was designed using the `PyQt5` framework [201].

Channel specific settings like the desired set voltage and ramp speed can be adjusted on separate tabs of the GUI for which an example is shown in figure 5.7.

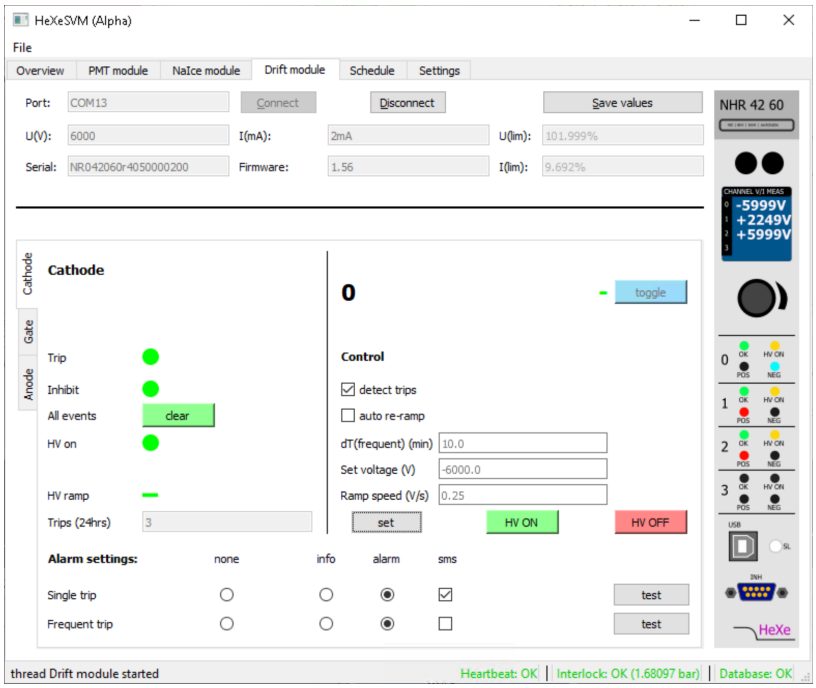

Figure 5.7: Screenshot of the graphical user interface of the developed software allowing to read out and control the HeXe high-voltage channels.

Despite the dedicated HV feed-through solution, HV break downs ("trips") still occur from time to time. In such a case, the electric current of the affected component quickly rises and exceeds the tightly set hardware limit. The HV module

will then immediately shut-off the supply voltage to this channel in order to prevent damage to the setup. In such a case, the software can issue E-Mail and/or SMS notifications to the HeXe operators. Furthermore, an automatized attempt can be made to ramp the channel back to its nominal voltage, if there was no previous trip of the same channel within a user-defined time interval. This feature has been especially useful before the improved HV feed-through has been installed and HV trips occurred more frequently.

Remote controlling the HV requires an interlock solution to prevent application of voltage as long as the system is not protected from accidental touch. By requiring an over pressure of at least 200 mbar in the cryostat, it can be ensured that the detector is fully closed, and HV bearing parts are not accessible anymore. Besides these safety relevant features, the program also offers the option to perform automatic voltage scans. For this a schedule containing the different electrode voltages, ramp speeds and holding times can be loaded and executed. This feature allows to perform field dependent studies with a high resolution of different fields. The optimal combination of electrode voltages for each field can be obtained from the electric field simulation described in the next section.

5.3 Electric field simulation

For the correct quantification of the electric field strength and its uncertainty, a detailed three dimensional detector model has been developed using the commercial software package COMSOL Multiphysics® [202]. The program allows to find a numerical solution for the scalar potential field $\Phi(\vec{r})$ for any point $\vec{r}$ within simulation volume. For this the volume is discretized into small tetrahedra and the finite element method (FEM) is applied. The distribution of the electric field $\vec{E}(\vec{r})$ can then be computed as $\vec{E}(\vec{r}) = -\nabla\Phi(\vec{r})$ [203].

Figure 5.8 shows a cut-away view of the used detector model for a median drift field of approximately 1.25 kV/cm. The absolute value of the drift field is shown by the orange color-scale along a central plane through the detector. The voltages applied to the different metallic components are indicated by the blue color-scale. Besides the three electrodes and FSRs, the model contains a detailed representation of both PMTs, as well as the HV cables for the electrodes.

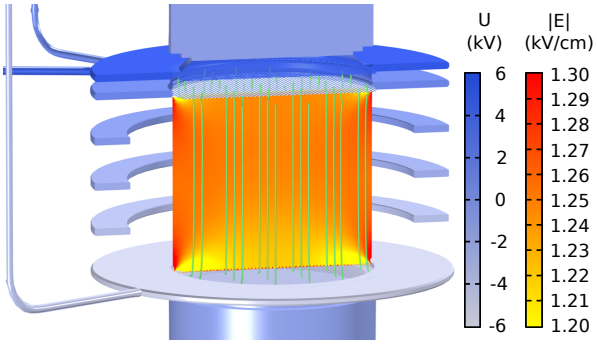

Figure 5.8: Three dimensional COMSOL model of the HeXe detector used for electric field simulation. Component voltages (blue) and absolute value of electric field (orange) are shown for a median drift field of 1.25 kV/cm. Figure published in [P2].

This section starts with a com-

parison between different electrode designs based on their transparency and the resulting homogeneity of the electric field. Afterwards, a superposition method is introduced which allows to considerably speed-up the computation of different fields.

5.3.1 Evaluation of different electrode designs

To allow for the detection of the xenon scintillation light by the PMTs and for the passage of electrons through the gate, the HeXe electrodes have a hexagonal mesh-like structure. However, this leads to a certain amount of "leakage" of the field between the two sides of each electrode. This leads to a less uniform electric field in the drift region of the detector. Therefore, the optical transparency of the electrode meshes needs to be balanced against the field non-uniformity caused by the field leakage through the electrodes.

Figure 5.9 sketches a section of a hexagonal shaped electrode mesh illustrating the two relevant geometric parameters p (short diagonal distance or pitch) and d (wire thickness). For an infinitely extended mesh, the mesh's transparency T can be approximated by the ratio of the uncovered surface A_{inner} inside of one cell to the surface A_{outer} of that cell (red hexagon),

$$T \approx \frac{A_{\text{inner}}}{A_{\text{outer}}} = \frac{p^2}{(p+d)^2} \,. \tag{5.1}$$

It should be noted however, that this geometric approximation does not account for the direction of the incoming light.

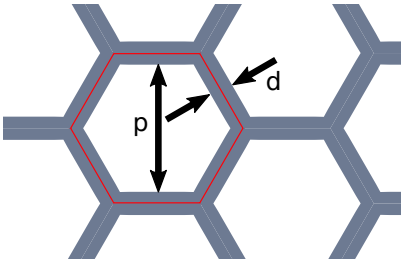

Figure 5.9: Section of a hexagonal meshed structure. The cell spacing or pitch p and the wire thickness d are labeled.

The dependence of equation 5.1 on the pitch and wire thickness is illustrated in figure 5.10. Selected transparency values are indicated

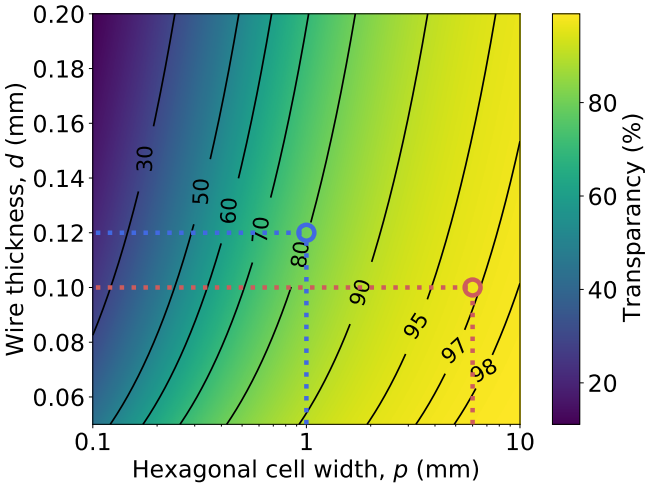

Figure 5.10: Transparency of hexagonal meshes as function of cell pitch p and wire diameter d. The transparency is estimated from the ratio between covered and open area using equation 5.1. The two corresponding grid options which are compared below are highlighted by blue and red circles.

by the black contour lines. Data from ^{83m}Kr decays has been acquired using two different sets of hexagonal electrodes with the HeXe system. The first one having a rather wide cell spacing of 6 mm with a wire thickness of 100 µm has an estimated transparency of 96.7% (red circle). The second set uses electrodes with a narrow pitch of only 1 mm and slightly thicker wires of 120 µm. Its transparency is estimated to be 79.7% (blue circle). Both have been acquired from the US company Great Lakes Engineering [204] where they have been produced via photo chemical etching from 0.1 mm thick stainless steel sheets. A subsequent chemical etching step was performed to improve their HV performance.

The homogeneity of the electric field has been evaluated using the COMSOL model for different combinations of the pitch and the wire thickness within an extended range of $p \in [1, 10]$ mm and $d \in [0.1, 1]$ mm [1]. Furthermore, the field homogeneity from electrodes made from parallel wires was studied. It is found that such electrodes can provide a slightly more uniform field compared to hexagonal electrodes of the same optical transparency. The reason for this is that the parallel wires block light only along one spatial dimension. This allows them to have a smaller wire pitch than a hexagonal electrode. For the HeXe setup however, electrodes with a hexagonal structure have been preferred due to their assumed higher mechanical stability.

Figure 5.11 shows a full comparison between the two types of hexagonal electrodes that have been tested in the HeXe setup. The results from the 6 mm and 1 mm pitched electrodes are shown in the left and right column respectively. The first row shows photographs of both electrodes.

The second row shows the absolute value of the simulated electric field distribution in the extraction and amplification region of the TPC. The PTFE support structure is shown in light gray, while the top PMT as well as the anode and gate electrodes are filled with a darker gray color. The liquid/gas interface is shown by the black line in between the anode and gate electrodes. As both media have different relative permittivities, the electric field is discontinuous along the phase transition. Below the steel body of the PMT the fused silica entrance window is visible, which is also included in the COMSOL model. As can be seen from the figure the field homogeneity in the extraction and amplification region is greatly improved when the electrodes with 1 mm pitch size are used.

The third row shows the simulated field distribution in the drift region as well as inside the full PTFE support structure. The electrode voltages for the simulation have been chosen to resemble a default configuration of the detector with a median applied drift field of approximately 400 V/cm as has been used for the studies presented in [100, 125]. Similar to the extraction region, also here the more narrow pitched electrodes lead to a clear improvement of the field homogeneity. Along the left side of both figures, local field distortions caused by the (non coaxial) HV connection cable can be seen. It is found to influence the drift field by less than 0.5%. Since the influence from a coaxial cable was found to be very similar, the mechanically more stable and less stiff non-coaxial solution was chosen.

[1] The effect of the sheet thickness on the amount of field leakage was found to be subdominant.

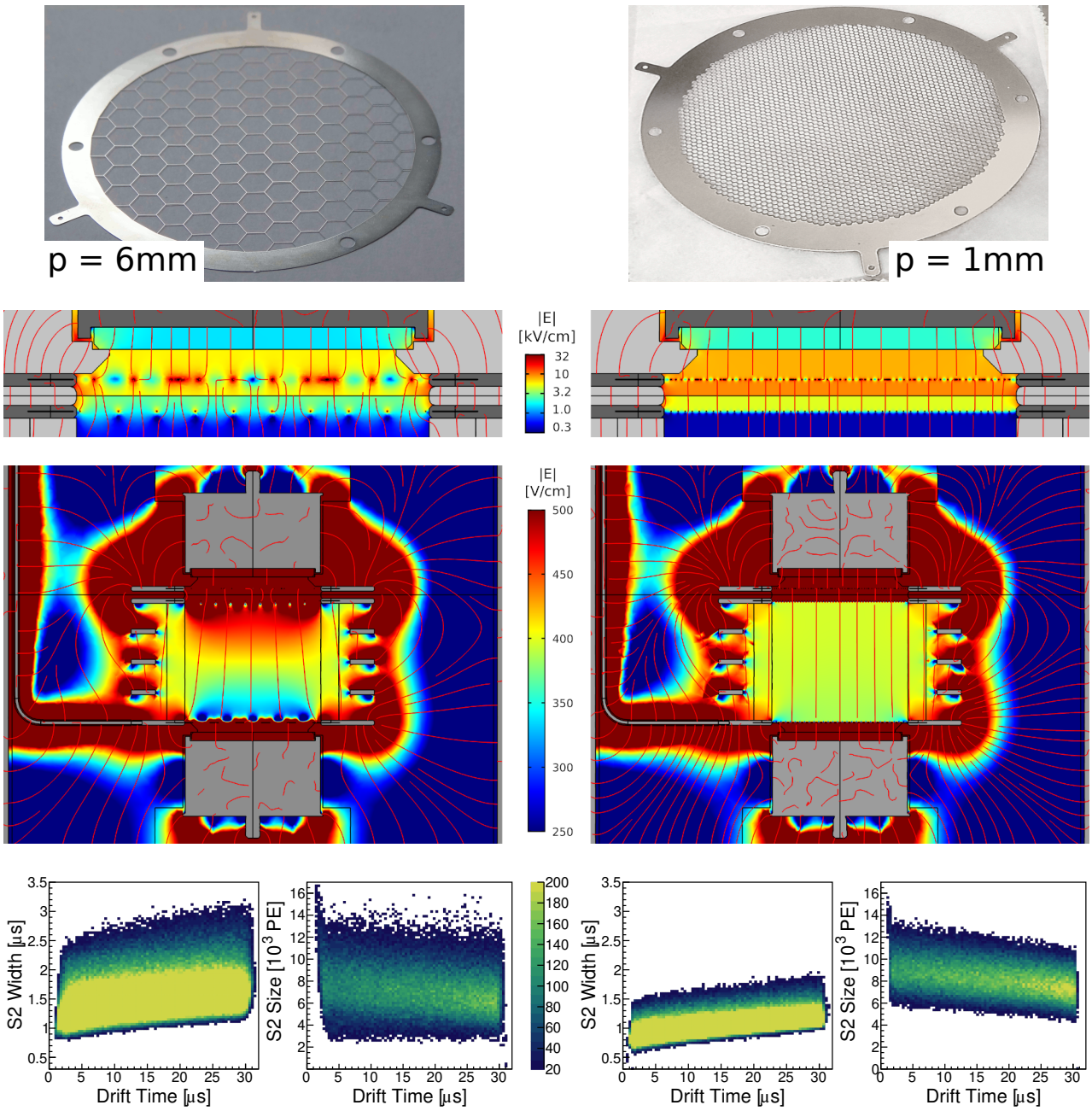

Figure 5.11: Comparison between hexagonal structured electrode meshes with pitch of 6 mm and wire thickness of 100 µm (left column) and pitch of 1 mm and 120 µm wire thickness (right column). **1st row:** Photograph of the etched electrodes. **2nd row:** Close-up of the simulated field in the extraction region of the HeXe detector. The logarithmic color scale represents the field magnitude. Components made from stainless steel and PTFE are drawn in dark and light gray respectively. **3rd row:** Overview of the field distribution inside the drift volume and the PTFE support structure. **4th row:** Distribution of the S2 width and S2 size as a function of the drift time for ^{83m}Kr data. The simulation and data correspond to a median electric drift-field of about 400 V/cm with -900 V and -950 V being applied to top and bottom PMT, and the anode, gate and cathode electrodes being at +3750 V, -5 V and -1950 V respectively. Figures previously published in [P2].

The last row of figure 5.11 compares the quality of S2 signals from ^{83m}Kr decays acquired with either set of electrodes. Further details on the selection of those events will be given in section 7.2.1. The left-hand panel in both columns shows the dependence of the S2 width on the drift time of the electron cloud in the LXe. The expected increase of the S2 width from the diffusion of the electrons during the drift is visible [2]. In the right-hand panel, the distribution of the observed S2 area as a function of the drift time is shown. The decrease of S2 size is due to the attachment of electrons to impurities in the LXe during the drift. It can be clearly seen that the distributions are much narrower and defined for both the S2 width as well as the S2 size in the case of the grids with smaller pitch size [205].

Figure 5.12 shows the differences in field homogeneity from the two different electrode types in dependence of the $z-$coordinate of the detector. The positions of the gate and cathode electrodes are indicated by dashed gray lines. The shown field configuration (approx. 400 V/cm), was chosen to match the one used in [100, 125] and shown in figure 5.11. The solid lines represent the median fields, while the shaded and hatched areas show the ranges of the central 68% of the field. In addition to the two previously compared electrodes (red and blue), the case in which the three electrodes are replaced by solid, non-transparent plates is shown (black). While the latter do not allow for passage of the scintillation light, such electrodes do not show any "field leakage". The remaining field in-homogeneity is then solely due to stray fields not compensated by the field cage. As can be seen from the figure, the more transparent electrodes (red) would lead to very significant distortions in the drift field, while the ones with narrow pitch (blue) show an excellent homogeneity.

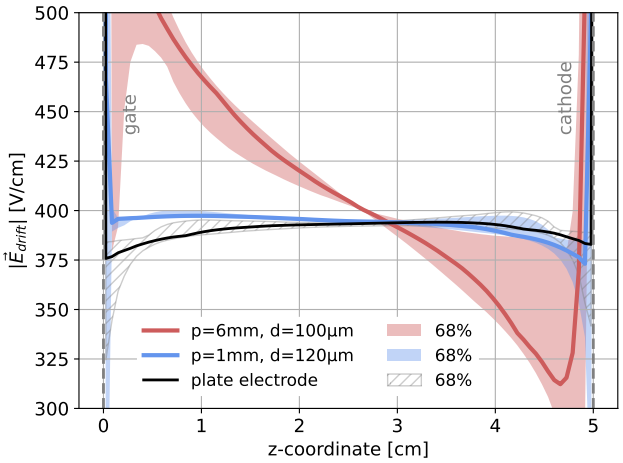

Figure 5.12: Simulated absolute value of the electric drift field in dependence of the $z-$coordinate. Two different hexagonal electrodes (red and blue) are compared with the field that would be produced by fully opaque plate electrodes (black). The shaded/hatched areas indicate the range of the central 68% of the field distribution. Figure previously published in [P2].

5.3.2 Superposition method and field optimization

The calculation of electric fields can be computationally expensive especially if a fully three-dimensional model is used. The computation can be sped up considerably when the superposition principle is used. It allows to compute the field by summing the fields of all individual electrical components [203]. To use this approximation, the electric field originating from each component at a potential of 1 V with all other components put to ground potential is computed. These field maps are then exported on a grid of $100 \times 100 \times 100$ points evenly spaced in (z, r^2, φ) throughout the detector volume. Afterwards, the field for any arbitrary voltage combination can be computed efficiently by multiplying the field of each component with the desired voltage and summing all the individual fields.

This method has been validated by comparison to a direct computation using COMSOL. For this, the reference field of 400 V/cm shown in figure 5.11 has been chosen. Figure 5.13 shows the absolute value of the relative difference between both methods in a r^2 vs. z map. The absolute value of the relative difference

$$\frac{|\Delta E|}{E_{\text{direct}}} = \left| \frac{(E_{\text{sup}} - E_{\text{direct}})}{E_{\text{direct}}} \right|$$

between the superposition method E_{sup} and the direct COMSOL evaluation E_{direct} is shown on the color scale. The points corresponding to the φ direction are averaged over in order to obtain a two dimensional map. The three electrodes are clearly visible in the difference map with the deviation reaching values up to 20% there. This is expected as the local field close to the thin electrode wires can become very large. The later analysis is carried out in the fiducial volume defined in section 7.2.1 and indicated by the dashed white lines in figure 5.13. Within this volume, the superposition approximation deviates at most by 2 *per mille*.

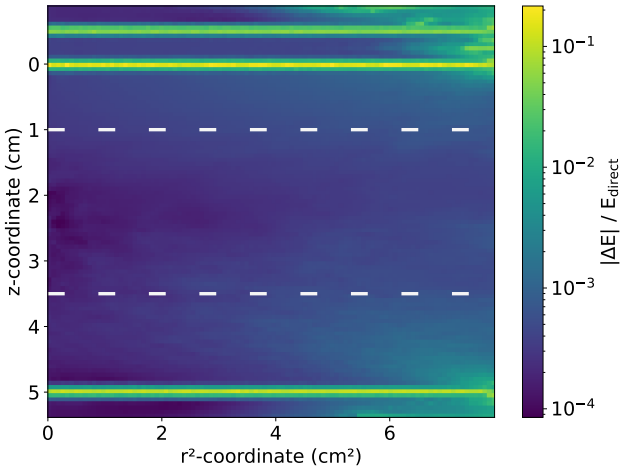

Figure 5.13: Relative difference between the result from the superposition method and a direct COMOSL simulation for a reference field of approximately 400 V/cm. Besides regions close to the three electrodes this approximation is found to deliver accurate results with the deviation within the fiducial volume (dashed white lines) being smaller than 2 *per mille*.

Optimization procedure

The fast computation using the superposition method allows to use an iterative optimization routine to find the combination of electrode voltages, which results in the least amount of field inhomogeneities. The L-BFGS-B algorithm from the `scipy.optimize.minimize` package [206] is used for the optimization, in order to respect the hardware limitations of the HV modules. The optimization is constrained to the drift field, since the field for amplification and extraction is kept constant in the later analyses presented in chapter 7. This is done by keeping a constant voltage difference between the gate and anode electrode of 3750 V resulting in an amplification field of approximately 10 kV/cm. Furthermore, the optimization is constrained to the same fiducial volume as is used in the later analyses.

Figure 5.14 shows the resulting optimal voltages for the cathode (green), gate (red) and anode (orange) electrodes needed to obtain a given median drift field (x-axis). The shown voltages are computed for 1000 values of the drift-field between

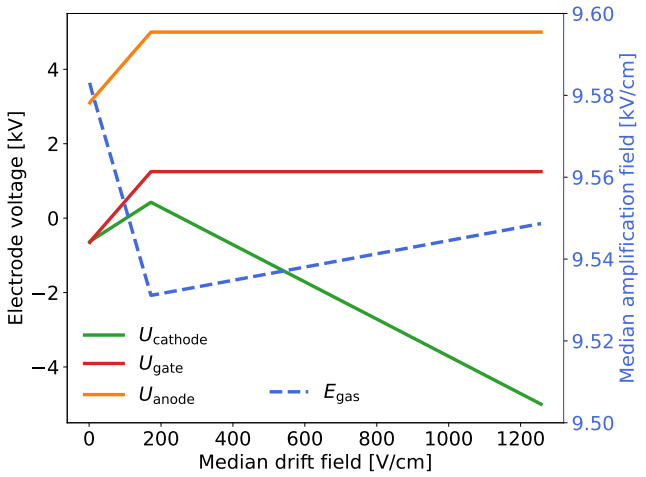

Figure 5.14: Optimal electrode voltages as a function of the desired drift field. Voltages of the top and bottom PMTs are set to -900 V and -950 V respectively. Shown in blue is also the median strength of the amplification field in the GXe phase.

0 V/cm and 1.25 kV/cm. For low drift fields close to zero V/cm the optimal cathode and gate voltages are close to the working potential of the bottom PMT (-950 V). For increasing fields, the cathode voltage becomes larger, such that it is effectively floating and the potential is defined by the bottom PMT. This prevents the high-field region usually present between the cathode and the bottom PMT. As soon as the anode reaches the set limit [2] of +5 kV at a drift field of $\sim$ 200 V/cm, the anode and gate electrode stay at a constant potential and the cathode voltage becomes lower in order to achieve higher drift fields.

Measurements of the LXe charge yield (see chapter 7) can be biased, if the extraction and amplification field does not stay constant while the drift field is being varied. Figure 5.14 shows how the value of the electric field in the GXe depends on the applied drift field (right blue scale). The slight decline of the field in the

[2] Due to the increased risk of electrical break-downs, the ±6 kV maximum voltage of the HV module are preferentially applied for limited duration and during normal working hours.

gas phase in the range for low drift fields can be explained by the increasing field between the anode and the top PMT. This field is directed in the opposite direction and therefore slightly reduces the field in the GXe. For drift-fields above 200 V/cm the anode voltage is not increased any further and the field above the anode stays constant. As the drift field increases, there is less "field leakage" from the extraction region into the lower field drift region. This leads to a slight increase of the amplification field. The overall variation of the amplification field is very small and of the order of 0.5%. Due to the linear dependence of the S2 signal size on the strength of the amplification field [207], this effect is small and can be neglected in the charge yield studies.

The size of the field inhomogeneities are quantified as the central 68% of the distribution of sampling points within the fiducial volume. Figure 5.15 shows how the relative deviation depends on the applied drift-field for the electrode with 6 mm pitch (red) and 1 mm pitch (blue). The relative uncertainty steeply increases for

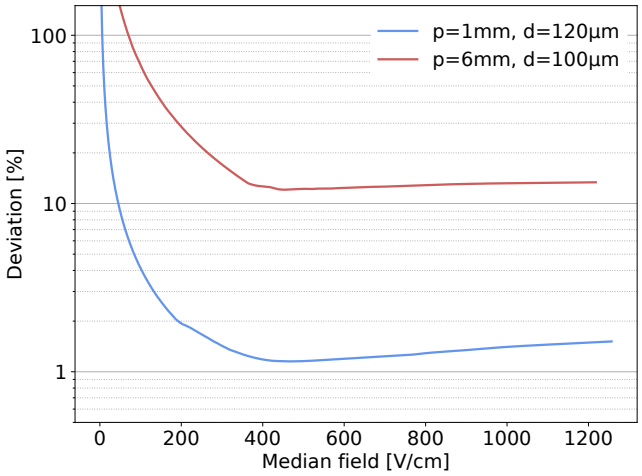

Figure 5.15: Expected amount of drift field deviation as function of the applied field for two different types of hexagonal electrodes. Figure previously published in [P2].

both electrode types in the regime of low drift fields due to the field leakage from the extraction and amplification region. In the case of the narrow pitched electrodes, the deviation is typically one order of magnitude lower than for the wider ones. The field homogeneity is best at a median drift field of about 460 V/cm. Here the field deviation of the 1 mm pitched electrodes show a minimum value of 1.2%. For higher fields, the deviation shows a slight increase up to 1.5% at 1.26 kV/cm. It is assumed that the increase is due to the increase of the reversed field between cathode and bottom PMT (see figure 5.14).

For all measurements discussed in the following chapters, all three electrodes of the HeXe detector were chosen to be with the narrow pitch (1 mm) to allow for the best possible field homogeneity.

5.4 Possible future upgrade of the detector

For future large-scale LXe detectors, background reduction will be very important. One promising method to reduce the radon induced background in such detectors using surface coatings has been presented in chapter 4. However, before such a coating can be applied, it needs to be validated that it does not diminish the chemical purity of the LXe (see section 4.4). The influence of novel PTFE surface cleaning methods on the LXe purity has been successfully tested in the past with the HeXe setup [100, 125]. For these tests, the attachment rate of electrons to impurities in the LXe is measured, as they drift upwards in the detector. Especially in the light of the unprecedented purity level achieved by the novel LXe purification technique (see section 1.2.1), an increase of the setup's sensitivity to this attachment rate will be required. This can be achieved for example by increasing the drift duration of the electrons [100]. Therefore, an upgrade of the drift length of the HeXe TPC from 5 cm to 10 cm drift length is being planned.

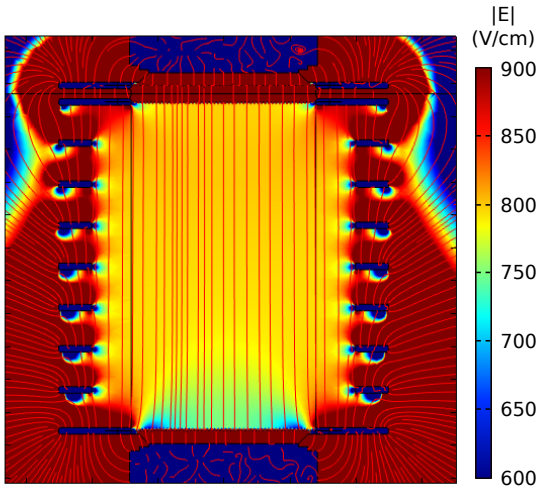

Figure 5.16: Electric field simulation of an potential upgrade for the HeXe TPC with 10 cm drift length. Result for a mean drift field of 800 V/cm with hexagonal electrodes using 1 mm pitch and 7 field shaping rings.

Figure 5.16 shows the simulated electric field for the detector with a drift length of 10 cm and hexagonal electrodes with a pitch of 1 mm. Since the described COMSOL model makes extensive use of parameters and parametric functions for geometric quantities like the drift length or the number of field shaping rings, it could be readily adapted for the upgraded geometry. The number of necessary FSRs was determined by varying their quantity in the simulation between 2 and 14 pieces in steps of two. It is found that for more than six FSRs only minor improvements can be expected, as the field distortions will be dominated by the "field leakage" through the semi-transparent electrodes. For the design it was therefore decided to use 7 FSRs, such that their distance stays the same as in the current 5 cm long version of the TPC. This will allow to re-use most of the parts from the current detector in the upgraded version.

6 Transmission of xenon scintillation light through PTFE

Polytetrafluoroethylene (PTFE) is a commonly used construction material for large-scale xenon dual-phase time projection chambers (TPCs) [51, 59, 208, 209]. It is mainly chosen because of its high optical reflectivity for xenon scintillation light. The reflectivity of PTFE has been measured in several studies and values as high as 100% were found depending on the surface finishing as well as the surrounding medium [210–213]. In the case of the XENONnT detector, most of the internal surfaces are made out of this material to increases the light collection efficiency (LCE). Despite this beneficial property, PTFE also has a large cross-section for (α, n) reactions [62]. Since the neutrons liberated in such reactions can mimic the interaction of dark matter particles, PTFE contributes to the background budget of experiments searching for dark matter via nuclear recoil (NR) interactions. Its total amount should therefore be minimized while maintaining the high reflectivity. Furthermore, the PTFE surfaces are needed to optically separate the detector volume from any additional liquid xenon (LXe) surrounding the active volume. If the PTFE enclosure is chosen too thin the detector performance might degrade due to light leakage between the two regions.

Such optimizations require knowledge of the transmission of vacuum ultraviolet (VUV) light through PTFE, for which no literature values existed in the past. A further motivation for such a study is the design of light attenuators needed for the measurement of alpha-particle interactions using the Heidelberg Xenon (HeXe) TPC which are presented in chapter 7. The photomultiplier tubes (PMTs) employed in the HeXe setup are very sensitive devices which enable detection of individual scintillation photons from the LXe target. Since typical alpha decay energies are in the MeV regime, the amount of scintillation photons from such events is very large [214]. These bright events can lead to signal distortions due to saturation. This can be caused for example by exceeding the dynamic range of the amplifier as well as the digitizer, but also due to charge depletion at the PMT base capacitors. Note that a software-based correction like the one described in [215] is not applicable as usually both PMTs are affected from saturation. Furthermore, prolonged exposure of the sensitive PMTs to high light intensities can lead to a sensitivity decrease due to aging effects [216].

For the design of these attenuators a dedicated measurement, also reported on in [P1], has been conducted. Data from two different setups are combined in this study, with the first one being a dedicated setup where the samples are in a gaseous xenon (GXe) atmosphere at room temperature. This setup allows to systematically investigate attenuation for many different values of the thickness. The results at

room temperature are compared to data acquired with the HeXe setup in LXe and GXe at cryogenic temperatures.

6.1 Transmittance of PTFE in gaseous xenon

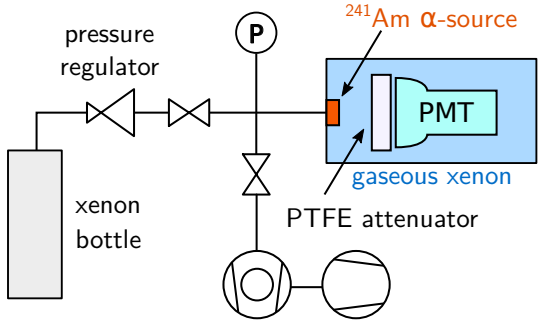

Figure 6.1: Sketch of the setup used to measure the transmission of xenon scintillation light through PTFE in gaseous xenon at room temperature. Xenon scintillation light is produced by the interaction of alpha-particles emitted from an ^{241}Am source with the xenon. Figure published in [P1].

Most data on the PTFE transmittance was acquired at room temperature using xenon scintillation light produced by the interaction of alpha-particles emitted by a 3.7 kBq ^{241}Am source. The used setup is sketched in figure 6.1 and consists of a 47 cm long GXe-filled stainless steel tube housing a Hamamatsu R11410-21 3-inch PMT. PTFE attenuator discs of six different thicknesses were then placed in front of the PMT window and the amount of transmitted scintillation light has been measured. The PMT and attenuator are fixed by three threaded rods which also ensure a constant distance of (14.0 ± 0.3) cm between the attenuator disc and the ^{241}Am source mounted on the top flange of the tube. The complete assembly, including an aluminum filler behind the PMT, is depicted in figure 6.2.

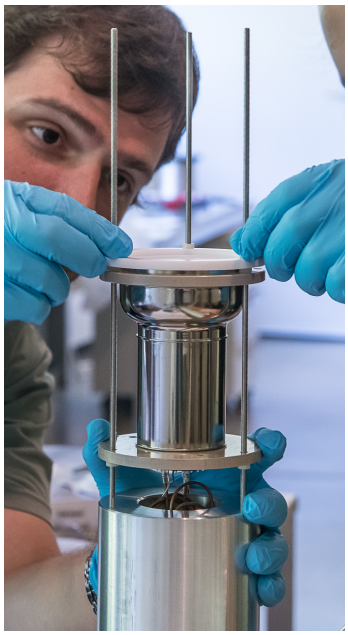

Figure 6.2: Photograph showing the assembly of PMT, aluminum filler and attenuator

The alpha particles with an energy of 5.6 MeV [76] produce xenon scintillation light at a peak wavelength of about 175 nm [55]. This is very similar to the emission wavelength of LXe [217, 218]. The produced VUV light is attenuated by some impurities typically present in ambient air like for example water vapor [58]. A changing impurity concentration between measurements would therefore lead to a bias in the estimated transmittance. To prevent this source of uncertainty, the attenuator discs were thoroughly cleaned using a detergent (ELMA CLEAN 65) and rinsed using de-ionized water. Afterwards they were wiped using ethanol and dried inside an air-tight vessel flushed with nitrogen at 200 SCCM at a pressure of about 50 mbar.

The PTFE discs were then stored in sealed plastic bags, filled with nitrogen at a slight overpressure, to prevent subsequent air exposure. To exclude further contamination of the discs during installation the setup was enclosed in a nitrogen-purged plastic glove bag. Additionally, a strictly timed schedule was followed for the installation, pumping and GXe filling of the setup, with variations being smaller than 2 minutes. To prevent correlation of time-dependent systematic effects with the measured PTFE thickness, the order in which the attenuators were measured has been shuffled according to the last column shown in table 6.1. An additional measurement without any attenuator in front of the PMT has also been carried out.

The investigated attenuator discs have been produced in two separate batches from virgin grade round PTFE material [219]. The first batch has been produced using a lathe with a steel back plate to support the PTFE sample. Material was then carefully removed from the surface until the desired thickness has been reached. This production mechanism was not suited for the production of very thin samples. Therefore, the second batch has been produced using a mill while the samples were fixed on a table by vacuum suction.

The attenuator thickness has been measured using a Mitutoyo ID-F150 digital dial gauge. Each attenuator was measured at 49 points evenly spaced in (r^2, φ) across the surface covering the PMT window. Table 6.1 reports for each attenuator the mean thickness as well as the observed standard deviation. Note that the samples produced using the vacuum suction support (batch 2), are on average, more homogeneous.

Table 6.1: Thicknesses of the used PTFE attenuators as measured across 49 different points spread over the disc surface. The two different production methods are indicated by the batch number. The order in which the attenuators have been measured is given in the last column. Table adapted from [P1].

Attenuator	Thickness [µm]	Production batch	Measurement
none	0	-	7
1	97 ± 2	2	1
2	283 ± 4	2	3
3	442 ± 6	1	5
4	737.6 ± 1.3	2	6
5	965 ± 4	1	4
6	1310 ± 30	1	2

Data analysis of the room temperature transmittance measurements

Signals from the PMT were recorded for exactly five minutes for each of the attenuators. The pulses were digitized using the HeXe data acquisition (DAQ) system

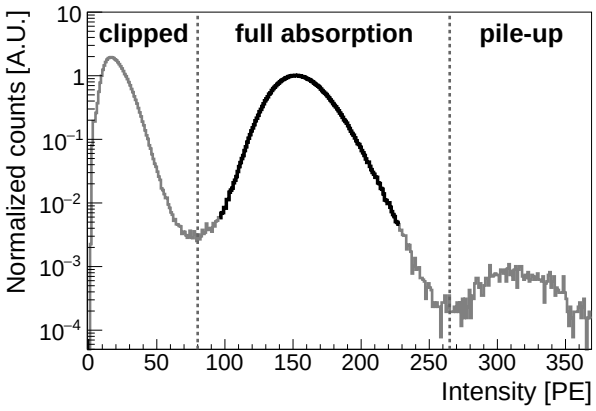

Figure 6.3: Full spectrum as recorded for the attenuator of thickness 0.3 mm.

and processed as detailed in section 5.1 and in [186, 195]. Figure 6.3 shows the distribution of the resulting pulse areas for the 0.3 mm thick attenuator. The spectrum of each measurement features three distinct populations which are detailed in the following.

Full absorption events occur when the full energy of the alpha particles is deposited in the xenon. Using the "stopping and range of ions in matter" (SRIM) code [121], the average range of the 5.6 MeV alpha particles in GXe at a pressure of 1100 mbar is determined to be 2.1 cm.

For the measurement of the transmittance, only this category of events is used. They are selected as the region in which the spectrum maintains at least 1% of the peak's height (black bins in figure 6.3).

Clipped track events are located in the low intensity part of the spectrum. Their area is typically found to be lower by about 25% with respect to the full absorption peak area. These events are caused by alpha particles which are partially absorbed by the source holder. Figure 6.4 shows the ^{241}Am source inside its aluminum holder ring attached to the vessel flange. The actual activity is visible as a slightly darker region of 5 mm in diameter across the source surface. The 1 mm thick holder ring has an opening diameter of about 1 cm.

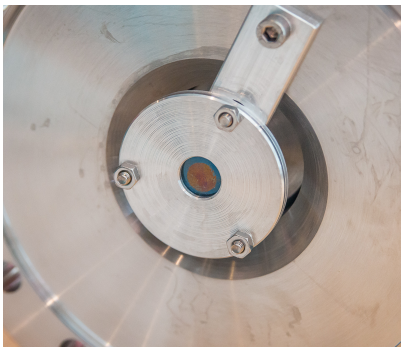

Figure 6.4: Picture of the ^{241}Am source in its source holder, attached to the CF-100 flange of the test setup. The actual size of the active surface is visible by its slightly darker color.

Alphas emitted from the source under shallow angles can hit the source holder and deposit only part of their energy in the GXe, which results in less bright scintillation signals from these events. This hypothesis

is investigated with a simulation of the energy deposition of alpha particles in the setup.

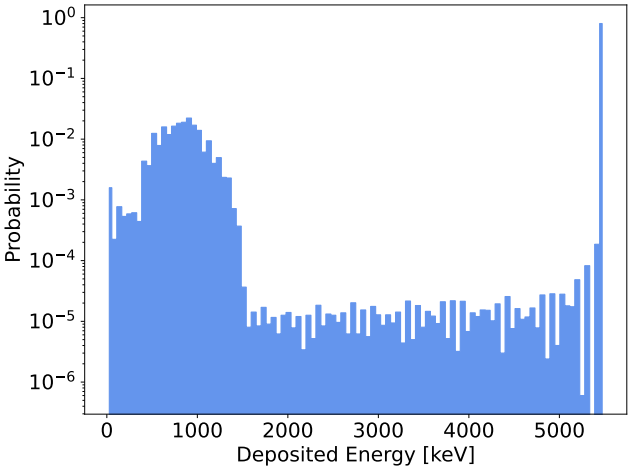

Figure 6.5: Simulated distribution of the deposited alpha particle energy in the setup. The low energy contribution is due to alpha tracks which deposit part of their energy in the source holder. The large peak at 5.6 MeV corresponds to the tracks with full energy deposition in the xenon.

Figure 6.5 shows the resulting simulated distribution. The simulation was done using SRIM to generate alpha tracks in GXe which were then shifted and rotated to approximate an isotropic emission from the ^{241}Am source. The resulting distribution shows the amount of energy deposited by the particles before being absorbed by the source holder. It can be seen, that approximately 20% of the tracks are expected to not deposit their full energy of 5.6 MeV in the xenon. The tracks which are absorbed by the source holder, deposit on average only approximately 1 MeV. Both observations agree qualitatively with the measured distribution of the light shown in figure 6.3.

Pile-up events can occur when two or more ^{241}Am decays happen close in time to each other. In these cases, their PMT pulses are overlapping and cannot be resolved separately by the data processor. They result in a single pulse with an area corresponding to the sum of both individual pulses. For cases where both underlying events were from the full absorption category the resulting pile-up peak is located at twice the area of the full absorption peak in the spectrum. This was confirmed by investigation of several waveforms from events falling into this region.

The collection of full absorption regions for all measured attenuators is shown in figure 6.6. A two-sided Gaussian function is fit to the data in order to extract the mean position. It has the form:

$$f(x) = N \cdot \begin{cases} e^{-\frac{1}{2}\left(\frac{x-\mu}{\sigma_1}\right)^2} & x < \mu \\ e^{-\frac{1}{2}\left(\frac{x-\mu}{\sigma_2}\right)^2} & x \geq \mu \end{cases}, \tag{6.1}$$

where μ is the mean position, $\sigma_{1,2}$ are the left and right-sided standard deviation and

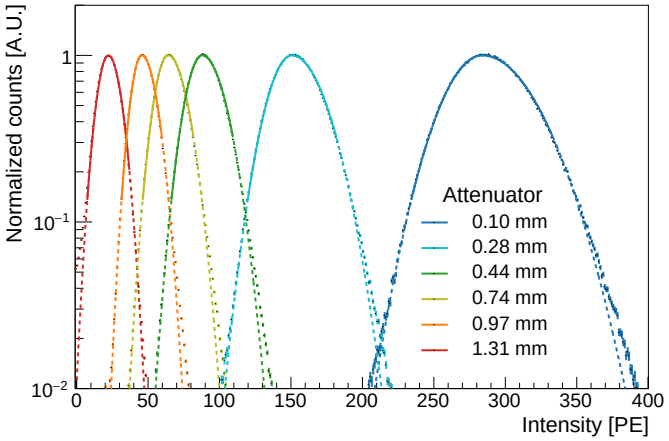

Figure 6.6: Collection of the full absorption peaks for all measured attenuators. Data is normalized such that the maximum of each peak equals to one. Solid lines indicate the fit of the data with a two-sided Gaussian function as given in equation 6.1. Figure published in [P1].

N is a scaling factor, chosen to be unity for the presentation in figure 6.6. Possible reasons for the asymmetric shape of the full absorption peak are dependencies of the light collection efficiency with the orientation of the alpha track as well as event pile-up between full absorption events and clipped tracks. First, a preliminary manual fit is done to obtain initial values for the parameters $\sigma_{1,2}$. These are then used to constrain the range of the final fit to the interval between $[\mu - 2 \cdot \sigma_1, \mu + 2 \cdot \sigma_2]$, as indicated by the solid lines in figure 6.6. The continuation of the fit function outside this range is indicated using dotted lines.

The uncertainty on the measured light level μ contains the statistical uncertainty due to the number of events as well as several systematic uncertainties. Variations in the distance between the ^{241}Am source and the attenuator surface would impact the detected light level by a different illumination of the PTFE surface. The possible variation of that distance amounts to 3 mm as this is the clearance between the holding structure of the PMT and the opposite flange (see figure 6.2). This translates to an uncertainty on the measured light level of about 4% as estimated using an optical GEANT4 [130] simulation of the setup. Though care was taken to mitigate outgassing of impurities from the samples a slight decrease of the detected light level has been observed throughout each measurement. This is illustrated in figure 6.7 for the measurement carried out with the 0.1 mm thick attenuator. A linear function (red) is fit to the mean profile of the data (black markers) and used to correct the detected intensity to its value at the beginning of the measurement ($t = 0$). Despite this correction, a remaining uncertainty of approximately 0.7% needs to be taken into account. It arises from the $\Delta t = 1$ min time variations between filling of the setup with GXe (i.e. start of the outgassing) and the start of the DAQ ($t = 0$). Also the PMT high voltage (HV) is only controlled down to a precision of $\Delta U = 1$ V. Since the PMT gain varies strongly with the applied HV, the resulting uncertainty is estimated to contribute with 0.6%. Finally the impact of the range in which the two-sided Gaussian function is fit to the data is estimated by varying that range within $\pm 1\sigma ... \pm 3\sigma$. This results in a variation of the inferred value of μ of 1.5%. The GXe

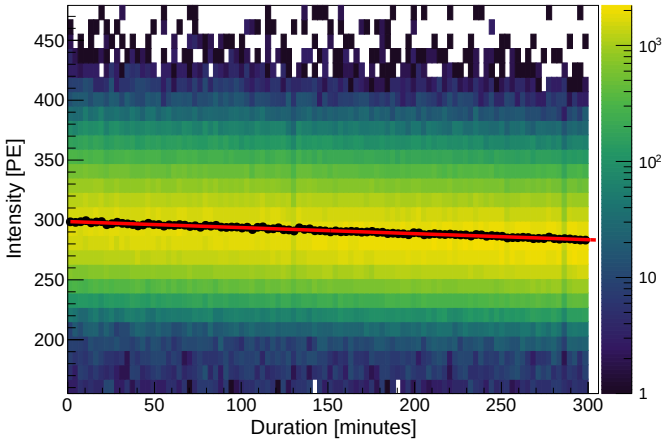

Figure 6.7: The outgassing during each measurement causes a slight decrease of the light yield. The mean profile of the distribution (black markers) is fit with a linear function (red), which is used to correct for that decrease.

pressure varied by approximately 0.6% in between the measurements. The impact on the xenon scintillation yield however is expected to be negligible [220]. Therefore, it is not considered in the uncertainty.

The extracted data from the room temperature measurement are further analyzed to conclude on the transmittance of PTFE in section 6.3.

6.2 Transmittance of PTFE in liquid xenon

The room temperature measurements are complemented by a study of the transmittance inside a xenon dual-phase TPC. Two measurements have been carried out in which different attenuators were installed in front of the top and bottom PMT of the HeXe setup which is introduced in section 5.1. Table 6.2 lists the different attenuators together with their measured thickness as well as the location in the TPC they have been installed at.

Table 6.2: Thicknesses of the PTFE attenuators used in the HeXe setup for studies on the VUV transitivity of PTFE under operational conditions in a liquid xenon TPC. Table published in [P1].

Attenuator	Measurement	PMT	Phase	Thickness
1	a	top	GXe	175 µm
2		bottom	LXe	550 µm
3	b	top	GXe	3.3 mm *
4		bottom	LXe	700 µm

* Attenuator with inhomogeneous thickness due to a pinhole with a diameter of 300 µm.

After their installation the normal schedule of the measurement was followed as is described in [100, 186]. For these measurements, the gaseous ^{222}Rn introduced in

section 5.1.1 was used. The scintillation light produced by the alpha particles in the LXe is then partially transmitted through the bottom and top attenuator discs and detected by the PMTs. The LCE describes the probability with which the PMTs detect these photons and is typically dependent on the location of the interaction in the detector (see also figure 7.9). Bias from this dependence is avoided by a tight selection on the drift time of the events, such that only the central 2 mm of the drift volume are selected.

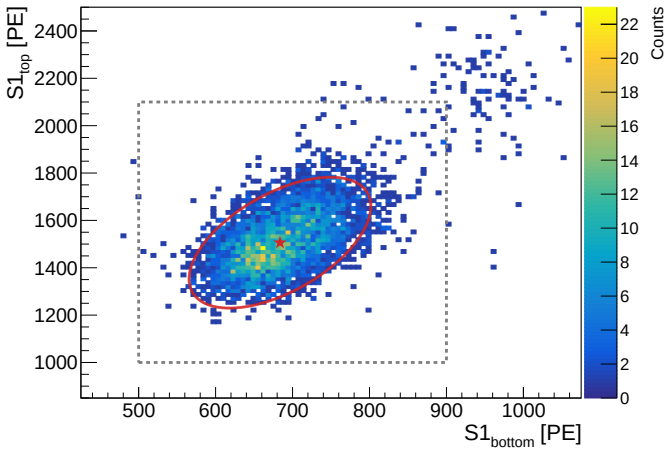

Figure 6.8: Amount of light detected by the bottom PMT as a function of light seen in the top PMT for ^{222}Rn alpha events. Shown is data from measurement *a* given in table 6.2. Figure published in [P1].

Figure 6.8 shows the amount of light detected by the top PMT as a function of the light seen in the bottom PMT for data from measurement *a* listed in table 6.2. The red ellipse shows the fit of the data with a two-dimensional Gaussian function for events falling inside the gray dashed box. This function is used to determine the mean amount of detected light $LY^{\mathrm{HeXe}}(\mathrm{Rn})_{i=\{t,b\}}$ in the top (t) and bottom (b) PMT (red star). The relative attenuation factor $\gamma_{i=\{t,b\}}$ for the PTFE attenuators can then be computed as

$$\gamma_i = \left[\frac{LY^{\mathrm{HeXe}}_{\text{with attenuators}}(\mathrm{Rn})}{LY^{\mathrm{HeXe}}_{\text{no attenuators}}(\mathrm{Rn})} \right]_{i=\{t,b\}} . \tag{6.2}$$

This requires a measurement of the ^{222}Rn light level without the attenuators being present. As mentioned in the introduction such a measurement cannot be done precisely in the HeXe setup due to saturation. Therefore, the unattenuated light level of alpha events needs to be estimated differently.

The light level from $^{83\mathrm{m}}$Kr $LY^{\mathrm{HeXe}}(\mathrm{Kr})_{i=\{t,b\}}$ can be measured without saturation and the need for attenuators. This value is then scaled by the ratio between the light yield of $^{83\mathrm{m}}$Kr and ^{222}Rn as observed in the XENON100 experiment [150]. In the larger detector saturation effects are usually less severe and can be corrected for. The light yield for $^{83\mathrm{m}}$Kr was extracted from [221], whereas for ^{222}Rn the values reported in [214] have been used. The resulting ratio between the light level from

both sources in the XENON100 detector is

$$LY^{\mathrm{XE100}}(\mathrm{Kr})/LY^{\mathrm{XE100}}(\mathrm{Rn}) = 173 \pm 4\,, \tag{6.3}$$

where the uncertainty is estimated as the inaccuracy from reading-off of the values.

Besides the attenuation the presence of the PTFE discs also changes the LCE in the HeXe detector due to their high reflectivity. This necessitates one further correction factor which accounts for the altered photon detection probability between the ^{222}Rn and $^{83\mathrm{m}}$Kr measurement in the HeXe setup. In order to evaluate this effect the optical simulation described in [186] is employed, allowing to evaluate the probability $P_{i=\{t,b\}}$ of photons to hit either of the two PMTs for the case of an attenuator being present or not. For this, the attenuation inside the PTFE is switched off in the simulation to only account for the effect of altered LCE due to the reflection. The reflectivity of PTFE is also dependent on whether it is surrounded by GXe or LXe [210–213]. For the attenuator in front of the top PMT (GXe) a reflectivity of 76% is assumed as has been determined from the room temperature data (see section 6.3). Whereas for the reflectivity of the bottom attenuator (LXe), a value of 96% as reported in [213] is taken. Both values have been varied by ±30% in the simulation, such that values reported in the literature [210] are covered. Additionally, the impact from the assumed reflectivity of the stainless steel meshes, as well from changes in the height of the liquid level were investigated and added to the systematic uncertainty of the measurement. The effect of the latter tow, however, is found to be subdominant. The attenuation factor γ_i is then multiplied by the ratio of these probabilities to account for this effect:

$$\gamma_i = \left[\frac{LY^{\mathrm{HeXe}}(\mathrm{Rn})}{LY^{\mathrm{HeXe}}(\mathrm{Kr})}\right]_{i=\{t,b\}} \cdot \left[\frac{P(\text{no attenuators})}{P(\text{with attenuators})}\right]_{i=\{t,b\}} \cdot \frac{LY^{\mathrm{XE100}}(\mathrm{Kr})}{LY^{\mathrm{XE100}}(\mathrm{Rn})}\,. \tag{6.4}$$

6.3 Results of transmittance measurements

The transmittance of PTFE is measured by evaluating the amount of transmitted light for each attenuator as a function of the attenuator thickness. This is shown in figure 6.9 for the data collected in the room temperature setup (purple markers) as well as for the measurement using the HeXe setup (orange and green markers).

For the data acquired at room temperature the mean amount of light transmitted through each PTFE attenuator is given by the parameter μ of the two-sided Gaussian fit function. The size of the error bars in the x-direction represents the measured variation of the attenuator thickness as listed in table 6.1 whereas the size of the y error bars includes the sources of uncertainty discussed in section 6.1. Two different models are found to be in agreement with the obtained data. The first one describes the observed attenuation by a Beer-Lambert law (red line), which is modified in order to account for the possibility of a light leak in the setup. The second model

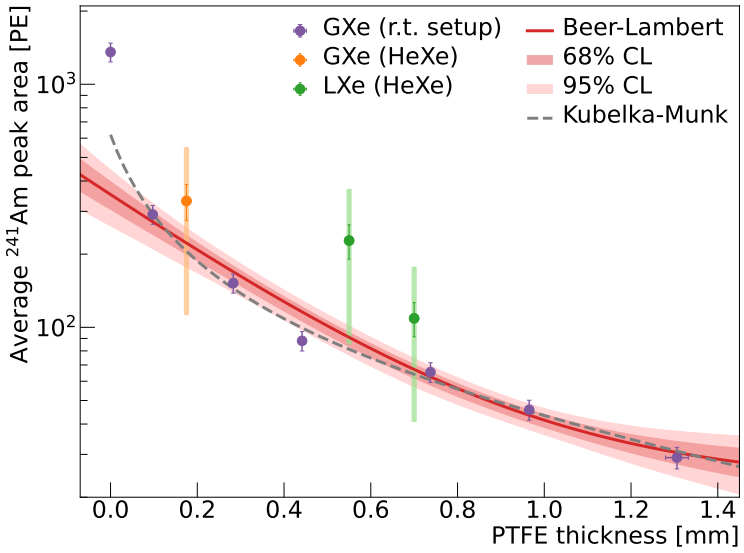

Figure 6.9: Resulting plot with fit of transmission of PTFE for xenon scintillation light. The red line indicates a fit to the data with the modified Beer-Lambert law while the dashed gray line indicates the fit with the *two-flux* model. Figure adapted from [P1].

(gray dashed line) considers light scattering within the medium and is referred to as the *two-flux* model after Kubelka and Munk [222, 223].

Modified Beer-Lambert law

Neglecting the Fresnel reflection at the surface of the attenuator, the thickness dependence of the transmitted intensity $I(d)$ can be explained by a modified Beer-Lambert law, given as

$$I(d) = A \cdot e^{-\frac{d}{\lambda_t}} + B\,, \tag{6.5}$$

where λ_t is the transmission coefficient and A describes the amount of transmitted light through an infinitely thin attenuator. The additional constant B needs to be introduced to sufficiently describe the data. It is attributed to a small light leak allowing a constant amount of light to bypass the attenuator disc without being attenuated by the PTFE. Its size is estimated to be (23 ± 6) PE. Using this model the transmission coefficient of PTFE is determined to be

$$\lambda_t = \left(350\,^{+60}_{-0}\,(\text{sys}) \,\pm\, 50\,(\text{stat})\right)\,\mu\text{m} \tag{6.6}$$

The statistical uncertainty of $\pm 50\,\mu$m reflects the uncertainty from thickness variations of the PTFE discs, as well as the uncertainty on the light level.

The systematic uncertainty needs to be added to account for the non-collimated

illumination of the attenuators. As the light is produced by an alpha source, the xenon scintillation photons are emitted isotropically from the interaction region. Some of these photons get reflected on the stainless steel surface of the vessel and reach the PTFE surface at non-perpendicular incidence angles. The amount of material traversed by these photons before reaching the PMT is larger than the attenuator thickness itself. This effect has been evaluated using an optical simulation of the room temperature setup [224]. In this simulation the light is produced isotropically and homogeneously within a 2.1 cm large hemisphere centered around the ^{241}Am source. The reflectivity of unpolished stainless steel for the VUV scintillation light is assumed to be 30% as estimated by extrapolation of the values reported in [225]. This results in an increase of the average traversed thickness by of a factor of 1.16 which translates to an increase of the measured attenuation length by 16%. For the highest reported values of the reflectivity of stainless steel of 57% [226] and the conservative assumption of purely specular reflection, an increase by a factor of 1.47 is found, which corresponds to the reported asymmetric systematic uncertainty of $+60\,\mu$m [224].

Figure 6.9 also shows the light level observed in the measurement without any attenuator present in front of the PMT. As can be seen it is significantly higher than the light level predicted from extrapolation of the Beer-Lambert law to an attenuator thickness of zero. This difference is explained by the Fresnel reflection at the front of the PTFE which reduces the amount of light being available for transmission if an attenuator is present. Since the model does not include this reflection, this datapoint has been excluded for the determination of the transmittance. By comparison of the fit value for $A = (330 \pm 50)$ PE and the measured intensity without attenuator the reflectivity of the used PTFE can be estimated to be around 76%.

The figure also shows the data points from measurements in the HeXe TPC setup (orange and green markers). Note that the 3.3 mm thick attenuator installed in front of the top PMT during measurement b was omitted due to its inhomogeneous thickness. To compare the TPC data with the ones from the room temperature setup, the observed attenuation factors $\gamma_{i=\{t,b\}}$ are multiplied by the light level of the room temperature setup (parameter A from the Beer-Lambert fit). The solid error bars of these points reflect the statistical uncertainty of the fit as shown in figure 6.8, whereas the shaded error bars indicate the spread of the systematic uncertainty discussed earlier. The three data points agree within their combined systematic and statistical uncertainty with the fit function from the room temperature data.

Two-flux model (Kubelka-Munk)

The so-called *two-flux* model based on Kubelka and Munk [222, 223] can be used to describe light propagation and attenuation in intensely scattering media. For the following discussion, a one-dimensional model is chosen in which the light propagation is described by two light fluxes going either in the positive or negative direction. Figure 6.10 shows a sketch of the problem. The light fluxes at any position x inside the medium of thickness d are referred to as $f_{\pm}(x)$. The quantities λ_{scatter} and λ_{atten} are the effective attenuation and scattering lengths of the medium respectively. The problem is then described by the coupled system of differential equations as shown below:

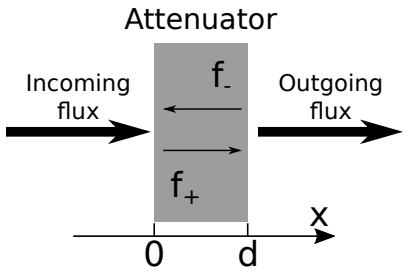

Figure 6.10: Sketch of the two-flux model describing light propagation in intensely light scattering media.

$$\begin{aligned}\frac{d}{dx}f_+(x) &= -\left(\frac{1}{\lambda_{\text{atten}}} + \frac{1}{2\lambda_{\text{scatter}}}\right) f_+(x) + \frac{1}{2\lambda_{\text{scatter}}} f_-(x) \\ \frac{d}{dx}f_-(x) &= \left(\frac{1}{\lambda_{\text{atten}}} + \frac{1}{2\lambda_{\text{scatter}}}\right) f_-(x) - \frac{1}{2\lambda_{\text{scatter}}} f_+(x)\,. \end{aligned} \tag{6.7}$$

The following conditions can be imposed onto the light fluxes entering the medium at the left and right boundaries:

$$\begin{aligned} f_+(0) &= A \\ f_-(d) &= 0\,. \end{aligned} \tag{6.8}$$

As for the modified Beer-Lambert law, any reflection directly on the surface is neglected and the light flux entering the attenuator from the left is given by A. The second condition ensures that no light is entering the attenuator from the right hand side, meaning that no light is being reflected backwards into the PTFE from the PMT window. The boundary value problem is then solved numerically using the Python `scipy` [206] package to determine the light flux reaching the PMT ($f_+(d)$). The model is then fit to the data of the room temperature setup yielding the following parameters [227]:

$$\begin{aligned} A &= (620 \pm 180)\,\text{PE} \\ \lambda_{\text{scatter}} &= (44 \pm 18)\,\mu\text{m} \\ \lambda_{\text{atten}} &= (30 \pm 30)\,\text{mm}\,. \end{aligned}$$

The evaluation of this function is indicated by the gray dashed line in figure 6.9 showing good agreement with the data. As can be seen the attenuation length is

not well constrained by the measured data. It is found to be much larger than the maximum thickness of the tested attenuators leading to a weak handle onto this parameter. An independent measurement has been carried out around the same time, in which thicker PTFE pieces have been investigated [63]. They find a good agreement between their data and the one obtained in this work and derive values for $\lambda_{\text{scatter}} = (52 \pm 6)\,\mu\text{m}$ and $\lambda_{\text{atten}} = (40 \pm 2)\,\text{mm}$ after combining the data from both studies.

6.4 Summary and discussion

In this chapter, a measurement of the transmittance of PTFE to xenon scintillation light has been presented. This material is a common choice for the construction of LXe TPCs due to its high reflectivity for VUV light. To meet the stringent background requirements in future large-scale experiments it is required to minimize the amount of PTFE in the detector while maintaining its optical properties. Therefore the previously unmeasured transmittance of PTFE to xenon scintillation light is an important material property for the design of future large-scale LXe TPCs.

The transmittance was studied using two setups. Most measurements were carried out in a dedicated setup operated at room temperature in a GXe atmosphere. These data are complemented by additional measurement using the HeXe setup which allowed to test the transmittance under real operating conditions inside a dual-phase LXe TPC. Both measurements are found to be in agreement within their uncertainties. A sufficiently accurate description of the observed light attenuation as a function of the PTFE thickness using two different models is shown. The first one is a Beer-Lambert law which has been extended to account for a constant light leak in the setup. The second one is a *two-flux* model which accounts for both attenuation and scattering of light inside the PTFE. An independent study [63] shows good agreement with the values extracted from this model.

The results from this study have been furthermore used as input for the design of the light attenuators for the HeXe setup. They were a necessary addition allowing the measurements of alpha interactions in LXe that will be detailed in the next chapter.

7 Study of alpha and electron interactions in liquid xenon

Detector simulations have become an essential ingredient for the design, modeling, and event reconstruction of liquid xenon (LXe) detectors. A commonly applied simulation tool for this is the "Noble Element Simulation Technique" (NEST) framework [228, 229]. For the correct modeling of the underlying physical processes, it relies on input from dedicated measurements. Especially in the regime of electric drift fields $\lesssim 50\,\mathrm{V/cm}$, however, only little data exists in the literature. As large-scale xenon time projection chambers (TPCs) continue to fall behind their design goals with respect to their electric fields [230], an improved understanding of this low field regime becomes relevant. Profiting from the enhanced electric field homogeneity in the Heidelberg Xenon (HeXe) setup (see chapter 5), measurements of the interactions of alpha particles and electrons have been carried out over an extended field range between $7.5\,\mathrm{V/cm}$ up to $1\,640\,\mathrm{V/cm}$.

The first measurements concern the electron drift velocity in LXe, which is important for the reconstruction of the z-coordinate of an interaction in the detector. This is followed by a study of the ionization and scintillation response of LXe to low energy electrons and alpha particles. Especially for the latter, the available data in the literature is very scarce [231, 232]. The results in this chapter are also published in [P2].

7.1 Measurements of the drift velocity in liquid xenon

One of the strengths of the dual-phase xenon TPC technology is the ability to reconstruct the three-dimensional position of the events. As detailed in section 1.2.1, their $x-y$ positions are reconstructed by the distribution of secondary scintillation light (S2) seen by the photomultiplier tubes (PMTs) at the top of the detector. The S2 signal is delayed with respect to the spontaneous scintillation signal (S1) by the time the electrons take to drift from the interaction point to the liquid/gas interface. While in vacuum the applied drift field would constantly accelerate these electrons, in LXe they move at a constant average velocity due to their interactions with the xenon atoms. From the time difference between both signals the $z-$coordinate of an interaction can be reconstructed if the drift velocity v_d of the electrons is known. Its dependence on the strength of the applied drift field is, therefore, an important input for the event reconstruction in such detectors.

In this section, two measurements of the electron drift velocity are presented using the HeXe setup. The first one was done with electrons produced in the interaction of alpha particles from the ^{222}Rn source in an electric field range between 7.4 V/cm up to 1 642 V/cm and at a LXe temperature of (174.4±0.2) K. Its results are found to be in agreement with a second measurement at a similar temperature which uses events from the decay of ^{83m}Kr and covers a field range from 13.5 V/cm to 1 245 V/cm. The low field regime (< 100 V/cm) has been emphasized in both measurements by a more narrow spacing between the investigated field values in that region.

7.1.1 Method to determine drift velocity

The drift velocity is extracted by dividing the geometric distance Δz between the cathode and gate electrode by the time Δt which the electrons need to drift between both electrodes:

$$v_d = \frac{\Delta z}{\Delta t} = \frac{|z_{\text{cathode}} - z_{\text{gate}}|}{|t_{\text{cathode}} - t_{\text{gate}}|} \,. \tag{7.1}$$

From the design of the HeXe TPC, the distance between both electrodes at room temperature amounts to $\Delta z^{\text{RT}} = (50.0 \pm 0.3)$ mm, with the uncertainty being from the machining precision according to the DIN ISO 2768-m norm [233]. At the liquid xenon temperature, this distance is slightly less because of the thermal contraction of the components. Using the (linear) thermal expansion coefficient for polytetrafluoroethylene (PTFE) of $\alpha_{\text{PTFE}} = (113 \pm 3) \times 10^{-6}$ 1/K as reported in [234], the drift length in the cold state can be calculated to be

$$\Delta z^{\text{LXe}} = \Delta z^{\text{RT}} \cdot (1 - \alpha_{\text{ptfe}} \cdot \Delta T) = (49.3 \pm 0.3)\, mm \,. \tag{7.2}$$

For stainless steel, thermal contraction is much lower ($\alpha_{\text{steel}} \approx 10 \times 10^{-6}$ 1/K) [235], and can therefore be neglected.

The different methods by which the drift duration of the electrons between both electrodes is measured are explained in the two following paragraphs.

Identification of electrodes using alpha events

The bright S1 scintillation pulses that are produced by the interaction of the alpha particles lead to the release of electrons from the stainless steel surfaces of the electrode meshes via the photoelectric effect. These electrons are released in time coincidence with the S1 signal. They then drift towards the extraction and amplification region where they produce small S2 signals. As shown in figure 7.1, both electrodes show up as clear peaks in the drift time distribution of S2 signals with areas less than 25 photoelectrons (PE). Shown in the insets are the enlarged regions close to the gate (left) and cathode (right) electrodes. The position of the gate electrode is estimated by fitting the data with a Gaussian function. For the cathode, a Gaussian function can be used only for fields larger than 17 V/cm, while for smaller

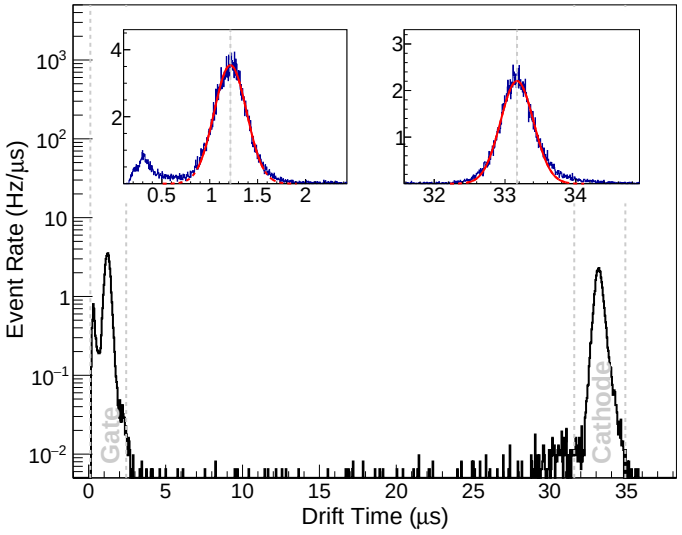

Figure 7.1: Identification of high-voltage electrodes in the HeXe setup using data from alpha interactions. Electrons are released from the stainless steel surfaces of the electrodes by the photoelectric effect, causing an accumulation of events at their positions. The insets show zoomed-in versions of the histogram for the gate region (left) and the cathode region (right). Figure published in [P2].

fields the position is determined using the mirrored Crystal-Ball (CB) function as defined in the appendix (see equation D.2). Both fits are repeated 20 times while the bounds of the fit region are varied within $[\pm 1\sigma, ... \pm 2\sigma]$. The uncertainty of the electrode positions is determined from the maximum variation of the fitted mean values.

Identification of electrodes in ^{83m}Kr data

Due to the lower decay energy of ^{83m}Kr, the S1 signals from these events are less bright and therefore the photoelectric effect is less pronounced. The time positions of the electrodes are therefore extracted differently in this case. To select good ^{83m}Kr events, their characteristic decay signature and the distribution of scintillation light among both PMTs is used (see also section 7.2.1). The upper-left panel of figure 7.2 shows the distribution of events for the full drift region of the HeXe TPC. Since less electrons can be drifted upwards from below the cathode electrode, its position coincides with a steep decrease of the event rate, as indicated by the red line. As has been done in e.g. [236], this point is determined using the (negative) derivative of the event distribution, which is shown in the lower-left panel of figure 7.2. The peak position is then determined using the `TSpectrum` class [237] of the `ROOT` data analysis framework [238].

In the right panel of figure 7.2, the S2 area of ^{83m}Kr events from the top part of the detector is shown. The S2 signal is strongly correlated with the electric field at the interaction site (see section 7.2). As can be seen from figure 5.11, the electric field in the LXe strongly increases at the transition between drift and extraction region. This transition is also visible in the mean S2 size (pink data points), which is fit by an appropriately scaled sigmoid function (cyan line) as defined in appendix D.2. The position of the gate electrode is inferred from the inflection point of this function and its uncertainty is taken from the statistical uncertainty of the fit.

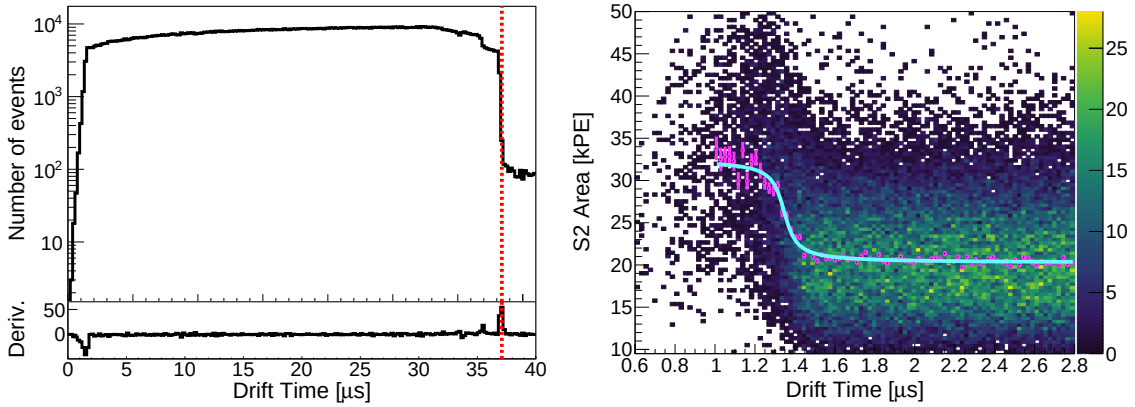

Figure 7.2: Method for electrode identification in data acquired with the ^{83m}Kr source for a drift field of approximately 425 V/cm. **Left:** Event rate distribution (top) and its negative derivative (bottom). The cathode position is determined by the steep decrease of the event rate (red line). **Right:** The position of the gate electrode is determined via the decrease of the S2-size due to the different electric fields in the drift region and the region above the gate electrode.

7.1.2 Results and comparison with literature data

With the electrode times as derived above, the drift velocity is computed for each applied drift field using equation 7.1. Figure 7.3 shows the resulting data obtained from alpha interactions using the ^{222}Rn source. Note that for the electron drift velocity only the vertical component E_z of the electric field is relevant and shown on the x-axis of the figure. The gray error bars indicate the range of the central 68% of the distribution of this component, as described in section 5.3. An important difference is that, for the drift velocity measurement, a fiducial volume selection cannot be applied since the electrons drift through the full height of the TPC. Therefore, the uncertainty on the field becomes larger. The error on the drift velocity is too small to be visible in the figure. It includes the variation from the fitting of the

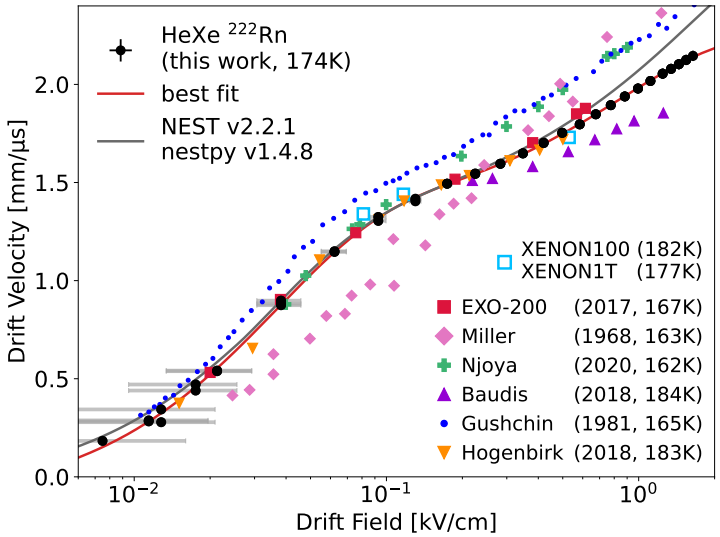

Figure 7.3: Drift velocity of electrons in liquid xenon as a function of applied drift field. Liquid xenon temperature of 174.4 K. A comparison with the drift velocity determined using the ^{83m}Kr data is shown in figure 7.5. Figure published in [P2]. Data is made publicly available at [239].

electrode positions as well as the uncertainty on the geometric distance. Furthermore, the measurement of each field has been repeated at different times of the data taking campaign. For most fields these additional points are however not visible, as they fall exactly on top of each other. An exception of this is the measurement at 13 V/cm, where the data quality was found to be significantly reduced in one of the two measurements, possibly related to charge-up following a high voltage (HV) breakdown.

The dependence of the drift velocity v_d as a function of applied drift field E_z is fit with the phenomenological function

$$v_d(E_z) = A_1 \cdot e^{-E/B_1} + A_2 \cdot e^{-E/B_2} + C\,, \tag{7.3}$$

which is based on the function used in the NEST framework [228]. The result is indicated by the red line and the values of the fit parameters $A_{1,2}$, $B_{1,2}$ and C are reported together with the ones from the ^{83m}Kr data-set in table 7.1. Shown by

Table 7.1: Fit parameters from ^{222}Rn and ^{83m}Kr data for the drift velocity of electrons in liquid xenon. Values are reported together with their statistical uncertainty. Table published in [P2]

Parameter	^{83m}Kr	^{222}Rn	Unit
Temperature	173.41 ± 0.11	174.4 ± 0.2	K
A_1	-1.38 ± 0.02	-1.458 ± 0.013	mm/µs
A_2	-0.95 ± 0.13	-0.95 ± 0.02	
B_1	38.0 ± 1.8	34.7 ± 1.2	V/cm
B_2	1000 ± 300	830 ± 70	
C	2.33 ± 0.15	2.27 ± 0.04	mm/µs

the dark gray line is the drift velocity predicted by the NEST [228, 229] simulation framework. Good agreement with the present measurement for fields below $\lesssim 700$ V/cm is found, while for higher fields the NEST model yields significantly larger drift velocities. Additional drift velocity measurements which were reported by the EXO-200 [97], XENON100 [150], and XENON1T [108] experiments as well as from dedicated setups [236, 240–243] are shown for comparison. Though there is an overall reasonable agreement, the different data sets show systematic differences. This is not unexpected, since there is a known temperature dependence of the drift velocity (see e.g. [241]).

A qualitative evaluation of this dependence is illustrated in figure 7.4. It is based on a combination of the present measurement and the data available from the literature. For each data set, the drift velocities at six different fields are shown in different colors. In cases where no measurement is reported at the selected field, a value is obtained from interpolation between neighboring data points. The dashed

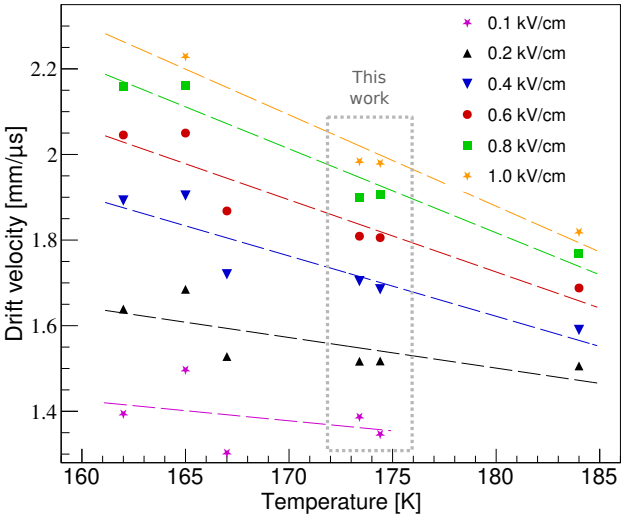

Figure 7.4: Electron drift velocity as function of the LXe temperature for different drift fields [244]. Shown data originates from this work as well as from literature measurements. Figure published in [P2].

lines show a linear fit of the data to visualize the general decrease of the drift velocity as the LXe temperature increases. This generally agrees with the observations made in e.g. [243, 245]. The proportionality of the electron mobility ($\mu_e = v_d/E_z$) with $T^{-2/3}$ as proposed in [241] however, is found to be incompatible with the steep increase of the velocity for low temperatures and fields above 600 V/cm. Figure 7.4 also shows that the measurements from this work (gray box) close a rather wide temperature gap in the measurements from the literature. Since this roughly coincides with the LXe temperature in the XENONnT experiment (177 K, see section 2.1.3), they are of special interest.

Figure 7.5 shows a comparison between the drift velocity that has been measured with the ^{83m}Kr source (red ▲) and the one from ^{222}Rn alpha particles (blue ▼). For

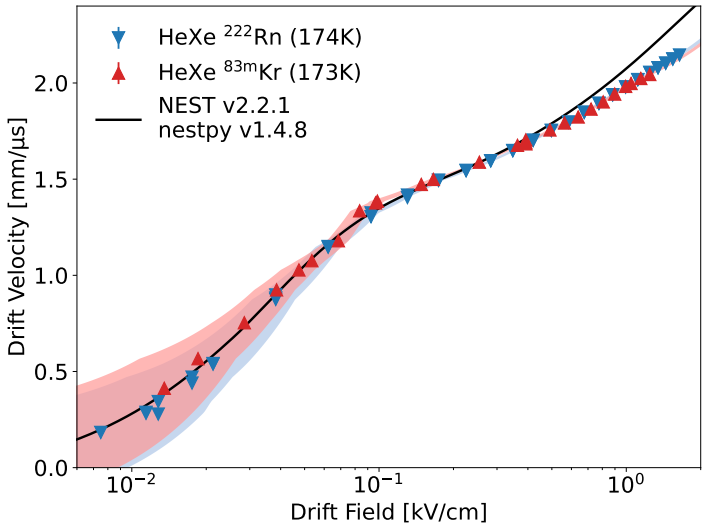

Figure 7.5: Comparison between the measured electron drift velocity in LXe as measured using the ^{222}Rn data (blue ▼) and the ^{83m}Kr data set (red ▲). In addition the prediction of the NEST [228, 229] simulation framework is shown by the black line.

better visibility, the horizontal gray error bars indicating the systematic variation of the drift field are replaced by the colored bands. The black line indicates again

the drift velocity predicted by the NEST simulation framework for the average LXe temperature of both measurements. Despite the different radioactive sources and analysis methods, both measurements are found to be in good agreement with each other.

7.2 Field dependence of the light and charge yield in LXe

The generation of the scintillation light and ionization charge in LXe is a highly complex process, which has been subject to extensive studies in the past and present [191, 232, 240, 246–248].

Boiled down to its essential components, the process can be expressed as sketched in figure 7.6, with three main channels in which deposited energy can be dissipated in the LXe. First, it can lead to a direct formation of excited xenon atoms (cyan arrow), which decay via the formation of excited dimers (Xe_2^*). In the decay, they emit scintillation photons at a wavelength of 175 nm [55], that can be registered as the S1 signal by the PMTs. Additionally, the interactions can lead to the production of free electron-ion pairs via ionization (orange arrow). The electrons can be drifted away from the interaction site by the applied electric field and lead to the production of the S2 signal. If electrons are not removed fast enough, they can recombine with the xenon ions (bent arrow), which gives rise to additional scintillation photons by the formation of excimers in the recombination process. This recombination process leads to an anti-correlation between the amount of light (S1) and charge (S2) signal as a function of the electric field and the ionization density of the interaction. The numbers of produced scintillation photons n_γ and electron-ion pairs n_e are related to the deposited energy E_{depos} via

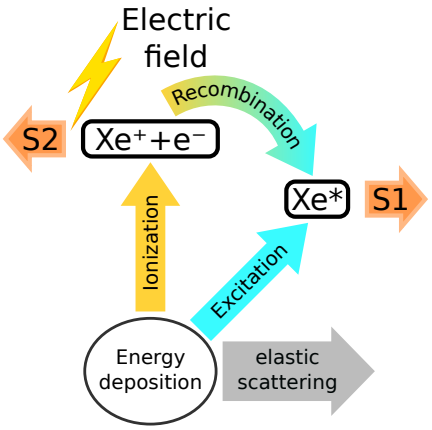

Figure 7.6: Sketch of the anti-correlation between the charge (S2) and spontaneous scintillation (S1) signal in LXe TPCs (highly simplified).

$$E_{depos} = W \cdot (n_\gamma + n_e)\,. \tag{7.4}$$

Where $W = 11.5\,\text{eV}$ [249, 250] corresponds to the average xenon excitation energy. It is the mean amount of energy needed to produce a single detectable quantum in the LXe. This relation neglects the fraction of the interaction energy which is dissipated as heat via elastic scattering (gray arrow). A more complete account of the xenon micro physics can be found for example in [251]. In this section, a measurement of

the field dependent charge and light response of LXe for alpha particles and electrons is presented.

7.2.1 Data selection and signal correction

The selection of high-quality events is important for a reliable estimation of the S1 and S2 signals size. For both radioactive sources, different selection criteria and signal corrections are necessary, which are detailed in the following.

Basic event selection criteria

The large energy of the alpha particles emitted by ^{222}Rn and its decay products, leads to bright S1 light signals in the LXe. Therefore, these events can be efficiently selected by requiring an S1 area between 400 PE and 1500 PE. This rejects the low-energetic background from beta and gamma interactions (see also figure 7.11). Furthermore, event pile-up is suppressed by demanding that any secondary S1 needs to be smaller than 8 PE. Following the main S1 peak, at least one S2 peak must be found in the event, while any secondary S2 peak must be smaller than 250 PE. The latter criterion helps to avoid double scatter events along the z-direction.

High quality events from the decay of ^{83m}Kr are best selected by their characteristic signature of two subsequent S1 signals (see figure 7.7 and example waveform in figure 5.5). For this, the largest S1 in the event is required to have an area between 40 PE and 400 PE and needs to be followed by a smaller S1 signal with an area larger than 20 PE and smaller than 200 PE. This selection is illustrated in figure 7.7 for ^{83m}Kr S1 signals at a field strength of approximately 400 V/cm. The smaller

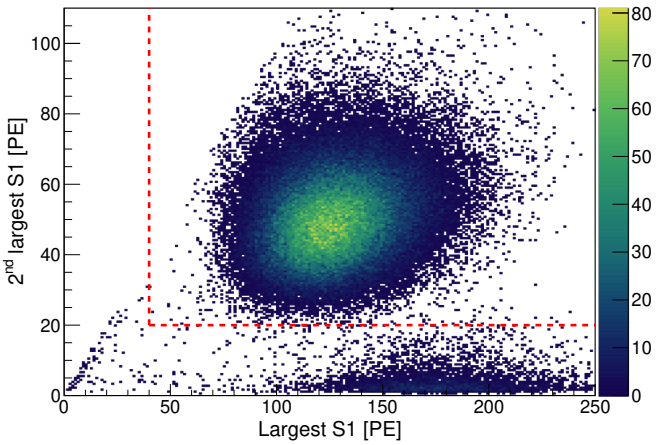

Figure 7.7: Events from the decay of ^{83m}Kr in the space of largest S1 and second-largest S1 at a median electric field of approx. 400 V/cm. The applied criterion to select the time-coincident double S1 topology is indicated by the dashed red lines. The population below the horizontal red line at values of around 175 PE, corresponds to the merged 41.5 keV signal. Figure published in [P2].

S1 needs to be then followed by an S2 with an area between 5 kPE and 100 kPE. Previous studies [252, 253] found that the light yield from the 32.1 keV and 9.4 keV transition of ^{83m}Kr is dependent on the time delay between the two signals. To avoid this correlation, a minimum time difference between both S1 peaks of 300 ns is required.

For both sources, the relative amount of the S1 light detected by the top PMT (area fraction top, AFT) is used to reject non-physical events. Such events can be caused by an incorrect pairing between the S1 and S2 signals. Since the two transitions of ^{83m}Kr events happen at the same location in the detector, it can be required that the AFT of both S1 signals agrees within ±20%. This is not possible for radon alpha events, where only accidental matches between S1 signals from below the cathode and S2 signals out of the drift region can be removed. Due to the opacity of the cathode electrode, the top PMT typically detects less than 10% of the S1 light from such events, which is used as the selection threshold. Furthermore, the increase of the S2 signal width due to the diffusion of the electron cloud during the drift is used as a selection criterion (see also left panels in the fourth row of figure 5.11). Good events are selected from the central 80% of the drift time dependent width distribution.

At very low fields ($E < 20\,\mathrm{V/cm}$), a slight increase of the data quality with time is found. This manifests by an increase of the resolution in the cathode position, as well as an increased statistics in the radon events. Therefore, only the second half of the measured intervals are considered for fields below 60 V/cm.

Fiducial volume selection

Two additional criteria are applied to constrain the possible locations of events to the central part of the detector (fiducial volume), where the electric field is most homogeneous. For the z-coordinate, this is done via the drift time and the field-dependent drift velocity as determined in section 7.1. From the full drift length of 50 mm, only the interval between 10 mm<z<35 mm is selected. Systematic effects due to this choice are evaluated by repeating the analysis in the upper (10 mm<z<22.5 mm) and lower (22.5 mm<z<35 mm) half of that volume.

Though the x- and y-position of the events cannot be reconstructed in the HeXe TPC, an approximate radial selection is still possible. This is done via the S2 AFT value, which features a characteristic double-peak structure as illustrated in the right panel of figure 7.8. It is caused by the small inclined PTFE pieces used to fix the PMTs as well as a wedge located at the outer radius of the detector (see figure 5.11). They lead to a reduced AFT value for S2 signals produced at large radii.

This has been confirmed using the optical detector simulation detailed in [186] as is illustrated in the left panel of figure 7.8. It can be seen that events from the center of the TPC ($r^2 \lesssim 2\,\mathrm{cm}^2$) feature large S2 AFT values, while it is significantly decreased for the ones at large radii ($\gtrsim 6\,\mathrm{cm}^2$). From the simulation it becomes evident, that a projection of the events onto the S2 AFT axis leads to a similar double-peak distribution as is observed in data (right panel of figure 7.8). Note, however, that the comparison is qualitative only, as the optical parameters, for example the PTFE reflectivity, have not been matched between the simulation and the detector. The required minimum S2 AFT value of 0.565 for the events is indicated by a dashed red line in the right panel of figure 7.8. Possible systematic effects from this criterion are evaluated by variation of this value within the range of 0.555 to 0.575.

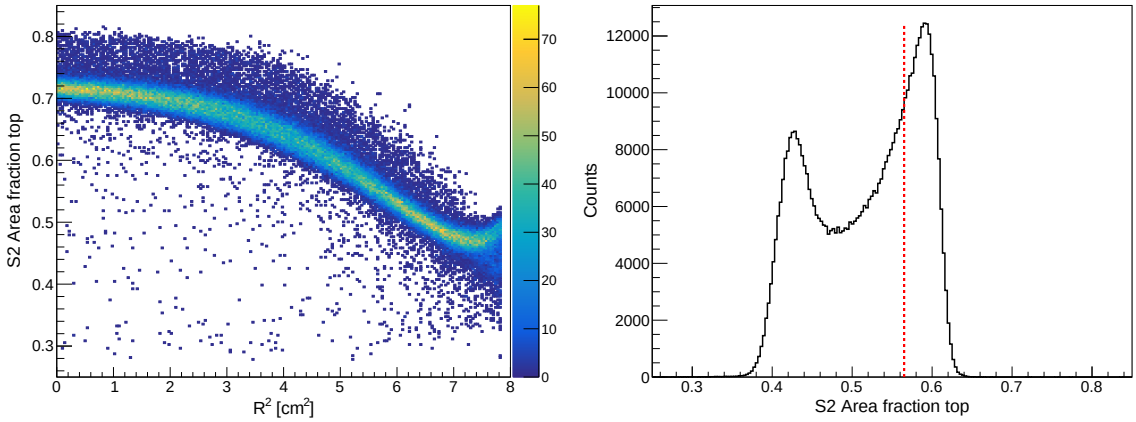

Figure 7.8: Qualitative comparison between the S2 area fraction top (AFT) distribution in simulation (left) and data (right). **Left:** Expected correlation between the AFT of S2 events and their radial position extracted from the optical simulation [254]. **Right:** Observed AFT distribution for S2 events from ^{222}Rn alphas. The dashed red line indicates the required minimum value of the area fraction top as used for this study.

Correction of light and charge signals

Both the S1 scintillation and the S2 charge signal show a clear dependence on the interaction position inside the detector. These are caused by geometry-dependent differences in the light collection efficiency (LCE) for the scintillation photons (S1), as well as the attachment of electrons (S2) to electronegative impurities during their drift (see e.g. [255] for further details). In order to increase the resolution of both, these dependencies need to be corrected for.

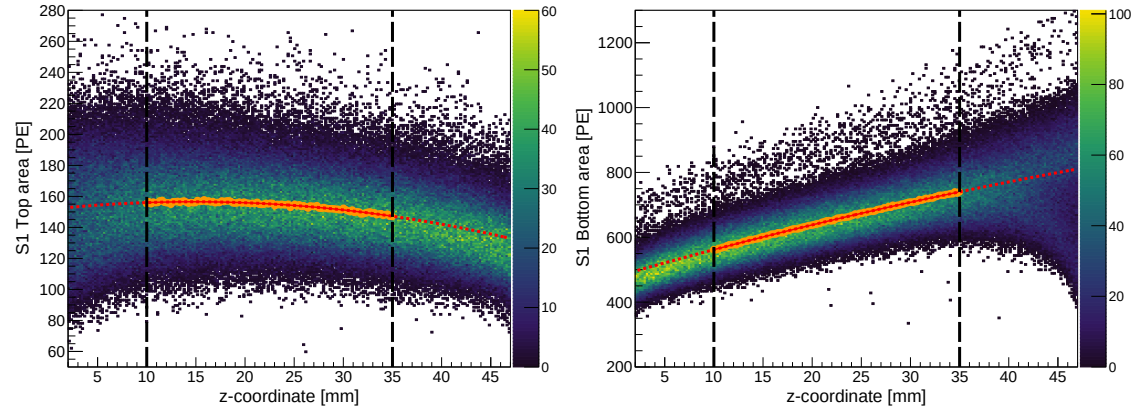

Figure 7.9: Depth dependence of the S1 scintillation signal of alpha particles at a field of 420 V/cm. The amount of detected light by the top PMT (left) and the bottom PMT (right) are corrected separately by fitting the mean profile of each distribution (orange markers) within the fiducial volume (vertical dashed black lines).

Figure 7.9 shows the dependence of the detected S1 scintillation signal for the top (left) and bottom (right) PMT on the depths (z-coordinate) of the event. The data corresponds to interactions of alpha particles at an electric field of 420 V/cm. For

both PMTs the mean profile of the distribution is determined and fit by a quadratic function. The fit range is constrained to the size of the fiducial volume as indicated by the vertical black lines. These functions are then used to correct the S1 signal sizes detected by both PMTs relative to their value in the center of the detector. Since this correction accounts for a geometric effect, it needs to be derived only once and can be applied to all field intervals alike. Note, however, that a separate S1 corrections is required for the measurement using ^{83m}Kr, because the LCE is changed due to the presence of the PTFE attenuators needed for the ^{222}Rn measurement.

The attachment of electrons to electronegative impurities causes the S2 signal size to decrease exponentially as a function of the drift time (z-coordinate). Figure 7.10 shows the natural logarithm of the S2 area from alpha events at an applied electric field of 420 V/cm as a function of the z-coordinate. The logarithm turns the

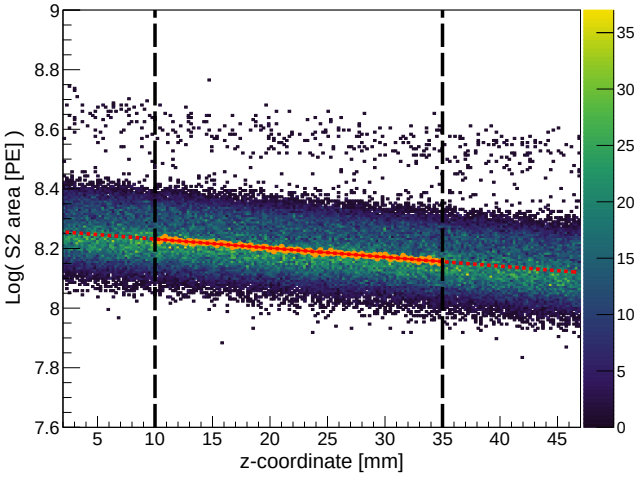

Figure 7.10: Depth dependence of the (natural) logarithm of the S2 charge signal from alpha interactions for a field of 420 V/cm. The decrease is due to attachment of electrons to electronegative impurities in the xenon during the drift. It is corrected for by fitting the median profile of the distribution (orange markers) with a linear function (red line). The fit range is constrained to the fiducial volume as indicated by the vertical black dashed lines.

exponential decrease into a linear one, in which the slope is proportional to the reciprocal of the electron lifetime in the LXe. It can be determined from the fit of the median profile of the distribution (orange markers) with a linear function (red line). The fit range is constrained to the size of the fiducial volume used in the analysis (vertical black lines). This function is then used to correct the detected S2 area to the expected value at the top of the TPC.

Unlike the S1 correction, this correction is subject to changes throughout the data taking period. First, the electron attachment rate dependents on the electron energy, which in turn depends on their velocity and therefore on the applied electric field [2, 57]. This makes it necessary to derive the correction for each field interval separately. Additionally, the continuous purification introduces a time variation of the impurity concentration in the LXe. However, since this change is below the percent level during the four hours in which each field has been measured its effect can be neglected.

Signal size estimation

For each of the measured fields, the average size of the corrected S1 (cS1) and S2 (cS2) signal needs to be determined. In case of the alpha interactions from ^{222}Rn, ^{218}Po, and ^{214}Po, this is done as is shown in figure 7.11. Populations of all

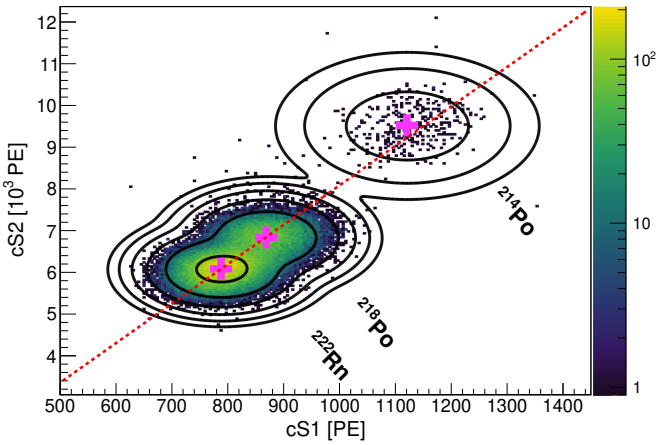

Figure 7.11: Corrected charge (cS2) and light (cS1) signal sizes for alpha events from ^{222}Rn, ^{218}Po and ^{214}Po for a median electric field of 1.24 kV/cm. The pink markers (✚) indicate the mean position for each isotope as determined from the fit of the data (black contours). A linear fit of the three mean positions is indicated by the dashed red line. Figure published in [P2].

three isotopes can be distinguished based on their position in cS1 and cS2. Their determined mean positions are derived from a fit to the data using the sum of three individual two-dimensional Gaussian functions. It should be noted, that the expected anti-correlation between the cS1 and cS2 due to the recombination is not observed within the resolution of the detector. Most likely this is owed to the high recombination fraction caused by the high ionization density of the alpha particles. The average resolution, defined as the standard deviation divided by the mean, is found to be 5% for cS1 and cS2 from alpha particles at a field of 1.2 kV/cm. While the S1 resolution is constant as a function of the electric field, the S2 resolution is found to get slightly worse as the field decreases.

Furthermore, the rate of ^{214}Po is found to be strongly suppressed with respect to the other two isotopes. This is caused by plate-out of the positively charged radon daughters [97, 214] onto the cathode or other detector components. A significant overlap between ^{222}Rn and ^{218}Po is visible, which makes both populations indistinguishable for electric fields lower than 70 V/cm. This is mainly due to the reduced S2 size and therefore worsened resolution, requiring to fit the combination of both lines using a single 2D Gaussian with a correlation term. A bias of about 4% is arising from this combined fit, which is corrected for.

For ^{83m}Kr, the corrected S1 signal sizes of the 9.4 keV and 32.1 keV transitions can be measured separately using a two dimensional Gaussian fit to the distribution of events similar to the one shown in figure 7.7. However, their S2 signals typically feature a large overlap. Therefore, they are treated as originating from a single 41.5 keV transition and a Gaussian function is fit to them. At an electric field of 1.2 kV/cm, the S1 resolution of the 9.4 keV and 32.1 keV line are found to be 29% and 20% respectively, while the S2 signals show a resolution of 19%.

7.2.2 Normalization and field dependence of charge and light yields

Changes of the light and charge signal in LXe can be expressed most universally when they are normalized. Their dependence with the electric field E is then explained by the phenomenological model proposed by Thomas and Imel [256]. This model is modified as done in [191] and given by:

$$\frac{L(E)}{L(0)}, \frac{Q(E)}{Q_0} = a_1 \cdot a_2 \cdot E \cdot \ln\left(1 + \frac{1}{a_2 \cdot E}\right) + a_3\,, \tag{7.5}$$

with $L(E)$ and $Q(E)$ being the field dependent light and charge yields which are normalized using $L(0)$ and Q_0. The methods used to derive the normalization constants will be introduced first, followed by a discussion of the results obtained from the ^{83m}Kr and ^{222}Rn data.

Normalization of charge and light yields

The normalization constant for the charge yield can be derived via the observed anti-correlation between the charge and light signal, using a similar method as is applied in [191]. Figure 7.12 shows the relation between the observed charge and light yields for the combined 41.5 keV transition and for ^{222}Rn and ^{218}Po alpha particles, acquired at various electric field values. Note that the scales from both panels cannot

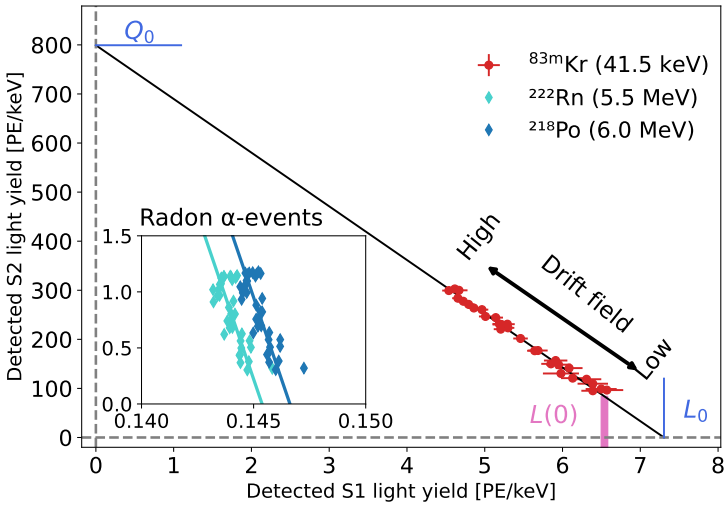

Figure 7.12: Observed anti-correlation between light (S1) and charge (S2) signals from the 41.5 keV transition of ^{83m}Kr (red •), together with the data from alpha decays (♦) of ^{222}Rn (cyan) and ^{218}Po (blue) in the inset. For the alpha data, only points for a drift field higher than 70 V/cm are shown. For better visibility, the data from ^{214}Po is left out. Additionally the estimated axis intersections Q_0 and L_0, as well as the value of $L(0)$ obtained from extrapolation of the light yield (see figure 7.13) are shown. Figure published in [P2].

be compared directly due to the PTFE attenuators used for the alpha measurement,

which affect the LCE. Furthermore, the overall high recombination fraction in the alpha tracks requires the x-axis to be strongly zoomed-in. Since the quality of the alpha data set is significantly better for fields larger than 70 V/cm, only these points are shown and used for determining the normalization. A systematic shift of about 1% between the data points obtained from ^{222}Rn and ^{218}Po is visible. It might introduced by the used fit method, shown in figure 7.11 or from a physical origin such as a different ionization density due to the different decay energies of both isotopes. Since the normalization constants are derived for each isotope separately, its subsequent influence is canceled out.

As stated in equation 7.4, the sum of produced electrons and photons is modeled as constant. Therefore, the data points acquired at different fields are fit using the linear function

$$Q(E) = Q_0 - \frac{Q_0}{L_0} \cdot L(E)\,. \tag{7.6}$$

By extrapolation of the function to its intersection with the charge yield axis, the value of Q_0 is derived. It can be understood as the maximum possible value for the charge yield if the total energy were to be converted into electron-ion pairs only. Note, that even if an infinitely strong electric field could be applied, the charge yield would still be diminished by the amount of energy converted by direct excitation of the medium. Similarly, L_0 is defined by the intersection of the linear fit with the horizontal axis and describes the theoretical maximum value of the light yield. However, some of the produced electrons will evade recombination even if no electric field is applied. This reduces the light yield at zero field ($L(0)$) with respect to L_0, as indicated by the pink line in figure 7.12. The value of $L(0)$ is determined by extrapolation of the detected S1 signal to zero field using equation 7.5. It is found to be smaller by about 10% compared to L_0, therefore it can be concluded, that the charge recombination at zero field is $(90 \pm 2)\%$.

The measured charge yield values are then normalized by Q_0. For the light yield of the two individual transitions of the ^{83m}Kr source $L(0)$ is chosen for the normalization, whereas the light yield of radon alphas is normalized by their respective value of L_0. In both cases, the uncertainty of the normalization arising from the respective extrapolation is treated as a systematic uncertainty and propagated to the results which are discussed next.

Field dependence of charge and light yield from electron interactions

Figure 7.13 shows the field dependence of the normalized light yield of the 9.4 keV and 32.1 keV ^{83m}Kr transitions and of the normalized charge yield from the combined 41.5 keV signal. The presented measurement includes several values at fields below 200 V/cm, which have not been measured systematically before. The data agrees well with the phenomenological fit function introduced in equation 7.5. Best fit values for the three model parameters a_1, a_2 and a_3 are reported in table 7.2. For the light yield of the 9.4 keV and 32.1 keV transition, the parameter a_3 has been

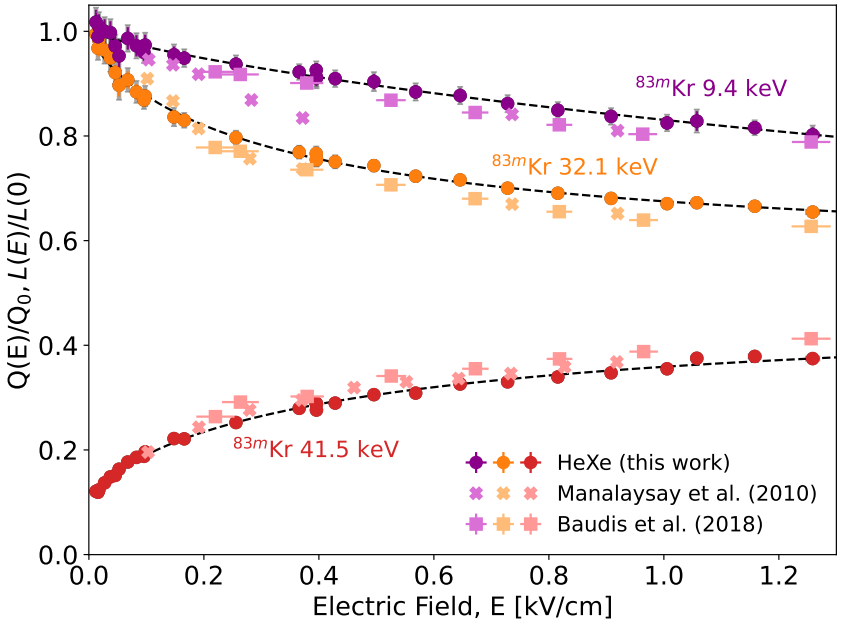

Figure 7.13: Normalized charge (red), and light yields (orange and purple) for ^{83m}Kr transitions in dependence of the applied electric field E. Data obtained in this work (●) is compared to the ones reported by Manalaysay et al. (✖) [191] and Baudis et al. (■) [236]. The dependencies are fit with the modified Thomas-Imel box model introduced in equation 7.5 (black dashed lines). Data available in [239]. Figure published in [P2].

fixed to one, due to the extrapolation used to determine $L(0)$.

Table 7.2: Parameters and their statistical uncertainties extracted from the fit of the normalized light and charge yield dependencies of the ^{83m}Kr transitions shown in figure 7.13. They correspond to the parameters of the modified Thomas-Imel model given in equation 7.5. Table published in [P2].

Transition	a_1	a_2 [cm/kV]	a_3
9.4 keV	-1.0 ± 0.3	0.06 ± 0.03	1 (fixed)
32.1 keV	-0.443 ± 0.011	1.41 ± 0.10	1 (fixed)
41.5 keV	0.375 ± 0.008	1.11 ± 0.11	0.091 ± 0.004

For comparison, figure 7.13 also shows the measurements reported in Manalaysay et al. [191] and Baudis et al. [236]. The absolute yields reported in the latter have been converted to the normalization used here. This is done by estimating values for Q_0 and L_0 based on the information provided in [236] in combination with their values of g_1 and g_2. Finally, the light yields are scaled using the recombination fraction at zero field estimated above. Furthermore, the charge yield values reported in [191], have been scaled by 0.943 to match the definition of Q_0 used in this work. The shape

of the charge yield dependence from the combined 41.5 keV signal agrees well with the measurements from literature, with the values from this work being about 8% lower. Also, the light yield dependence shows a similarly good agreement for fields above 400 V/cm, with the present values being roughly 5% larger on average. For lower fields, the shape differs slightly from the one reported in [191], especially for the 9.4 keV signal.

From figure 7.13 it can be seen, that the light yield of the 9.4 keV line features a reduced dependence on the electric field when compared to the 32.1 keV transition. This difference is due to the reduced recombination probability for electronic recoils (ERs) with energies $\lesssim$10 keV, when compared to ERs of higher energy (see also [228, 257]). Due to this, the ratio between the two S1 signals is sensitive to the local electric field in the detector. Since the half-life of the intermediate state is only 154 ns [192], light from both transitions is emitted from the same position in the detector. Therefore, this ratio is a very attractive probe for the magnitude and variation of the electric field in large-scale detectors as reported, for example, in [258].

Figure 7.14 shows the field dependence of the ratio between the light yields (PE/keV) of both ^{83m}Kr transitions. The ratio follows a single exponential function with a con-

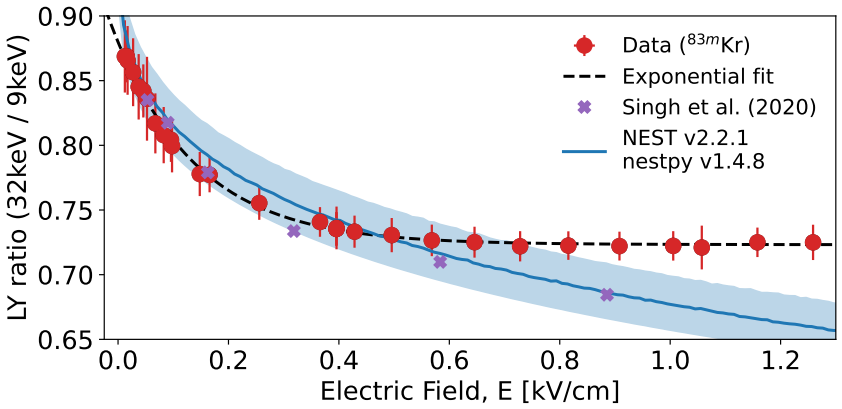

Figure 7.14: Field dependence of the light yield ratio between both ^{83m}Kr transitions. Data from this work (●, red) are compared to the data reported in [253] (purple, ✖), as well as to the prediction made by the NEST [228, 229] framework (blue line). The shaded blue region corresponds to the predicted spread due to different time separations ($\Delta t > 300$ ns) of the two ^{83m}Kr transitions. A fit of the measured dependence with the model from equation 7.7 is shown by the black dashed line. Data available at [239]. Figure published in [P2].

stant offset:

$$R(E) = \frac{\mathrm{LY}\,(32\,\mathrm{keV})}{\mathrm{LY}\,(9\,\mathrm{keV})} = b_1 \cdot e^{-b_2 \cdot E} + b_3\,. \tag{7.7}$$

This function is fit to the data and the values for $b_1 = 0.156 \pm 0.012$, $b_2 = (6.6 \pm 1.1)\,\mathrm{cm/kV}$, and $b_3 = 0.723 \pm 0.004$ are obtained. The ratio predicted by the NEST [228, 229] simulation framework is shown for comparison. Additionally, the data reported in [253] is shown, where the same requirement of $\Delta t > 300$ ns as ap-

plied in this work has been used. For both, a good agreement is found for fields lower than approximately 500 V/cm, where the ratio predicted from NEST is higher by only 2%. For larger electric fields, however, the data from this work indicates that the ratio stays constant at the value of $b_3 = 0.723 \pm 0.004$, which is in contradiction to the decrease observed in [253] and predicted by NEST.

Field dependence of charge and light yield of alpha particles

Compared to low energy electrons, alpha particles feature a much higher energy loss (dE/dx) in LXe, which leads to an increased ionization density along their tracks. Therefore, the degree of charge recombination is typically very large, which results in a low charge signal when compared to electrons or photons with the same energy [229]. The measured field dependence of the charge and light yield of alpha particles emitted by ^{222}Rn and its decay products is shown in figure 7.15. Note that

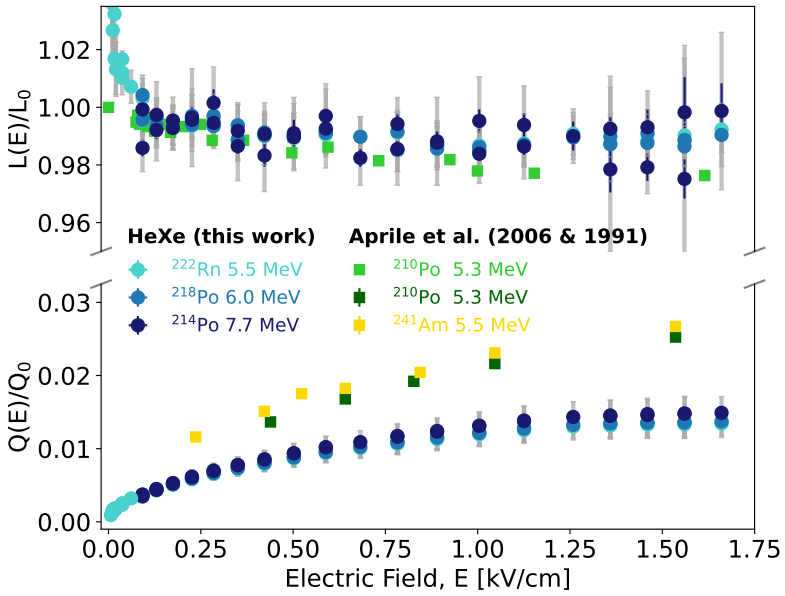

Figure 7.15: Field dependence of the normalized charge and light yield of alpha particles in LXe. Data acquired in this work (•) is compared to the published results from Aprile et al. [231, 232] (■). Systematic uncertainties are indicated by gray error bars. The y-axis is split for a better visualization of the small relative changes in the normalized yields. Data points available at [239]. Figure published in [P2].

the absolute value of the charge yield increases by a factor of 17 over the field range from 10 V/cm (1‰) to 1.6 kV/cm (1.7%). As discussed in section 7.2.1, the lines of ^{222}Rn and ^{218}Po are resolved separately only for fields above 70 V/cm. Therefore, only the yield of ^{222}Rn is shown for lower fields.

The uncertainties of the electric field strength (too small to be visible in the figure), correspond to the range of the central 68% of the field distribution in the fiducial volume as described in section 5.3. The uncertainty on the normalized yields contains the statistical uncertainty (vertical colored bars), as well as a systematic uncertainty

(vertical gray bars). The latter reflects the uncertainty related to the normalization constant, as well as the one estimated by variation of the event selection criteria (see section 7.2.1). The dominant contribution to the uncertainty of the charge yield is due to the long lever arm required to determine Q_0 as shown in figure 7.12, while the light yield is mostly affected by the variation of the analysis parameters.

Though the LXe temperature and pressure inside the cryostat were stable within 1% throughout the measurement (see figure 5.4), possible time-varying detector effects need to be controlled for. This was realized by a particular arrangement of the measured fields into five individual field scans, combined with intermediate measurements of a reference field of 400 V/cm. Additionally, the full measurement was repeated such that all fields are measured at least twice. Figure 7.16 shows the time evolution of the scintillation light yield of ^{222}Rn evaluated from the reference measurements. The values are scattering within 0.3% from their mean value, which

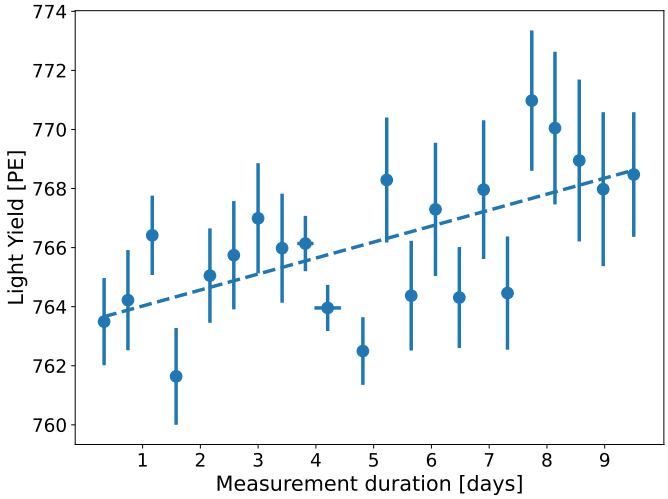

Figure 7.16: Time stability of the ^{222}Rn light yield evaluated from regular reference measurements at a field of 400 V/cm. The slight increase as indicated by the dashed line is attributed to the xenon purification.

is small compared to uncertainty attributed to the choice of the analysis parameters. Therefore, the slight linear increase, which is likely caused by the continuous purification of the xenon, can be neglected.

Figure 7.15 additionally shows the data reported in Aprile et al. [231, 232] for comparison. Given the systematic uncertainties of the light yield, both measurements are in agreement for fields $\gtrsim 70$ V/cm, while the normalized light yield found in this study exceeds values of one for lower fields. It is explained by the electric field leakage between the extraction and drift region of the detector. This lessens the efficiency of the globally defined light yield correction at low fields. Therefore, these fields are not taken into account for the normalization shown in figure 7.12.

To compare the charge yield values, the data from [231] needs to scaled such, that its normalization agrees with the one used in this work. The charge signal in [231] is normalized using the ionization energy $W_i = 15.6$ eV needed to produce an electron-ion pair in LXe. For this work, the normalization is derived using the simultaneous detection of charge and light, therefore relating to the average xenon excitation energy $W = 11.5$ eV [249, 250]. The literature values therefore need to

be multiplied by W/W_i. Still, the data from this work is found to be significantly lower and shows a slight flattening for fields above 1.3 kV/cm. Possible reasons for this discrepancy are discussed in the following.

In [231], a LXe temperature of 195 K is stated, which is about 20 K higher compared to this work. Therefore, a difference of 5.1% in the LXe density can be assumed [95], which results in different ionization densities of the alpha particles. The higher ionization density in this work should lead to enhanced charge recombination and, subsequently, to a lower charge yield.

Another important difference is the distribution of the radioactive sources within the setups. The sources employed in [231, 232] have been deposited directly on the cathode, while in this work the source is homogeneously distributed in the detector. In the latter case, alpha particles emitted under all possible angles can be detected, while only the ones going in the upwards direction can be seen in [231, 232]. A slightly reduced charge yield is expected for tracks which are vertically aligned relative to the electric field (see also [231]). Since electrons produced in the lower region of the track need to drift through the upper region of the track, they have a higher probability for recombination due to the high ionization density. Therefore, these tracks are expected to feature a slightly lower charge yield with respect to horizontally aligned tracks. Additionally, order of 100 keV of the energy released in the alpha decay are carried away by the daughter nucleus, which recoils in the opposite direction of the alpha particle. While in this work the sum of both interactions is detected, the recoiling nucleus is absorbed by the cathode electrode and therefore evades detection in [231, 232].

Using a homogeneous source allows to define a fiducial volume, in which the field and its uncertainty are well known from the detailed 3D field simulation introduced in section 5.3, while the local field close to the cathode surface might be enhanced due to surface irregularities. Though this has been considered in [231, 232] and was mitigated by polishing of the cathode surface, a slight influence might remain.

7.3 Summary and discussion

Measurements of the electron drift velocity and the charge and light response of LXe to interactions from alpha particles and electrons have been carried out using the HeXe TPC. Their field dependence has been studied over an extended range of electric fields between 8 V/cm and 1.64 kV/cm, with a special emphasis on the regime of low fields. This regime is of particular interest for current and future large-scale LXe experiments. The data is made publicly available [239] to ease its incorporation into upcoming versions of simulation frameworks such as for example NEST. This could help to improve the simulation and reconstruction accuracy in LXe detectors.

For the drift velocity, a good agreement with values reported in literature is found. Systematic differences are attributed to the temperature dependence of the drift velocity, which has been evaluated qualitatively by combining the measurements in this

work with data from literature [P2]. For drift fields below approximately 700 V/cm, good agreement with the NEST [228, 229] simulation framework is observed. In the regime of higher fields, velocities predicted by NEST are significantly larger with respect to the ones measured here. Currently NEST models the electron drift velocity only via a phenomenological formula which is interpolated for different LXe temperatures. Implementing a physical model that is validated on the available data would be a great improvement.

For the light and charge yield of low energy electrons, the data is found to agree with the model proposed by Thomas and Imel [256] and modified as in [191]. The comparison with literature measurements [191, 236] also shows a reasonable agreement. Additionally, the field dependence of the light yield ratio between both ^{83m}Kr transitions has been evaluated. This data can readily be applied to probe the electric field in large-scale detectors (see e.g. [258]).

The variation of the normalized light and charge yield from ^{222}Rn-induced alpha particles is found to be very small over the investigated field range. This is expected from the high recombination fraction in these tracks due to their high ionization density. While for the light yield a comparable dependence to the one reported in [232] is found, the charge yield differs significantly from the one reported in [231]. Though the exact cause remains unknown, possible reasons are discussed. They include differences in the analysis methods as well as in the used experimental approaches. This discrepancy should be clarified in a future measurement. Such a measurement would greatly profit from the evaluation of the S2 size produced by a single electron (single electron gain). This would allow to use the same normalization procedure as done in Aprile et al. [231], in order to exclude a bias from the normalization. Such an evaluation was unattainable in this work due to the used PTFE attenuators. Given the small change of the light yield it would be also beneficial to extend the investigated field range to also include higher electric fields. This would help to better derive the normalization via the anti-correlation between charge and light signal. Furthermore, it would clarify the slight flattening in the charge yield trend that has been observed for fields above 1.3 kV/cm.

Summary

Striking evidence was gathered over the past decades, which proofs that the majority of the matter in our universe exists in the form of dark matter (DM). These indications cover many scales, ranging from galaxy rotation curves over collisions of galaxy clusters up to the large-scale structure in the universe and the temperature fluctuations imprinted in the cosmic microwave background (CMB). Despite its dominant role, only very little is known about the nature of DM. Many experimental searches are set out to clarify this urgent question. Among them is the recently commissioned XENONnT experiment [6] introduced in section 1.2. It belongs to the latest generation of experiments endeavoring the direct detection of DM in a dual-phase xenon time projection chamber (TPC).

The background of the XENONnT detector is expected to be dominated by decays of ^{222}Rn emanated from detector materials. In chapter 2, a first measurement of this important background is presented. For this a dedicated S1-only analysis was developed, to cope with the challenging detector conditions during its commissioning phase. A baseline radon concentration of $\left(3.6\,^{+0.7}_{-0.3}\right)$ µBq/kg is found, which is about 15% lower than the one predicted by the radon measurement campaign reported in [70]. This result is confirmed on an order of magnitude level by the independent analysis carried out in the nitrogen-filled detector detailed in section 2.2. Furthermore, the performance of the new radon removal system has been evaluated. The gaseous xenon (GXe) distillation mode of this system which was also applied during the first scientific data-taking campaign, allows to reach a ^{222}Rn concentration of slightly less than 2 µBq/kg. Usage of the system's additional liquid xenon (LXe) distillation mode, showed the potential to even slightly surpass the ambitious design goal of 1 µBq/kg [6]. To meet the high requirements on the chemical purity of the xenon, the experiment is the first large-scale LXe experiment to employ a liquid purification plant. In this work, the radon release of both filter types that can be used with this plant has been measured. As expected, the high-efficiency filter showed a prohibitively high emanation radon rate for its use during scientific data taking. It has been used to purify the bulk of the xenon inventory, and was then replaced by a filter with low-radon emanation. The analysis showed no significant radon release from this filter, while it proved to be capable of maintaining the high xenon purity.

Despite the promising results obtained with the radon removal unit in XENONnT, future detectors such as DARWIN [39] will require even further reductions in their ^{222}Rn concentration (see section 1.3). Achieving this goal will require a combination of established and novel methods for radon mitigation. For both of them, the

availability of reliable sources of radon emanation is a necessary ingredient. A new approach for the production of radon sources by implantation of radium into stainless steel has been explored and is described in chapter 3. For this, two samples that have been implanted with approximately 8 Bq of ^{226}Ra at the ISOLDE facility [71], have been thoroughly characterized in this work. The amount of implanted activity has been confirmed by HPGe and alpha spectrometry (sec. 3.1.2) and the available ^{222}Rn emanation was measured to be roughly 2 Bq for both samples. The emanation fraction of roughly 25% is in good agreement with a recoil-dominated emanation process as shown in section 3.3, which is further confirmed by the absence of a temperature dependence of the emanation. Additionally, ^{220}Rn emanating samples have been produced by implantation of ^{224}Ra utilizing the recoil from the alpha decay of ^{228}Th. The short half-life of the implanted activity as well as of the emanated radon isotope, limits the usability of these samples. On the other hand, they can be more easily obtained using a home-made implantation setup. Both types of samples have been applied to study a novel method of radon mitigation using surface coatings.

Such coatings bear great potential to mitigate the radon-induced background in future large-scale LXe experiments. Building on the experience of past investigations [71, 126, 148, 149], the so-far most promising deposition technique has been identified to be electrochemical plating (ECP) of copper at a surface current density of 10 mA/cm^2. While past studies were mostly limited to the investigation of ^{220}Rn emanation from tungsten surfaces, with the coating procedure introduced in section 4.2 this method could be applied to the radium implanted stainless steel samples. This allowed for the first time to measure the ^{222}Rn reduction on a realistic sample. A reduction by more than three orders of magnitude is obtained, which clearly exceeds the requirement of a future large-scale experiment. Still, there are several challenges of this technique which remain to be addressed in the future. Besides the up-scaling of the setup and guaranteeing the radio purity of the coating layer, its compatibility with the cryogenic environment and high purity demands of LXe TPCs needs to be ensured.

The Heidelberg Xenon (HeXe) setup offers an ideal testbed for such a verification. Its dual-phase xenon TPC with an active mass of 345 grams has been applied for LXe purity studies already in the past [100, 125]. The detector is introduced in chapter 5 with a special emphasis on the generation and simulation of its electric fields. For the latter, a detailed three-dimensional COMSOL Multiphysics® [202] model has been created. Its evaluation is accelerated considerably by a superposition method, allowing for an iterative drift field optimization. Additionally, a software with an associated graphical user interface (GUI) has been developed to monitor and control all high voltage (HV) relevant parameters. In this work, the HeXe TPC was employed to carry out field resolved measurements of the electron drift velocity as well as of the scintillation and ionization yields of low energy electrons and alpha particles.

Especially for the measurement of alpha interactions, special polytetrafluoroethy-

lene (PTFE) light attenuators were necessary to prevent signal saturation. Their design has been based on the result of a dedicated measurement of the transmittance of xenon scintillation light by PTFE. This previously unmeasured material property is also an important input for the reduction of the radiogenic neutron background in future large-scale LXe detectors. The transmittance has been measured for various thicknesses of PTFE in GXe at room temperature as well as in LXe at cryogenic temperatures. Both results are found to be compatible within their uncertainties and are reported in chapter 6 as well as in [P1]. Furthermore, they are compatible with the result of an independent study reported in [63].

For the measurements of the scintillation and ionization yields, electrons from ^{83m}Kr and alphas from the decay of ^{222}Rn and its decay products have been used. Particularly for the interactions of alpha particles in LXe, only very few measurement are reported in the literature. Additionally, the drift velocity of electrons in LXe has been measured. The results show good agreement with past studies, except for the alpha particle charge yield, which is found to be significantly lower. Possible reasons for the discrepancy are discussed in detail in section 7.2.2. The measurements have been carried out over an extended field range between 8 V/cm and 1.64 kV/cm, with a special emphasis put on fields $\lesssim$ 100 V/cm. Despite the relevance of this low field regime for current and future large-scale detectors, it is not well covered in the literature. Therefore, the measurements presented in chapter 7, are an important contribution to improve the modeling and reconstruction in such experiments. The results from this chapter have also been published in [P2] and the data has been made publicly available [239].

Part I

Appendix

A Lists

A.1 List of Figures

A.2 List of Tables

Acronyms

0νββ neutrinoless double beta decay. 7, 12, 63

BSM beyond standard model. 4

CB Crystal-Ball. 17, 36, 37, 54, 66, 121, 159, 160

CDM cold dark matter. 3

CEνNS coherent elastic neutrino-nucleus scattering. 6, 10

CMB cosmic microwave background. 3, 139

CVD chemical vapor deposition. 64, 65, 69, 70

DAQ data acquisition. 76, 87, 107, 110

DLC diamond like carbon. 70, 74

DM dark matter. 1–5, 7, 9, 11, 139, 145

ECP electrochemical plating. 64, 69, 71, 73, 75–79, 84, 85, 140, 148

ER electronic recoil. 7, 9–11, 13, 63, 134, 145

FEM finite element method. 68, 95

FSR field shaping ring. 88, 93, 95, 103

GPS general purpose separator. 34

GR general relativity. 1

GS gas system. 87, 89, 90

GUI graphical user interface. 72, 94, 140

GXe gaseous xenon. 8, 9, 25, 27, 32, 87–91, 93, 101, 102, 105–110, 113, 117, 139, 141

HDPE high density polyethylene. 36, 37, 53, 71, 82

HeXe Heidelberg Xenon. 85, 87, 88, 90, 92–97, 102, 103, 105–107, 111–113, 115, 117, 119–121, 127, 137, 140, 147, 159, 160

HPGe high purity germanium. 38, 39, 47, 48, 79–81, 140, 147

HRS high resolution separator. 61

HV high voltage. 8, 21, 43, 88, 92–95, 97, 101, 110, 123, 140

ISOLDE isotope separation online device. 33, 34, 49, 50, 52, 58, 59, 61, 73, 81, 140

LCE light collection efficiency. 15, 18, 19, 105, 112, 113, 128, 129, 132

LHC large hadron collider. 4

LNGS Laboratori Nazionali del Gran Sasso. 10

LXe liquid xenon. 6–15, 17, 18, 20–27, 29–32, 63, 64, 85, 87–91, 99, 101, 103, 105, 106, 112, 113, 117, 119–121, 124–126, 129, 131, 135–141, 145

MACHO massive compact halo objects. 2

MFM mass flow meter. 89

MOND modified Newtonian dynamics. 2

MPIK Max-Planck-Institut für Kernphysik. 38, 41, 44, 72, 85, 87

MSSM minimal supersymmetric standard model. 6

mwe meter water equivalent. 38

NEST "Noble Element Simulation Technique". 119, 123, 137, 138

NR nuclear recoil. 9, 10, 105, 145

ODE ordinary differential equation. 67

PDE partial differential equation. 66, 67

PDF probability density function. 37, 59, 155

PE photoelectron. 14, 29, 120, 126

PIN positive intrinsic negative. 36, 37, 43, 45, 53, 57, 65, 77

PMT photomultiplier tube. 5, 8, 14–16, 18, 26–29, 87–89, 91, 92, 95–97, 101, 102, 105–107, 109–113, 115, 116, 119, 121, 125, 127–129, 145

PTFE polytetrafluoroethylene. 10, 19–22, 85, 87–89, 93, 94, 97, 103, 105–107, 110–117, 120, 127, 129, 131, 138, 140, 141

PVD physical vapor deposition. 64, 69

QE quantum efficiency. 88

RIB radioactive ion beam. 33, 34, 38, 48, 49, 81

RILIS resonance ionization laser ion source. 61

ROI region of interest. 9, 10, 14, 15

SC slow control. 87, 90

SHV safe high voltage. 93

SM standard model. 4, 5

SMS Short message service. 95

SRIM "stopping and range of ions in matter". 34, 41, 59, 65, 108, 109, 155, 157

TES transition edge sensor. 5

TMP turbo molecular pump. 43

TPC time projection chamber. 1, 6–9, 12, 13, 15, 18, 20, 21, 31, 64, 84, 85, 87–89, 92, 97, 103, 105, 111, 115, 117, 119–122, 125, 127, 129, 137, 139, 140, 145

UV ultraviolet. 27

VUV vacuum ultraviolet. 7, 9, 22, 105, 106, 115, 117

WIMP weakly interacting massive particle. 4, 9, 10, 12, 13

WTh thoriated tungsten. 64–66, 69–72, 74, 75, 83–85

B Author's Publications used in this work

This list contains the publications of the author which are used in this work. The list is sorted by date of publication and the publications are referenced as P1 and P2 throughout the text.

Publication 1 [P1] [64]:

- Dominick Cichon, Guillaume Eurin, Florian Jörg, Teresa Marrodán Undagoitia and Natascha Rupp (2020). **Transmission of xenon scintillation light through PTFE**. *arXiv:2005.02444v2*, published in Journal of Instrumentation, 15(09), P09010.

Publication 2 [P2] [195]:

- Florian Jörg, Dominick Cichon, Guillaume Eurin, Luisa Hötzsch, Teresa Marrodán Undagoitia and Natascha Rupp (2021). **Characterization of alpha and beta interactions in liquid xenon**. *arXiv:2109.13735v1*, accepted for publication in European Physical Journal C.

C Further models of the emanation fraction due to recoil

A simplified model describing the radon emanation fraction of radium implanted samples is discussed in section 3.3. In this linear model, the simplifying assumption is made, that the all implanted radium is concentrated at a specific depth and that all recoiling radon atoms have exactly the same range in the material. In reality this is not true and both the depth and recoil range follow certain distributions. Therefore, this appendix introduces two additional models for the emanation fraction, taking these distributions into account.

Gaussian implantation and recoil distributions

The "stopping and range of ions in matter" (SRIM) Monte-Carlo code can be used to simulate the implantation and distribution, as well as the distribution of recoil ranges. Both are shown in figure C.1, and it can be seen that they roughly follow normal distribution functions $\mathcal{N}$.

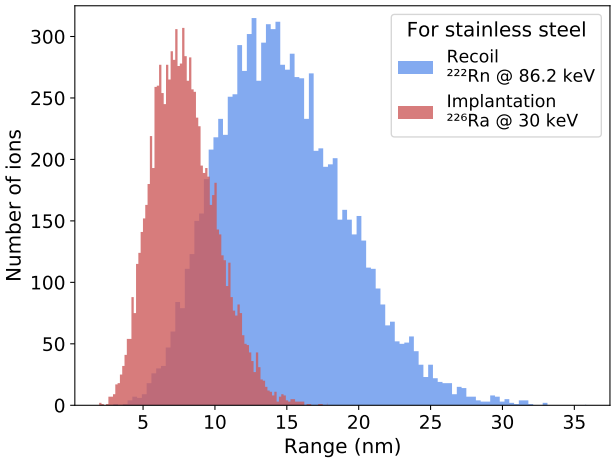

Figure C.1: Expected range distributions for stainless steel ($8.0\,\mathrm{g/cm^3}$) as simulated using SRIM [121]. The simulated distribution of implanted ^{226}Ra ions for a 30 keV beam energy is shown in red with the recoil range of ^{222}Rn in blue.

So, the values for the implantation depths z and recoil range r can be treated as random variables following these probability density functions (PDFs).

$$\begin{aligned} p_i(z) &\propto \mathcal{N}(z; \mu_i, \sigma_i) \\ p_r(r) &\propto \mathcal{N}(r; \mu_r, \sigma_r)\,. \end{aligned} \tag{C.1}$$

Here p_i and p_r describe the distribution of implantation depth and recoil range respectively with $\mu_{i,r}$ and $\sigma_{i,r}$ being their respective means and standard deviations.

For a certain combination of implantation depth z' and recoil range r' the emanation fraction can again be computed using equation 3.15 from above. This fraction now needs to be multiplied by the probability to find a radon atom at depth z' with a recoil range of r'. To get the overall emanation fraction all possible values for depth and range then need to be summed over. The emanation fraction can therefore be expressed by the double integration over implantation depth and recoil range as:

$$F = \frac{1}{A \cdot B} \cdot \int_0^\infty \int_0^\infty dr'\, dz'\, p_i(z') \cdot p_r(r') \cdot \begin{cases} \frac{1-z'/r'}{2} & , \text{ for z}' \leq \text{r}' \\ 0 & , \text{ else} \end{cases} \tag{C.2}$$

Remember that the condition $z' \leq r'$ needs to be introduced to prevent the emanation fraction to become nonphysical and negative. This constraint can then be absorbed by shifting the lower bound of the integration of the recoil distribution from zero to the value of z'.

Note that both integrations are evaluated only over the positive direction. The normalization of the normal distribution however is guaranteed when the full range from $-\infty$ to $+\infty$ is integrated over. Therefore the constants A and B are introduced to re-scale the result in order to account for the missing probability which falls outside of the positive z and r direction. They are calculated as

$$A = 1 - \int_{-\infty}^0 p_i(z')\, dz' \qquad \text{and} \qquad B = 1 - \int_{-\infty}^0 p_r(r')\, dr' \ . \tag{C.3}$$

The evaluation of equation C.2 is performed numerically using the `SciPy` library [206] for Python. For the case of the ^{226}Ra implanted samples the parameters $\mu_{i,r}$ and $\sigma_{i,r}$ of the distribution functions can be chosen using the results of the simulation shown in figure C.1.

$$\mu_i = 7.9\,\text{nm}, \qquad \sigma_i = 2.2\,\text{nm}$$
$$\mu_r = 14.8\,\text{nm}, \qquad \sigma_r = 4.4\,\text{nm}$$

The resulting emanation fraction for this combination is 21.6% which is very close to the one estimated using the linear approximation of equation 3.15.

The parameters μ_i and σ_i describing the implantation distribution can be varied in order to evaluate the expected dependence of the emanation fraction on the ratio between the mean implantation depth and mean recoil range μ_i/μ_r. For this it additionally needs to be assumed that the spread of the implantation distribution σ_i is proportional to the mean of the implantation μ_i. This dependence is shown in figure 3.22. It can be seen that again the emanation fraction approaches a value of 0.5 for very shallow implantations. The emanation fraction then decreases for the implantation becoming deeper with respect to the mean recoil range following quite close the dependence of the linear model. As the ratio becomes greater than approximately 0.7, the dependence of this model becomes more flat and only approaches

zero asymptotically. This is attributed to the tails of the normal distribution due to which there are always some radium atoms which are closer to the surface than the mean implantation depth as well some recoiling radon particles with significantly larger recoil range than the mean recoil distance.

Monte-Carlo method

As can be seen from figure C.1 the simulated implantation and recoil distributions are slightly skewed and deviate from a normal distribution. The last model therefore estimates the emanation fraction based directly on the simulation output without assuming that the profiles follow a normal distribution function.

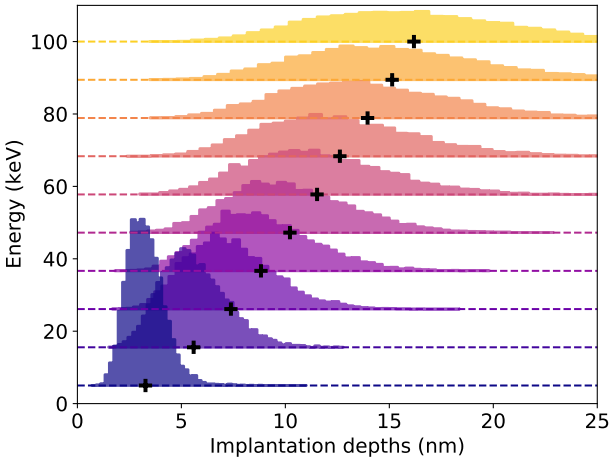

Figure C.2: Expected energy dependence of the implantation profile for ^{226}Ra ions. Each distribution is shifted by the amount of incident energy along the y-axis (colored dashed lines) for better visibility. The mean of each distribution is indicated by a black marker. Simulations done using SRIM [121].

The implantation and recoil distributions are estimated based on 9000 ions simulated using SRIM [121]. From the two distributions $N_{total} = 10^6$ random pairs of implantation depth and recoil range are then drawn with replacement. Each pair is then assigned a random emission angle β following the distribution function:

$$\beta = \arccos\left(\mathcal{U}(0,1)\right) \tag{C.4}$$

Where $\mathcal{U}$ is the uniform distribution and the sampling is constrained to the forward direction to save computational cost. For each event this angle is compared to its critical angle for emanation β_{crit} (see equation 3.12). The emanation fraction is then approximately given as the ratio between the number of successfully emanated radon atoms $N_{emanated}$ to twice the number of simulated particles.

$$F \approx \frac{N_{emanated}}{2 \cdot N_{total}} \tag{C.5}$$

Where the factor of two accounts for the fact that only angles of β pointing towards the surface of the sample are considered. The emanation fraction for the ^{226}Ra implanted samples predicted by this model is 21.4% which is almost identical to the one of the previous model assuming normal distribution functions.

Also for this model the dependence of the emanation fraction with the ratio between the mean implantation depth and recoil range can be evaluated. For this the implantation profiles of ^{226}Ra ions at ten different incident energies in the range between $[5, ..., 100]$ keV have been simulated. A compilation of the resulting profiles is shown in figure C.2. The resulting histograms for each energy are shown in different colors and offset by the incident ion energy along the y-axis. Black markers indicate the position of the mean implantation depth for each energy. The recoil range distribution is held fixed to the distribution resulting from the 86.2 keV recoil of ^{222}Rn in stainless steel as shown in figure C.1.

Results from both models are compared to the data obtained with the implanted samples, as well as to the prediction of the linear model in figure 3.22 shown in section 3.3.

D Function definitions

D.1 Crystal-Ball function

Standard Crystal-Ball function

The Crystal-Ball (CB) function [124] is a combination of a normal distribution with a pronounced power-law tailing towards the left-hand side. It can be used, for instance, to describe processes and spectra where part of the energy evades detection as it is the case for most alpha spectra which are described in chapter 3.

$$f(x) = N \cdot \begin{cases} \exp\left(-\frac{(x-\mu)^2}{2\sigma^2}\right), & \text{for } \frac{x-\mu}{\sigma} > -\alpha \\ \left(\frac{n}{|\alpha|}\right)^n \cdot \exp\left(-\frac{|\alpha|^2}{2}\right) \cdot \left(\frac{n}{|\alpha|} - |\alpha| - \frac{x-\mu}{\sigma}\right)^{-n}, & \text{for } \frac{x-\mu}{\sigma} \leq -\alpha \end{cases} \tag{D.1}$$

The parameters μ and σ describe the mean and standard deviation of the normal distributed right hand side of the function. The parameter α defines the distance from the peak position μ at which the normal distribution transitions into the left-hand power-law tail. Alpha is given in units of the standard deviation of the normal distribution. The slope of the power-law tailing is defined by the parameter n, and N is the normalization of the function.

Mirrored Crystal-Ball function

This function is introduced to describe the event distribution from events produced in the cathode region in the Heidelberg Xenon (HeXe) setup as shown in figure 7.1. It is constructed by mirroring the regular CB (equation D.1) function at an axis going through the peak position μ. This is done by transformation of the coordinates $x \to -x$ and $\mu \to -\mu$.

$$f(x) = N \cdot \begin{cases} \exp\left(-\frac{(x-\mu)^2}{2\sigma^2}\right), & \text{for } \frac{x-\mu}{\sigma} < \alpha \\ \left(\frac{n}{|\alpha|}\right)^n \cdot \exp\left(-\frac{|\alpha|^2}{2}\right) \cdot \left(\frac{n}{|\alpha|} - |\alpha| + \frac{x-\mu}{\sigma}\right)^{-n}, & \text{for } \frac{x-\mu}{\sigma} \geq \alpha \end{cases} \tag{D.2}$$

Crystal-Ball function with exponential right flank

For the approximate description of the ^{212}Po alpha emission line it is found to be necessary to include a tailing towards the right side in addition to the low-energy

tailing (see e.g. figure 3.17). The reason is the coincidence counting due to the short half-life of ^{212}Po as explained in section 3.2.2. The proposed function is based on the CB function definition above with an additional section falling off as an exponential function with constant λ towards the right hand side.

$$f(x) = N \cdot \begin{cases} \exp\left(-\lambda \cdot (x-\mu)\right), & \text{for } \frac{x-\mu}{\sigma} \geq \alpha \\ \exp\left(-\frac{(x-\mu)^2}{2\sigma^2}\right), & \text{for } -\alpha < \frac{x-\mu}{\sigma} < \alpha \\ \left(\frac{n}{|\alpha|}\right)^n \cdot \exp\left(-\frac{|\alpha|^2}{2}\right) \cdot \left(\frac{n}{|\alpha|} - |\alpha| - \frac{x-\mu}{\sigma}\right)^{-n}, & \text{for } \frac{x-\mu}{\sigma} \leq -\alpha \end{cases} \tag{D.3}$$

Note that continuity is only given at the intersection towards the left and is not guaranteed for the transition to the exponential part. Also there was no closed solution found which preserves the right-hand side intersection to be differentiable.

D.2 Sigmoid function

The drift time position of the gate electrode in the HeXe setup can be determined from the change in charge yield of ^{83m}Kr events. For this the following function is fit to the distribution shown in the right panel of figure 7.2

$$A(t) = -2\pi \cdot A_0 \cdot \arctan(w \cdot (t - t_0)) + c\,. \tag{D.4}$$

Where t denotes the drift time and A is the area of the S2 peaks. The amplitude A_0, offset c and width w of the function are determined by the fit, as well as the estimated position of the transition t_0 from which the gate position is inferred.

E Bibliography

[1] **Planck** Collaboration, N. Aghanim *et al.*, "Planck 2018 results. VI. Cosmological parameters," *Astron. Astrophys.* **641** (2020) A6, arXiv:1807.06209 [astro-ph.CO]. [Erratum: Astron.Astrophys. 652, C4 (2021)].

[2] E. Aprile, A. E. Bolotnikov, A. L. Bolozdynya, and T. Doke, *Noble Gas Detectors*. Wiley, 2008.

[3] T. Marrodán Undagoitia and L. Rauch, "Dark matter direct-detection experiments," *J. Phys.* **G43** no. 1, (2016) 013001, arXiv:1509.08767.

[4] M. Schumann, "Direct Detection of WIMP Dark Matter: Concepts and Status," *J. Phys. G* **46** no. 10, (2019) 103003, arXiv:1903.03026 [astro-ph.CO].

[5] J. Silk *et al.*, *Particle Dark Matter: Observations, Models and Searches*. Cambridge Univ. Press, Cambridge, 2010.

[6] **XENON** Collaboration, E. Aprile *et al.*, "Projected WIMP sensitivity of the XENONnT dark matter experiment," *JCAP* **11** (2020) 031, arXiv:2007.08796 [physics.ins-det].

[7] F. Zwicky, "Die Rotverschiebung von extragalaktischen Nebeln," *Helv. Phys. Acta* **6** (1933) 110–127.

[8] V. C. Rubin, W. K. Ford, Jr., and N. Thonnard, "Extended rotation curves of high-luminosity spiral galaxies. IV. Systematic dynamical properties, Sa through Sc," *Astrophys. J. Lett.* **225** (1978) L107–L111.

[9] E. Corbelli and P. Salucci, "The Extended Rotation Curve and the Dark Matter Halo of M33," *Mon. Not. Roy. Astron. Soc.* **311** (2000) 441–447, arXiv:astro-ph/9909252.

[10] R. S. Park, W. M. Folkner, A. S. Konopliv, J. G. Williams, D. E. Smith, and M. T. Zuber, "Precession of Mercury's Perihelion from Ranging to the MESSENGER Spacecraft," *Astron. J.* **153** no. 3, (2017) 121.

[11] R. P. Baum and W. Sheehan, *In search of planet Vulcan: The ghost In Newton's clockwork universe*. Springer, 2013.

[12] M. Milgrom, "A Modification of the Newtonian dynamics as a possible alternative to the hidden mass hypothesis," *Astrophys. J.* **270** (1983) 365–370.

[13] M.Markevitch, U.Arizona, D.Clowe and others. https://chandra.harvard.edu/photo/2006/1e0657/index.html. [online; accessed 28-March-2022].

[14] B. Paczynski, "Gravitational microlensing by the galactic halo," *Astrophys. J.* **304** (1986) 1–5.

[15] **EROS-2** Collaboration, P. Tisserand *et al.*, "Limits on the Macho Content of the Galactic Halo from the EROS-2 Survey of the Magellanic Clouds," *Astron. Astrophys.* **469** (2007) 387–404, arXiv:astro-ph/0607207.

[16] B. Carr, K. Kohri, Y. Sendouda, and J. Yokoyama, "Constraints on primordial black holes," *Rept. Prog. Phys.* **84** no. 11, (2021) 116902, arXiv:2002.12778 [astro-ph.CO].

[17] M. Bartelmann and P. Schneider, "Weak gravitational lensing," *Phys. Rept.* **340** (2001) 291–472, arXiv:astro-ph/9912508.

[18] D. Clowe, M. Bradač, A. H. Gonzalez, M. Markevitch, S. W. Randall, C. Jones, and D. Zaritsky, "A direct empirical proof of the existence of dark matter," *Astron. J.* **648** no. 2, (2006) L109.

[19] D. Harvey, R. Massey, T. Kitching, A. Taylor, and E. Tittley, "The non-gravitational interactions of dark matter in colliding galaxy clusters," *Science* **347** (2015) 1462–1465, arXiv:1503.07675 [astro-ph.CO].

[20] J. R. Bond, L. Kofman, and D. Pogosyan, "How filaments are woven into the cosmic web," *Nature* **380** (1996) 603–606, arXiv:astro-ph/9512141.

[21] **2DFGRS** Collaboration, M. Colless *et al.*, "The 2dF Galaxy Redshift Survey: Spectra and redshifts," *Mon. Not. Roy. Astron. Soc.* **328** (2001) 1039, arXiv:astro-ph/0106498.

[22] **SDSS** Collaboration, D. G. York *et al.*, "The Sloan Digital Sky Survey: Technical Summary," *Astron. J.* **120** (2000) 1579–1587, arXiv:astro-ph/0006396.

[23] M. J. Geller and J. P. Huchra, "Mapping the universe," *Science* **246** (1989) 897–903.

[24] V. Springel *et al.*, "Simulating the joint evolution of quasars, galaxies and their large-scale distribution," *Nature* **435** (2005) 629–636, arXiv:astro-ph/0504097.

[25] V. Springel, C. S. Frenk, and S. D. M. White, "The large-scale structure of the Universe," *Nature* **440** (2006) 1137, arXiv:astro-ph/0604561.

[26] S. Dodelson, *Modern Cosmology*. Academic Press, Amsterdam, 2003.

[27] M. Taoso, G. Bertone, and A. Masiero, "Dark Matter Candidates: A Ten-Point Test," *JCAP* **03** (2008) 022, arXiv:0711.4996 [astro-ph].

[28] **Super-Kamiokande** Collaboration, Y. Fukuda *et al.*, "Evidence for oscillation of atmospheric neutrinos," *Phys. Rev. Lett.* **81** (1998) 1562–1567, arXiv:hep-ex/9807003.

[29] S. Tremaine and J. E. Gunn, "Dynamical Role of Light Neutral Leptons in Cosmology," *Phys. Rev. Lett.* **42** (1979) 407–410.

[30] M. Shaposhnikov and I. Tkachev, "The nuMSM, inflation, and dark matter," *Phys. Lett. B* **639** (2006) 414–417, arXiv:hep-ph/0604236.

[31] A. Ringwald, "Exploring the Role of Axions and Other WISPs in the Dark Universe," *Phys. Dark Univ.* **1** (2012) 116–135, arXiv:1210.5081 [hep-ph].

[32] L. Roszkowski, "Particle dark matter: A Theorist's perspective," *Pramana* **62** (2004) 389–401, arXiv:hep-ph/0404052.

[33] F. Kahlhoefer, "Review of LHC Dark Matter Searches," *Int. J. Mod. Phys. A* **32** no. 13, (2017) 1730006, arXiv:1702.02430 [hep-ph].

[34] **ATLAS** Collaboration, M. Aaboud *et al.*, "Combination of searches for invisible Higgs boson decays with the ATLAS experiment," *Phys. Rev. Lett.* **122** no. 23, (2019) 231801, arXiv:1904.05105 [hep-ex].

[35] **ATLAS, CMS** Collaboration, N. Trevisani, "Collider Searches for Dark Matter (ATLAS + CMS)," *Universe* **4** no. 11, (2018) 131.

[36] M. Cirelli, G. Corcella, A. Hektor, G. Hutsi, M. Kadastik, P. Panci, M. Raidal, F. Sala, and A. Strumia, "PPPC 4 DM ID: A Poor Particle Physicist Cookbook for Dark Matter Indirect Detection," *JCAP* **03** (2011) 051, arXiv:1012.4515 [hep-ph]. [Erratum: JCAP 10, E01 (2012)].

[37] J. D. Lewin and P. F. Smith, "Review of mathematics, numerical factors, and corrections for dark matter experiments based on elastic nuclear recoil," *Astropart. Phys.* **6** (1996) 87–112.

[38] **Particle Data Group** Collaboration, P. A. Zyla *et al.*, "Review of Particle Physics," *PTEP* **2020** no. 8, (2020) 083C01.

[39] **DARWIN** Collaboration, J. Aalbers *et al.*, "DARWIN: towards the ultimate dark matter detector," *JCAP* **1611** (2016) 017, arXiv:1606.07001.

[40] E. A. Bagnaschi *et al.*, "Supersymmetric Dark Matter after LHC Run 1," *Eur. Phys. J. C* **75** (2015) 500, arXiv:1508.01173 [hep-ph].

[41] R. Bernabei *et al.*, "The DAMA project: Achievements, implications and perspectives," *Prog. Part. Nucl. Phys.* **114** (2020) 103810.

[42] **XENON** Collaboration, E. Aprile *et al.*, "Search for Electronic Recoil Event Rate Modulation with 4 Years of XENON100 Data," *Phys. Rev. Lett.* **118** no. 10, (2017) 101101, arXiv:1701.00769 [astro-ph.CO].

[43] J. Amare *et al.*, "Annual Modulation Results from Three Years Exposure of ANAIS-112," *Phys. Rev. D* **103** no. 10, (2021) 102005, arXiv:2103.01175 [astro-ph.IM].

[44] C. A. J. O'Hare, "New Definition of the Neutrino Floor for Direct Dark Matter Searches," *Phys. Rev. Lett.* **127** no. 25, (2021) 251802, arXiv:2109.03116 [hep-ph].

[45] H. Päs, and W. Rodejohann, "Neutrinoless Double Beta Decay," *New J. Phys.* **17** no. 11, (2015) 115010, arXiv:1507.00170.

[46] **XENON** Collaboration, J. Angle *et al.*, "First Results from the XENON10 Dark Matter Experiment at the Gran Sasso National Laboratory," *Phys. Rev. Lett.* **100** (2008) 021303, arXiv:0706.0039 [astro-ph].

[47] **XENON100** Collaboration, E. Aprile *et al.*, "Dark Matter Results from 225 Live Days of XENON100 Data," *Phys. Rev. Lett.* **109** (2012) 181301, arXiv:1207.5988 [astro-ph.CO].

[48] **LUX** Collaboration, D. S. Akerib *et al.*, "First results from the LUX dark matter experiment at the Sanford Underground Research Facility," *Phys. Rev. Lett.* **112** (2014) 091303, arXiv:1310.8214 [astro-ph.CO].

[49] **XENON** Collaboration, E. Aprile *et al.*, "Dark Matter Search Results from a One Ton-Year Exposure of XENON1T," *Phys. Rev. Lett.* **121** no. 11, (2018) 111302, arXiv:1805.12562 [astro-ph.CO].

[50] **PandaX-II** Collaboration, Q. Wang *et al.*, "Results of dark matter search using the full PandaX-II exposure," *Chin. Phys. C* **44** no. 12, (2020) 125001, arXiv:2007.15469 [astro-ph.CO].

[51] **LZ** Collaboration, D. S. Akerib *et al.*, "The LUX-ZEPLIN (LZ) Experiment," *Nucl. Instrum. Methods Phys. Res. A* **953** (2020) 163047, arXiv:1910.09124.

[52] **PandaX-4T** Collaboration, Y. Meng *et al.*, "Dark Matter Search Results from the PandaX-4T Commissioning Run," *Phys. Rev. Lett.* **127** no. 26, (2021) 261802, arXiv:2107.13438 [hep-ex].

[53] **DARWIN** Collaboration, J. Aalbers *et al.*, "Solar neutrino detection sensitivity in DARWIN via electron scattering," *Eur. Phys. J. C* **80** no. 12, (2020) 1133, arXiv:2006.03114 [physics.ins-det].

[54] Marrodán Undagoitia, Teresa, "Dark matter searches with liquid xenon detectors." XII International Conference on Interconnections between Particle Physics and Cosmology, 2018.

[55] F. Keiko *et al.*, "High-accuracy measurement of the emission spectrum of liquid xenon in the vacuum ultraviolet region," *Nucl. Instrum. Meth.* **A795** (2015) 293.

[56] I. O. E.M. Gushchin, A.A. Kruglov, "Emission of "hot" electrons from liquid and solid argon and xenon," *JETP* **55** (1982) 860.

[57] G. Bakale, U. Sowada, and W. F. Schmidt, "Effect of an electric field on electron attachment to sulfur hexafluoride, nitrous oxide, and molecular oxygen in liquid argon and xenon," *J. Phys. Chem.* **80** no. 23, (1976) 2556–2559.

[58] K. Ozone, *Liquid Xenon Scintillation Detector for the New $\mu \to e\gamma$ Search Experiment*. PhD thesis, Tokyo U., 2005.

[59] **XENON** Collaboration, E. Aprile *et al.*, "The XENON1T Dark Matter Experiment," *Eur. Phys. J.* **C77** no. 12, (2017) 881, arXiv:1708.07051.

[60] E. R. Shockley, *Study of Excess Electronic Recoil Events in XENON1T*. PhD thesis, The University of Chicago, 2020-12, 2020. http://knowledge.uchicago.edu/record/2743.

[61] **XENON** Collaboration, E. Aprile *et al.*, "Observation of two-neutrino double electron capture in ^{124}Xe with XENON1T," *Nature* **568** no. 7753, (2019) 532–535, arXiv:1904.11002 [nucl-ex].

[62] R. Heaton *et al.*, "Neutron production from thick-target (α, n) reactions," *Nucl. Instrum. Methods Phys. Res. A* **276** no. 3, (1989) 529 – 538.

[63] L. Althueser, S. Lindemann, M. Murra, M. Schumann, C. Wittweg, and C. Weinheimer, "VUV Transmission of PTFE for Xenon-based Particle Detectors," arXiv:2006.05827v1 [physics.ins-det].

[64] D. Cichon, G. Eurin, F. Jörg, T. Marrodán Undagoitia, and N. Rupp, "Transmission of xenon scintillation light through PTFE," *JINST* **15** (2020) 09, arXiv:2005.02444.

[65] **PandaX-II** Collaboration, X. Cui *et al.*, "Dark Matter Results from 54-Ton-Day Exposure of PandaX-II Experiment," *Phys. Rev. Lett.* **119** (2017) 181302, arXiv:1708.06917.

[66] **XENON** Collaboration, E. Aprile *et al.*, "XENON1T Dark Matter Data Analysis: Signal Reconstruction, Calibration and Event Selection," *Phys. Rev. D* **100** no. 5, (2019) 052014, arXiv:1906.04717 [physics.ins-det].

[67] L. Miramonti, "European underground laboratories: An Overview," *AIP Conf. Proc.* **785** no. 1, (2005) 3–11, arXiv:hep-ex/0503054.

[68] **XENON1T** Collaboration, E. Aprile *et al.*, "Conceptual design and simulation of a water Cherenkov muon veto for the XENON1T experiment," *JINST* **9** (2014) P11006, arXiv:1406.2374 [astro-ph.IM].

[69] **XENON** Collaboration, E. Aprile *et al.*, "Material Radioassay and Selection for the XENON1T Dark Matter Experiment," *Eur. Phys. J. C* **77** no. 12, (2017) 890, arXiv:1705.01828.

[70] E. Aprile *et al.*, "Material radiopurity control in the XENONnT experiment," arXiv:2112.05629 [physics.ins-det].

[71] F. Jörg, "Investigation of coating-based radon barriers and studies towards their applicability in liquid xenon detectors," Master's thesis, University of Heidelberg, 2017.

[72] **XENON** Collaboration, E. Aprile *et al.*, "Removing krypton from xenon by cryogenic distillation to the ppq level," *Eur. Phys. J. C* **77** no. 5, (2017) 275, arXiv:1612.04284 [physics.ins-det].

[73] **XENON** Collaboration, E. Aprile *et al.*, "Application and modeling of an online distillation method to reduce krypton and argon in XENON1T," arXiv:2112.12231 [physics.ins-det].

[74] J. Bieringer, C. Schlosser, H. Sartorius, and S. Schmid, "Trace analysis of aerosol bound particulates and noble gases at the BfS in Germany," *Appl. Radiat. Isot.* **67** no. 5, (2009) 672–677.

[75] S. Lindemann and H. Simgen, "Krypton assay in xenon at the ppq level using a gas chromatographic system and mass spectrometer," *Eur. Phys. J. C* **74** (2014) 2746, arXiv:1308.4806 [physics.ins-det].

[76] M.-M. Bé, V. Chisté, C. Dulieu, M. Kellett, X. Mougeot, A. Arinc, V. Chechev, N. Kuzmenko, T. Kibédi, A. Luca, and A. Nichols, *Table of Radionuclides*, vol. 8 of *Monographie BIPM-5*. Bureau International des Poids et Mesures, 2016.

[77] S. Bruenner, D. Cichon, S. Lindemann, T. Marrodán Undagoitia, and H. Simgen, "Radon depletion in xenon boil-off gas," *Eur. Phys. J.* **C77** no. 3, (2017) 143, arXiv:1611.03737.

[78] **XENON100** Collaboration, E. Aprile *et al.*, "Online ^{222} Rn removal by cryogenic distillation in the XENON100 experiment," *Eur. Phys. J. C* **77** no. 6, (2017) 358, arXiv:1702.06942 [physics.ins-det].

[79] **XENON** Collaboration, E. Aprile *et al.*, "^{222}Rn emanation measurements for the XENON1T experiment," *Eur. Phys. J. C* **81** no. 4, (2021) 337, arXiv:2009.13981 [physics.ins-det].

[80] D. Schulte, *Online radon removal for the dark matter Experiment XENONnT (in preparation)*. PhD thesis, WWU Münster(main), expected 2022.

[81] J. Aalbers *et al.*, "A Next-Generation Liquid Xenon Observatory for Dark Matter and Neutrino Physics," arXiv:2203.02309 [physics.ins-det].

[82] M. Yamashita, "Rn rate in various LXe dark matter exeriments." https://github.com/masaki-yamashita/public/blob/main/Rn/experiments/plot_rn_bg_experiments.ipynb, 2019.

[83] **DARWIN** Collaboration, F. Agostini *et al.*, "Sensitivity of the DARWIN observatory to the neutrinoless double beta decay of ^{136}Xe," *Eur. Phys. J. C* **80** no. 9, (2020) 808, arXiv:2003.13407 [physics.ins-det].

[84] M. Schumann, L. Baudis, L. Bütikofer, A. Kish, and M. Selvi, "Dark matter sensitivity of multi-ton liquid xenon detectors," *JCAP* **10** (2015) 016, arXiv:1506.08309 [physics.ins-det].

[85] L. Baudis, A. Ferella, A. Kish, A. Manalaysay, T. Marrodan Undagoitia, and M. Schumann, "Neutrino physics with multi-ton scale liquid xenon detectors," *JCAP* **01** (2014) 044, arXiv:1309.7024 [physics.ins-det].

[86] **XENON** Collaboration, E. Aprile *et al.*, "Design and Performance of the XENON10 Dark Matter Experiment," *Astropart. Phys.* **34** (2011) 679–698, arXiv:1001.2834 [astro-ph.IM].

[87] **PandaX-II** Collaboration, A. Tan *et al.*, "Dark Matter Results from First 98.7 Days of Data from the PandaX-II Experiment," *Phys. Rev. Lett.* **117** no. 12, (2016) 121303, arXiv:1607.07400 [hep-ex].

[88] A. Bradley *et al.*, "Radon-related Backgrounds in the LUX Dark Matter Search," *Phys. Procedia* **61** (2015) 658–665.

[89] K. Abe *et al.*, "XMASS detector," *Nucl. Instrum. Meth. A* **716** (2013) 78–85, arXiv:1301.2815 [physics.ins-det].

[90] **XENON** Collaboration, E. Aprile *et al.*, "Excess electronic recoil events in XENON1T," *Phys. Rev. D* **102** no. 7, (2020) 072004, arXiv:2006.09721 [hep-ex].

[91] J. Aalbers *et al.*, "Streaming analysis for xenon experiments (strax)." https://github.com/AxFoundation/strax, Nov., 2021.

[92] J. Angevaare *et al.*, "Streaming analysis for XENON(nT) (straxen)." https://github.com/XENONnT/straxen, Oct., 2021.

[93] M. T. Subbotin, "On the law of frequency of error," *Mat. Sb.* **31** no. 2, (1923) 296–301.

[94] Cichon, Dominick. Personal communication, July 27th, 2021.

[95] AIR LIQUIDE, France, "Gas Encyclopedia." www.encyclopedia.airliquide.com/xenon. [online; accessed 21-September-2021].

[96] Stillwell, Ben. Internal communication, April, 2019.

[97] **EXO-200** Collaboration, J. B. Albert *et al.*, "Measurement of the Drift Velocity and Transverse Diffusion of Electrons in Liquid Xenon with the EXO-200 Detector," *Phys. Rev.* **C95** no. 2, (2017) 025502, arXiv:1609.04467.

[98] E. S. Morrison, T. Frels, E. H. Miller, R. W. Schnee, and J. Street, "Radon Daughter Plate-out onto Teflon," *AIP Conf. Proc.* **1921** no. 1, (2018) 090002, arXiv:1708.08534 [physics.ins-det].

[99] C. Hasterok, *Gas Purity Analytics, Calibration Studies, and Background Predictions towards the First Results of XENON1T*. PhD thesis, U. Heidelberg (main), 2017.

[100] N. Rupp, *Radon Induced Background in the XENON1T Dark Matter Search Experiment and Studies on Xenon Purity in the HeXe System*. PhD thesis, U. Heidelberg (main), 2021.

[101] Murra, Michael. Internal communication, Feb, 2021.

[102] **Pierre Auger** Collaboration, A. Aab *et al.*, "The Pierre Auger Cosmic Ray Observatory," *Nucl. Instrum. Meth. A* **798** (2015) 172–213, arXiv:1502.01323 [astro-ph.IM].

[103] T. Waldenmaier, J. Bluemer, and H. Klages, "Spectral resolved measurement of the nitrogen fluorescence emissions in air induced by electrons," *Astropart. Phys.* **29** (2008) 205–222, arXiv:0709.1494 [astro-ph].

[104] T. Dandl, T. Heindl, and A. Ulrich, "Fluorescence of nitrogen and air," *JINST* **7** no. 11, (2012) P11005.

[105] A. Lyashenko, T. Nguyen, A. Snyder, H. Wang, and K. Arisaka, "Measurement of the absolute Quantum Efficiency of Hamamatsu model R11410-10 photomultiplier tubes at low temperatures down to liquid xenon boiling point," *JINST* **9** no. 11, (2014) P11021, arXiv:1410.3890 [astro-ph.IM].

[106] A. E. Grün and E. Schopper, "Über die Fluoreszenz von Gasen bei Anregung durch α-Teilchen," *Z. Naturforsch.* **6a** no. 11, (1951) 698–700.

[107] J. Sand, *Alpha Radiation Detection via Radioluminescence of Air*. Tampere University of Technology. Publication. Tampere University of Technology, 12, 2016.

[108] **XENON** Collaboration, E. Aprile *et al.*, "XENON1T dark matter data analysis: Signal and background models and statistical inference," *Phys. Rev. D* **99** no. 11, (2019) 112009, arXiv:1902.11297 [physics.ins-det].

[109] Aalbers, Jelle. Internal communication, May 11th, 2020.

[110] J. Howlett, G. Plante, E. Aprile, Y. Zhang, and M. Kobayashi, "Results from the Xeclipse Liquid Purification Test System for XENONnT." LIght Detection In Noble Elements (LIDINE), 2021.

[111] United Nations Department for General Assembly and Conference Management, *Report of the United Nations Scientific Committee on the Effects of Atomic Radiation (UNSCEAR) 2018*. United Nations, 2018 ed., 2021.

[112] **LZ** Collaboration, D. S. Akerib *et al.*, "The LUX-ZEPLIN (LZ) radioactivity and cleanliness control programs," *Eur. Phys. J. C* **80** no. 11, (2020) 1044, arXiv:2006.02506 [physics.ins-det].

[113] **PandaX** Collaboration, Z. Qian *et al.*, "Low Radioactive Material Screening and Background Control for the PandaX-4T Experiment," arXiv:2112.02892 [physics.ins-det].

[114] Florian Mertes and Stefan Röttger and Annette Röttger, "A new primary emanation standard for Radon-222," *Appl. Radiat. Isot.* **156** (2020) 108928.

[115] P. Herrero Gómez, "Investigation of surface cleaning procedures for the removal of radon daughters from PTFE surfaces and their applicability in liquid xenon detectors," Master's thesis, University of Heidelberg, 2018.

[116] V. Pizzella, *Sub-ppb xenon purity control and study of PTFE surface contamination towards the first results of XENONnT*. PhD thesis, University of Heidelberg, 2021.

[117] S. Armbruster, "Cryogenic ^{222}Rn detector," Bachelor's thesis, University of Heidelberg, 2021.

[118] H. Ryssel and I. Ruge, *Ionenimplantation*. Teubner, Stuttgart, 1. aufl. ed., 1978.

[119] D. Forkel-Wirth, "Exploring solid state physics properties with radioactive isotopes," *Rep. Prog. Phys.* **62** no. 4, (1999) 527.

[120] E. Kugler, D. Fiander, B. Johnson, H. Haas, A. Przewloka, H. Ravn, D. Simon, K. Zimmer, I. Collaboration, *et al.*, "The new CERN-ISOLDE on-line mass-separator facility at the PS-Booster," *Nucl. Instrum. Methods Phys. Res. B* **70** no. 1-4, (1992) 41–49.

[121] J. F. Ziegler, M. D. Ziegler, and J. P. Biersack, "SRIM - The stopping and range of ions in matter (2010)," *Nucl. Instrum. Meth.* **B268** (2010) 1818.

[122] Hamamatsu, *Large photosensitive area Si PIN photodiodes (S3204/S3584 series)*, 2021.

[123] J. Kiko, "Noise reduction for proportional counter signals in the GNO solar neutrino experiment," *Nucl. Instrum. Meth. A* **482** (2002) 434–440.

[124] T. Skwarnicki, *A study of the radiative CASCADE transitions between the Upsilon-Prime and Upsilon resonances*. PhD thesis, Cracow, INP, 1986.

[125] S. Bruenner, D. Cichon, G. Eurin, P. Herrero Gómez, F. Jörg, T. Marrodán Undagoitia, H. Simgen, and N. Rupp, "Radon daughter removal from PTFE surfaces and its application in liquid xenon detectors," *Eur. Phys. J. C* **81** no. 4, (2021) 343, `arXiv:2009.08828 [physics.ins-det]`.

[126] M. Lecher, "Exploring the applicability of electrodeposited copper for reducing the radon background in liquid xenon detectors," Bachelor's thesis, University of Heidelberg, 2019.

[127] D. Budjáš, W. Hampel, M. Heisel, G. Heusser, M. Keillor, M. Laubenstein, W. Maneschg, G. Rugel, S. Schönert, H. Simgen, *et al.*, "Highly sensitive gamma-spectrometers of GERDA for material screening: part 2," `arXiv:0812.0768`.

[128] D. Budjáš, *Germanium detector studies in the framework of the GERDA experiment*. PhD thesis, University of Heidelberg, Heidelberg, May, 2009.

[129] M. Laubenstein, M. Hult, J. Gasparro, D. Arnold, S. Neumaier, G. Heusser, M. Köhler, P. Povinec, J.-L. Reyss, M. Schwaiger, *et al.*, "Underground measurements of radioactivity," *Appl. Radiat. Isot.* **61** no. 2-3, (2004) 167–172.

[130] **GEANT4** Collaboration, S. Agostinelli *et al.*, "GEANT4: A Simulation toolkit," *Nucl. Instrum. Meth. A* **506** (2003) 250–303.

[131] G. Zuzel and H. Simgen, "High sensitivity radon emanation measurements," *Appl. Radiat. Isot.* **67** no. 5, (2009) 889 – 893.

[132] R. Wink, P. Anselmann, D. Doerflinger, W. Hampel, G. Heusser, T. Kirsten, P. Moegel, E. Pernicka, R. Plaga, and C. Schlosser, "The Miniaturized proportional counter HD-2 (Fe) / (Si) for the GALLEX solar neutrino experiment," *Nucl. Instrum. Meth. A* **329** (1993) 541–550.

[133] S. A. Brünner, *Mitigation of ^{222}Rn induced background in the XENON1T dark matter experiment*. PhD thesis, University of Heidelberg, 2017.

[134] P. Pagelkopf and J. Porstendörfer, "Neutralisation rate and the fraction of the positive 218Po-clusters in air," *Atmos. Environ.* **37** no. 8, (Mar, 2003) 1057–1064.

[135] S. Chu, L. Ekström, and R. Firestone, "WWW Table of Radioactive Isotopes," 02, 1999. http://nucleardata.nuclear.lu.se/nucleardata/toi/. accessed May 10, 2020.

[136] F. Mertes, N. Kneip, R. Heinke, T. Kieck, D. Studer, F. Weber, S. Röttger, A. Röttger, K. Wendt, and C. Walther, "Ion implantation of 226Ra for a primary 222Rn emanation standard," *Appl. Radiat. Isot.* **181** (2022) 110093.

[137] P. A. Tipler, R. A. Llewellyn, and G. Czycholl, *Moderne Physik*. Oldenbourg, 2003.

[138] R. F. Lang, A. Brown, E. Brown, M. Cervantes, S. Macmullin, D. Masson, J. Schreiner, and H. Simgen, "A ^{220}Rn source for the calibration of low-background experiments," *JINST* **11** no. 04, (2016) P04004, arXiv:1602.01138 [physics.ins-det].

[139] A. Rytz, "Nouvelles Experiences sur le Spectre Magnetique Alpha du Thorium C et des Longs Parcours du Thorium C'," *C. R. Acad. Sci.* **233** (1951) 790–792.

[140] G. Bertolini, F. Cappellani, G. Restelli, and A. Rota, "Excited states of Tl-208 and Po-212," *Nuclear Physics* **30** (1962) 599–612.

[141] C.-F. Leang, "Spectres alpha de long parcours des poloniums 214 (RaC) et 212 (ThC)," *C. R. Acad. Sci.* **260** no. 11, (1965) 3037.

[142] H. Bateman, "Solution of a system of differentail equations occuring in the theory of radiactive transformations," *Math. Proc. Camb. Philos. Soc.* **15** (1910) 423–427.

[143] L. Moral and A. Pacheco, "Algebraic approach to the radioactive decay equations," *Am. J. Phys.* **71** no. 7, (2003) 684–686.

[144] V. Fedosseev, K. Chrysalidis, T. D. Goodacre, B. Marsh, S. Rothe, C. Seiffert, and K. Wendt, "Ion beam production and study of radioactive isotopes with the laser ion source at ISOLDE," *J. Phys. G* **44** no. 8, (2017) 084006.

[145] **nEXO** Collaboration, G. Adhikari *et al.*, "nEXO: neutrinoless double beta decay search beyond 10^{28} year half-life sensitivity," *J. Phys. G* **49** no. 1, (2022) 015104, arXiv:2106.16243 [nucl-ex].

[146] R. K. Pachauri, M. R. Allen, V. R. Barros, J. Broome, W. Cramer, R. Christ, J. A. Church, L. Clarke, Q. Dahe, P. Dasgupta, *et al.*, *Climate change 2014: synthesis report. Contribution of Working Groups I, II and III to the fifth assessment report of the Intergovernmental Panel on Climate Change*. Ipcc, 2014.

[147] K. Abe *et al.*, "Radon removal from gaseous xenon with activated charcoal," *Nucl. Instrum. Methods Phys. Res. A* **661** no. 1, (2012) 50 – 57.

[148] L. Fischer, "Investigation of material coatings in order to reduce the emanation of radon," Bachelor's thesis, University of Heidelberg, 2016.

[149] M. Piotter, "Investigation of coating methods for radon background reduction in liquid xenon experiments," Bachelor's thesis, University of Heidelberg, 2020.

[150] **XENON100** Collaboration, E. Aprile *et al.*, "The XENON100 Dark Matter Experiment," *Astropart. Phys.* **35** (2012) 573–590, arXiv:1107.2155 [astro-ph.IM].

[151] J. Crank, *The mathematics of diffusion*. Oxford university press, 1979.

[152] M. Wojcik, W. Wlazlo, G. Zuzel, and G. Heusser, "Radon diffusion through polymer membranes used in the solar neutrino experiment Borexino," *Nucl. Instrum. Meth. A* **449** (2000) 158–171.

[153] M. Jiranek and Z. Svoboda, "Transient radon diffusion through radon-proof membranes: a new technique for more precise determination of the radon diffusion coefficient," *Building and Environment* **44** no. 6, (2009) 1318–1327.

[154] **SuperNEMO** Collaboration, F. Mamedov, P. Čermák, K. Smolek, and I. Štekl, "Measurement of radon diffusion through shielding foils for the SuperNEMO experiment," *JINST* **6** (2011) C01068.

[155] Wolfram Research, Inc., "Mathematica, Version 13.0.0." https://www.wolfram.com/mathematica. Champaign, IL, 2021.

[156] J. A. Thornton, "High rate thick film growth," *Annu. Rev. Mater. Res.* **7** no. 1, (1977) 239–260.

[157] EC Europ Coating GmbH. https://www.europcoating.com/. [online; accessed 29-December-2021].

[158] S. Swann, "Magnetron sputtering," *Physics in technology* **19** no. 2, (1988) 67.

[159] J. A. Thornton, "Influence of apparatus geometry and deposition conditions on the structure and topography of thick sputtered coatings," *J. Vac. Sci. Technol.* **11** no. 4, (1974) 666–670.

[160] Y. Mishin, C. Herzig, J. Bernardini, and W. Gust, "Grain boundary diffusion: fundamentals to recent developments," *International Materials Reviews* **42** no. 4, (1997) 155–178.

[161] K. Von Niessen and M. Gindrat, "Plasma spray-pvd: a new thermal spray process to deposit out of the vapor phase," *J. Therm. Spray Tech.* **20** no. 4, (2011) 736–743.

[162] Dr. Laure Plasmatechnologie, Forschung, Entwicklung und Produktions GmbH. http://laure-plasma.de/. [online; accessed 21-February-2022].

[163] Innovative Coating Solutions SA. https://www.incosol4u.com/. [online; accessed 20-February-2022].

[164] D. Franceschini, "Growth, structure, and properties of plasma-deposited amorphous hydrogenated carbon–nitrogen films," in *Advances in Plasma-Grown Hydrogenated Films*, M. H. Francombe, ed., vol. 30 of *Thin Films and Nanostructures*, pp. 217–276. Academic Press, 2002.

[165] X. R. Liu, "Ultra-low level radon assays in gases," *AIP Conference Proceedings* **1672** no. 1, (2015) 070002.

[166] Henkel, "Technical data sheet LOCTITE STYCAST 2850FT (August 2016)." https://bit.ly/2YNZQUu, accessed 2021-10-14.

[167] E. W. Hoppe, C. E. Aalseth, O. T. Farmer, T. W. Hossbach, M. Liezers, H. S. Miley, N. R. Overman, and J. H. Reeves, "Reduction of radioactive backgrounds in electroformed copper for ultra-sensitive radiation detectors," *Nucl. Instrum. Meth. A* **764** (2014) 116–121.

[168] A. M. Suriano, S. M. Howard, C. D. Christofferson, I. J. Arnquist, and E. W. Hoppe, "Developing radiopure copper alloys for high strength low background applications," *AIP Conf. Proc.* **1921** no. 1, (2018) 080001.

[169] M. Schlesinger and M. Paunovic, *Modern electroplating*. John Wiley & Sons, 2011.

[170] R. Winand, "Electrodeposition of metals and alloys—new results and perspectives," *Electrochimica Acta* **39** no. 8-9, (1994) 1091–1105.

[171] M. G. Fontana, "Corrosion of stainless steels corrosion.," *Industrial & Engineering Chemistry* **44** no. 3, (1952) 89A–92A.

[172] Hardy Simgen and Florian Jörg and Mona Piotter, "Suppressing radon emanation by coating techniques." DPG-Frühjahrstagung (Materie und Kosmos), 2021.

[173] Chkvorets, Oleg. Personal communication, January, 2022.

[174] M. Jiránek, K. Rovenská, and A. Froňka, "Radon diffusion coefficient—a material property determining the applicability of waterproof membranes as radon barriers," *Proceedings of the American Association of Radon Scientists and Technologists, Las Vegas NV* (2008) .

[175] G. Rickers and G. Sørensen, "Diffusion of inert gases in copper," *physica status solidi (b)* **32** no. 2, (1969) 597–608.

[176] S. Kawasaki, "Diffusion of xenon in copper," *Journal of Nuclear Materials* **22** no. 2, (1967) 192–196.

[177] H. Mehrer, *Diffusion in solids: fundamentals, methods, materials, diffusion-controlled processes*, vol. 155. Springer Science & Business Media, 2007.

[178] D. Stoychev, I. Tomov, and I. Vitanova, "Recovery and recrystallization of electrodeposited bright copper coatings at room temperature. i. microhardness in relation to coating structure," *Journal of applied electrochemistry* **15** no. 6, (1985) 879–886.

[179] M. Chen, S. Rengarajan, P. Hey, Y. Dordi, H. Zhang, I. Hashim, P. Ding, and B. Chin, "Room temperature self-annealing of electroplated and sputtered copper films," *MRS Online Proceedings Library* **564** no. 1, (1999) 413–420.

[180] W. Teh, L. Koh, S. Chen, J. Xie, C. Li, and P. Foo, "Study of microstructure and resistivity evolution for electroplated copper films at near-room temperature," *Microelectronics Journal* **32** no. 7, (2001) 579–585.

[181] W. Dong, J. Zhang, J. Zheng, and J. Sheng, "Self-annealing of electrodeposited copper thin film during room temperature storage," *Materials Letters* **62** no. 10-11, (2008) 1589–1591.

[182] N. Alshwawreh, M. Militzer, D. Bizzotto, and J.-C. Kuo, "Resistivity-microstructure correlation of self-annealed electrodeposited copper thin films," *Microelectronic engineering* **95** (2012) 26–33.

[183] S.-C. Chang, J.-M. Shieh, B.-T. Dai, M.-S. Feng, and Y.-H. Li, "The effect of plating current densities on self-annealing behaviors of electroplated copper films," *Journal of The Electrochemical Society* **149** no. 9, (2002) G535.

[184] S. Lagrange, S. Brongersma, M. Judelewicz, A. Saerens, I. Vervoort, E. Richard, R. Palmans, and K. Maex, "Self-annealing characterization of electroplated copper films," *Microelectronic Engineering* **50** no. 1-4, (2000) 449–457.

[185] L. Baudis, Y. Biondi, M. Galloway, F. Girard, A. Manfredini, N. McFadden, R. Peres, P. Sanchez-Lucas, and K. Thieme, "Design and construction of Xenoscope — a full-scale vertical demonstrator for the DARWIN observatory," *JINST* **16** no. 08, (2021) P08052, arXiv:2105.13829 [physics.ins-det].

[186] D. Cichon, *Liquid xenon detector physics with XENON1T and HeXe: electric noise stability, background discrimination studies and measurements of the scintillation pulse shape*. PhD thesis, U. Heidelberg (main), 2017.

[187] D. Cichon, G. Eurin, F. Jörg, T. Marrodán Undagoitia, and N. Rupp, "Scintillation decay-time constants for alpha particles and electrons in liquid xenon," arXiv:2201.12483.

[188] D. Cichon, "Identifying ^{222}Rn decay chain events in liquid xenon detectors," Master's thesis, Ruprecht-Karls-Universität Heidelberg, 2015.

[189] P. Barrow *et al.*, "Qualification Tests of the R11410-21 Photomultiplier Tubes for the XENON1T Detector," *JINST* **12** no. 01, (2017) P01024, arXiv:1609.01654.

[190] R. Saldanha, L. Grandi, Y. Guardincerri, and T. Wester, "Model Independent Approach to the Single Photoelectron Calibration of Photomultiplier Tubes," *Nucl. Instrum. Meth.* **A863** (2017) 35, arXiv:1602.03150.

[191] A. Manalaysay *et al.*, "Spatially uniform calibration of a liquid xenon detector at low energies using 83m-Kr," *Rev. Sci. Instrum.* **81** (2010) 073303, arXiv:0908.0616.

[192] S. C. WU, "Nuclear Data Sheets for A = 83," *Nucl. Data Sheets* **92** (2001) 893–1028.

[193] National Instruments. https://www.ni.com/en-us/shop/labview.html. [online; accessed 16-March-2020].

[194] PostgreSQL Global Development Group. https://www.postgresql.org/. [online; accessed 16-March-2020].

[195] F. Jörg, D. Cichon, G. Eurin, L. Hötzsch, T. Marrodán Undagoitia, and N. Rupp, "Characterization of alpha and beta interactions in liquid xenon," arXiv:2109.13735 [physics.ins-det].

[196] iseg Spezialelektronik GmbH, "Technical information NHQ high voltage power supplies (March 2021)." https://bit.ly/3BzqYpM, accessed 2022-02-18.

[197] iseg Spezialelektronik GmbH, "Technical documentation NHR series (January 2022)." https://bit.ly/3v0GrxI, accessed 2022-02-18.

[198] L. Norman, K. Silva, B. J. P. Jones, A. D. McDonald, M. R. Tiscareno, and K. Woodruff, "Dielectric strength of noble and quenched gases for high pressure time projection chambers," *Eur. Phys. J. C* **82** no. 1, (2022) 52, arXiv:2107.07521 [physics.ins-det].

[199] A. Russell, "The dielectric strength of air," *London, Edinburgh Dublin Philos. Mag. J. Sci.* **11** no. 62, (1906) 237–276.

[200] "pySerial." https://github.com/pyserial/pyserial, Sept., 2020.

[201] Riverbank Computing Limited, "PyQt5 Reference Guide." https://www.riverbankcomputing.com/static/Docs/PyQt5/. [online; accessed 20-May-2021].

[202] COMSOL AB, Stockholm, Sweden, "Comsol multiphysics® (v. 5.6)." www.comsol.com. [online; accessed 15-September-2021].

[203] J. D. Jackson, *Klassische Elektrodynamik*. De Gruyter, 2013.

[204] Great Lakes Engineering, Inc. https://www.greatlakeseng.com/. [online; accessed 10-January-2022].

[205] Rupp, Natascha. Personal communication, July, 2021.

[206] P. Virtanen *et al.*, "SciPy 1.0: Fundamental Algorithms for Scientific Computing in Python," *Nature Methods* **17** (2020) 261–272.

[207] C. M. B. Monteiro, L. M. P. Fernandes, J. A. M. Lopes, L. C. C. Coelho, J. F. C. A. Veloso, J. M. F. d. Santos, K. Giboni, and E. Aprile, "Secondary Scintillation Yield in Pure Xenon," *JINST* **2** (2007) P05001, arXiv:physics/0702142.

[208] **PandaX** Collaboration, X. Cao *et al.*, "PandaX: A Liquid Xenon Dark Matter Experiment at CJPL," *Sci. China Phys. Mech. Astron.* **57** (2014) 1476, arXiv:1405.2882.

[209] M. Auger *et al.*, "The EXO-200 detector, part I: Detector design and construction," *JINST* **7** (2012) P05010, arXiv:1202.2192.

[210] C. Silva *et al.*, "Reflectance of Polytetrafluoroethylene (PTFE) for Xenon Scintillation Light," *J. Appl. Phys.* **107** (2010) 064902, arXiv:0910.1056.

[211] C. Levy, "Light propagation and reflection off Teflon in liquid xenon detectors for the XENON100 and XENON1T experiments," *PhD Thesis, University of Münster (Germany)* (2014) .

[212] **LUX** Collaboration, D. S. Akerib *et al.*, "Technical Results from the Surface Run of the LUX Dark Matter Experiment," *Astropart. Phys.* **45** (2013) 34, arXiv:1210.4569.

[213] F. Neves *et al.*, "Measurement of the absolute reflectance of polytetrafluoroethylene (PTFE) immersed in liquid xenon," *JINST* **12** no. 01, (2017) P01017, arXiv:1612.07965.

[214] **XENON** Collaboration, E. Aprile *et al.*, "Intrinsic backgrounds from Rn and Kr in the XENON100 experiment," *Eur. Phys. J. C* **C78** no. 2, (2018) 132, arXiv:1708.03617.

[215] **XENON** Collaboration, E. Aprile *et al.*, "Energy resolution and linearity of XENON1T in the MeV energy range," *Eur. Phys. J. C* **80** no. 8, (2020) 785, arXiv:2003.03825 [physics.ins-det].

[216] M. Y. Barnyakov and A. V. Mironov, "Photocathode aging in MCP PMT," *JINST* **6** (2011) C12026.

[217] J. Jortner *et al.*, "Localized Excitations in Condensed Ne, Ar, Kr, and Xe," *J. Chem. Phys.* **42** no. 12, (1965) 4250–4253.

[218] C. Wahl, M. Hoffmann, T. vom Hoevel, F. Vewinger, and M. Weitz, "Vacuum-ultraviolet absorption and emission spectroscopy of gaseous, liquid, and supercritical xenon," *Phys. Rev. A* **103** (Feb, 2021) 022831.

[219] Auer Kunststofftechnik GmbH & Co. KG, "Material datasheet PTFE." http://www.auer-kunststofftechnik.de/pdf/Datenblatt%20PTFE.PDF, accessed 2020-07-16.

[220] L. M. P. Fernandes *et al.*, "Primary and secondary scintillation measurements in a xenon gas proportional scintillation counter," *JINST* **5** no. 09, (2010) P09006.

[221] **XENON** Collaboration, E. Aprile *et al.*, "Signal Yields of keV Electronic Recoils and Their Discrimination from Nuclear Recoils in Liquid Xenon," *Phys. Rev.* **D97** no. 9, (2018) 092007, arXiv:1709.10149.

[222] P. Kubelka and F. Munk, "Ein Beitrag zur Optik der Farbanstriche," *Zeitschrift für technische Physik* **12** (1931) 593–601.

[223] P. Kubelka, "New Contributions to the Optics of Intensely Light-Scattering Materials. Part I," *J. Opt. Soc. Am.* **38** no. 5, (May, 1948) 448–457.

[224] Cichon, Dominick. Personal communication, April 6th, 2020.

[225] B. Karlsson and C. G. Ribbing, "Optical constants and spectral selectivity of stainless steel and its oxides," *J. Appl. Phys.* **53** no. 9, (1982) 6340–6346.

[226] S. Bricola *et al.*, "Noble-gas liquid detectors: measurement of light diffusion and reflectivity on commonly adopted inner surface materials," *Nucl. Phys. B Proc. Suppl.* **172** (2007) 260 – 262.

[227] Cichon, Dominick. Personal communication, September 6th, 2020.

[228] M. Szydagis *et al.*, "NEST: a comprehensive model for scintillation yield in liquid xenon," *JINST* **6** no. 10, (2011) P10002, arXiv:1106.1613.

[229] S. Andaloro, C. Tunnell, G. R. Rischbieter, and N. Carrara, "Nestcollaboration/nestpy:," June, 2021. https://doi.org/10.5281/zenodo.4897887.

[230] B. Rebel *et al.*, "High Voltage in Noble Liquids for High Energy Physics," *JINST* **9** (2014) T08004, arXiv:1403.3613 [physics.ins-det].

[231] E. Aprile, R. Mukherjee, and M. Suzuki, "Ionization of liquid xenon by ^{241}Am and ^{210}Po alpha particles," *Nucl. Instrum. Meth.* **A307** no. 1, (1991) 119.

[232] E. Aprile *et al.*, "Simultaneous measurement of ionization and scintillation from nuclear recoils in liquid xenon as target for a dark matter experiment," *Phys. Rev. Lett.* **97** (2006) 081302, arXiv:astro-ph/0601552.

[233] S. Labisch and C. Weber, *Technisches Zeichnen*. Springer, 2017.

[234] R. K. Kirby, "Thermal expansion of polytetrafluoroethylene," *Journal of research of the national bureau of standards* **57** no. 2, (1956) 91.

[235] J. Carvill, *Mechanical engineer's data handbook*. Butterworth-Heinemann, 1994.

[236] L. Baudis *et al.*, "A Dual-phase Xenon TPC for Scintillation and Ionisation Yield Measurements in Liquid Xenon," *Eur. Phys. J.* **C78** (2018) 351, arXiv:1712.08607.

[237] M. Morháč, J. Kliman, V. Matoušek, M. Veselskỳ, and I. Turzo, "Identification of peaks in multidimensional coincidence γ-ray spectra," *Nucl. Instrum. Methods Phys. Res. A* **443** no. 1, (2000) 108–125.

[238] R. Brun and F. Rademakers, "ROOT: An object oriented data analysis framework," *Nucl. Instrum. Meth. A* **389** (1997) 81–86.

[239] Online data repository of this work. https://www.doi.org/10.5281/zenodo.5525214.

[240] E. Hogenbirk, M. P. Decowski, K. McEwan, and A. P. Colijn, "Field dependence of electronic recoil signals in a dual-phase liquid xenon time projection chamber," *JINST* **13** no. 10, (2018) P10031, arXiv:1807.07121.

[241] L. Miller, S. Howe, and W. Spear, "Charge Transport in Solid and Liquid Ar, Kr, and Xe," *Phys. Rev.* **166** (1968) 871.

[242] A. K. E.M. Gushchin and I. Obodovskii, "Electron dynamics in condensed argon and xenon," *Sov. Phys. JETP* **55(4)** (1982) 650.

[243] O. Njoya *et al.*, "Measurements of electron transport in liquid and gas Xenon using a laser-driven photocathode," *Nucl. Instrum. Meth. A* **972** (2020) 163965, arXiv:1911.11580.

[244] Marrodán Undagoitia, Teresa. Personal communication, July, 2021.

[245] P. Benetti *et al.*, "A Simple and effective purifier for liquid xenon," *Nucl. Instrum. Meth. A* **329** (1993) 361–364.

[246] E. Aprile *et al.*, "Observation of Anti-correlation between Scintillation and Ionization for MeV Gamma-Rays in Liquid Xenon," *Phys. Rev.* **B76** (2007) 014115, arXiv:0704.1118.

[247] Q. Lin, Y. Wei, J. Bao, J. Hu, X. Li, W. Lorenzon, K. Ni, M. Schubnell, M. Xiao, and X. Xiao, "High Resolution Gamma Ray Detection in a Dual Phase Xenon Time Projection Chamber," *JINST* **9** (2014) P04014, arXiv:1309.5561.

[248] D. J. Temples, J. McLaughlin, J. Bargemann, D. Baxter, A. Cottle, C. E. Dahl, W. H. Lippincott, A. Monte, and J. Phelan, "Measurement of charge and light yields for Xe127 L-shell electron captures in liquid xenon," *Phys. Rev. D* **104** no. 11, (2021) 112001, arXiv:2109.11487 [physics.ins-det].

[249] L. Baudis, P. Sanchez-Lucas, and K. Thieme, "A measurement of the mean electronic excitation energy of liquid xenon," *Eur. Phys. J. C* **81** no. 12, (2021) 1060, arXiv:2109.07151 [physics.ins-det].

[250] **EXO-200** Collaboration, G. Anton *et al.*, "Measurement of the scintillation and ionization response of liquid xenon at MeV energies in the EXO-200 experiment," *Phys. Rev. C* **101** no. 6, (2020) 065501, arXiv:1908.04128 [physics.ins-det].

[251] D. Lorents, "The physics of electron beam excited rare gases at high densities," *Physica B+ C* **82** no. 1, (1976) 19–26.

[252] L. Baudis, H. Dujmovic, C. Geis, A. James, A. Kish, A. Manalaysay, T. Marrodán Undagoitia, and M. Schumann, "Response of liquid xenon to Compton electrons down to 1.5 keV," *Phys. Rev.* **D87** (2013) 115015, arXiv:1303.6891.

[253] A. G. Singh *et al.*, "Analysis of ^{83m}Kr prompt scintillation signals in the PIXeY detector," *JINST* **15** no. 01, (2020) P01023, arXiv:1911.03999 [physics.ins-det].

[254] Cichon, Dominick. Personal communication, January 21st, 2022.

[255] **XENON100** Collaboration, E. Aprile *et al.*, "Analysis of the XENON100 Dark Matter Search Data," *Astropart. Phys.* **54** (2014) 11, arXiv:1207.3458.

[256] J. Thomas and D. Imel, "Recombination of electron-ion pairs in liquid argon and liquid xenon," *Phys. Rev. A* **36** (1987) 6146.

[257] C. E. Dahl, *The physics of background discrimination in liquid xenon, and first results from Xenon10 in the hunt for WIMP dark matter*. PhD thesis, Princeton U., 2009.

[258] **LUX** Collaboration, D. S. Akerib *et al.*, "^{83m}Kr calibration of the 2013 LUX dark matter search," *Phys. Rev. D* **96** no. 11, (2017) 112009, arXiv:1708.02566 [physics.ins-det].

Acknowledgments

I want to dedicate these last lines to the amazing people who supported me throughout the last years and without whom this work would never have been possible. First and foremost, I want to thank my splendid supervisors PD Dr. Teresa Marrodán Undagoitia and Dr. Hardy Simgen, who were always happily sharing their knowledge and experience with me. From personal skills such as time management strategies over thorough feedback to this work, to everyday topics such as the "high art of Karopapier"; I was always certain of their support, advice and their help. I also want to thank JProf. Loredana Gastaldo for happily agreeing to be a second referee to this work. Prof. Manfred Lindner I want to especially thank for giving me the opportunity to become part of his XENON group at MPIK. Growing professionally as well as personally in this excellent group, has enriched my life since the day I joined several years ago as a summer intern.

Working with our miniature XENON detector was a very instructive experience. Though many things turned out to be more difficult than initially thought, working in the HeXe team made every late evening in the lab more bearable and every success much more rewarding. Therefore, I like to thank the "witches" and "wizards" Dr. Natascha Rupp, Dr. Guillaume Eurin, Dr. Dominick Cichon, Luisa Hötzsch and Mona Piotter for making this a truly unique experience. I also like to express again my gratitude to Teresa, who guided the team and was always there for us with good advice. Furthermore, I want to explicitly thank Dominick, Luisa and Mona for their valuable feedback to the content of this work, as well as Sophie Klett for her help with the electric field simulations.

I also like to thank the radon mitigation experts of our group. Together we had the pleasure to discover many ways how radon cannot be blocked, before we finally found a method that is working. Foremost, I want to thank Hardy for his guidance and advice, as well as Manfred for his continued support of the project. Furthermore, I like to thank my former supervisor, XENON1T co-shifter, and "pool-table-decision-maker" Guillaume for providing valuable feedback to the analyses and measurements of this work, though he has already left our group. I am also thankful for the contributions made by Maja Lecher and Mona to the success of this project. Dr. Oleg Chkvorets I want to thank for drawing my interest to the topic of radon diffusion, as well as for many interesting discussions.

None of the measurements in this work could have been done without the great support of our technicians, with whom I always enjoyed to work. I especially want to thank Jonas Westermann for conducting the radon measurements with the miniaturized proportional counters, as well as Steffen Form and Hannes Bonet for their

support during the operation and maintenance of the HeXe detector (sorry that you had to fix so many of our broken wires). A lot of this work is owed to the skill and ingenuity of Michael Reißfelder, which he demonstrated during the production of the PTFE attenuators that proved to be essential for this work. I am also very grateful for the great support I received from our chemist Benjamin Gramlich during the electrochemical depositions, as well as from our radio protection team around Dr. Jochen Schreiner, Ralf Lackner and Dennis Groß, who also carried out the HPGe measurements.

I also like to thank the other members of the XENON group at MPIK: Dr. Joaquim Palacio with whom I share a passion for biking and accounting of the xenon bottles as well as Dr. Tim Wolf and my office companion Dr. Andrii Terliuk, who have provided me with very helpful feedback to this work. But also to the other members of our great group Dr. Veronica Pizzella, Robert Hammann, Matteo Guida as well as the members who have already left our group Dr. Stefan Brünner, Dr. Constanze Hasterok, Dr. Ludwig Rauch, Oliver Wack and Pablo Herrero Gómez. I also like to thank my part-time office mate Pablo Martinez-Mirave for keeping me sane during writing and the special (crochet) snow-flakes. This list could be continued by many more names and I apologize for not being able to include everyone who made the last years so enjoyable!

Zu guter Letzt geht mein Dank an meine Familie und Freunde. Meinen Eltern Kordula und Wolfgang möchte ich dafür danken, dass sie meinen Forscherdrang trotz gelegentlicher "Sicherheitsbedenken" immer gefördert haben und mir meinen Werdegang möglich gemacht haben. Auch bei Ursula und Ralf will ich mich für die vielen tollen Momente bedanken. Ein ganz besonderer Dank geht an meine wunderbare Partnerin Jule, die mich immer unterstützt und motiviert hat und viel Verständnis für die gelegentlichen Ruhestörungen durch bedürftige Detektoren zeigen musste. Ohne euch hätte ich das niemals geschafft!

Thank you very much!

Heidelberg, 11.04.2022 Florian Jörg